



Hyndman, Lauren (2021) *Mathematical modelling to guide experimental protocols for in vitro cell culture*. PhD thesis.

<https://theses.gla.ac.uk/82510/>

Copyright and moral rights for this work are retained by the author

A copy can be downloaded for personal non-commercial research or study, without prior permission or charge

This work cannot be reproduced or quoted extensively from without first obtaining permission in writing from the author

The content must not be changed in any way or sold commercially in any format or medium without the formal permission of the author

When referring to this work, full bibliographic details including the author, title, awarding institution and date of the thesis must be given

Enlighten: Theses

<https://theses.gla.ac.uk/>
research-enlighten@glasgow.ac.uk

**Mathematical modelling to guide experimental protocols for
in vitro cell culture**

Lauren Hyndman

Submitted in fulfilment of the requirements for the
Degree of Doctor of Philosophy

James Watt School of Engineering
College of Science and Engineering
University of Glasgow



University
of Glasgow

October 2021

Abstract

The development of a single drug from discovery to approval is a long and expensive process. Often, many potential drugs that appear promising in preclinical studies are subsequently eliminated during human clinical trials. In recent years, there has been a move away from animal testing in favour of cell-based *in vitro* methods, so to improve the correlation between the outcome of preclinical studies and clinical trials, and therefore to increase the efficiency of the drug development process, it is essential that *in vitro* tests provide physiologically relevant results. There have been great advances in the development of *in vitro* cell culture techniques, from the traditional static monolayer to the advent of flow-based bioreactor devices, and a common approach is to combine conventional cell culture methods with sophisticated systems that expose cells to conditions that are more representative of their native environment. One of the drawbacks associated with the advancement of *in vitro* techniques is that there is a lack of knowledge and understanding of the physical and chemical environment generated within complex cell culture systems. To overcome this obstacle, mathematical models can be employed to characterise the conditions to which cells are exposed within novel *in vitro* devices. Mathematical analysis can offer insight to aid in the effective tailoring of operating parameters and interpretation of experimental results, as well as providing estimations of quantities that can be difficult or impossible to obtain experimentally.

The aim of this thesis is to use mathematical models to describe the environment within static and dynamic *in vitro* cell culture systems, with the aim of highlighting the relationships between key model parameters and, ultimately, guiding the design and set-up of experiments. Mathematical models of varying complexity are developed, ranging from 1D diffusion-reaction partial differential equations to coupled 3D models of fluid flow and solute transport. A variety of mathematical techniques are employed to solve each model: in Chapter 2, analytical approaches are used to derive approximations to the numerical solutions, and the models in Chapter 3 are solved using the finite element method, implemented via commercially available software. In each chapter, simple expressions are derived from the governing equations to provide information on how to adjust experimentally controllable operating parameters such that the desired cell culture conditions can be achieved. In Chapter 4, the main goal of the thesis is realised by applying the models developed in Chapter 3 to help determine the optimal configuration of a commercially available bioreactor device for two different applications.

Contents

Abstract	i
Acknowledgements	xi
Declaration	xiii
Presentations and publications	xiv
1 Introduction	1
2 Modelling solute transport in a static <i>in vitro</i> cell culture system	10
2.1 Existing models from the literature	11
2.2 The mathematical model	12
2.3 Method of Laplace transforms	17
2.4 Solutions for case A	20
2.4.1 Deriving the VIE	20
2.4.2 Approximate solutions	21
2.4.3 Numerical method for solving the VIEs	28
2.4.4 Comparing the solution of the VIE with the approximate solutions . . .	30
2.5 Solutions for case B	35
2.5.1 Deriving the VIE	35
2.5.2 Approximate solutions	37
2.5.3 Numerical method for solving the VIEs	46
2.5.4 Comparing the solution of the VIE with the approximate solutions . . .	48
2.6 Discussion	54
2.6.1 Model limitations	54
2.6.2 Utility of the model	55
3 Modelling fluid flow and solute transport in a dynamic <i>in vitro</i> cell culture system	59
3.1 Existing models from the literature	60
3.2 Modelling fluid flow and solute transport in an arbitrary bioreactor device . . .	62
3.2.1 Fluid dynamics	62

3.2.2	Solute transport	63
3.2.3	Interaction between the solute and the cells	63
3.2.4	Solving the model	64
3.3	Modelling fluid flow and solute transport in the Kirkstall QV900	65
3.3.1	Single chamber models	66
3.3.2	Connected chamber model	68
3.3.3	Numerical implementation	70
3.4	Results	77
3.4.1	Fluid dynamics	77
3.4.2	Solute transport	79
3.5	Discussion	95
3.5.1	Utility of the models	95
3.5.2	Challenges associated with mathematical modelling	107
4	Informing experimental set-up in the Kirkstall QV900 for two different applica- tions	109
4.1	Overview of the mathematical modelling	110
4.2	Application to liver zonation	112
4.2.1	The mathematical model	113
4.2.2	The experiments	118
4.2.3	Summary	121
4.3	Application to parasite infection	121
4.3.1	The mathematical model	122
4.3.2	The experiments	128
4.3.3	Summary	130
4.3.4	Conclusions	132
5	Conclusions and future work	134
A	Solutions of the multiple pathway models from Chapter 2	139
A.1	Solutions for case A	139
A.2	Solutions for case B	142
B	Solutions of the linear models from Chapter 2	148
B.1	Solutions for case A	148
B.2	Solutions for case B	150

List of Tables

3.1	Parameter values. *Representative cell number chosen following discussions with experimental researchers. †Area covered by the cells calculated by assuming the cells occupy the entire base of the chamber. ‡Height of cell region calculated by multiplying the total number of cells by the volume of a smooth muscle cell, then dividing by the area covered by the cells ($h = NV_{cell}/A$). **Nominal value chosen for inlet sirolimus concentration. ††Cell density calculated by dividing the total number of cells by the area covered by the cells ($d = N/A$).	74
3.2	Percentage difference in cell surface shear stress, cell surface O ₂ concentration and mass flux at the inlet when comparing results between consecutive mesh settings. These results have been provided for chamber 1 as an example, with similar errors calculated for the remaining chambers.	76
3.3	Number of mesh elements and typical simulation time for each model using a quad core Intel® Core™ i7-6700 CPU @ 3.40GHz.	76
4.1	Number of mesh elements and typical simulation time for each insert height using a quad core Intel® Core™ i7-6700 CPU @ 3.40GHz.	115
4.2	Parameter values. *Input flow rate used in experiments. †Cell number chosen assuming 20% of 1 million hepatocytes attach to the cover slip during cell culture. ‡Area covered by the cells on a 13 mm diameter cover slip. **Cell density calculated by dividing the total number of cells by the area covered by the cells ($d = N/A$).	115
4.3	Mean O ₂ concentration and maximum shear stress observed at the cell surface for each insert height.	117
4.4	The number of mesh elements in a single chamber and the typical simulation time for each insert height using a quad core Intel® Core™ i7-6700 CPU @ 3.40GHz.	124
4.5	Parameter values. *Input flow rate used in experiments. †Number of cells used in experiments. ‡Area covered by the cells on a 12 mm diameter cover slip. **Cell density calculated by dividing the total number of cells by the area covered by the cells ($d = N/A$).	125
4.6	Mean flow speed just above the cell surface and maximum shear stress at the cell surface in a single chamber for each insert height.	126

List of Figures

1.1	Schematic drawing illustrating the key stages of the drug development process.	1
1.2	The advancement of <i>in vitro</i> cell culture methods.	3
1.3	Comparison of some key features of 2D and 3D cell culture systems, where green and red represent advantages and limitations, respectively.	5
1.4	Some advantages of microfluidic cell culture systems.	7
2.2.1	Schematic drawing illustrating a typical static <i>in vitro</i> experimental set-up (not to scale).	12
2.2.2	Schematic drawing illustrating the behaviour of M-M kinetics.	13
2.3.1	Schematic drawing of the Bromwich contour, C	18
2.4.1	Schematic drawing illustrating the 1D domain and non-dimensional equations for case A.	20
2.4.2	Schematic drawing illustrating the area under the curve $e^{-x^2/t}$ and an approximation to this area using lower (left) and upper (right) Riemann sums.	26
2.4.3	Solution to the VIE from case A for various values of α with $\beta = 1$, showing the dependence of the solute concentration at the cell surface, $c(1, t)$, on the non-dimensional parameter α	31
2.4.4	Comparing the solution to the VIE from case A and the small β solution for various values of β , with $\alpha = 1$	32
2.4.5	Comparing the solution to the VIE from case A and the large β solution for various values of β , with $\alpha = 1$. Note that when $\beta = 1$, the large β solution to second order is equal to 1, i.e. the large β solution to leading order, so the red and blue lines in the upper plot are overlapping.	33
2.4.6	Comparing the solution to the VIE from case A and the small t solution for $0 \leq t \leq 1$, with $\alpha = \beta = 1$. The inset plot highlights the good agreement between the solutions for $0 \leq t \leq 0.1$	34
2.5.1	Schematic drawing illustrating the 1D domain and non-dimensional equations for case B.	35
2.5.2	Schematic drawing illustrating the area under the curve $e^{-x^2/4t}$ and an approximation to this area using lower (left) and upper (right) Riemann sums.	42
2.5.3	Solution to the VIE from case B for various values of α with $\beta = \mu = 1$, showing the dependence of the solute concentration at the cell surface, $c(1, t)$, on the non-dimensional parameter α	49

2.5.4 Comparing the solution to the VIE from case B and the steady-state solution, with $\alpha = 10$ and $\beta = \mu = 1$	49
2.5.5 Solution to the VIE from case B for various values of μ with $\alpha = \beta = 1$, showing the dependence of the solute concentration at the cell surface, $c(1, t)$, on the non-dimensional parameter μ	50
2.5.6 Comparing the solution to the VIE from case B with the small β solution for various values of β , with $\alpha = \mu = 1$	51
2.5.7 Comparing the solution to the VIE from case B with the large β solution for various values of β , with $\alpha = \mu = 1$. Note that when $\beta = 1$, the large β solution to second order is equal to 1, i.e. the large β solution to leading order, so the red and blue lines in the upper plot are overlapping.	52
2.5.8 Comparing the solution to the VIE from case B with the small t solution for $0 \leq t \leq 1$, with $\alpha = \beta = \mu = 1$. The inset plot highlights the good agreement between the solutions for $0 \leq t \leq 0.1$	53
3.3.1 The Kirkstall QV900 cell culture system [1].	65
3.3.2 Idealised 3D representation of a single QV900 chamber generated in COMSOL Multiphysics [®] 5.3, showing the orientation of the x -, y - and z - axes with the origin located at the centre of the base of the chamber (indicated by the red dot). Note that length scales on the axes are in metres.	66
3.3.3 Idealised 3D representation of two connected QV900 chambers generated in COMSOL Multiphysics [®] 5.3, showing the orientation of the x -, y - and z - axes with the origin located at the centre of the base of the first chamber (indicated by the red dot). Note that length scales on the axes are in metres.	69
3.3.4 Schematic drawing of the computational geometry for a single QV900 chamber where the cell region is represented by a separate domain (not to scale). Here, Ω and Γ are used to label domains and boundaries, respectively.	71
3.3.5 Schematic drawing of the computational geometry for a single QV900 chamber where the cell region is represented by a flux boundary condition. Here, Ω and Γ are used to label domains and boundaries, respectively.	72
3.3.6 Schematic drawing of the computational geometry for two connected QV900 chambers where the cell region is represented by a flux boundary condition. Here, Ω and Γ are used to label domains and boundaries, respectively.	73
3.4.1 Streamlines and magnitude of velocity through the centre of the chamber (y, z plane, upper plots), magnitude of velocity through the centre of the chamber in a log scale (y, z plane, middle plots) and magnitude of shear stress at the cell surface (y, x plane), for $Q = 100 - 200 \mu\text{l min}^{-1}$	82

3.4.2 Streamlines and magnitude of velocity through the centre of the chamber (y, z plane, upper plots), magnitude of velocity through the centre of the chamber in a log scale (y, z plane, middle plots) and magnitude of shear stress at the cell surface (y, x plane), for $Q = 300 - 400 \mu\text{l min}^{-1}$	83
3.4.3 Streamlines and magnitude of velocity through the centre of the chamber (y, z plane, upper plots), magnitude of velocity through the centre of the chamber in a log scale (y, z plane, middle plots) and magnitude of shear stress at the cell surface (y, x plane), for $Q = 500 - 600 \mu\text{l min}^{-1}$	84
3.4.4 Streamlines and magnitude of velocity through the centre of the chamber (y, z plane, upper plots), magnitude of velocity through the centre of the chamber in a log scale (y, z plane, middle plots) and magnitude of shear stress at the cell surface (y, x plane), for $Q = 700 - 800 \mu\text{l min}^{-1}$	85
3.4.5 Streamlines and magnitude of velocity through the centre of the chamber (y, z plane, upper plots), magnitude of velocity through the centre of the chamber in a log scale (y, z plane, middle plots) and magnitude of shear stress at the cell surface (y, x plane), for $Q = 900 - 1000 \mu\text{l min}^{-1}$	86
3.4.6 Relationships between input flow rate and maximum flow speed at the cell surface (upper plot) and maximum shear stress magnitude at the cell surface (lower plot), with the inset plots highlighting each relationship for $Q = 100 - 400 \mu\text{l min}^{-1}$. Note that since the velocity is equal to zero on the cell surface, the flow speed is evaluated just above the cell surface at a height of $z = h$	87
3.4.7 Streamlines and magnitude of velocity through the centre of each connected chamber (y, z plane, upper plots), magnitude of velocity through the centre of each connected chamber in a log scale (y, z plane, middle plots) and magnitude of shear stress at the cell surface of each connected chamber (y, x plane), for $Q = 100 \mu\text{l min}^{-1}$. . .	88
3.4.8 APAP concentration profiles through the centre of the chamber (y, z plane) and at the cell surface (y, x plane), for $Q = 100 - 300 \mu\text{l min}^{-1}$ and $c_{APAP}^{in} = 0.4 \text{ mol m}^{-3}$. . .	89
3.4.9 APAP concentration profiles through the centre of the chamber (y, z plane) and at the cell surface (y, x plane), for $Q = 400 - 600 \mu\text{l min}^{-1}$ and $c_{APAP}^{in} = 0.4 \text{ mol m}^{-3}$. . .	90
3.4.10 APAP concentration profiles through the centre of the chamber (y, z plane) and at the cell surface (y, x plane), for $Q = 700 - 1000 \mu\text{l min}^{-1}$ and $c_{APAP}^{in} = 0.4 \text{ mol m}^{-3}$. .	91
3.4.11 O_2 concentration profiles through the centre of the chamber (y, z plane) and at the cell surface (y, x plane) for different cell types, for $Q = 100 \mu\text{l min}^{-1}$ and $c_{\text{O}_2}^{in} = 0.21 \text{ mol m}^{-3}$	92
3.4.12 Relationships between input flow rate and mean APAP concentration at the cell surface (upper plot) and mean O_2 concentration at the cell surface (lower plot), for $c_{APAP}^{in} = 0.4 \text{ mol m}^{-3}$ and $c_{\text{O}_2}^{in} = 0.21 \text{ mol m}^{-3}$, respectively.	93

3.4.1	O_2 concentration profiles through the centre of each connected chamber (y, z plane) and at the cell surface of each connected chamber (y, x plane), for $Q = 100 \mu\text{l min}^{-1}$ and $c_{\text{O}_2}^{\text{in}} = 0.21 \text{ mol m}^{-3}$	94
3.5.1	Values of $K_{\text{O}_2}/c_{\text{O}_2}$ calculated over a range of inlet concentrations from $c_{\text{O}_2}^{\text{in}} = 0.01 - 0.10 \text{ mol m}^{-3}$ (left) and from $c_{\text{O}_2}^{\text{in}} = 0.15 - 1.00 \text{ mol m}^{-3}$ (right), for the lowest and highest input flow rates of $Q = 100$ and $1000 \mu\text{l min}^{-1}$	100
3.5.2	Comparison between simulated cell surface O_2 concentration profiles for the original inlet concentration ($c_{\text{O}_2}^{\text{in}} = 0.21 \text{ mol m}^{-3}$) and a new inlet concentration ($c_{\text{O}_2}^{\text{in}*} = 0.30 \text{ mol m}^{-3}$), for $Q = 100 \mu\text{l min}^{-1}$. The prediction obtained from (3.5.7) is illustrated by the dashed line.	101
3.5.3	Values of γ calculated over a range of new inlet concentrations from $c_{\text{O}_2}^{\text{in}*} = 0.01 - 1.00 \text{ mol m}^{-3}$ for the lowest and highest input flow rates of $Q = 100$ and $1000 \mu\text{l min}^{-1}$, using $c_{\text{O}_2}^{\text{in}} = 0.21 \text{ mol m}^{-3}$ as the original inlet concentration.	101
3.5.4	Comparison between simulated and predicted mean cell surface O_2 concentrations for $Q = 100 \mu\text{l min}^{-1}$ (left) and $Q = 1000 \mu\text{l min}^{-1}$ (right).	102
3.5.5	Comparison of the total and convective fluxes at the inlet to each chamber (left) and the velocity profiles along the diameter (from bottom to top) of each chamber inlet (right), for $Q = 100 \mu\text{l min}^{-1}$	105
3.5.6	Comparison between simulated (solid lines) and predicted (dashed lines) cell surface O_2 concentration profiles for $c_{\text{O}_2}^{\text{in}} = 0.21 \text{ mol m}^{-3}$ and $Q = 100 \mu\text{l min}^{-1}$ (upper left), $Q = 300 \mu\text{l min}^{-1}$ (upper right), $Q = 500 \mu\text{l min}^{-1}$ (lower left) and $Q = 700 \mu\text{l min}^{-1}$ (lower right).	106
4.1.1	Schematic drawing of the computational geometry for a single QV900 chamber where the cells reside on a cover slip at the base of the chamber. Here, Ω and Γ are used to label domains and boundaries, respectively.	111
4.2.1	Zonation of liver metabolism. High oxygen exposure of hepatocytes in the periportal region compared to low exposure in the perivenous zone. Glucose production carried out through gluconeogenesis in the periportal zone. Glucose utilisation carried out by glycolysis in the perivenous zone. [2]	113
4.2.2	Idealised 3D representation of a single QV900 chamber generated in COMSOL Multiphysics [®] 5.3, showing the orientation of the x -, y - and z - axes with the origin located at the centre of the base of the chamber (indicated by the red dot). Here, H_{in} and H_{out} denote the height of the chamber at the inlet side and the outlet side, respectively, and h is the height of the insert. Note that length scales on the axes are in metres.	114
4.2.3	Simulated cell surface O_2 concentration profiles for each value of h . For each insert height, the concentration profiles are plotted across the diameter of the cover slip from the inlet to the outlet side of the chamber (left to right).	116

4.2.4 Simulated O ₂ concentration profiles across the centre of the cell surface for $h = 7$ mm (periportal), $h = 4$ mm (central) and $h = 0$ mm (perivenous), illustrating the estimated O ₂ gradient that could be achieved across three QV900 chambers.	117
4.2.5 Schematic setup on the inside of the QV900 wells. [2]	118
4.2.6 Functional analysis of primary rat hepatocytes in each zone compared to standard 2D static conditions. After 48 h under flow conditions or static conditions functional parameters were assessed (A) ATP ($n = 4$), (B) Albumin secretion ($n = 4$). Both were normalised to protein concentration calculated using a Bradford assay, and (C) Cytotoxicity of shear stress analysed by LDH assay. Data shown as LDH released (in media)/Total LDH (present in cells + media). [2]	119
4.2.7 Left: Verification of zonation. Western blot analysis of zone specific protein markers. Right: Confirmation of zone specific metabolism. Cells were dosed with 50 mM paracetamol for 48 h. Viability (calculated using ATP assay) was normalised to protein concentration calculated using a Bradford assay. $n = 3$, student's test used for statistical analysis. $*p < 0.05$. [2]	121
4.3.1 Idealised 3D representation of a single QV900 chamber generated in COMSOL Multiphysics [®] 5.3, showing the orientation of the x -, y - and z - axes with the origin located at the centre of the base of the chamber (indicated by the red dot). Here, H_{in} and H_{out} denote the height of the chamber at the inlet side and the outlet side, respectively, and h is the height of the insert. Note that length scales on the axes are in metres.	123
4.3.2 Idealised 3D representation of the final experimental configuration of six connected QV900 chambers generated in COMSOL Multiphysics [®] 5.3, showing the orientation of the x -, y - and z - axes with the origin located at the centre of the base of the first chamber (indicated by the red dot). Note that length scales on the axes are in metres.	124
4.3.3 Streamlines and magnitude of velocity through the centre of the chamber (y, z plane, upper plots) and magnitude of shear stress at the base of the chamber (x, y plane, lower plots), for chamber 1 containing no insert (left) and chamber 4 containing a 9 mm insert (right).	127
4.3.4 Simulated O ₂ concentration profiles at the base of chambers 1, 2 and 3 containing no inserts (left) and chambers 4, 5 and 6 containing 9 mm inserts (right). Note that the concentration profiles are plotted across the diameter of the base of each chamber from the inlet to the outlet side of the chamber (left to right).	127
4.3.5 Box and whisker diagram showing the percentage of infected cells over a range of different infection ratios, of parasite:macrophage number, and different flow conditions. Significance tested using a two tailed t-test $p < 0.01 = **$ $p < 0.0001 = ****$ ns = not significant $N = 6$. [3]	129

- 4.3.6 Bar graph showing percentage of *L. major* amastigotes that incorporated the EdU marker into DNA at the three different conditions, static (0 m/s), low flow (1.45×10^{-9} m/s) and high flow (1.23×10^{-7} m/s). * = $p < 0.05$ $N = 3$. [3] 129
- 4.3.7 Phagocytosis of fluorescent latex beads ($2\mu\text{m}$) by infected PEMs in the three culture systems (static, slow flow rate 1.45×10^{-9} m/s and fast flow rate 1.23×10^{-7} m/s). Phagocytosis is significantly higher in static than in flow system ($p < 0.05$ by one-way ANOVA). The data are means \pm standard deviations (SD), $N = 3$. Infection rate $> 80\%$. [3] 131
- 4.3.8 Macropinocytosis of pHrodo Red dextran by infected PEMs in the three culture systems (static, slow flow rate 1.45×10^{-9} m/s and fast flow rate 1.23×10^{-7} m/s). Macropinocytosis is significantly higher in static than in flow system ($p < 0.05$ by one-way ANOVA). The data are means \pm standard deviations (SD), $N = 3$. Infection rate $> 80\%$. [3] 131

Acknowledgements

Firstly, I would like to thank my primary supervisor, Dr Sean McGinty, for providing me with the opportunity to work on this project. Your guidance has been invaluable, and I would especially like to thank you for encouraging me to persevere through the tougher parts of the project. The completion of this thesis would not have been possible without your patience and understanding, and I consider myself lucky to have had such a supportive supervisor. Secondly, I must extend thanks to my second supervisor, Prof Sean McKee, who has been a source of great knowledge and wisdom. Your feedback and advice is always highly appreciated, and I thank you for taking the time to supervise me during this project. It has been a pleasure to work with you both over the past few years.

Besides my supervisors, there are a number of people I would like to acknowledge their contribution towards my PhD journey.

- To the research group: thank you for listening to my presentations during the monthly meetings and for participating in the useful conversations that often followed.
- To Prof Nigel Mottram: thank you for offering your valuable time and advice, the discussions we had with you were most helpful and greatly appreciated.
- To Kirkstall: thank you to the various staff members who were responsible for supplying a financial donation to cover the cost of the COMSOL license, for sending a spare QV900 device and for answering my questions.
- To our experimental collaborators: thank you for providing me with the opportunity to put my models to use in the ‘real world’, allowing me to see the impact my work could have in a practical setting. It was refreshing to think about things from a different perspective and I am grateful I had the chance to work as part of an interdisciplinary team.

Without financial support, I would never have had the opportunity to spend all these years at university. I feel very privileged to have been provided with a free education, and for this research project, I gratefully acknowledge funding from the EPSRC.

Finally, I would like to thank my family for their unwavering love and support. You have always taught me that all I can do is try my best, but without putting me under any pressure you have also encouraged me to have the confidence to aim high. A special thank you goes to my fiancé Jonny, words can't describe how much you have helped me during this past year and I know I would not have been able to finish this project without you. Thank you for always believing in me. I hope I have made you all proud!

Declaration

With the exception of introductory material appearing in each chapter, and experimental work appearing in Chapter 4, all work in this thesis was carried out by the author unless otherwise explicitly stated.

Presentations and publications

Poster and oral presentation, conference proceedings

IVTS 2016, Glasgow, UK

doi: 10.1089/aivt.2016.29007.abstracts

Oral presentation

CMALS ECR symposium 2016, Glasgow, UK

Conference proceedings

CMBE 2017, Pittsburg, USA

isbn: 9780956291448

Poster and oral presentation

BME away day 2017, Glasgow, UK

Poster and oral presentation

MEDDS 2018, Glasgow, UK

Publication of research article

L. Tomlinson, **L. Hyndman**, J. W. Firman, R. Bentley, J. A. Kyffin, S. D. Webb, S. McGinty, and P. Sharma. *In vitro* liver zonation of primary rat hepatocytes. *Front Bioeng Biotechnol*, 7:17, 2019. doi: 10.3389/fbioe.2019.00017.

Video presentation

CMALS creative presentation competition 2019, Glasgow, UK

Poster and oral presentation

ACTC 2019, Cardiff, UK

Poster presentation

3DbioNet 2019, Sheffield, UK

Publication of research article

A. O’Keeffe, **L. Hyndman**, S. McGinty, A. Riezk, S. Murdan and S. L. Croft. Development of an *in vitro* media perfusion model of *Leishmania major* macrophage infection. *PLoS One*, 14(7):e0219985, 2019. doi: 10.1371/journal.pone.0219985.

Poster and oral presentation

BME away day 2020, Glasgow, UK

Publication of research article

L. Hyndman, S. McKee, N. J. Mottram, B. Singh, S. D. Webb, and S. McGinty. Mathematical modelling of fluid flow and solute transport to define operating parameters for *in vitro* perfusion cell culture systems. *Interface Focus*, 10:20190045, 2020. doi:10.1098/rsfs.2019.0045.

Chapter 1

Introduction

The development of drugs is a lengthy and expensive process; on average, bringing a single drug from initial research to market costs billions of pounds and takes over a decade to complete. These costs are exacerbated by the development of potential drugs that are later deemed unsuccessful, so it is vital that each stage of the drug development process is as efficient as possible so that unlikely drug candidates can be eliminated at the earliest opportunity. The key stages of the drug development process are illustrated in Fig. 1.1, and a detailed description of each stage is provided in [4].

Before the drug development process can begin, a target for the potential drug must be determined: this is typically a protein that has been identified as causing or leading to the disease of interest. The conventional approach to the discovery stage involves screening thousands of

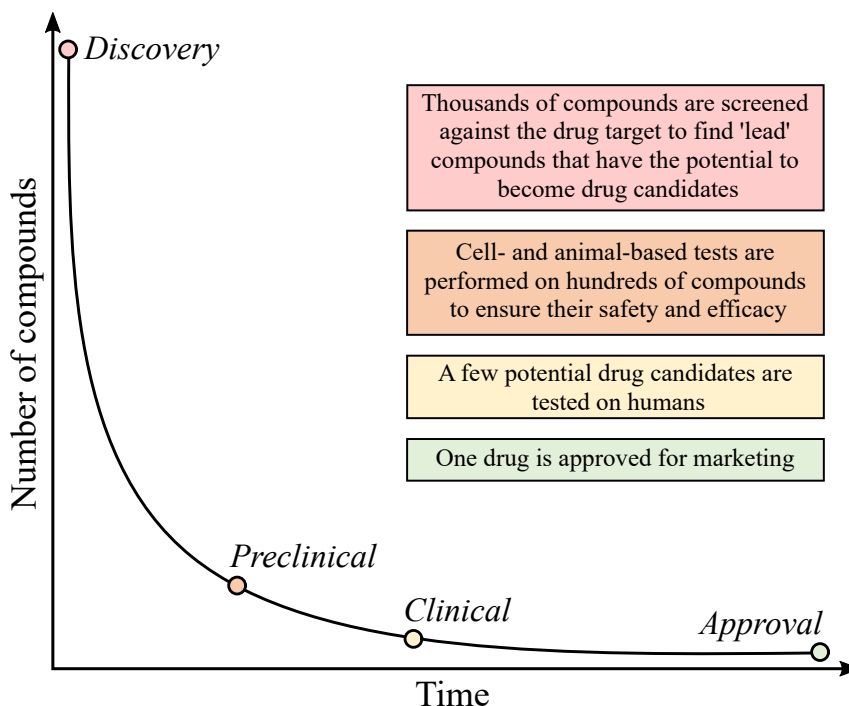


Figure 1.1: Schematic drawing illustrating the key stages of the drug development process.

compounds to establish those that interact with the drug target. Traditionally, the compounds are extracted from natural materials which have been collected for this purpose, then screened manually. Clearly this is highly inefficient, but advancements in robotics have led to the development of high-throughput screening, allowing this process to be automated in order to reduce the time and costs associated with screening thousands of compounds using traditional laboratory techniques. Further technological advancements have led to a more modern approach to drug discovery whereby computer simulations are utilised to design a potential drug based on knowledge of the molecular structure of the drug target. This approach significantly improves the likelihood of obtaining a successful drug and reduces unnecessary costs associated with the further development of potential drugs that are likely to fail.

A small number of promising compounds progress to the preclinical stage of drug development where the pharmacokinetics, pharmacodynamics and toxicity of potential drugs are evaluated using *in vitro* and *in vivo* methods. Cell-based techniques are employed to study pharmacokinetics and pharmacodynamics, which provide information about the action of a potential drug on the body and the target, respectively. Toxicity studies, essential for demonstrating the safety of a potential drug before it can progress to human clinical trials, are traditionally performed using animal models.

Many of the potential drug candidates that pass the preclinical stage of development ultimately fail in clinical trials, where it is not uncommon for previously unknown adverse effects to be discovered. The primary reason for this is that animal models can be poor predictors of the human response: species differences in key metabolic processes, such as the way in which chemicals are absorbed, altered and excreted from the body, mean that a drug deemed safe during animal studies may induce toxic effects when administered to humans [5, 6]. The disparity between preclinical and clinical data is one of the major barriers for clinicians and pharmaceutical companies who wish to gain approval for carrying out human clinical trials; since this stage of the drug development process is expensive and time-consuming, it is necessary to provide statistically robust evidence from preclinical studies that indicates the trial is likely to succeed. Therefore, it is vital that new techniques are developed in order to improve the physiological relevance of the results acquired in the preclinical stage of development.

In order to obtain a realistic representation of the effects of a drug on humans, it is important to achieve a balance between using human cells in an artificial *in vitro* environment and performing experiments in animals, which are poorly predictive of the human response but provide complex natural surroundings within which to monitor drug metabolism. The key cellular processes involved in the breakdown of a compound are greatly influenced by physiological features such as fluid flow and the interactions between 3D tissue structures composed of various cell types. Thus, it is important to assess the effect of a drug under experimental conditions that accurately reflect the complexity of the *in vivo* environment. Whilst this is one advantage of animal models, their poor predictivity coupled with their associated expense and ethical concerns

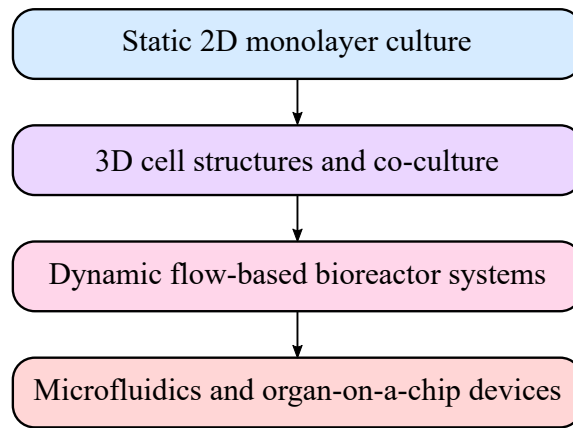


Figure 1.2: The advancement of *in vitro* cell culture methods.

is leading to their gradual replacement in favour of novel *in vitro* methods [6, 7]. In recent news, the Wellcome Sanger Institute announced the closure of their animal research facility in May 2019, a move only made possible by the emergence of sophisticated cell-based techniques. The advancement of cell culture methods (Fig. 1.2) means it is now possible to incorporate important features of the physiological environment (such as 3D cellular structure and fluid flow) within *in vitro* devices, helping to bridge the gap between traditional cell-based assays and the benefits provided by controversial animal models.

Traditional 2D cell culture methods have been employed for over a century and remain one of the most popular techniques in drug screening and toxicity studies, due to their ease of use and reproducibility [8, 9]. Typically, cells of a single type are cultured in a monolayer within a glass or polystyrene petri dish, and are immersed in culture medium. The uniform distribution of nutrients that these conditions provide results in cells that are more flattened and stretched than their native state [10]. However, the development of micropatterning technologies allows for greater control over cell shape by enabling the modification of cell culture surfaces, whilst the use of sandwich culture, where cells are placed between layers of collagen or extracellular matrix (ECM), aids in the retention of physiological morphology [8].

Despite these advances, the simplicity of 2D cell culture fails to adequately represent the complexity of the *in vivo* environment. The absence of gradients (of, for example, waste or nutrients) across the surface of the monolayer creates homogeneous conditions that poorly mimic the physiological milieu where concentration gradients may be observed [9, 11]. In reality, cells are surrounded by ECM, a 3D network of extracellular molecules that offer structural and biochemical support. The physical stresses exerted on the cells by the ECM play a role in the maintenance of normal cell morphology, so a lack of ECM can impact the efficiency of drug binding due to the non-physiological organisation of receptors on the surface of the cells [12]. Furthermore, mechanical and chemical cues between the ECM and the cells are vital for regulating important cellular functions, including proliferation and differentiation, as well as gene and protein expression, so the artificial nature of the 2D environment has the potential to affect

how the cells respond to drugs. Therefore, it is crucial that more sophisticated *in vitro* cell culture systems are developed in order to better replicate the conditions that are present within the human body.

Since cells are the building blocks of 3D tissues and organs, a number of techniques have been established for culturing 3D structures of cells [8, 9, 11, 12]. One common method involves the use of a scaffold, where cells are cultured within a natural or synthetic material to promote spheroid formation and the development of a more physiologically relevant ECM. A popular choice of scaffold are hydrogels, selected for their ease of use and tissue-like properties. Scaffold-free methods allow 3D aggregates of cells, known as spheroids, to grow freely by preventing the adhesion of cells to a culture surface. Examples of such techniques are the hanging drop method, where the generation of spheroids is controlled by gravity and occurs within hanging droplets of culture medium, and the magnetic levitation method, which involves injecting cells with magnetic nanoparticles before exposing them to an external magnet that can be used to control the formation of the spheroid. Another approach which does not require the use of a scaffold and has the potential to allow for co-culture of multiple cell types is to create 3D structures by stacking thin layers of cells known as cell sheets.

The 3D architecture of spheroids gives rise to cells that are at different stages of the cell cycle: cells in the outer layers of the spheroid are in direct contact with the nutritious culture medium and so are viable and tend to proliferate, compared to cells located at the core of the spheroid where a lack of oxygen (O_2) and nutrients induces a state of hypoxia and leads to necrosis. The presence of a mixture of cells and the fact that the 3D structure allows cells to retain their native morphology leads to interactions between the cells and the ECM that are more representative of the *in vivo* environment than in traditional 2D culture [9, 11]. A comparison of some of the key features of 2D and 3D cell culture systems [9, 12] is provided in Fig. 1.3.

Whilst 3D techniques offer more physiologically relevant cell culture conditions than conventional 2D methods, there are some obstacles associated with these new approaches. Using standard imaging methods which work well in 2D cultures can be challenging due to the complex architecture of 3D cell structures, and for some assays it is necessary to use enzymes to break down spheroids into a cell suspension in order to perform the analysis, often ending the experiment prematurely [12]. The existence of a wide array of approaches to 3D cell culture, each of which provide their own benefits, means that different cell types will perform better under the use of different methods. Thus, standardisation of 3D techniques proves challenging which leads to a lack of reproducibility and compatibility. Furthermore, 3D cell culture methods tend to be more expensive than their 2D counterparts and can be more time consuming to implement [8, 9]. Thus, 2D cell culture methods are still highly valuable and widely used due to their simplicity and convenience, but the benefits provided by culturing 3D structures of cells remain desirable.

One of the most significant limitations of both 2D and 3D cell culture techniques is a lack

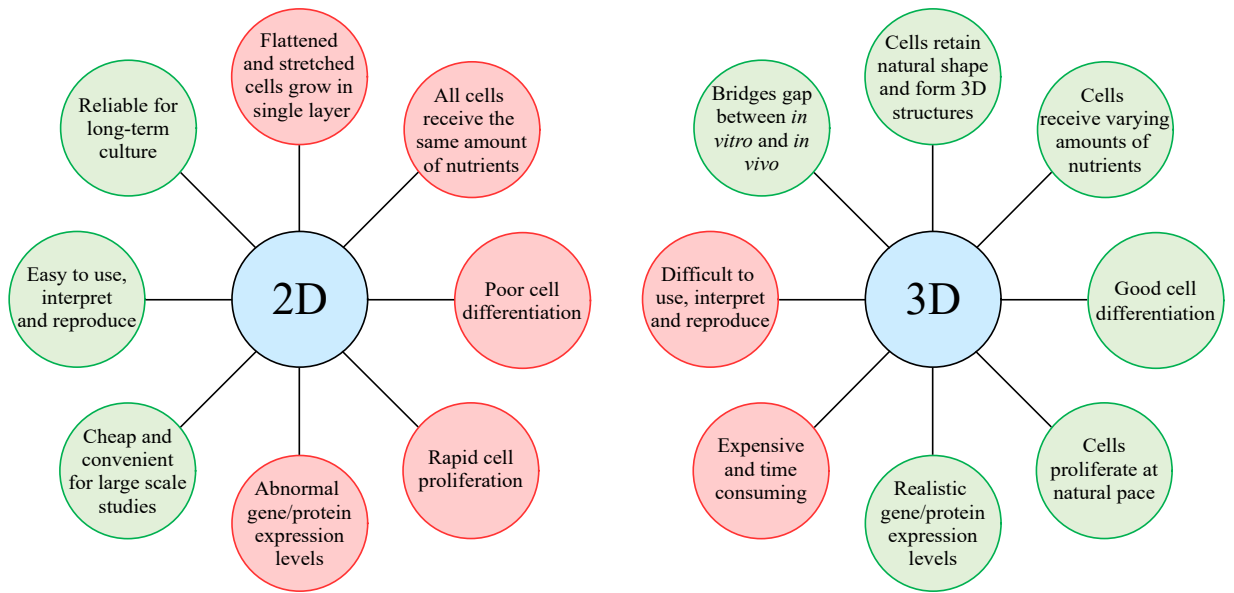


Figure 1.3: Comparison of some key features of 2D and 3D cell culture systems, where green and red represent advantages and limitations, respectively.

of fluid flow; traditional static conditions *in vitro* provide an unrealistic representation of the *in vivo* environment where cells are continuously nourished by the flow of blood and interstitial fluid. Cells lining blood vessels (e.g. endothelial cells) are typically exposed to high levels of shear stress, induced by perfusion speeds ranging from approximately 10^{-5} to 10^{-2} m s^{-1} [13], whereas cells embedded in tissue experience slower interstitial flow speeds of approximately 10^{-7} to 10^{-6} m s^{-1} [14]. The ability of cells to sense and respond to changes in their surroundings is vital for the regulation of physiological functions, such as cell growth, proliferation, differentiation and apoptosis, so precise control over the mechanical and chemical properties of the *in vitro* environment is crucial [15–17]. Therefore, a number of flow-based technologies have been developed, including dynamic bioreactors, microfluidic devices and organ-on-a-chip systems [18, 19].

A dynamic bioreactor is an *in vitro* device that has the ability to provide physiologically relevant cell culture conditions through the application of fluid flow. The flow environment generated within a dynamic bioreactor system enables the supply of O_2 and nutrients within 3D structures of cells, overcoming the mass transfer limitations that are often observed under static conditions [16, 20]. By exercising fine control of the fluid flow, as well as other important parameters such as mechanical stimulation, temperature, pH and solute concentration, dynamic bioreactors have proven to be an effective solution to bridging the gap between traditional static cell culture methods and animal models. Dynamic bioreactor systems can be used for a variety of applications, such as in drug discovery, where they can be used to perform *in vitro* tests on drugs to reduce the number of animal studies that are required, in the study of disease progression, where they can be used to develop models of diseased animal and human tissues, and in tissue engineering, where they can be used to generate artificial tissues for human transplantation [16].

There are two main types of dynamic bioreactors: mixed vessels and perfusion systems. Within these devices, various methods can be used to generate a flow field, providing cells with different flow environments and mass transfer rates [20, 21]. Examples of mixed vessels include spinner flasks, wave bioreactors and rotating-wall bioreactors. Cellular scaffolds suspended in spinner flasks are exposed to turbulent flow generated by a central magnetic stirrer, and wave bioreactors use rockers to induce turbulent fluid mixing to facilitate solute transport. Whilst the presence of fluid flow is beneficial for cell proliferation, turbulence prevents homogeneous cell growth. Uniform cell distribution can be achieved in rotating-wall bioreactors where a rotating cylinder filled with culture medium exposes cells to laminar flow. Perfusion systems offer a higher degree of control over solute transport compared with mixed vessels, and these types of devices often seek to mimic the vascular system by driving fluid directly through 3D structures of cells. Examples of perfusion systems include column and hollow-fibre bioreactors, where culture medium is distributed through cellular scaffolds that are packed within a column, and through hollow fibres within which cells reside, respectively.

Whilst they provide benefits over static cell culture techniques, there are a number of limitations associated with the operation of dynamic bioreactors [16]. The fine control over operating parameters that is provided by these sophisticated devices can be difficult to achieve and often requires manual optimisation through a process of trial and error. As well as being time consuming and inefficient, this provides opportunities for contamination and variability, thus affecting the reproducibility of the systems. These issues can be overcome by introducing automation at stages such as cell seeding and replenishment of the culture medium, but this can be difficult to implement due to the complex geometry of most devices. Another major drawback associated with dynamic bioreactors is the inability for the majority of systems to incorporate real-time sensing devices, but challenges such as this can be addressed by employing microfluidics to produce scaled-down versions of large bioreactor devices.

Microfluidic technology allows for the precise control of small volumes of fluid within device geometries on the sub-millimetre scale [17, 22]. The miniaturisation of larger bioreactor systems provides a number of benefits: the small footprint of microfluidic systems saves space and reduces costs associated with the materials required for fabrication of the device, and less reagents (such as cells or culture medium) are required since experiments can be performed using only a small volume of fluid [17, 22–24]. Additionally, microfluidic systems can be used to apply mechanical stimulation to the cells with less force and higher precision than larger bioreactor devices, which is crucial for maintaining cell viability, and the smaller dimensions of microfluidic systems provide a more relevantly sized environment within which to recreate physiological flow profiles [17]. A summary of some other advantages offered by microfluidic systems [17, 22–24] is provided in Fig. 1.4.

A wide variety of microfluidic devices have been developed, including concentration gradient generators, paper-based devices and slip-driven flow systems where the culture medium

<i>Generation of laminar flow</i>
<ul style="list-style-type: none"> • The relatively simple geometry of microfluidic devices allows for the generation of laminar flow which is ideal for providing cells with a continuous supply of oxygen and nutrients whilst minimising flow-induced damage such as shear stress.
<i>Fine control of solute concentrations</i>
<ul style="list-style-type: none"> • Stable concentration gradients can be generated, providing cells with a more physiologically relevant culture environment, and solute concentrations can be adjusted over time to meet the requirements of the cells at different stages of the experiment. • Multiple solute concentrations can be tested simultaneously which increases throughput and reduces costs. Since this can be performed using one batch of cells, variability is also reduced. • Useful for clinical applications, thresholds can be determined by testing over a continuous range of drug concentrations, and combination therapies can be developed by monitoring the effects of multiple drugs simultaneously.
<i>Co-culture of multiple cell types</i>
<ul style="list-style-type: none"> • Direct co-culture: different cell types can be cultured together within the same device. • Indirect co-culture: cells can be cultured within a conditioned medium that has been enriched with chemicals released by another cell type, or different cell types can be cultured in-line within the same device, e.g. in different cell culture chambers that are connected by the fluid flow.
<i>Real-time sensing</i>
<ul style="list-style-type: none"> • The simplicity of microfluidic systems enables the incorporation of real-time sensing devices to allow for continuous imaging, monitoring and measuring of parameters of interest.

Figure 1.4: Some advantages of microfluidic cell culture systems.

is manipulated by the simple movement of two parallel plates [23]. Additionally, microfluidic techniques can be used to generate droplets for use as independent reaction vessels for drug testing. Typically, each droplet encapsulates a drug, the drug target and a fluorescent marker indicating the viability of the target, with the fluorescence of the droplet changing when the target is sensitive to the drug [23, 24].

Developments in the field of microfluidics have led to the emergence of organ-on-a-chip devices, systems which aim to simulate functional human tissues and organs by providing cells with a highly regulated, physiologically relevant culture environment [22–25]. The ultimate goal of this technology is to develop so called ‘human-on-a-chip’ systems which integrate multiple organ models in a single microfluidic device [25]. Such systems would provide insight into how different organs interact with each other, and would be highly useful for studying the effect of drugs at the level of the whole organism [22]. Since organ-on-a-chip devices have the ability to mimic the complex *in vivo* environment, these systems are able to better predict the human response compared to traditional cell culture methods, and provide a potential future alternative to animal studies [22, 23]. For a recent review of several organ-on-a-chip systems, including liver-, lung-, kidney- and heart-on-a-chip devices, the reader is referred to [25].

Clearly, significant progress has been made in the advancement of *in vitro* cell culture systems, from simple 2D static techniques to the most recent breakthrough of organ-on-a-chip technology. However, as cell-based methods increase in sophistication, the environment to which cells are exposed becomes more complex. A good understanding of the cell culture conditions within novel devices is essential for their optimal design and set-up, so that the *in vitro* environment is suitable for the cells of interest.

One of the most critical design considerations for *in vitro* cell culture systems are solute transport limitations, particularly in relation to O_2 levels, since an adequate supply of O_2 is fundamental for the physiological function of all cells [20]. Another important factor to consider in the design of *in vitro* devices is the application of shear stress induced by fluid flow. The presence of shear stress has a significant effect on the regulation of key cellular functions such as gene expression, but unnaturally high levels can be detrimental to the survival of the cells [15, 20]. Therefore, it is crucial to gain insight into the relationships between, for example, O_2 supply and consumption, or fluid flow and shear stress, in order to ensure that cultured cells are subjected to the appropriate conditions for maintaining their viability and function.

A number of experimental methods exist for quantifying key features of the cell culture environment, including flow patterns, shear stress levels and O_2 concentrations. For example, the velocity field of the fluid can be characterised via particle image velocimetry (PIV), where the fluid is seeded with small particles that are traced using cameras, lights and lasers [26], whilst shear stress levels and O_2 concentrations can be measured using probes and sensors [27, 28]. However, in practice, there are significant limitations to implementing these measurement techniques due to the growing complexity of *in vitro* devices. PIV requires the use of specialised equipment that can be expensive and may be incompatible with certain bioreactor systems, since this visual method relies on the device possessing good optical properties. Furthermore, probes and sensors are highly sensitive so can be difficult to calibrate, and it may be impossible to incorporate these instruments within bioreactors without interfering with the flow field. Therefore, rather than performing experiments that can help to describe the physical features of the cell culture environment, it is more common to infer this information by assessing the response of the cells to their surroundings. Typical parameters such as cell viability and protein expression are often measured via destructive techniques, where the cell population is broken down into a suspension on which assays are performed; this means results are presented on an average basis, and whilst this is an effective tool for gaining insight into the overall behaviour of the cells, no detailed spatiotemporal information can be obtained using these methods.

Mathematical modelling is an invaluable tool for achieving a greater understanding of the conditions generated within complex cell culture devices. Models can be employed to characterise important features of the *in vitro* environment that are often difficult to measure experimentally, such as the flow velocity and streamlines, shear stress levels, pressure gradients, solute concentrations and reaction kinetics [16, 20, 29, 30]. Systems of equations can be developed to describe the fluid flow, solute transport and biochemical reactions within specific device geometries following two main approaches [31]. Discrete mathematical models use sets of rules to describe the behaviour of individual cells, so this approach can be useful if it is desirable to track population dynamics at a single cell level; however, these types of models generally need to be solved numerically, often at a high computational cost. Since experimental measurements are not routinely performed on a per cell basis, it is often appropriate to model

the cell population as a continuum where partial differential equations can be used to describe processes such as proliferation on an average basis. Using a continuum approach can allow for the derivation of analytical solutions that provide more insight into relationships between key system parameters than purely numerical solutions. In order to reap the benefits of both discrete and continuum modelling, multiscale techniques can be used to incorporate discrete effects into continuum models [30], and a hybrid approach can be adopted where some processes modelled as discrete are coupled with others that are modelled as continuous [32].

Although one of the main advantages of mathematical models is that they provide insight into the features of *in vitro* cell culture systems that are challenging to quantify experimentally, this means that there is often a lack of experimentally measured data with which to validate mathematical models. In order to overcome this issue, good communication is required between modellers and experimentalists to ensure that model validation can be completed, which is necessary if mathematical models are to be utilised in a predictive capacity. Once validated, models may be used to confidently predict the outcome of specific experiments to aid in the determination of optimal device design and configuration, thus reducing the time and resources spent on a trial-and-error experimental approach.

The aim of this thesis is to develop mathematical models that describe the fluid flow and solute transport within static and dynamic *in vitro* cell culture systems, with the objective of using analytical and numerical techniques to derive simple relationships between important system parameters. Such relationships would allow researchers from an experimental background to gain insight from the mathematical models, without requiring a deep understanding of the mathematics itself. The primary goal is to use these mathematical models to guide experimental design and set-up in order to achieve desirable *in vitro* cell culture conditions.

The remainder of this thesis is dedicated to the derivation and solution of mathematical models of various experimental set-ups. Chapter 2 describes a mathematical model of solute transport in a static *in vitro* cell culture system, whilst in Chapter 3, mathematical models are developed to describe the fluid flow and solute transport within a dynamic bioreactor device. In Chapter 4, the models described in Chapter 3 are employed in a practical setting to determine the configuration of a commercially available bioreactor system in collaboration with two experimental groups, each working in different areas of research.

Chapter 2

Modelling solute transport in a static *in vitro* cell culture system

As described in Chapter 1, the requirement for more physiologically relevant *in vitro* cell culture conditions has led to the development of a vast array of techniques, advancing from the traditional static monolayer to more sophisticated 3D and flow-based methods. Whilst the ultimate goal is to eventually replace all simple *in vitro* cell culture systems with more complex devices that better replicate the *in vivo* environment, traditional 2D methods are still widely used today, both alone and in conjunction with more advanced cell culture systems. For example, multiwell plates are commonly utilised to culture cells to a desired confluency prior to being transferred to flow-based devices like perfusion bioreactors. In other cases, such as with organ-on-a-chip devices, the technology is still in the early stages of development and is not yet widely implemented, so static monolayer culture remains the ‘gold standard’ in many areas of research [33]. Therefore, it is of interest to mathematically model the static cell culture environment to gain insight into some commonly asked questions, such as:

- How much solute has been metabolised at each stage of the experiment?
- How long does it take for the solute concentration to reach steady-state?
- How can the experiment be configured to ensure that the solute remains above a desired concentration for a certain amount of time?

Understanding the key features of the *in vitro* environment through the use of mathematical modelling is important for efficiently tailoring experimental conditions so that the desired cell culture environment is achieved. This chapter describes the development of a mathematical model of solute transport and metabolism within a static *in vitro* cell culture system. Solutions to the governing equations are derived using both analytical and numerical techniques, and the key results are discussed in the context of aiding in the set-up of experiments where specific conditions are desired.

2.1 Existing models from the literature

The diffusion equation forms the basis of a large number of mathematical models existing across a wide range of application areas, including (but not limited to) the energy sector [34], geochemistry [35, 36], tumour growth [37] and drug delivery [38]. Most relevant to the work presented in this thesis are diffusion problems derived in the context of cell culture, and several mathematical models exist that characterise solute transport and metabolism within traditional static experimental set-ups.

Various studies in the literature use diffusion and Michaelis-Menten (M-M) kinetics to describe the transport and metabolism of oxygen (O_2), respectively. For example, mathematical models containing these equations have been solved numerically to estimate the O_2 concentrations within a cell-seeded hydrogel submerged in culture medium [39], and within a cell-seeded scaffold placed at the base of a static cell culture system [40]. Of particular relevance to the models that will be developed in this chapter are those that characterise O_2 transport and metabolism within a petri dish containing a monolayer of cells. A computational model provided by Przekwas et al. [41] was used to predict the O_2 concentrations within such a set-up, for various depths of culture medium. Also describing the diffusion of O_2 throughout a petri dish, Burova et al. [42] and Yarmush et al. [43] use a flux boundary condition to represent the metabolism of O_2 by a layer of cells. With a focus on cell growth, the former mathematical model is solved numerically and parameterised by comparing experimental and simulated data, whilst the latter study considers only steady-state, and so the resulting system of differential equations can easily be solved analytically to provide an expression for the O_2 concentration at the cell surface.

Although it is clear that mathematical models of solute transport and metabolism within static cell culture systems already exist in the literature, the selection of studies outlined above have all been solved numerically (with the exception of [43], which as discussed, only considers the steady-state solution). Whilst computational methods can produce visual results that are useful for predicting the outcome of a specific set-up, they provide little information on the dependence of the solution on the underlying model parameters, so there is often limited scope for generalising the results to account for variations in experimental configuration. Furthermore, solving a model computationally can be time-consuming and provides only an approximation to the true solution, whereas analytical methods offer the exact solution to a set of governing equations. Therefore, where possible, an analytical approach should be adopted to allow for the derivation of mathematical expressions that clearly highlight the relationships between key parameters in the model; as well as enabling further insight into the interplay between the various processes in the system, this also means that the solution can easily be adapted to account for any modifications to experimental design, such as a change of cell type or solute.

2.2 The mathematical model

Consider a typical static *in vitro* experimental set-up, as illustrated by the schematic drawing in Fig. 2.2.1. Here, the base of a petri dish is lined with a single layer of cells and the dish is filled to a depth d with fluid which contains a solute.

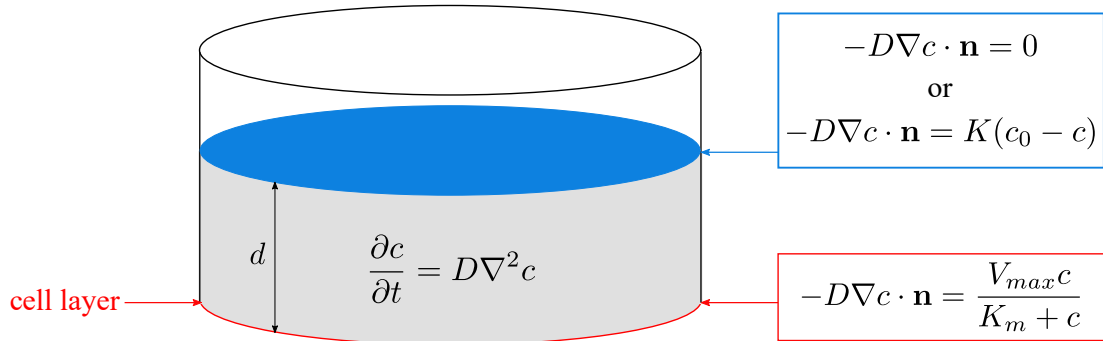


Figure 2.2.1: Schematic drawing illustrating a typical static *in vitro* experimental set-up (not to scale).

In the following equations, ∇ denotes the gradient operator in a 3D cylindrical polar co-ordinate system. Transport of the solute through the fluid is described via diffusion, i.e.

$$\frac{\partial c}{\partial t} = D\nabla^2 c,$$

where $c(r, \theta, z, t)$ (mol m^{-3}) is the solute concentration and D ($\text{m}^2 \text{s}^{-1}$) is the constant isotropic diffusion coefficient. Initially, the concentration of the solute within the fluid is assumed to be constant and equal to c_0 , i.e.

$$c = c_0 \quad \text{at} \quad t = 0.$$

For solutes that have purposefully been added to the fluid, such as drugs or nutrients, the initial concentration is usually known. However, for solutes (more specifically, gases) that are naturally present in the fluid, such as O_2 , the initial concentration is calculated using Henry's law (see page 13).

The boundary condition at the surface of the fluid will differ depending on the type of solute under consideration. For solutes which *cannot* cross the fluid-air interface (e.g. drugs/nutrients), the flux across this boundary is zero, i.e.

$$-D\nabla c \cdot \mathbf{n} = 0,$$

where \mathbf{n} is a normal in the positive z direction. However, for solutes which *can* cross the fluid-air interface (e.g. O_2), the flux across this boundary is non-zero. Since solutes diffuse from areas of high to low concentration, the flux at the fluid-air interface is proportional to the difference

Henry's law [44, 45]

Henry's law describes the relationship between the concentration of the solute in the fluid and the partial pressure of the solute in the air via the following equation:

$$c = \frac{P}{K_H},$$

where c (mol m^{-3}) is the solute concentration in the fluid, P (atm) is the partial pressure of the solute in the air and K_H ($\text{atm mol}^{-1} \text{m}^3$) is Henry's constant, the value of which depends on the solute, the fluid and the temperature. Put simply, P and K_H describe the likelihood of the solute entering and leaving the fluid, respectively.

Michaelis-Menten kinetics [45–47]

As illustrated in Fig. 2.2.2, M-M kinetics describe the relationship between the solute concentration and the rate of the reaction: as the concentration of the solute increases, the reaction rate also increases before approaching a maximum for higher solute concentrations.

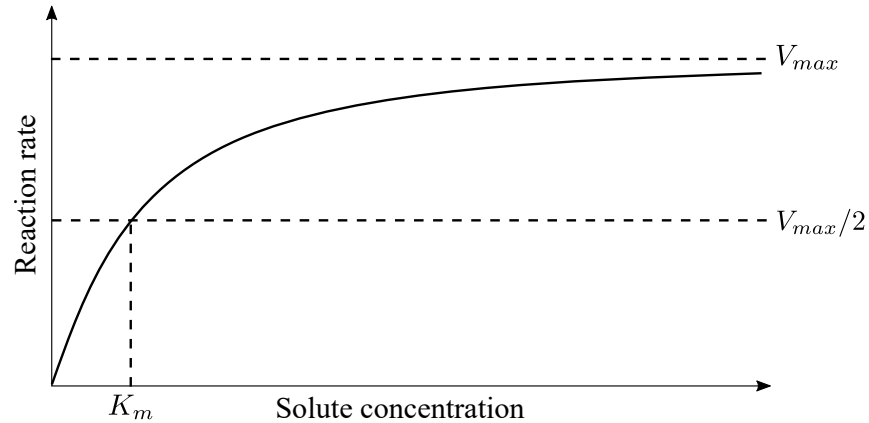


Figure 2.2.2: Schematic drawing illustrating the behaviour of M-M kinetics.

Note that a solute may be metabolised by more than one process; for example, APAP is broken down in the body via three metabolic pathways, namely glucuronidation, sulpha-tion and oxidation [48], each of which may be described by M-M kinetics [49]. Therefore a general M-M reaction term has the following form:

$$\sum_{i=1}^m \frac{V_{max,i} c}{K_{m,i} + c},$$

where m denotes the number of metabolic pathways.

between the solute concentration in the air and the solute concentration in the fluid, i.e.

$$-D\nabla c \cdot \mathbf{n} = K(c_0 - c),$$

where K (m s^{-1}) is the mass transfer coefficient. It is noted that, when using Henry's law to calculate c_0 , it is inherently assumed that the solute concentrations in the fluid and the air are equal, so here, the solute concentration in the air is given by c_0 .

At the base of the petri dish, it is assumed that the cell population is fixed: cellular processes such as proliferation and apoptosis are neglected since these typically take place over a much larger timescale than diffusion. It is further assumed that the thickness of the cell layer is significantly smaller than the depth of the fluid. Thus, diffusion through the cell layer is negligible, and the interaction between the solute and the cells can be described by a flux boundary condition, the right-hand side of which may be modified to represent any type of reaction mechanism. Here, M-M kinetics (see page 13) are used to describe solute metabolism; this is a common approach in the literature [29], particularly when the solute is O_2 or a drug such as paracetamol (APAP). Hence, the loss of solute due to metabolism by the cells can be described by the following boundary condition applied at the base of the petri dish:

$$-D\nabla c \cdot \mathbf{n} = \frac{V_{max}c}{K_m + c},$$

where V_{max} ($\text{mol m}^{-2} \text{s}^{-1}$) is the maximum metabolic rate and K_m (mol m^{-3}) is the M-M constant. Although only one metabolic pathway is considered in the derivation of the solutions in subsequent sections, it may readily be shown that the solutions can be extended to account for m pathways (see Appendix A). It should be highlighted that the overall rate of solute metabolism is dependent on the total number of cells. Typically quantified on a per cell basis, V_{max} is often provided in units of mol s^{-1} . The dependence on cell density is incorporated by multiplying this parameter by the cell number and dividing by the area covered by the cells to obtain the appropriate units for applying M-M kinetics on the base of the petri dish ($\text{mol m}^{-2} \text{s}^{-1}$). It is noted that M-M kinetics may also be applied within a cell layer, where the cell density is given by the number of cells divided by the volume of the layer, and V_{max} is defined in units of $\text{mol m}^{-3} \text{s}^{-1}$. Finally, assuming that the outer wall of the petri dish is impermeable, the flux across this boundary is zero.

In general, it would be necessary to solve this type of model using 3D cylindrical polar coordinates. Since the interaction between the solute and the cells is described via M-M kinetics, metabolism of the solute depends on the concentration to which the cells are exposed. Typically, this means that solute metabolism has a spatial dependence and could be non-uniform across the base of the petri dish. However, due to the form of the initial and boundary conditions coupled with the simple geometry of the petri dish, it may be shown that, here, c is independent of r and θ . Since the initial solute concentration is uniform throughout the petri dish, which is

assumed to be of a uniform shape with impermeable walls, all cells are exposed to the same solute concentration and so metabolism is uniform across the base of the petri dish. Thus, a concentration gradient is generated in only the vertical direction, and the governing equations for the corresponding 1D problem are as follows, where x denotes the spatial co-ordinate:

$$\begin{aligned}\frac{\partial c}{\partial t}(x, t) &= D \frac{\partial^2 c}{\partial x^2}(x, t), \quad 0 < x < d, \quad t > 0, \\ c(x, 0) &= c_0, \quad 0 < x < d, \\ -D \frac{\partial c}{\partial x}(0, t) &= \begin{cases} 0, & t > 0, \quad \text{or} \\ K [c_0 - c(0, t)], & t > 0, \end{cases} \\ -D \frac{\partial c}{\partial x}(d, t) &= \frac{V_{max} c(d, t)}{K_m + c(d, t)}, \quad t > 0.\end{aligned}$$

As previously described, the two options for the boundary condition at $x = 0$ describe the cases where the solute cannot, or can, cross the fluid-air interface, respectively. Note that only one of these conditions may be applied at any one time, with the choice depending on the behaviour of the solute under consideration.

The solutions to these governing equations will depend on D , K , V_{max} and K_m , the values of which must be obtained experimentally. However, whilst these parameters are of interest mathematically, processes such as diffusion are often not the main focus of experiments and so are not routinely quantified. Where experimental measurements of such parameters do exist, it is not uncommon to find discrepancies in the available data due to variations in measurement techniques and experimental set-up. Therefore, it can be difficult to obtain a reliable and accurate estimate of important parameter values for use in mathematical models. To overcome this barrier, a common technique is to remove the physical dimensions from the system of governing equations by replacing all variables with suitably scaled quantities. The scalings are typically chosen in such a way that allows for the formation of common non-dimensional parameters that highlight relationships between different processes in the system, making it easier to spot parameter regimes for which the model can be simplified. By performing non-dimensionalisation, the governing equations can be solved in a general sense whilst still gaining insight into the relationships between the underlying system parameters. Using the scalings

$$c = c_0 c^*, \quad t = \frac{d^2}{D} t^*, \quad x = dx^*,$$

yields the following non-dimensionalised equations (stars omitted for convenience):

$$\frac{\partial c}{\partial t}(x, t) = \frac{\partial^2 c}{\partial x^2}(x, t), \quad 0 < x < 1, \quad t > 0, \quad (2.2.1)$$

$$c(x, 0) = 1, \quad 0 < x < 1, \quad (2.2.2)$$

$$\frac{\partial c}{\partial x}(0, t) = \begin{cases} 0, & t > 0, \\ -\mu[1 - c(0, t)], & t > 0, \end{cases} \quad (2.2.3A)$$

$$(2.2.3B)$$

$$\frac{\partial c}{\partial x}(1, t) = -\frac{\alpha c(1, t)}{1 + \beta c(1, t)}, \quad t > 0, \quad (2.2.4)$$

where the non-dimensional parameters μ , α and β are defined as

$$\mu = \frac{Kd}{D}, \quad \alpha = \frac{V_{max}d}{DK_m}, \quad \beta = \frac{c_0}{K_m}.$$

Here, μ is the ratio of the rate of mass transfer across the fluid-air interface and the rate of diffusion. In the limit as $\mu \rightarrow 0$, (2.2.3B) reduces to (2.2.3A), i.e. the flux of solute across the fluid-air interface is equal to zero, but as $\mu \rightarrow \infty$, (2.2.3B) is equivalent to a constant source of solute. The second non-dimensional parameter, α , is a Damköhler number comparing the rate of reaction with the rate of diffusion. For small values of α , the rate of reaction is much smaller than the rate of diffusion so the limiting process is the interaction between the solute and the cells. Conversely, for large values of α , the rate of reaction is much larger than the rate of diffusion so the limiting process is the diffusion of the solute to the cells. Finally, β is the ratio of the initial solute concentration and the M-M constant, and it is noted that the right-hand side of (2.2.4) can be reduced to the following linear kinetics:

$$\frac{\partial c}{\partial x}(1, t) \approx \begin{cases} -\alpha c(1, t), & \beta \ll 1 \\ -\frac{\alpha}{\beta}, & \beta \gg 1 \end{cases},$$

when this parameter is either small or large.

In subsequent sections, two cases (A and B) are considered which relate to the different types of solute under investigation: solutions to (2.2.1) - (2.2.4) are derived, using (2.2.3A) and (2.2.3B) in turn. Although each set of governing equations may be solved directly using a numerical scheme such as finite differences, this would give rise to a purely numerical solution that offers little insight into the interplay between the various model parameters; for this reason, an analytical approach is adopted. A number of mathematical techniques exist for solving systems of partial differential equations depending on the form of the initial and boundary conditions. A common choice for linear diffusion problems, here the method of Laplace transforms is employed to solve each model. It is noted that since the boundary condition at $x = 1$ is nonlinear, a closed-form solution can only be obtained by linearising the M-M kinetics for $\beta \ll 1$ and $\beta \gg 1$ (see Appendix B). For the full nonlinear M-M kinetics, convolution gives rise to a Volterra integral equation (VIE) that describes the concentration of the solute at the cell surface. Although it is necessary to solve the VIEs numerically, these equations allow for further analytical progress where approximate solutions are derived under certain parameter regimes.

2.3 Method of Laplace transforms

For a more detailed description of the theory in this section, the reader is referred to [50]. The Laplace transform of a function $f(t)$ is an expression of the form

$$\mathcal{L}\{f(t)\} = \bar{f}(s) = \int_0^{\infty} e^{-st} f(t) dt.$$

This formal definition may be used to compute the Laplace transform of any admissible function $f(t)$, but most standard Laplace transforms can be found in tables. The Laplace transform is particularly useful for solving initial-boundary value problems. A partial differential equation (PDE) can be transformed into a simpler ordinary differential equation (ODE) by taking Laplace transforms of the derivatives:

$$\begin{aligned} \mathcal{L}\left\{\frac{\partial u}{\partial t}(x, t)\right\} &= s\bar{u}(x, s) - u(x, 0), \\ \mathcal{L}\left\{\frac{\partial^2 u}{\partial x^2}(x, t)\right\} &= \frac{d^2\bar{u}}{dx^2}(x, s). \end{aligned}$$

The resulting ODE is then solved and the solution of the initial-boundary value problem is obtained by taking the inverse Laplace transform using the complex inversion formula.

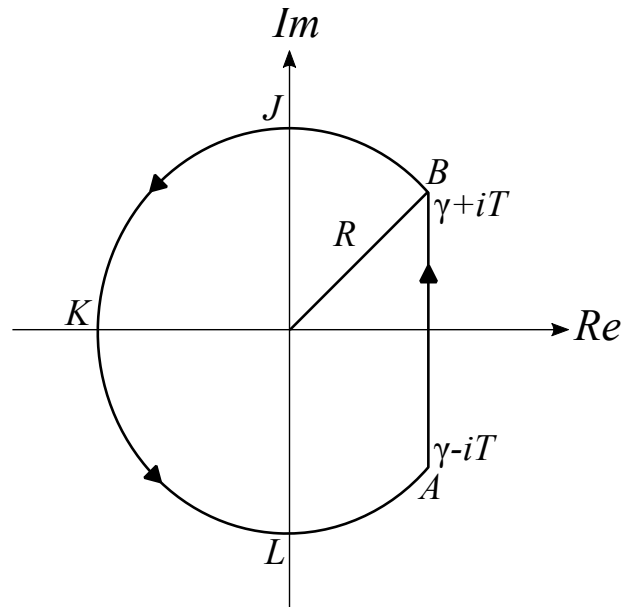
Complex inversion formula

If $\bar{f}(s)$ is the Laplace transform of a function $f(t)$, then $\mathcal{L}^{-1}\{\bar{f}(s)\}$ is given by

$$f(t) = \begin{cases} \frac{1}{2\pi i} \int_{\gamma-i\infty}^{\gamma+i\infty} e^{st} \bar{f}(s) ds, & t > 0, \\ 0, & t < 0, \end{cases}$$

where γ is a real number.

The right-hand side of the above equation is typically evaluated by making use of the Bromwich contour, a closed curve composed of the line AB and the arc $BJKLA$ of a circle of radius R (see Fig. 2.3.1). Note that the real number γ must be chosen such that all singularities of $\bar{f}(s)$ lie to the left of the line $s = \gamma$, but otherwise the choice is somewhat arbitrary. Types of singularities include branch points (where the ‘branches’ of a multi-valued function come together) as well as poles and essential singularities. The latter can be classified via the Laurent series expansion of a function $f(s)$ around a point a : if the principle part of the expansion has a finite number of terms, say m , then the singularity at $s = a$ is a pole of order m , whereas if the principle part has an infinite number of terms, the singularity at $s = a$ is an essential singularity.

Figure 2.3.1: Schematic drawing of the Bromwich contour, C .

The integral over the Bromwich contour, C , can be split into two parts as follows:

$$\frac{1}{2\pi i} \oint_C e^{st} \bar{f}(s) ds = \frac{1}{2\pi i} \left\{ \int_{\gamma-iT}^{\gamma+iT} e^{st} \bar{f}(s) ds + \int_{\Gamma} e^{st} \bar{f}(s) ds \right\},$$

where Γ denotes the arc $BJKLA$. In cases where the only singularities of $\bar{f}(s)$ are poles, the above equation may be simplified by employing the residue theorem.

Residue theorem

If a function $g(s)$ is analytic within a simple closed contour Ω , except for a finite number of singular points which are poles, then

$$\oint_{\Omega} g(s) ds = 2\pi i \times \sum (\text{residues of } g \text{ inside } \Omega).$$

Thus, it follows that

$$\frac{1}{2\pi i} \int_{\gamma-iT}^{\gamma+iT} e^{st} \bar{f}(s) ds = \sum (\text{residues of } e^{st} \bar{f}(s) \text{ inside } C) - \frac{1}{2\pi i} \int_{\Gamma} e^{st} \bar{f}(s) ds.$$

Taking the limit as $R \rightarrow \infty$ (and therefore as $T \rightarrow \infty$) gives

$$f(t) = \sum (\text{residues of } e^{st} \bar{f}(s) \text{ inside } C) - \lim_{R \rightarrow \infty} \left\{ \frac{1}{2\pi i} \int_{\Gamma} e^{st} \bar{f}(s) ds \right\}.$$

Now, it can be shown that if there exist constants $M, k > 0$ such that on Γ

$$|\bar{f}(s)| < \frac{M}{R^k},$$

then the integral over Γ of $e^{st}\bar{f}(s)$ approaches zero as $R \rightarrow \infty$, i.e.

$$f(t) = \sum (\text{residues of } e^{st}\bar{f}(s) \text{ inside } C).$$

The residues are calculated as follows, where a is a pole of order m :

$$\text{Res}_{s=a} = \frac{1}{(m-1)!} \lim_{s \rightarrow a} \left\{ \frac{d^{m-1}}{ds^{m-1}} \left\{ (s-a)^m e^{st} \bar{f}(s) \right\} \right\}.$$

To summarise, Laplace transforms may be used to solve an initial-boundary value problem using the following method:

1. Take Laplace transforms to convert the PDE into an ODE.
2. Solve the resulting simpler ODE problem.
3. Take the inverse Laplace transform to obtain the solution to the original problem, using the residue theorem where applicable.

In this chapter, the convolution theorem will be used extensively when inverting the Laplace transforms.

Convolution theorem

If $f(t)$ and $g(t)$ are functions with Laplace transforms $\bar{f}(s)$ and $\bar{g}(s)$, respectively, then

$$\mathcal{L}^{-1}\{\bar{f}(s)\bar{g}(s)\} = (f * g)(t),$$

where the symbol $*$ denotes convolution, an operation that, when given two functions $f(t)$ and $g(t)$, returns another function $(f * g)(t)$ according to the formula

$$(f * g)(t) = \int_0^t f(\tau)g(t - \tau) d\tau.$$

This gives rise to VIEs, which are integral equations of the form

$$y(t) = x(t) + \int_0^t k(t, u)y(u) du,$$

where $x(t)$ and $k(t, u)$ are known. Although in general it is necessary to proceed numerically to obtain the solution of these types of equations, the VIEs may be used to derive further (semi-)

analytical solutions under certain parameter regimes, thus providing additional insight into the behaviour of the models.

2.4 Solutions for case A

In this case, it is assumed that the solute cannot cross the fluid-air interface so the boundary condition at $x = 0$ is given by (2.2.3A). An example of such a solute is a drug (e.g. APAP) which is dissolved in the fluid and can only leave by being metabolised by the cells. Fig. 2.4.1 displays the 1D domain and the equations that will be solved in this section, where $x = 0$ and $x = 1$ represent the fluid-air interface and the base of the petri dish (i.e. the cell surface), respectively.

$$\frac{\partial c}{\partial t}(x, t) = \frac{\partial^2 c}{\partial x^2}(x, t)$$

$\frac{\partial c}{\partial t}(0, t) = 0$

$\frac{\partial c}{\partial t}(1, t) = -\frac{\alpha c(1, t)}{1 + \beta c(1, t)}$

Figure 2.4.1: Schematic drawing illustrating the 1D domain and non-dimensional equations for case A.

2.4.1 Deriving the VIE

Using the method of Laplace transforms and defining $\mathcal{L}\{c(x, t)\} = \bar{c}(x, s)$, (2.2.1) is solved subject to the initial condition (2.2.2) to obtain

$$\bar{c}(x, s) = a(s) \cosh(\sqrt{s}x) + b(s) \sinh(\sqrt{s}x) + \frac{1}{s}.$$

By applying (2.2.3A), it may be deduced that $b(s) = 0$ so

$$\bar{c}(x, s) = a(s) \cosh(\sqrt{s}x) + \frac{1}{s}.$$

Differentiating, applying (2.2.4) and re-arranging gives

$$a(s) = -\frac{1}{\sqrt{s} \sinh(\sqrt{s})} \frac{\alpha \bar{c}(1, s)}{1 + \beta \bar{c}(1, s)},$$

so it follows that

$$\bar{c}(1, s) = \frac{1}{s} - \bar{k}_A(s) \frac{\alpha \bar{c}(1, s)}{1 + \beta \bar{c}(1, s)}, \quad (2.4.1)$$

where

$$\bar{k}_A(s) = \frac{\cosh(\sqrt{s})}{\sqrt{s} \sinh(\sqrt{s})}. \quad (2.4.2)$$

By taking the inverse Laplace transform of (2.4.1) and using the convolution theorem, the following VIE is obtained:

$$c(1, t) = 1 - \alpha \int_0^t k_A(t - \tau) \frac{c(1, \tau)}{1 + \beta c(1, \tau)} d\tau, \quad (2.4.3)$$

where

$$k_A(t) = \mathcal{L}^{-1} \left\{ \frac{\cosh(\sqrt{s})}{\sqrt{s} \sinh(\sqrt{s})} \right\}. \quad (2.4.4)$$

Now, given that no branch points exist, the residue theorem may be employed to evaluate (2.4.4); by writing $\cosh(\sqrt{s})$ and $\sinh(\sqrt{s})$ in their series expansion forms, it is clear that there are no branch points. It may readily be shown that there is a simple pole at $s = 0$ and infinitely many simple poles at $s_n = -n^2\pi^2$ for $n \in \mathbb{N}$. Using L'Hôpital's rule to calculate the residues yields

$$\begin{aligned} \text{Res}_{s=0} &= \lim_{s \rightarrow 0} \left\{ \frac{\sqrt{s} \cosh(\sqrt{s}) e^{st}}{\sinh(\sqrt{s})} \right\} = 1, \\ \text{Res}_{s=s_n} &= \lim_{s \rightarrow s_n} \left\{ \frac{s - s_n}{\sinh(\sqrt{s})} \right\} \lim_{s \rightarrow s_n} \left\{ \frac{\cosh(\sqrt{s}) e^{st}}{\sqrt{s}} \right\} = 2e^{-n^2\pi^2 t}. \end{aligned}$$

Thus, applying the residue theorem gives

$$k_A(t) = \text{Res}_{s=0} + \sum_{n=1}^{\infty} \text{Res}_{s=s_n} = 1 + 2 \sum_{n=1}^{\infty} e^{-n^2\pi^2 t}.$$

2.4.2 Approximate solutions

In this section, perturbation theory and other analytical techniques are used to derive approximations to the full solution of the VIE that are valid within specific parameter regimes. Using an analytical approach can highlight the dependence of the solution on the chosen parameters, providing information that is often not attainable via a fully numerical approach.

Recall that when the non-dimensional parameter β is either small or large, the M-M kinetics are approximately linear. Since β clearly has an important effect on the interaction between the solute and the cells, the behaviour of the solution will be investigated for $\beta \ll 1$ and $\beta \gg 1$. Note that for each of these parameter regimes, the first terms in the approximate solution should be equivalent to the full solution of the model where the nonlinear M-M term is replaced by the appropriate linear kinetics. Another important parameter is t , and since experiments can be both short- and long-term, it is of particular interest to monitor the behaviour of the solution for early and late times. Therefore, approximate solutions are derived when $t \ll 1$, where the

leading-order term should return the initial condition, and for the solution as $t \rightarrow \infty$, simple analytical techniques are used to solve the steady-state problem.

Perturbation theory

When it is not possible to directly solve the full problem analytically, perturbation theory may be employed to approximate the full solution by ‘perturbing’ the solution of a simpler, related problem which can be solved analytically. Using this technique, the full solution is approximated by a series expansion about a small parameter, say ε , i.e.

$$f = f_0 + \varepsilon f_1 + \varepsilon^2 f_2 + \cdots ,$$

where f_0 is the solution to the simpler problem. Since successive terms in the series are smaller, higher-order terms provide a less significant contribution to the approximation and so it is usually only necessary to derive the leading- and first-order terms in the expansion.

Small β solution for case A

Here, assume $\beta \ll 1$ and consider the following perturbation expansion:

$$c(1, t) = c_0(1, t) + \beta c_1(1, t) + \mathcal{O}(\beta^2). \quad (2.4.5)$$

Substituting this expression into (2.4.3) gives

$$\begin{aligned} & c_0(1, t) + \beta c_1(1, t) + \mathcal{O}(\beta^2) \\ &= 1 - \alpha \int_0^t k_A(t - \tau) \frac{c_0(1, \tau) + \beta c_1(1, \tau) + \mathcal{O}(\beta^2)}{1 + \beta [c_0(1, \tau) + \beta c_1(1, \tau) + \mathcal{O}(\beta^2)]} d\tau \\ &= 1 - \alpha \int_0^t k_A(t - \tau) [c_0(1, \tau) + \beta c_1(1, \tau) + \mathcal{O}(\beta^2)] [1 - \beta c_0(1, \tau) + \mathcal{O}(\beta^2)] d\tau, \end{aligned}$$

by taking a series expansion of

$$\left(1 + \beta [c_0(1, \tau) + \beta c_1(1, \tau) + \mathcal{O}(\beta^2)]\right)^{-1}$$

about $\beta = 0$. Multiplying out the brackets and equating powers of β yields

$$c_0(1, t) = 1 - \alpha \int_0^t k_A(t - \tau) c_0(1, \tau) d\tau, \quad (2.4.6)$$

$$c_1(1, t) = -\alpha \int_0^t k_A(t - \tau) [c_1(1, \tau) - c_0(1, \tau)^2] d\tau. \quad (2.4.7)$$

First, (2.4.6) may be solved to obtain an analytical expression for $c_0(1, t)$. Taking Laplace

transforms, using the convolution theorem and re-arranging results in

$$\bar{c}_0(1, s) = \frac{1}{s[1 + \alpha \bar{k}_A(s)]}.$$

Using (2.4.2) and taking inverse Laplace transforms gives

$$c_0(1, t) = \mathcal{L}^{-1} \left\{ \frac{\sinh(\sqrt{s})}{\sqrt{s}[\sqrt{s} \sinh(\sqrt{s}) + \alpha \cosh(\sqrt{s})]} \right\}.$$

After verifying that no branch points exist, the residue theorem may be used to evaluate this inverse Laplace transform where the poles are given by

$$\sqrt{s} = 0 \quad \text{and} \quad \sqrt{s} \sinh(\sqrt{s}) + \alpha \cosh(\sqrt{s}) = 0.$$

For convenience, setting $\sqrt{s} = i\kappa$ in the transcendental equation gives

$$\kappa \sin(\kappa) - \alpha \cos(\kappa) = 0. \quad (2.4.8)$$

There is a simple pole at $s = 0$ and infinitely many simple poles at $s_n = -\kappa_n^2$ for $n \in \mathbb{N}$, where κ_n are the roots of (2.4.8). After a trivial calculation, it is clear that the residue at $s = 0$ is equal to zero. The residue at $s = s_n$ is obtained by employing L'Hôpital's rule, and it follows from the residue theorem that

$$c_0(1, t) = \sum_{n=1}^{\infty} \frac{2 \sin(\kappa_n) e^{-\kappa_n^2 t}}{\kappa_n \cos(\kappa_n) + (\alpha + 1) \sin(\kappa_n)}. \quad (2.4.9)$$

This expression for $c_0(1, t)$ may be substituted into (2.4.7) which can then be solved numerically to obtain $c_1(1, t)$. Thus, from (2.4.5), the solution when $\beta \ll 1$ is given by

$$c(1, t) = \sum_{n=1}^{\infty} \frac{2 \sin(\kappa_n) e^{-\kappa_n^2 t}}{\kappa_n \cos(\kappa_n) + (\alpha + 1) \sin(\kappa_n)} + \beta c_1(1, t) + \mathcal{O}(\beta^2). \quad (2.4.10)$$

It is verified in Appendix B that, to leading-order, the solution when $\beta \ll 1$ is equivalent to the solution obtained from solving the full model with the nonlinear flux boundary condition (2.2.4) replaced by

$$\frac{\partial c}{\partial x}(1, t) = -\alpha c(1, t).$$

Large β solution for case A

The solution when β is large may be derived by adopting a similar approach to the case when β is small. Note that in this case, it is possible to derive expressions for all terms in the approximate solution, so higher-order terms are included in the expansion to demonstrate this. Here, assume

$\beta \gg 1$ and let $\varepsilon = 1/\beta$. Then, consider the following perturbation expansion about the small parameter ε :

$$c(1, t) = c_0(1, t) + \varepsilon c_1(1, t) + \varepsilon^2 c_2(1, t) + \varepsilon^3 c_3(1, t) + \varepsilon^4 c_4(1, t) + \mathcal{O}(\varepsilon^5). \quad (2.4.11)$$

Substituting this expression into (2.4.3) and taking a series expansion of

$$\left(1 + \varepsilon^{-1} [c_0(1, \tau) + \varepsilon c_1(1, \tau) + \varepsilon^2 c_2(1, \tau) + \varepsilon^3 c_3(1, \tau) + \varepsilon^4 c_4(1, \tau) + \mathcal{O}(\varepsilon^5)]\right)^{-1}$$

about $\varepsilon = 0$ gives

$$\begin{aligned} & c_0(1, t) + \varepsilon c_1(1, t) + \varepsilon^2 c_2(1, t) + \varepsilon^3 c_3(1, t) + \varepsilon^4 c_4(1, t) + \mathcal{O}(\varepsilon^5) \\ &= 1 - \alpha \int_0^t k_A(t - \tau) [c_0(1, \tau) + \varepsilon c_1(1, \tau) + \varepsilon^2 c_2(1, \tau) + \varepsilon^3 c_3(1, \tau) + \varepsilon^4 c_4(1, \tau) + \mathcal{O}(\varepsilon^5)] \\ & \quad \times \left\{ \frac{\varepsilon}{c_0(1, \tau)} - \frac{\varepsilon^2}{c_0(1, \tau)^2} [c_1(1, \tau) + 1] + \frac{\varepsilon^3}{c_0(1, \tau)^3} [(c_1(1, \tau) + 1)^2 - c_2(1, \tau)c_0(1, \tau)] \right. \\ & \quad \left. - \frac{\varepsilon^4}{c_0(1, \tau)^4} [(c_1(1, \tau) + 1)^3 - c_2(1, \tau)c_0(1, \tau)(2c_1(1, \tau) + 1) + c_3(1, \tau)c_0(1, \tau)^2] \right. \\ & \quad \left. + \mathcal{O}(\varepsilon^5) \right\} d\tau. \end{aligned}$$

Multiplying out the brackets and equating powers of ε yields

$$\begin{aligned} c_0(1, t) &= 1, \\ c_1(1, t) &= -\alpha \int_0^t k_A(t - \tau) d\tau, \\ c_2(1, t) &= \alpha \int_0^t k_A(t - \tau) d\tau = -c_1(1, t), \\ c_3(1, t) &= -\alpha \int_0^t k_A(t - \tau) [c_1(1, \tau) + 1] d\tau, \\ c_4(1, t) &= \alpha \int_0^t k_A(t - \tau) [c_1(1, \tau) + 1]^2 d\tau, \\ & \quad \vdots \\ c_n(1, t) &= (-1)^n \alpha \int_0^t k_A(t - \tau) [c_1(1, \tau) + 1]^{n-2} d\tau. \end{aligned} \quad (2.4.12)$$

Note that (2.4.12) may be solved analytically: taking Laplace transforms, using the convolution theorem and re-arranging gives

$$\bar{c}_1(1, s) = -\frac{\alpha \bar{k}_A(s)}{s}.$$

Using (2.4.2) and taking inverse Laplace transforms results in

$$c_1(1, t) = -\alpha \mathcal{L}^{-1} \left\{ \frac{\cosh(\sqrt{s})}{s^{3/2} \sinh(\sqrt{s})} \right\}.$$

Again, it may readily be shown that no branch points exist and so the residue theorem can be employed to calculate this inverse Laplace transform. The poles are given by

$$s^{3/2} = 0 \quad \text{and} \quad \sinh(\sqrt{s}) = 0.$$

There is a pole of order 2 at $s = 0$ and infinitely many simple poles at $s_n = -n^2\pi^2$ for $n \in \mathbb{N}$. Using L'Hôpital's rule to calculate the residues gives

$$\begin{aligned} \text{Res}_{s=0} &= \lim_{s \rightarrow 0} \left\{ \frac{\partial}{\partial s} \left\{ \frac{\sqrt{s} \cosh(\sqrt{s}) e^{st}}{\sinh(\sqrt{s})} \right\} \right\} = t + \frac{1}{3}, \\ \text{Res}_{s=s_n} &= -\frac{2e^{-n^2\pi^2 t}}{n^2\pi^2}. \end{aligned}$$

Then, it follows from the residue theorem that

$$c_1(1, t) = -\alpha \left(t + \frac{1}{3} - 2 \sum_{n=1}^{\infty} \frac{e^{-n^2\pi^2 t}}{n^2\pi^2} \right).$$

This expression for $c_1(1, t)$ may be substituted into (2.4.13) which can then be solved numerically to obtain $c_n(1, t)$ for $n \geq 2$. Thus, from (2.4.11), the solution when $\beta \gg 1$ is given by

$$\begin{aligned} c(1, t) &= 1 - \frac{\alpha}{\beta} \left(t + \frac{1}{3} - 2 \sum_{n=1}^{\infty} \frac{e^{-n^2\pi^2 t}}{n^2\pi^2} \right) \\ &\quad + \sum_{n=2}^{\infty} \frac{(-1)^n \alpha}{\beta^n} \int_0^t k_A(t - \tau) [c_1(1, \tau) + 1]^{n-2} d\tau. \end{aligned} \tag{2.4.14}$$

It is verified in Appendix B that, to first-order, the solution when $\beta \gg 1$ is equivalent to the solution obtained from solving the full model with the nonlinear flux boundary condition (2.2.4) replaced by

$$\frac{\partial c}{\partial x}(1, t) = -\frac{\alpha}{\beta}.$$

Small t solution for case A

In order to derive a solution for $c(1, t)$ at early times, it is necessary to first examine the behaviour of $k_A(t)$ for $t \ll 1$. Recall that

$$k_A(t) = 1 + 2 \sum_{n=1}^{\infty} e^{-n^2\pi^2 t}.$$

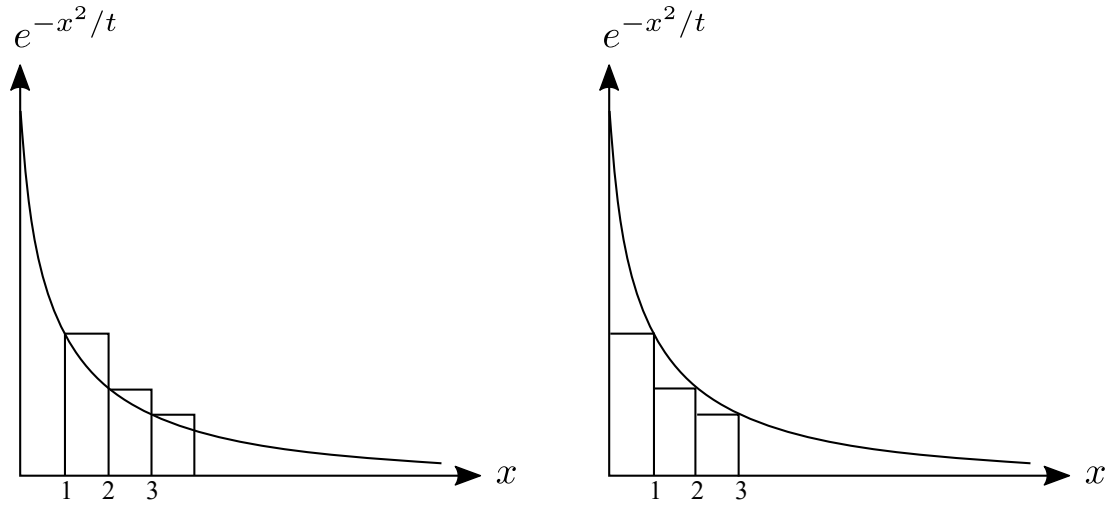


Figure 2.4.2: Schematic drawing illustrating the area under the curve $e^{-x^2/t}$ and an approximation to this area using lower (left) and upper (right) Riemann sums.

For the following analysis, it is desirable for t to appear on the denominator of the exponent so that the exponential term decays as $t \rightarrow 0$. Using result (5) in [51], $k_A(t)$ may be re-written in the following more convenient form:

$$k_A(t) = \frac{1}{\sqrt{\pi t}} \left(1 + 2 \sum_{n=1}^{\infty} e^{-n^2/t} \right). \quad (2.4.15)$$

A lower and upper bound for $k_A(t)$ may be obtained by using Riemann sums to approximate the area under the curve $e^{-x^2/t}$. From Fig. 2.4.2, it is clear that

$$\int_1^{\infty} e^{-x^2/t} dx < \sum_{n=1}^{\infty} e^{-n^2/t} < \int_0^{\infty} e^{-x^2/t} dx.$$

Using the substitution $u = x^2/t$ to evaluate the integrals yields

$$\frac{\sqrt{\pi t}}{2} \operatorname{erfc} \left(\frac{1}{\sqrt{t}} \right) < \sum_{n=1}^{\infty} e^{-n^2/t} < \frac{\sqrt{\pi t}}{2},$$

and from (2.4.15), it follows that

$$\frac{1}{\sqrt{\pi t}} + \operatorname{erfc} \left(\frac{1}{\sqrt{t}} \right) < k_A(t) < \frac{1}{\sqrt{\pi t}} + 1.$$

For $t \ll 1$,

$$\operatorname{erfc} \left(\frac{1}{\sqrt{t}} \right) = \frac{\sqrt{t}}{\sqrt{\pi}} e^{-1/t} \left(1 - \frac{t}{2} + \dots \right) \approx 0,$$

since the exponential term dominates and rapidly decays. Thus, for small t

$$\frac{1}{\sqrt{\pi t}} < k_A(t) < \frac{1}{\sqrt{\pi t}},$$

i.e.

$$k_A(t) \sim \frac{1}{\sqrt{\pi t}} \quad \text{as } t \rightarrow 0. \quad (2.4.16)$$

Now, consider the following expansion in t :

$$c(1, t) = a_1 + a_2 t^{1/2} + a_3 t + a_4 t^{3/2} + \mathcal{O}(t^2). \quad (2.4.17)$$

Substituting this expression into (2.4.3), using (2.4.16) and taking a series expansion of

$$\left(1 + \beta[a_1 + a_2 \tau^{1/2} + a_3 \tau + a_4 \tau^{3/2} + \mathcal{O}(t^2)]\right)^{-1}$$

about $\tau = 0$ gives

$$\begin{aligned} & a_1 + a_2 t^{1/2} + a_3 t + a_4 t^{3/2} + \mathcal{O}(t^2) \\ &= 1 - \frac{\alpha}{\sqrt{\pi}} \int_0^t (t - \tau)^{-1/2} [a_1 + a_2 \tau^{1/2} + a_3 \tau + a_4 \tau^{3/2} + \mathcal{O}(t^2)] \\ & \quad \times \left[\frac{1}{a_1 \beta + 1} - \frac{a_2 \beta}{(a_1 \beta + 1)^2} \tau^{1/2} + \frac{(a_2^2 - a_1 a_3) \beta^2 - a_3 \beta}{(a_1 \beta + 1)^3} \tau + \mathcal{O}(\tau^{3/2}) \right] d\tau. \end{aligned}$$

Multiplying out the brackets gives

$$\begin{aligned} & a_1 + a_2 t^{1/2} + a_3 t + a_4 t^{3/2} + \mathcal{O}(t^2) \\ &= 1 - \frac{\alpha}{\sqrt{\pi}} \left[\frac{a_1}{a_1 \beta + 1} I_1 + \frac{a_2}{(a_1 \beta + 1)^2} I_2 + \frac{a_3 + \beta(a_1 a_3 - a_2^2)}{(a_1 \beta + 1)^3} I_3 + \dots \right], \quad (2.4.18) \end{aligned}$$

where

$$\begin{aligned} I_1 &= \int_0^t (t - \tau)^{-1/2} d\tau = 2t^{1/2}, \\ I_2 &= \int_0^t (t - \tau)^{-1/2} \tau^{1/2} d\tau = \frac{\pi}{2} t, \\ I_3 &= \int_0^t (t - \tau)^{-1/2} \tau d\tau = \frac{4}{3} t^{3/2}, \end{aligned}$$

are easily evaluated using simple integration, substitution and integration by parts, respectively.

Substituting these expressions into (2.4.18) and equating powers of t gives

$$\begin{aligned} a_1 &= 1, \\ a_2 &= -\frac{2\alpha}{\sqrt{\pi}(\beta + 1)}, \end{aligned}$$

$$a_3 = \frac{\alpha^2}{(\beta + 1)^3},$$

$$a_4 = -\frac{4\alpha^3(\pi - 4\beta)}{3\pi^{3/2}(\beta + 1)^5}.$$

Thus, from (2.4.17), the solution when $t \ll 1$ is given by

$$c(1, t) = 1 - \frac{2\alpha}{\sqrt{\pi}(\beta + 1)}t^{1/2} + \frac{\alpha^2}{(\beta + 1)^3}t - \frac{4\alpha^3(\pi - 4\beta)}{3\pi^{3/2}(\beta + 1)^5}t^{3/2} + \mathcal{O}(t^2). \quad (2.4.19)$$

Steady-state solution for case A

For this case, where the solute cannot cross the fluid-air interface, it is clear that $c(x, t) \rightarrow 0$ as $t \rightarrow \infty$, since without replenishment, the solute will fully deplete due to metabolism by the cells. To derive this trivial solution, the steady diffusion equation is solved subject to (2.2.3A) and (2.2.4) to obtain $c(x, \infty) = 0$, as expected.

2.4.3 Numerical method for solving the VIEs

In order to obtain the solution of the VIE given by (2.4.3), product integration methods are applied to derive an implicit numerical scheme for solving this equation. It is noted that a simpler explicit Euler scheme could be derived instead; however, due to the form of this numerical method, it is necessary to significantly decrease the time step, Δt , as α increases in order to obtain sufficient accuracy. This in turn greatly increases the computational cost, and since in subsequent sections the value of α will be varied, in this instance an implicit method is preferable. Using $k_A(t)$ as defined in (2.4.15), recall that the VIE is given by

$$c(1, t) = 1 - \frac{\alpha}{\sqrt{\pi}} \int_0^t \frac{1}{\sqrt{t - \tau}} \left(1 + 2 \sum_{n=1}^{\infty} e^{-n^2/(t-\tau)} \right) \frac{c(1, \tau)}{1 + \beta c(1, \tau)} d\tau.$$

Replacing t by $t_i = i\Delta t$, where $i = 1, 2, \dots, T$ such that $T\Delta t$ is the final time of interest, the integral can be re-written as a sum of integrals over smaller intervals:

$$c(1, t_i) = 1 - \frac{\alpha}{\sqrt{\pi}} \sum_{j=0}^{i-1} \int_{t_j}^{t_{j+1}} \frac{1}{\sqrt{t_i - \tau}} \left(1 + 2 \sum_{n=1}^{\infty} e^{-n^2/(t_i - \tau)} \right) \frac{c(1, \tau)}{1 + \beta c(1, \tau)} d\tau.$$

Now, assuming that

$$\left(1 + 2 \sum_{n=1}^{\infty} e^{-n^2/(t-\tau)} \right) \frac{c(1, \tau)}{1 + \beta c(1, \tau)} \approx \left(1 + 2 \sum_{n=1}^{\infty} e^{-n^2/(t-t_{j+1})} \right) \frac{c(1, t_{j+1})}{1 + \beta c(1, t_{j+1})}$$

over $[t_j, t_{j+1}]$ gives

$$c(1, t_i) \approx 1 - \frac{\alpha}{\sqrt{\pi}} \sum_{j=0}^{i-1} \left(\int_{t_j}^{t_{j+1}} \frac{1}{\sqrt{t_i - \tau}} d\tau \right) \left(1 + 2 \sum_{n=1}^{\infty} e^{-n^2/(t_i - t_{j+1})} \right) \frac{c(1, t_{j+1})}{1 + \beta c(1, t_{j+1})}.$$

Performing the integration with $t_j = j\Delta t$ yields

$$\int_{t_j}^{t_{j+1}} \frac{1}{\sqrt{t_i - \tau}} d\tau = 2\sqrt{\Delta t} \left(\sqrt{i-j} - \sqrt{i-j-1} \right),$$

so then

$$c(1, t_i) \approx 1 - \frac{2\alpha\sqrt{\Delta t}}{\sqrt{\pi}} \sum_{j=0}^{i-1} \left(\sqrt{i-j} - \sqrt{i-j-1} \right) \left(1 + 2 \sum_{n=1}^{\infty} e^{-n^2/(t_i - t_{j+1})} \right) \frac{c(1, t_{j+1})}{1 + \beta c(1, t_{j+1})}.$$

Note that

$$\begin{aligned} & \sum_{j=0}^{i-1} \left(\sqrt{i-j} - \sqrt{i-j-1} \right) \left(1 + 2 \sum_{n=1}^{\infty} e^{-n^2/(t_i - t_{j+1})} \right) \frac{c(1, t_{j+1})}{1 + \beta c(1, t_{j+1})} \\ &= \frac{c(1, t_i)}{1 + \beta c(1, t_i)} + \sum_{j=0}^{i-2} \left(\sqrt{i-j} - \sqrt{i-j-1} \right) \left(1 + 2 \sum_{n=1}^{\infty} e^{-n^2/(t_i - t_{j+1})} \right) \frac{c(1, t_{j+1})}{1 + \beta c(1, t_{j+1})}, \end{aligned}$$

so an approximation to $c(1, t_i)$ may be obtained by finding the roots, c_i , of the following implicit equation:

$$\begin{aligned} c_i + \frac{2\alpha\sqrt{\Delta t}}{\sqrt{\pi}} \frac{c_i}{1 + \beta c_i} \\ = 1 - \frac{2\alpha\sqrt{\Delta t}}{\sqrt{\pi}} \sum_{j=0}^{i-2} \left(\sqrt{i-j} - \sqrt{i-j-1} \right) \left(1 + 2 \sum_{n=1}^{\infty} e^{-n^2/(t_i - t_{j+1})} \right) \frac{c_{j+1}}{1 + \beta c_{j+1}}. \end{aligned}$$

In order to obtain the small β solution to first order, an additional VIE must be solved. In the next section, the accuracy of the small β solution will be highlighted for decreasing values of β , with the value of α arbitrarily fixed at 1; therefore, since α is not large, an explicit Euler scheme is sufficient for solving (2.4.7). Recall that the first order term from the small β solution is given by

$$c_1(1, t) = -\alpha \int_0^t k_A(t - \tau) [c_1(1, \tau) - c_0(1, \tau)^2] d\tau,$$

where $c_0(1, t)$ is given by (2.4.9). Replacing t by t_i and re-writing the integral as a sum of integrals over smaller intervals gives

$$c_1(1, t_i) = -\alpha \sum_{j=0}^{i-1} \int_{t_j}^{t_{j+1}} k_A(t_i - \tau) [c_1(1, \tau) - c_0(1, \tau)^2] d\tau.$$

Then, using the argument of Riemann sums yields

$$c_1(1, t_i) \approx -\alpha \Delta t \sum_{j=0}^{i-1} k_A(t_i - t_j) [c_1(1, t_j) - c_0(1, t_j)^2].$$

The accuracy of these numerical solutions depends on Δt , the spacing between consecutive time points, and N , the finite number of terms at which the infinite sums are truncated. It should be noted that the optimal choice for Δt and N may vary depending on the values of other model parameters that also influence the behaviour of the solution. Thus, it is necessary to perform a sensitivity study across a range of parameter values to determine the choice of Δt and N that provides the best balance between computational cost and an acceptable level of accuracy.

To optimise the time spacing for the implicit method, the numerical solution was computed for various values of Δt , using the highest and lowest values of α and β considered in the next section. The percentage error between the numerical solutions was calculated for consecutive values of Δt , and the value of Δt was considered to be sufficient when this error was less than 1%. In all cases, $\Delta t = 1 \times 10^{-3}$ was chosen as the optimal value. Since the infinite sum that appears in the implicit method is a decaying exponential, successive terms will provide a smaller contribution to the overall solution. Therefore, the number of terms in the infinite sum may be truncated as long as the solution is of an acceptable accuracy, and the choice of $N = 100$ was deemed sufficient in all cases. These values of Δt and N were also found to provide an acceptable level of accuracy for the explicit method.

2.4.4 Comparing the solution of the VIE with the approximate solutions

In order to demonstrate the dependence of the solutions on the values of the non-dimensional parameters and to illustrate the validity of the approximate solutions derived in §2.4.2, the solution of the VIE is compared with the approximate solutions over the following parameter ranges:

$$\alpha = 0.01, 0.1, 1, 10, 100,$$

$$\beta = 0.01, 0.1, 1, 10, 100.$$

First, the solution of the VIE given by (2.4.3) is generated for various values of α . Recall that α is the ratio of the reaction rate and the diffusion rate, so as α increases, the reaction rate also increases; this is reflected in the solutions illustrated in Fig. 2.4.3. As expected, for the smallest value of α and therefore for a negligible rate of solute metabolism, the solution decreases from the initial condition extremely slowly. In contrast, for the largest value of α and therefore for a significant rate of solute metabolism, the solution rapidly drops to zero. It is clear from Fig. 2.4.3 that as $t \rightarrow \infty$, the steady-state solution of zero is approached at different rates depending on the value of α .

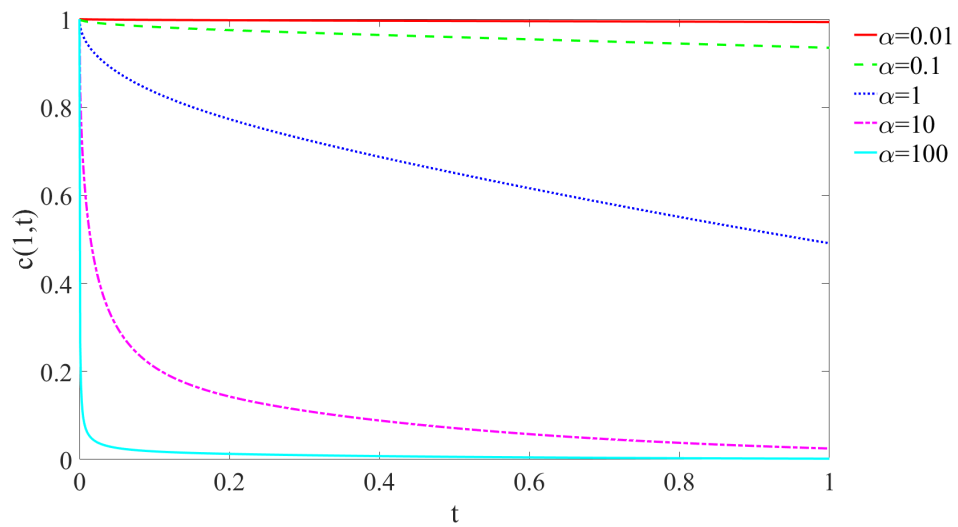


Figure 2.4.3: Solution to the VIE from case A for various values of α with $\beta = 1$, showing the dependence of the solute concentration at the cell surface, $c(1, t)$, on the non-dimensional parameter α .

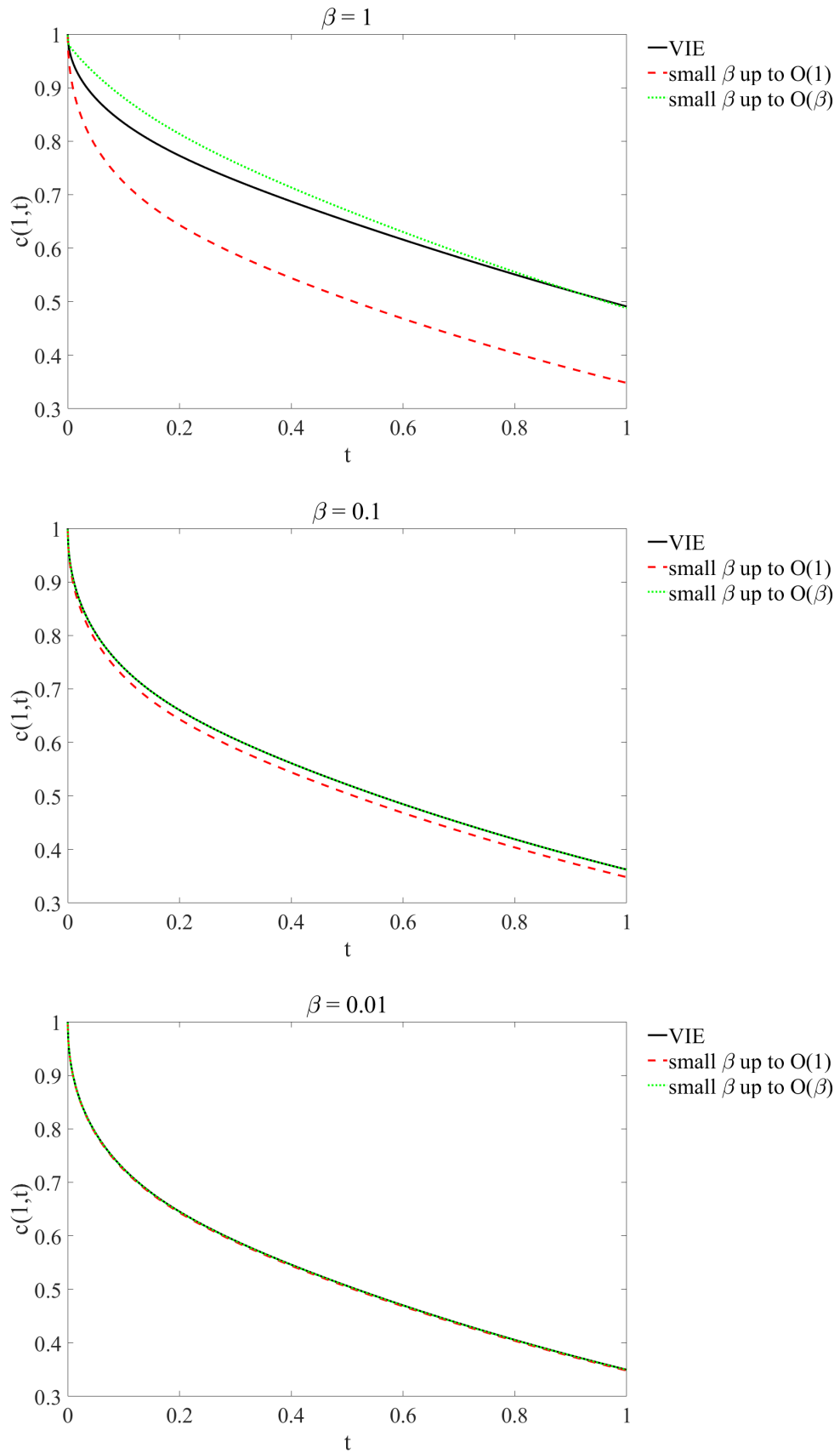


Figure 2.4.4: Comparing the solution to the VIE from case A and the small β solution for various values of β , with $\alpha = 1$.

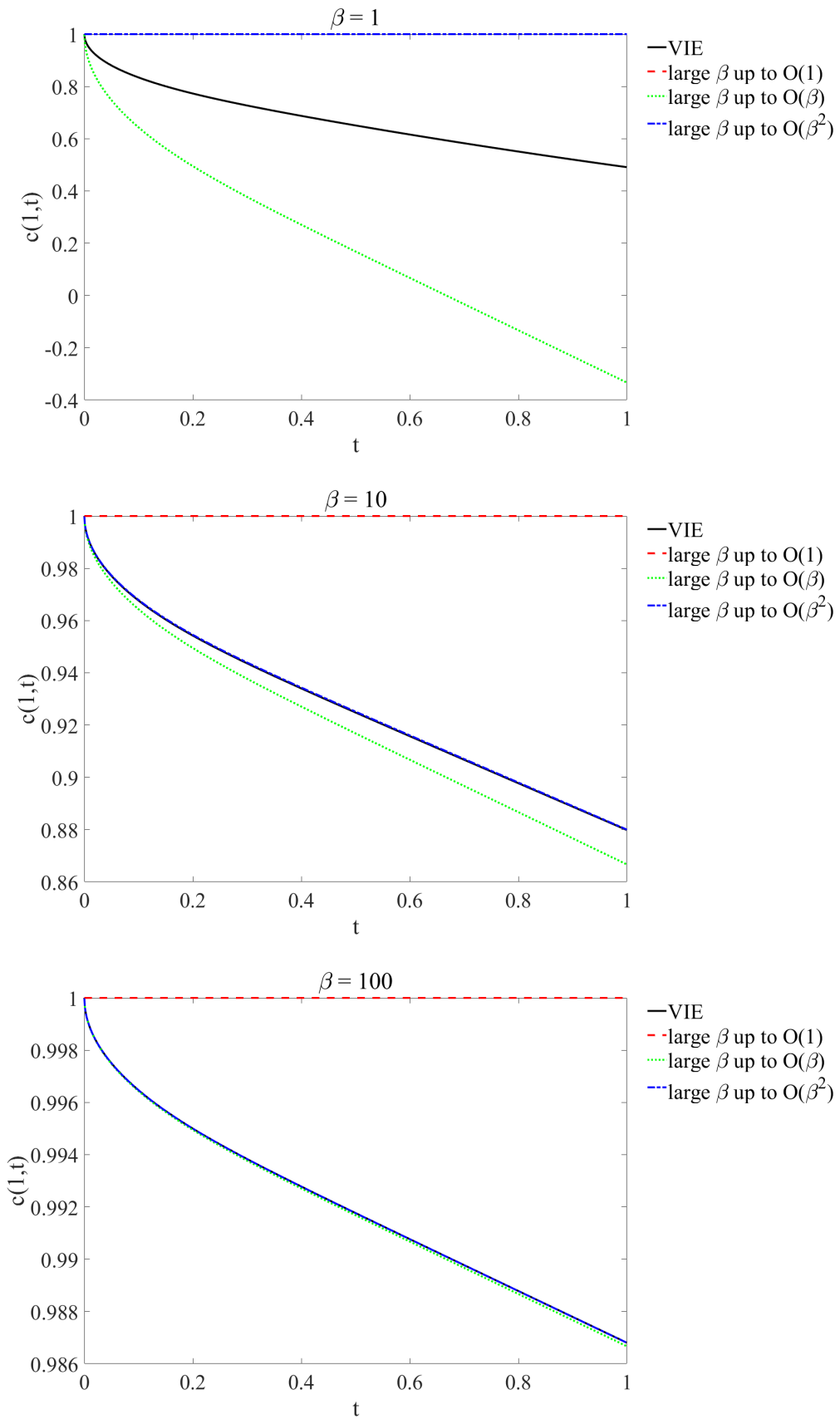


Figure 2.4.5: Comparing the solution to the VIE from case A and the large β solution for various values of β , with $\alpha = 1$. Note that when $\beta = 1$, the large β solution to second order is equal to 1, i.e. the large β solution to leading order, so the red and blue lines in the upper plot are overlapping.

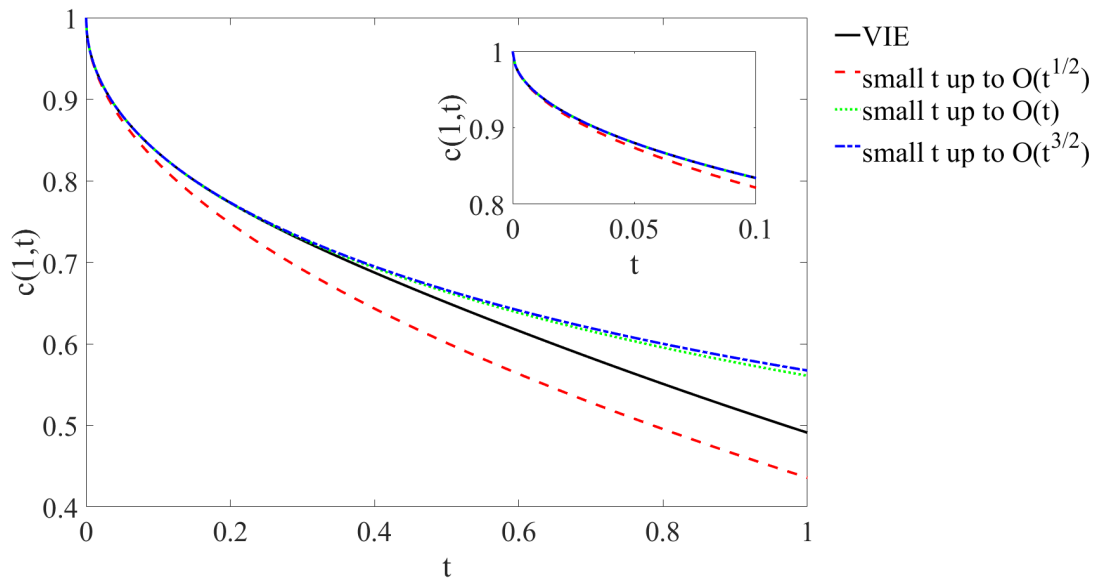


Figure 2.4.6: Comparing the solution to the VIE from case A and the small t solution for $0 \leq t \leq 1$, with $\alpha = \beta = 1$. The inset plot highlights the good agreement between the solutions for $0 \leq t \leq 0.1$.

Figs. 2.4.4 and 2.4.5 compare the solution of the VIE with the small and large β solutions, respectively, for various values of β . Recall that the small β solution is valid when $\beta \ll 1$ so, as expected, the agreement between this approximate solution and the solution of the VIE improves as β decreases. When $\beta = 1$, the agreement between the solution of the VIE and the large β solution is somewhat poor, and non-physical values of $c(1, t)$ are generated. However, it is noted that this is no cause for concern since the large β solution is only valid when $\beta \gg 1$, and the agreement between this approximate solution and the solution of the VIE does improve as β increases. As expected, for all values of β , the approximations become more accurate as higher order terms are added to the solutions.

Fig. 2.4.6 compares the solution of the VIE with the small t solution for $0 \leq t \leq 1$. It is noted that, since the approximate solution is only valid when $t \ll 1$, the agreement between the solution of the VIE and the small t solution deteriorates as t increases. However, within the region of validity, the agreement is excellent as demonstrated by the inset plot, where the solutions are shown for $0 \leq t \leq 0.1$.

2.5 Solutions for case B

In this case, it is assumed that the solute can cross the fluid-air interface so the boundary condition at $x = 0$ is given by (2.2.3B). An example of such a solute is O_2 which is present in both the fluid and the air and may pass freely between both regions. Fig. 2.5.1 displays the 1D domain and the equations that will be solved in this section, where $x = 0$ and $x = 1$ represent the fluid-air interface and the base of the petri dish (i.e. the cell surface), respectively.

$$\frac{\partial c}{\partial t}(x, t) = \frac{\partial^2 c}{\partial x^2}(x, t)$$

$\frac{\partial c}{\partial t}(0, t) = -\mu [1 - c(0, t)]$

$\frac{\partial c}{\partial t}(1, t) = -\frac{\alpha c(1, t)}{1 + \beta c(1, t)}$

Figure 2.5.1: Schematic drawing illustrating the 1D domain and non-dimensional equations for case B.

2.5.1 Deriving the VIE

As in case A, (2.2.1) is solved subject to the initial condition (2.2.2) to give

$$\bar{c}(x, s) = a(s) \cosh(\sqrt{s}x) + b(s) \sinh(\sqrt{s}x) + \frac{1}{s}.$$

By applying (2.2.3B), it may be deduced that

$$b(s) = \frac{\mu a(s)}{\sqrt{s}},$$

and so

$$\bar{c}(x, s) = a(s) \cosh(\sqrt{s}x) + \frac{\mu a(s)}{\sqrt{s}} \sinh(\sqrt{s}x) + \frac{1}{s}.$$

Differentiating, applying (2.2.4) and re-arranging gives

$$a(s) = -\frac{\alpha \bar{c}(1, s)}{[\sqrt{s} \sinh(\sqrt{s}) + \mu \cosh(\sqrt{s})] [1 + \beta \bar{c}(1, s)]},$$

so it follows that

$$\bar{c}(1, s) = \frac{1}{s} - \bar{k}_B(s) \frac{\alpha \bar{c}(1, s)}{1 + \beta \bar{c}(1, s)}, \quad (2.5.1)$$

where

$$\bar{k}_B(s) = \frac{\sqrt{s} \cosh(\sqrt{s}) + \mu \sinh(\sqrt{s})}{\sqrt{s} [\sqrt{s} \sinh(\sqrt{s}) + \mu \cosh(\sqrt{s})]}. \quad (2.5.2)$$

By taking the inverse Laplace transform of (2.5.1) and using the convolution theorem, the following VIE is obtained:

$$c(1, t) = 1 - \alpha \int_0^t k_B(t - \tau) \frac{c(1, \tau)}{1 + \beta c(1, \tau)} d\tau, \quad (2.5.3)$$

where

$$k_B(t) = \mathcal{L}^{-1} \left\{ \frac{\sqrt{s} \cosh(\sqrt{s}) + \mu \sinh(\sqrt{s})}{\sqrt{s} [\sqrt{s} \sinh(\sqrt{s}) + \mu \cosh(\sqrt{s})]} \right\}. \quad (2.5.4)$$

Similarly to case A, there are no branch points and so (2.5.4) can be evaluated by employing the residue theorem. The poles are given by

$$\sqrt{s} = 0 \quad \text{and} \quad \sqrt{s} \sinh(\sqrt{s}) + \mu \cosh(\sqrt{s}) = 0,$$

and, for convenience, setting $\sqrt{s} = i\lambda$ in the transcendental equation gives

$$\mu \cos(\lambda) - \lambda \sin(\lambda) = 0. \quad (2.5.5)$$

There is a simple pole at $s = 0$ and infinitely many simple poles at $s_n = -\lambda_n^2$ for $n \in \mathbb{N}$, where λ_n are the roots of (2.5.5). After a simple calculation, it may be shown that the residue at $s = 0$ is equal to zero. The residue at $s = s_n$ is obtained using L'Hôpital's rule and then, by the residue theorem, it follows that

$$k_B(t) = \sum_{n=1}^{\infty} \frac{2[\lambda_n \cos(\lambda_n) + \mu \sin(\lambda_n)] e^{-\lambda_n^2 t}}{\lambda_n \cos(\lambda_n) + (\mu + 1) \sin(\lambda_n)}.$$

2.5.2 Approximate solutions

Using similar methods as in §2.4.2, the VIE given by (2.5.3) is now used to derive further (semi-) analytical solutions under certain parameter regimes, namely $\beta \ll 1$, $\beta \gg 1$, $t \ll 1$ and $t \rightarrow \infty$. Note that the VIEs from both case A and case B are of the following general form:

$$c(1, t) = 1 - \alpha \int_0^t f(t - \tau) \frac{c(1, \tau)}{1 + \beta c(1, \tau)} d\tau,$$

where $f(t)$ is replaced by $k_A(t)$ and $k_B(t)$ in cases A and B, respectively. Furthermore, it may be shown that in the limit as $\mu \rightarrow 0$, the VIEs from both cases are equivalent. Thus, the approximate solutions derived here are of a similar form to the approximate solutions derived in §2.4.2.

Small β solution for case B

Here, assume $\beta \ll 1$ and consider the following perturbation expansion:

$$c(1, t) = c_0(1, t) + \beta c_1(1, t) + \mathcal{O}(\beta^2). \quad (2.5.6)$$

Substituting this expression into (2.5.3) and equating powers of β gives

$$c_0(1, t) = 1 - \alpha \int_0^t k_B(t - \tau) c_0(1, \tau) d\tau, \quad (2.5.7)$$

$$c_1(1, t) = -\alpha \int_0^t k_B(t - \tau) [c_1(1, \tau) - c_0(1, \tau)^2] d\tau. \quad (2.5.8)$$

First, an analytical expression for $c_0(1, t)$ is obtained by solving (2.5.7). Taking Laplace transforms, using the convolution theorem and re-arranging yields

$$\bar{c}_0(1, s) = \frac{1}{s[1 + \alpha \bar{k}_B(s)]}.$$

Using (2.5.2) and taking inverse Laplace transforms results in

$$c_0(1, t) = \mathcal{L}^{-1} \left\{ \frac{\sqrt{s} \sinh(\sqrt{s}) + \mu \cosh(\sqrt{s})}{\sqrt{s} [(s + \alpha\mu) \sinh(\sqrt{s}) + \sqrt{s}(\alpha + \mu) \cosh(\sqrt{s})]} \right\}.$$

Again, no branch points exist and therefore the residue theorem may be used to evaluate this inverse Laplace transform where the poles are given by

$$\sqrt{s} = 0 \quad \text{and} \quad (s + \alpha\mu) \sinh(\sqrt{s}) + \sqrt{s}(\alpha + \mu) \cosh(\sqrt{s}) = 0.$$

For convenience, setting $\sqrt{s} = i\xi$ in the transcendental equation gives

$$(\alpha\mu - \xi^2) \sin(\xi) + \xi(\alpha + \mu) \cos(\xi) = 0. \quad (2.5.9)$$

There is a simple pole at $s = 0$ and infinitely many simple poles at $s_n = -\xi_n^2$ for $n \in \mathbb{N}$, where ξ_n are the roots of (2.5.9). Using L'Hôpital's rule, the residues are given by

$$\begin{aligned} \text{Res}_{s=0} &= \frac{\mu}{\alpha\mu + \alpha + \mu}, \\ \text{Res}_{s=s_n} &= \frac{2[\mu \cos(\xi_n) - \xi_n \sin(\xi_n)] e^{-\xi_n^2 t}}{(\alpha\mu + \alpha + \mu - \xi_n^2) \cos(\xi_n) - \xi_n(2 + \alpha + \mu) \sin(\xi_n)}, \end{aligned}$$

and applying the residue theorem gives

$$c_0(1, t) = \frac{\mu}{\alpha\mu + \alpha + \mu} + \sum_{n=1}^{\infty} \frac{2[\mu \cos(\xi_n) - \xi_n \sin(\xi_n)] e^{-\xi_n^2 t}}{(\alpha\mu + \alpha + \mu - \xi_n^2) \cos(\xi_n) - \xi_n(2 + \alpha + \mu) \sin(\xi_n)}. \quad (2.5.10)$$

This expression for $c_0(1, t)$ may be substituted into (2.5.8) which can then be solved numerically to obtain $c_1(1, t)$. Thus, from (2.5.6), the solution when $\beta \ll 1$ is given by

$$\begin{aligned} c(1, t) &= \frac{\mu}{\alpha\mu + \alpha + \mu} + \sum_{n=1}^{\infty} \frac{2[\mu \cos(\xi_n) - \xi_n \sin(\xi_n)] e^{-\xi_n^2 t}}{(\alpha\mu + \alpha + \mu - \xi_n^2) \cos(\xi_n) - \xi_n(2 + \alpha + \mu) \sin(\xi_n)} \\ &+ \beta c_1(1, t) + \mathcal{O}(\beta^2). \end{aligned} \quad (2.5.11)$$

It is verified in Appendix B that, to leading-order, the solution when $\beta \ll 1$ is equivalent to the solution obtained from solving the full model with the nonlinear boundary condition (2.2.4) replaced by

$$\frac{\partial c}{\partial x}(1, t) = -\alpha c(1, t).$$

Large β solution for case B

Here, assume $\beta \gg 1$ and let $\varepsilon = 1/\beta$. Then, consider the following perturbation expansion about the small parameter ε :

$$c(1, t) = c_0(1, t) + \varepsilon c_1(1, t) + \mathcal{O}(\varepsilon^2). \quad (2.5.12)$$

Substituting this expression into (2.5.3) and equating powers of ε gives

$$\begin{aligned} c_0(1, t) &= 1, \\ c_1(1, t) &= -\alpha \int_0^t k_B(t - \tau) d\tau, \end{aligned} \quad (2.5.13)$$

$$c_n(1, t) = (-1)^n \alpha \int_0^t k_B(t - \tau) [c_1(1, \tau) + 1]^{n-2} d\tau, \quad n \geq 2. \quad (2.5.14)$$

Note that (2.5.13) may be solved analytically: taking Laplace transforms, using the convolution theorem and re-arranging yields

$$\bar{c}_1(1, s) = -\frac{\alpha \bar{k}_B(s)}{s}.$$

Taking inverse Laplace transforms and using (2.5.2) gives

$$c_1(1, t) = -\alpha \mathcal{L}^{-1} \left\{ \frac{\sqrt{s} \cosh(\sqrt{s}) + \mu \sinh(\sqrt{s})}{s^{3/2} [\sqrt{s} \sinh(\sqrt{s}) + \mu \cosh(\sqrt{s})]} \right\}.$$

Again, it may readily be shown that no branch points exist and so the residue theorem can be used to calculate this inverse Laplace transform. The poles are given by

$$s^{3/2} = 0 \quad \text{and} \quad \sqrt{s} \sinh(\sqrt{s}) + \mu \cosh(\sqrt{s}) = 0.$$

Note that this is the same transcendental equation that appears in the derivation of the VIE, and as before, setting $\sqrt{s} = i\lambda$ gives rise to (2.5.5), i.e.

$$\mu \cos(\lambda) - \lambda \sin(\lambda) = 0.$$

There is a pole of order 2 at $s = 0$ and infinitely many simple poles at $s_n = -\lambda_n^2$ for $n \in \mathbb{N}$, where λ_n are the roots of (2.5.5). Using L'Hôpital's rule, the resulting residues are

$$\begin{aligned} \text{Res}_{s=0} &= 1 + \frac{1}{\mu}, \\ \text{Res}_{s=s_n} &= -\frac{2[\lambda_n \cos(\lambda_n) + \mu \sin(\lambda_n)] e^{-\lambda_n^2 t}}{\lambda_n^2 [\lambda_n \cos(\lambda_n) + (\mu + 1) \sin(\lambda_n)]}. \end{aligned}$$

Then, applying the residue theorem gives

$$c_1(1, t) = -\alpha \left(1 + \frac{1}{\mu} - \sum_{n=1}^{\infty} \frac{2[\lambda_n \cos(\lambda_n) + \mu \sin(\lambda_n)] e^{-\lambda_n^2 t}}{\lambda_n^2 [\lambda_n \cos(\lambda_n) + (\mu + 1) \sin(\lambda_n)]} \right).$$

This expression for $c_1(1, t)$ may be substituted into (2.5.14) which can then be solved numerically to obtain $c_n(1, t)$ for $n \geq 2$. Thus, from (2.5.12), the solution when $\beta \gg 1$ is given by

$$\begin{aligned} c(1, t) &= 1 - \frac{\alpha}{\beta} \left(1 + \frac{1}{\mu} - \sum_{n=1}^{\infty} \frac{2[\lambda_n \cos(\lambda_n) + \mu \sin(\lambda_n)] e^{-\lambda_n^2 t}}{\lambda_n^2 [\lambda_n \cos(\lambda_n) + (\mu + 1) \sin(\lambda_n)]} \right) \\ &\quad + \sum_{n=2}^{\infty} \frac{(-1)^n \alpha}{\beta^n} \int_0^t k_B(t - \tau) [c_1(1, \tau) + 1]^{n-2} d\tau. \end{aligned} \quad (2.5.15)$$

It is verified in Appendix B that, to first-order, the solution when $\beta \gg 1$ is equivalent to the solution obtained from solving the full model with the nonlinear flux boundary condition (2.2.4) replaced by

$$\frac{\partial c}{\partial x}(1, t) = -\frac{\alpha}{\beta}.$$

Small t solution for case B

In order to derive a solution for $c(1, t)$ at early times, it is necessary to first examine the behaviour of $k_B(t)$ for $t \ll 1$. Recall that

$$k_B(t) = \sum_{n=1}^{\infty} \frac{2[\lambda_n \cos(\lambda_n) + \mu \sin(\lambda_n)] e^{-\lambda_n^2 t}}{\lambda_n \cos(\lambda_n) + (\mu + 1) \sin(\lambda_n)}.$$

Similarly to case A, the current form of this expression is not desirable for the following analysis since t appears on the numerator of the exponent. Thus, using the corollary and lemma shown on page 41, the governing equations are re-characterised such that a new, more convenient form of the VIE may be obtained. From the governing equations, it is clear that

$$\begin{aligned} f(x) &= 1, \\ \phi_1(t) &= c(0, t), \\ \phi_2(t) &= c(1, t), \\ F(t, c(0, t)) &= -\mu(1 - c(0, t)), \\ G(t, c(1, t)) &= -\frac{\alpha c(1, t)}{1 + \beta c(1, t)}. \end{aligned}$$

Now, $\theta(x, t)$ is calculated for $x = 0$ and $x = \pm 1$:

$$\begin{aligned} \theta(0, t) &= \frac{1}{\sqrt{4\pi t}} \left(1 + 2 \sum_{m=1}^{\infty} e^{-m^2/t} \right) = \frac{1}{2} k_A(t), \\ \theta(\pm 1, t) &= \frac{1}{\sqrt{4\pi t}} (2e^{-1/4t} + 2e^{-9/4t} + 2e^{-25/4t} + \dots) = g(t), \end{aligned}$$

where

$$g(t) = \frac{1}{\sqrt{\pi t}} \sum_{m=1}^{\infty} e^{-(2m-1)^2/4t}. \quad (2.5.16)$$

Thus, using Corollary 2.1 and Lemma 2.2, the following coupled VIEs are derived:

$$c(0, t) = 1 + \int_0^t \mu k_A(t - \tau) [1 - c(0, \tau)] - 2g(t - \tau) \frac{\alpha c(1, \tau)}{1 + \beta c(1, \tau)} d\tau, \quad (2.5.17)$$

$$c(1, t) = 1 + \int_0^t 2\mu g(t - \tau) [1 - c(0, \tau)] - k_A(t - \tau) \frac{\alpha c(1, \tau)}{1 + \beta c(1, \tau)} d\tau. \quad (2.5.18)$$

Corollary 2.1 (Corollary 7.3.2 from [52])

For piecewise-continuous f and for continuous F and G , the solution u of the problem

$$\begin{aligned}\frac{\partial u}{\partial t}(x, t) &= \frac{\partial^2 u}{\partial x^2}(x, t), \quad 0 < x < 1, \quad t > 0, \\ u(x, 0) &= f(x), \quad 0 < x < 1, \\ \frac{\partial u}{\partial x}(0, t) &= F(t, u(0, t)), \quad t > 0, \\ \frac{\partial u}{\partial x}(1, t) &= G(t, u(1, t)), \quad t > 0,\end{aligned}$$

has the form

$$u(x, t) = w(x, t) - 2 \int_0^t \theta(x, t - \tau) F(\tau, \phi_1(\tau)) d\tau + 2 \int_0^t \theta(x - 1, t - \tau) G(\tau, \phi_2(\tau)) d\tau,$$

where

$$\begin{aligned}w(x, t) &= \int_0^1 [\theta(x - \zeta, t) + \theta(x + \zeta, t)] f(\zeta) d\zeta, \\ \theta(x, t) &= \sum_{m=-\infty}^{\infty} K(x + 2m, t), \\ K(x, t) &= \frac{1}{\sqrt{4\pi t}} e^{-x^2/4t},\end{aligned}$$

if and only if $\phi_1(t), \phi_2(t)$ are piecewise-continuous functions that satisfy

$$\begin{aligned}\phi_1(t) &= w(0, t) - 2 \int_0^t \theta(0, t - \tau) F(\tau, \phi_1(\tau)) d\tau + 2 \int_0^t \theta(-1, t - \tau) G(\tau, \phi_2(\tau)) d\tau, \\ \phi_2(t) &= w(1, t) - 2 \int_0^t \theta(1, t - \tau) F(\tau, \phi_1(\tau)) d\tau + 2 \int_0^t \theta(0, t - \tau) G(\tau, \phi_2(\tau)) d\tau.\end{aligned}$$

Lemma 2.2 (Lemma 2.2 from [53])

For $0 \leq x \leq 1$ and $t \geq 0$,

$$w_1(x, t) = \int_0^1 \theta(x - \zeta, t) + \theta(x + \zeta, t) d\zeta = 1.$$

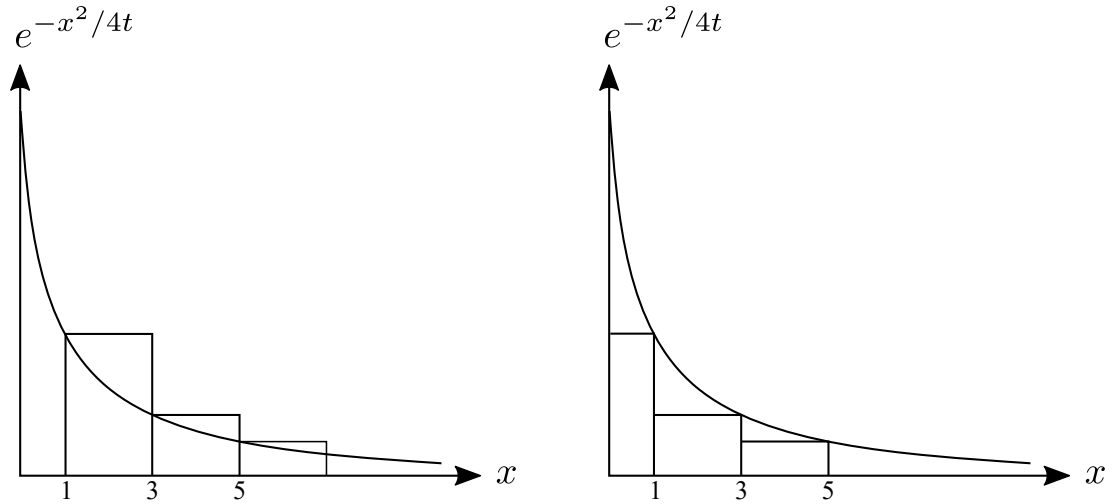


Figure 2.5.2: Schematic drawing illustrating the area under the curve $e^{-x^2/4t}$ and an approximation to this area using lower (left) and upper (right) Riemann sums.

Note that (2.5.18) is an alternative form of the VIE given by (2.5.3), and in this new form, it is particularly clear that the VIEs from cases A and B are equivalent in the limit as $\mu \rightarrow 0$.

Now, (2.5.17) and (2.5.18) are used to derive a solution for $c(1, t)$ at early times. Recall that in case A, Riemann sums were employed to deduce that $k_A(t) \sim 1/\sqrt{\pi t}$ as $t \rightarrow 0$. Here, a similar approach is used to examine the behaviour of $g(t)$ for $t \ll 1$. A lower bound for $g(t)$ may be obtained by using lower Riemann sums to approximate the area under the curve $e^{-x^2/4t}$ (Fig. 2.5.2, left):

$$2 \sum_{n=1}^{\infty} e^{-(2n-1)^2/4t} > \int_1^{\infty} e^{-x^2/4t} dx.$$

Using the substitution $u = x^2/4t$ to evaluate the integral gives

$$2 \sum_{n=1}^{\infty} e^{-(2n-1)^2/4t} > \sqrt{\pi t} \operatorname{erfc} \left(\frac{1}{2\sqrt{t}} \right),$$

and it follows from (2.5.16) that

$$g(t) > \frac{1}{2} \operatorname{erfc} \left(\frac{1}{2\sqrt{t}} \right). \quad (2.5.19)$$

To obtain an upper bound for $g(t)$, the area under the curve $e^{-x^2/4t}$ is approximated using upper Riemann sums (Fig. 2.5.2, right):

$$e^{-1/4t} + 2 \sum_{n=2}^{\infty} e^{-(2n-1)^2/4t} < \int_0^{\infty} e^{-x^2/4t} dx = \sqrt{\pi t},$$

by using the substitution $u = x^2/4t$ to evaluate the integral. Adding $e^{-1/4t}$ to both sides of this

equation and re-arranging yields

$$g(t) < \frac{1}{2} \left(1 + \frac{1}{\sqrt{\pi t}} e^{-1/4t} \right). \quad (2.5.20)$$

Now, (2.5.19) and (2.5.20) can be combined to obtain

$$\frac{1}{2} \operatorname{erfc} \left(\frac{1}{2\sqrt{t}} \right) < g(t) < \frac{1}{2} \left(1 + \frac{1}{\sqrt{\pi t}} e^{-1/4t} \right).$$

For $t \ll 1$,

$$\operatorname{erfc} \left(\frac{1}{2\sqrt{t}} \right) = \frac{2\sqrt{t}}{\sqrt{\pi}} e^{-1/4t} (1 - 2t + \dots) \approx 0,$$

since the exponential term dominates and rapidly decays. Thus, for small t

$$0 < g(t) < \frac{1}{2},$$

and using the upper bound,

$$g(t) \sim \frac{1}{2} \quad \text{as } t \rightarrow 0.$$

Now, consider the following expansions in t :

$$c(0, t) = a_1 + a_2 t^{1/2} + a_3 t + a_4 t^{3/2} + a_5 t^2 + \mathcal{O}(t^{5/2}), \quad (2.5.21)$$

$$c(1, t) = b_1 + b_2 t^{1/2} + b_3 t + b_4 t^{3/2} + b_5 t^2 + \mathcal{O}(t^{5/2}), \quad (2.5.22)$$

where higher-order terms (compared with case A) have been included in order to demonstrate the dependence of the solution on μ . First, (2.5.21) and (2.5.22) are substituted into (2.5.17). Using the simplified expressions for $k_A(t)$ and $g(t)$ and taking a series expansion of

$$\left(1 + \beta [b_1 + b_2 \tau^{1/2} + b_3 \tau + b_4 \tau^{3/2} + b_5 \tau^2 + \mathcal{O}(\tau^{5/2})] \right)^{-1}$$

about $\tau = 0$ gives

$$\begin{aligned} & a_1 + a_2 t^{1/2} + a_3 t + a_4 t^{3/2} + a_5 t^2 + \mathcal{O}(t^{5/2}) \\ &= 1 + \int_0^t \frac{\mu}{\sqrt{\pi}} (t - \tau)^{-1/2} \left[1 - a_1 - a_2 \tau^{1/2} - a_3 \tau - a_4 \tau^{3/2} - a_5 \tau^2 - \mathcal{O}(\tau^{5/2}) \right] \\ & \quad - \alpha [b_1 + b_2 \tau^{1/2} + b_3 \tau + b_4 \tau^{3/2} + b_5 \tau^2 + \mathcal{O}(\tau^{5/2})] \\ & \quad \times \left[\frac{1}{b_1 \beta + 1} - \frac{b_2 \beta}{(b_1 \beta + 1)^2} \tau^{1/2} + \frac{(b_2^2 - b_1 b_3) \beta^2 - b_3 \beta}{(b_1 \beta + 1)^3} \tau + \mathcal{O}(\tau^{3/2}) \right] d\tau. \end{aligned}$$

Multiplying out the brackets yields

$$\begin{aligned}
& a_1 + a_2 t^{1/2} + a_3 t + a_4 t^{3/2} + a_5 t^2 + \mathcal{O}(t^{5/2}) \\
&= 1 + \frac{\mu}{\sqrt{\pi}} [(1 - a_1)I_1 - a_2 I_2 - a_3 I_3 - a_4 I_4 - \dots] \\
&\quad - \alpha \left[\frac{b_1}{b_1 \beta + 1} I_5 + \frac{b_2}{(b_1 \beta + 1)^2} I_6 + \frac{(b_1 b_3 - b_2^2)\beta + b_3}{(b_1 \beta + 1)^3} I_7 + \dots \right],
\end{aligned} \tag{2.5.23}$$

where

$$\begin{aligned}
I_1 &= \int_0^t (t - \tau)^{-1/2} d\tau = 2t^{1/2}, \\
I_2 &= \int_0^t (t - \tau)^{-1/2} \tau^{1/2} d\tau = \frac{\pi}{2}t, \\
I_3 &= \int_0^t (t - \tau)^{-1/2} \tau d\tau = \frac{4}{3}t^{3/2}, \\
I_4 &= \int_0^t (t - \tau)^{-1/2} \tau^{3/2} d\tau = \frac{3\pi}{8}t^2, \\
I_5 &= \int_0^t 1 d\tau = t, \\
I_6 &= \int_0^t \tau^{1/2} d\tau = \frac{2}{3}t^{3/2}, \\
I_7 &= \int_0^t \tau d\tau = \frac{1}{2}t^2,
\end{aligned}$$

are easily evaluated using simple integration, substitution and integration by parts. Substituting these expressions into (2.5.23) and equating powers of t gives

$$\begin{aligned}
a_1 &= 1, \\
a_2 &= 0, \\
a_3 &= -\frac{\alpha b_1}{b_1 \beta + 1},
\end{aligned} \tag{2.5.24}$$

$$a_4 = \frac{2\alpha(2\mu b_1^2 \beta + 2\mu b_1 - \sqrt{\pi} b_2)}{3\sqrt{\pi}(b_1 \beta + 1)^2}. \tag{2.5.25}$$

Now, similarly, (2.5.21) and (2.5.22) are substituted into (2.5.18) to obtain

$$\begin{aligned}
& b_1 + b_2 t^{1/2} + b_3 t + b_4 t^{3/2} + b_5 t^2 + \mathcal{O}(t^{5/2}) \\
&= 1 + \int_0^t \mu [1 - a_1 - a_2 \tau^{1/2} - a_3 \tau - a_4 \tau^{3/2} - a_5 \tau^2 - \mathcal{O}(\tau^{5/2})] \\
&\quad - \frac{\alpha}{\sqrt{\pi}} (t - \tau)^{-1/2} [b_1 + b_2 \tau^{1/2} + b_3 \tau + b_4 \tau^{3/2} + b_5 \tau^2 + \mathcal{O}(\tau^{5/2})] \\
&\quad \times \left[\frac{1}{b_1 \beta + 1} - \frac{b_2 \beta}{(b_1 \beta + 1)^2} \tau^{1/2} + \frac{(b_2^2 - b_1 b_3)\beta^2 - b_3 \beta}{(b_1 \beta + 1)^3} \tau \right. \\
&\quad \left. - \frac{(b_1^2 b_4 - 2b_1 b_2 b_3 + b_2^2)\beta^3 + 2(b_1 b_4 - b_2 b_3)\beta^2 + b_4 \beta}{(b_1 \beta + 1)^4} \tau^{3/2} + \mathcal{O}(\tau^2) \right] d\tau,
\end{aligned}$$

and multiplying out the brackets yields

$$\begin{aligned}
& b_1 + b_2 t^{1/2} + b_3 t + b_4 t^{3/2} + b_5 t^2 + \mathcal{O}(t^{5/2}) \\
&= 1 + \mu [(1 - a_1)I_5 - a_2 I_6 - a_3 I_7 - \dots] - \frac{\alpha}{\sqrt{\pi}} \left[\frac{b_1}{b_1 \beta + 1} I_1 + \frac{b_2}{(b_1 \beta + 1)^2} I_2 \right. \\
&\quad \left. + \frac{(b_1 b_3 - b_2^2) \beta + b_3}{(b_1 \beta + 1)^3} I_3 + \frac{(b_1^2 b_4 - 2b_1 b_2 b_3 + b_2^3) \beta^2 + 2(b_1 b_4 - b_2 b_3) \beta + b_4}{(b_1 \beta + 1)^4} I_4 + \dots \right].
\end{aligned}$$

Substituting the expressions for I_1 to I_7 and equating powers of t gives

$$\begin{aligned}
b_1 &= 1, \\
b_2 &= -\frac{2\alpha}{\sqrt{\pi}(\beta + 1)}, \\
b_3 &= \frac{\alpha^2}{(\beta + 1)^3}, \\
b_4 &= -\frac{4\alpha^3(\pi - 4\beta)}{3\pi^{3/2}(\beta + 1)^5}, \\
b_5 &= \frac{\alpha^4(\pi - (4 + 3\pi)\beta + 6\beta^2) + \alpha\mu\pi(\beta + 1)^6}{2\pi(\beta + 1)^7}.
\end{aligned}$$

Then, from (2.5.24) and (2.5.25), it follows that

$$\begin{aligned}
a_3 &= -\frac{\alpha}{\beta + 1}, \\
a_4 &= \frac{4\alpha(\mu(\beta + 1)^2 + \alpha)}{3\sqrt{\pi}(\beta + 1)^3}.
\end{aligned}$$

Thus, from (2.5.21) and (2.5.22), the solutions when $t \ll 1$ are given by

$$\begin{aligned}
c(0, t) &= 1 - \frac{\alpha}{\beta + 1} t + \frac{4\alpha(\mu(\beta + 1)^2 + \alpha)}{3\sqrt{\pi}(\beta + 1)^3} t^{3/2} - \mathcal{O}(t^2), \\
c(1, t) &= 1 - \frac{2\alpha}{\sqrt{\pi}(\beta + 1)} t^{1/2} + \frac{\alpha^2}{(\beta + 1)^3} t - \frac{4\alpha^3(\pi - 4\beta)}{3\pi^{3/2}(\beta + 1)^5} t^{3/2} \\
&\quad + \frac{\alpha^4(\pi - (4 + 3\pi)\beta + 6\beta^2) + \alpha\mu\pi(\beta + 1)^6}{2\pi(\beta + 1)^7} t^2 - \mathcal{O}(t^{5/2}).
\end{aligned} \tag{2.5.26}$$

As expected, the solute concentration depends on μ , although this dependence is relatively weak with μ first appearing in the third and fourth terms of the solutions at $x = 0$ and $x = 1$, respectively. Intuitively, the dependence on μ is slightly more significant at $x = 0$ since this is where mass transfer takes place across the fluid-air interface. Also, it is noted that the solution at $x = 1$ is identical to the small t solution derived in case A, up to and including the $t^{3/2}$ term, thus implying that the models are equivalent for $t \ll 1$. Since the initial condition is the same for each model and the generation of a concentration gradient at $x = 0$ is limited by the rate of diffusion, for early times the rate of mass transfer at $x = 0$ will be approximately zero and, as

previously described, the models are equivalent in the limit as $\mu \rightarrow 0$.

Steady-state solution for case B

For this case, where the solute can cross the fluid-air interface, it is clear that the solution as $t \rightarrow \infty$ will be a function of x , since the solute is replenished as it is metabolised and therefore will not fully deplete. To derive this non-trivial solution, the steady diffusion equation is solved subject to (2.2.3B) and (2.2.4). Integrating the steady diffusion equation twice with respect to x and then applying (2.2.3B) results in

$$c(x, \infty) = Ax + \frac{A}{\mu} + 1, \quad (2.5.27)$$

where A is a constant of integration. Applying (2.2.4) gives a quadratic equation in A which may be solved using the quadratic formula to obtain

$$A = \frac{-\mu(\beta + 1) - \alpha(\mu + 1) \pm \sqrt{[\mu(\beta + 1) + \alpha(\mu + 1)]^2 - 4\alpha\beta\mu(\mu + 1)}}{2\beta(\mu + 1)},$$

where either the positive or negative root should be chosen such that $c(x, \infty) > 0$.

2.5.3 Numerical method for solving the VIEs

As in case A, product integration methods are applied to derive an implicit numerical scheme for solving (2.5.3). Recall that the VIE is given by

$$c(1, t) = 1 - \alpha \int_0^t \sum_{n=1}^{\infty} \sigma_n e^{-\lambda_n^2(t-\tau)} \frac{c(1, \tau)}{1 + \beta c(1, \tau)} d\tau,$$

where σ_n is a constant defined as

$$\sigma_n = \frac{2[\lambda_n \cos(\lambda_n) + \mu \sin(\lambda_n)]}{\lambda_n \cos(\lambda_n) + (\mu + 1) \sin(\lambda_n)}.$$

With the approximation

$$\frac{c(1, \tau)}{1 + \beta c(1, \tau)} \approx \frac{c(1, t_{j+1})}{1 + \beta c(1, t_{j+1})}$$

over $[t_j, t_{j+1}]$, and replacing t by $t_i = i\Delta t$, where $i = 1, 2, \dots, T$ such that $T\Delta t$ is the final time of interest, the VIE can be re-written as follows:

$$c(1, t_i) \approx 1 - \alpha \sum_{j=0}^{i-1} \left(\int_{t_j}^{t_{j+1}} \sum_{n=1}^{\infty} \sigma_n e^{-\lambda_n^2(t_i-\tau)} d\tau \right) \frac{c(1, t_{j+1})}{1 + \beta c(1, t_{j+1})}.$$

Performing the integration with $t_j = j\Delta t$ yields

$$\int_{t_j}^{t_{j+1}} \sum_{n=1}^{\infty} \sigma_n e^{-\lambda_n^2(t_i - \tau)} d\tau = \sum_{n=1}^{\infty} \frac{\sigma_n}{\lambda_n^2} \left(e^{-\lambda_n^2 \Delta t(i-j-1)} - e^{-\lambda_n^2 \Delta t(i-j)} \right),$$

so then

$$c(1, t_i) \approx 1 - \alpha \sum_{j=0}^{i-1} \left[\sum_{n=1}^{\infty} \frac{\sigma_n}{\lambda_n^2} \left(e^{-\lambda_n^2 \Delta t(i-j-1)} - e^{-\lambda_n^2 \Delta t(i-j)} \right) \right] \frac{c(1, t_{j+1})}{1 + \beta c(1, t_{j+1})}.$$

Note that

$$\begin{aligned} & \sum_{j=0}^{i-1} \left[\sum_{n=1}^{\infty} \frac{\sigma_n}{\lambda_n^2} \left(e^{-\lambda_n^2 \Delta t(i-j-1)} - e^{-\lambda_n^2 \Delta t(i-j)} \right) \right] \frac{c(1, t_{j+1})}{1 + \beta c(1, t_{j+1})} \\ &= \left[\sum_{n=1}^{\infty} \frac{\sigma_n}{\lambda_n^2} \left(1 - e^{-\lambda_n^2 \Delta t} \right) \right] \frac{c(1, t_i)}{1 + \beta c(1, t_i)} \\ &+ \sum_{j=0}^{i-2} \left[\sum_{n=1}^{\infty} \frac{\sigma_n}{\lambda_n^2} \left(e^{-\lambda_n^2 \Delta t(i-j-1)} - e^{-\lambda_n^2 \Delta t(i-j)} \right) \right] \frac{c(1, t_{j+1})}{1 + \beta c(1, t_{j+1})}, \end{aligned}$$

so an approximation to $c(1, t_i)$ may be obtained by finding the roots, c_i , of the following implicit equation:

$$\begin{aligned} c_i + \alpha \left[\sum_{n=1}^{\infty} \frac{\sigma_n}{\lambda_n^2} \left(1 - e^{-\lambda_n^2 \Delta t} \right) \right] \frac{c_i}{1 + \beta c_i} \\ = 1 - \alpha \sum_{j=0}^{i-2} \left[\sum_{n=1}^{\infty} \frac{\sigma_n}{\lambda_n^2} \left(e^{-\lambda_n^2 \Delta t(i-j-1)} - e^{-\lambda_n^2 \Delta t(i-j)} \right) \right] \frac{c_{j+1}}{1 + \beta c_{j+1}}. \end{aligned}$$

Similarly to case A, in order to obtain the small β solution to first order, the VIE given by (2.5.8) must be solved. Derived using the same method as in §2.4.3, the following explicit Euler scheme can be used to provide an approximation of the first order term from the small β solution:

$$c_1(1, t_i) \approx -\alpha \Delta t \sum_{j=0}^{i-1} k_B(t_i - t_j) [c_1(1, t_j) - c_0(1, t_j)]^2.$$

As in case A, a sensitivity study was performed to determine the optimal values of Δt , the spacing between consecutive time points, and N , the finite number of terms at which the infinite sums are truncated, using the highest and lowest values of α , β and μ considered in the next section. For both the implicit and explicit numerical methods, $\Delta t = 1 \times 10^{-3}$ and $N = 100$ were found to provide an acceptable level of accuracy.

2.5.4 Comparing the solution of the VIE with the approximate solutions

Similarly to case A, the solution of the VIE is compared with the approximate solutions derived in §2.5.2 over the following parameter ranges:

$$\alpha = 0.01, 0.1, 1, 10, 100,$$

$$\beta = 0.01, 0.1, 1, 10, 100,$$

$$\mu = 0.01, 0.1, 1, 10, 100.$$

First, the solution of the VIE given by (2.5.3) is generated for various values of α , as illustrated in Fig. 2.5.3. As in case A, the rate at which the solution decreases from the initial condition increases with increasing α . In this case, the steady-state solution varies depending on the rate at which the solute is both supplied and metabolised. Using $\alpha = 10$, $\beta = 1$ and $\mu = 1$ as an example, Fig. 2.5.4 confirms that the solution of the VIE does indeed approach the steady-state solution.

Next, the solution of the VIE is generated for various values of μ . Recall that μ is the ratio of the rate of mass transfer across the fluid-air interface and the rate of diffusion, and in the limit as $\mu \rightarrow 0$, the solution from case B is equivalent to the solution from case A. From Fig. 2.5.5, it is clear that the solution of the VIE is not heavily dependent on the value of μ at early times, in agreement with the small t solution given by (2.5.26). As μ increases, and the boundary condition at $x = 0$ behaves more like a constant source of solute, the steady-state value that the solution approaches also increases.

Figs. 2.5.6 and 2.5.7 compare the solution of the VIE with the small and large β solutions, respectively, for various values of β . As in case A, the agreement between the solution of the VIE and the small β solution improves as β decreases, and the agreement between the solution of the VIE and the large β solution improves as β increases. As expected, for all values of β the approximations become more accurate as higher order terms are added to the solutions.

Fig. 2.5.8 compares the solution of the VIE with the small t solution for $0 \leq t \leq 1$. It is unsurprising that, as t increases, the agreement between the solution of the VIE and the approximate solution deteriorates, since the latter is only valid when $t \ll 1$. Note that when $\alpha = \beta = \mu = 1$, the small t solution given by (2.5.26) is equal to

$$c(1, t) = 1 - 0.5642t^{1/2} + 0.1250t + 0.0064t^{3/2} + 0.2447t^2 - \mathcal{O}(t^{5/2}).$$

Thus, for these parameter values, the contribution of the t^2 term is larger than that of the previous two terms, explaining the dramatic difference in the behaviour of the approximate solution when this term is included. The inset plot highlights that the agreement between the solution of the VIE and the small t solution is very good within the region of validity, where the solutions are shown for $0 \leq t \leq 0.1$

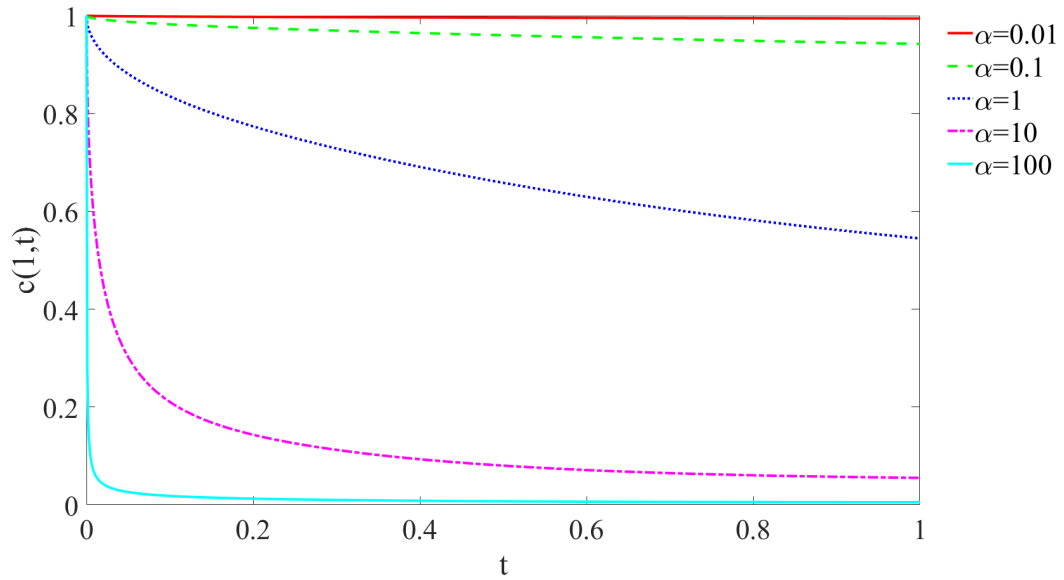


Figure 2.5.3: Solution to the VIE from case B for various values of α with $\beta = \mu = 1$, showing the dependence of the solute concentration at the cell surface, $c(1, t)$, on the non-dimensional parameter α .

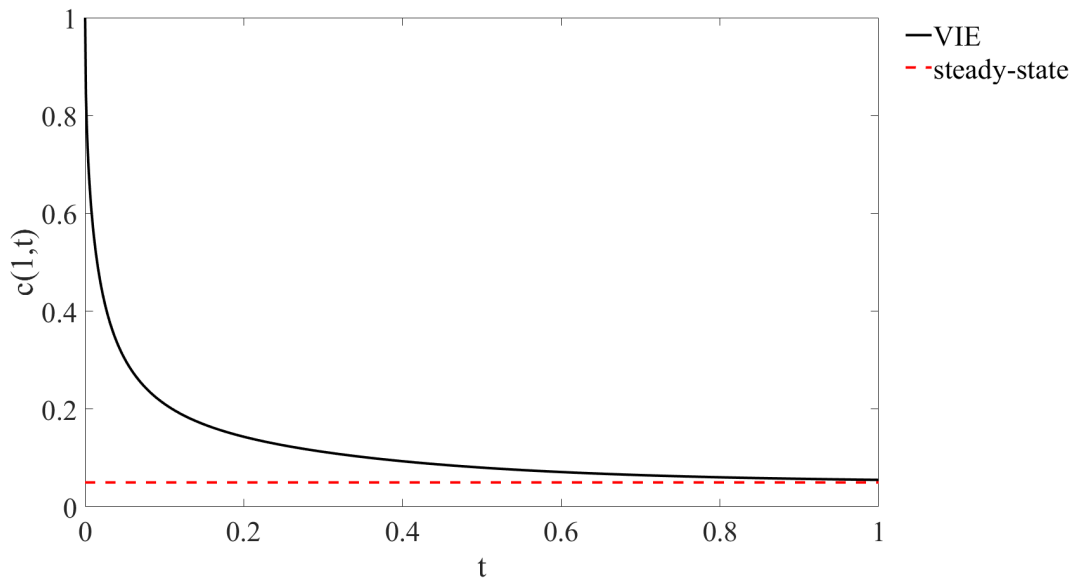


Figure 2.5.4: Comparing the solution to the VIE from case B and the steady-state solution, with $\alpha = 10$ and $\beta = \mu = 1$.

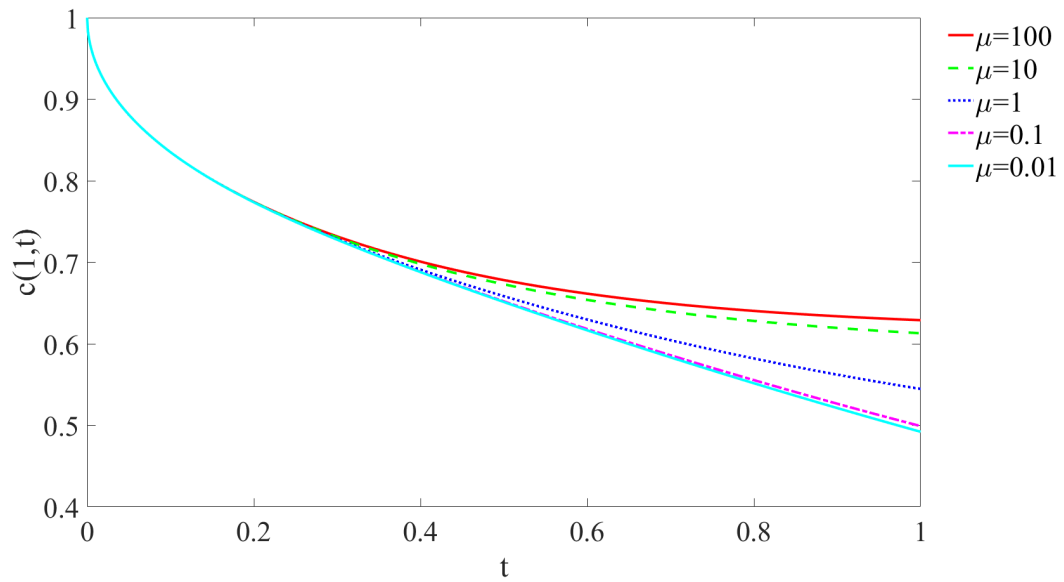


Figure 2.5.5: Solution to the VIE from case B for various values of μ with $\alpha = \beta = 1$, showing the dependence of the solute concentration at the cell surface, $c(1, t)$, on the non-dimensional parameter μ .

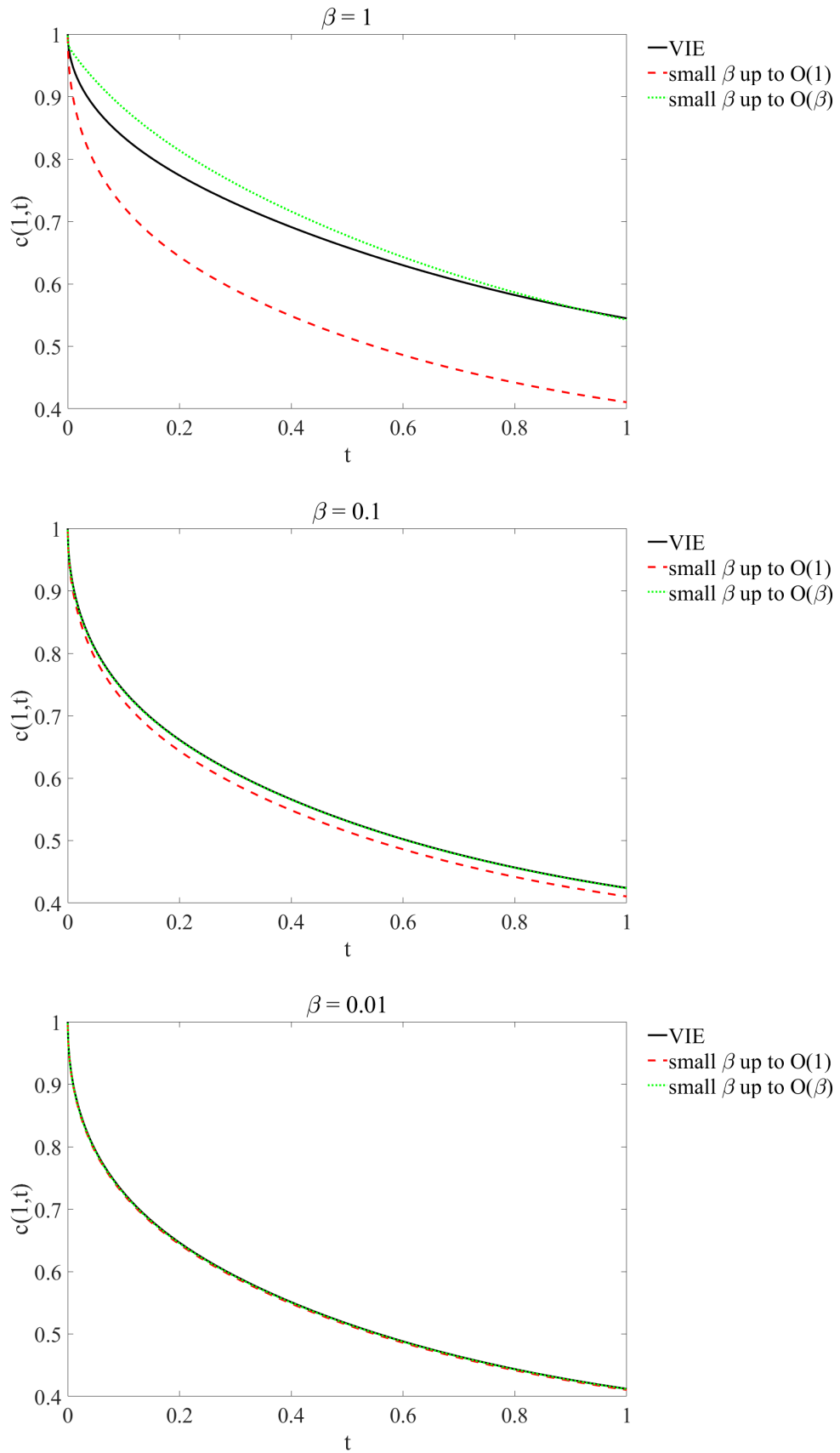


Figure 2.5.6: Comparing the solution to the VIE from case B with the small β solution for various values of β , with $\alpha = \mu = 1$.

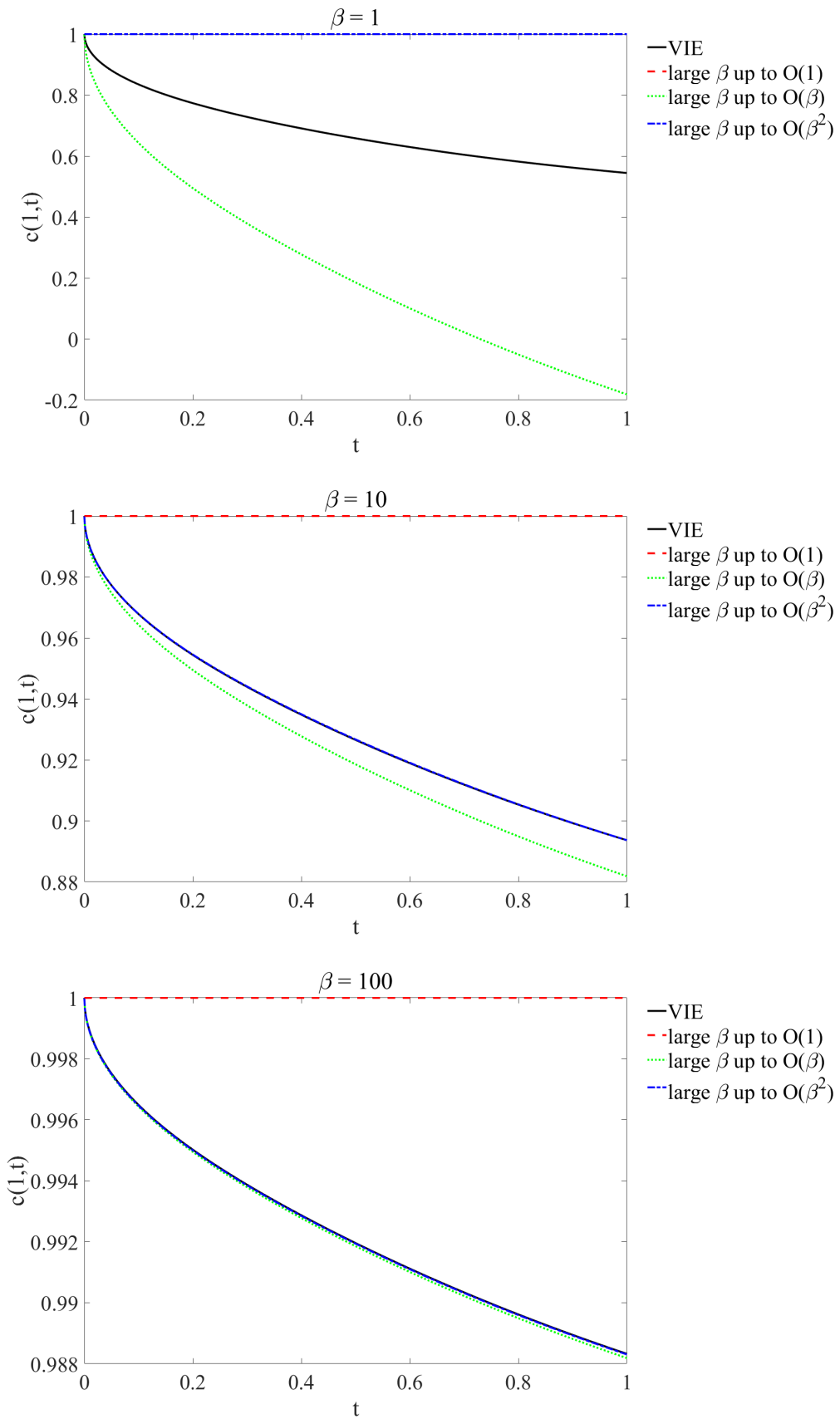


Figure 2.5.7: Comparing the solution to the VIE from case B with the large β solution for various values of β , with $\alpha = \mu = 1$. Note that when $\beta = 1$, the large β solution to second order is equal to 1, i.e. the large β solution to leading order, so the red and blue lines in the upper plot are overlapping.

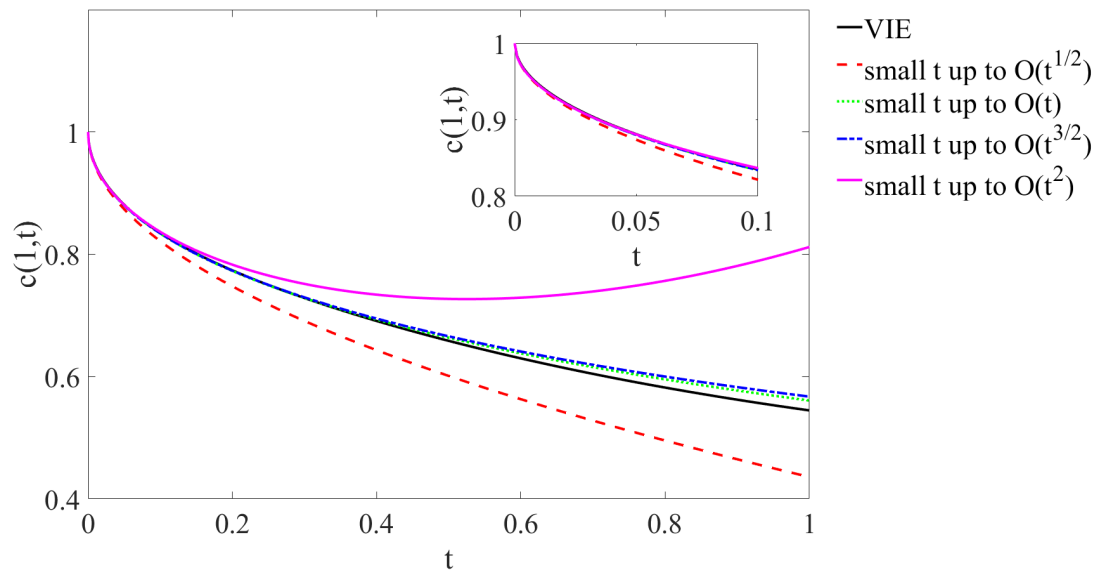


Figure 2.5.8: Comparing the solution to the VIE from case B with the small t solution for $0 \leq t \leq 1$, with $\alpha = \beta = \mu = 1$. The inset plot highlights the good agreement between the solutions for $0 \leq t \leq 0.1$.

2.6 Discussion

In this section, some limitations of the model developed in this chapter are addressed and the utility of the model is discussed, with simple but useful relationships being derived to aid in the set-up of experiments.

2.6.1 Model limitations

It is important to acknowledge that, whilst the results in this chapter provide valuable insight into the relationships between various model parameters, these results are only relevant to the specific conditions that are described by this particular model. Therefore, the application of these results is somewhat limited by the number of assumptions that are made during the development of the mathematical model, and in order to represent different experimental conditions, it would be necessary to redefine the model equations and revisit the analysis outlined in this chapter.

In this model, it is assumed that solute transport is governed solely by diffusion, but it should be noted that not all experiments are performed under completely static conditions; for example, fluid movement could be introduced through the use of shakers, rockers or stirrers. In such cases, there would also be an advective component to solute transport and so the governing equations would need to be adjusted to account for this.

Initially, it is assumed that the solute is uniformly distributed throughout the fluid, since typically the solute is mixed with the cell culture medium prior to the beginning of the experiment. However, if the solute was to be added to the fluid at the start of the experiment, the solute would not yet be evenly dispersed and so the initial condition would need to be amended to account for this.

In this chapter, it is assumed that the thickness of the cell layer is significantly smaller than the depth of the fluid, so solute metabolism is represented by a flux boundary condition at the base of the petri dish. This is only valid if the cell region has a negligible volume, as is the case when the cells are in a monolayer formation. However, if the petri dish contained a 3D structure of cells, such as within a scaffold or spheroid, it would be more appropriate to represent the cell region as a separate domain within the model. Furthermore, it is assumed that the cells occupy the entire base of the petri dish; however, if the cells were only present on a portion of the base of the dish, the one-dimensionality of the model would no longer be viable.

It is also assumed that solute metabolism is governed by M-M kinetics, but there are a vast array of mechanisms by which the cells might interact with the solute, depending on the cell type and solute under consideration; for example, rather than being metabolised by the cells via M-M or other kinetics, the solute may instead bind to receptors on the surface of the cells. To represent such interactions, the boundary condition at the base of the petri dish would need to be adjusted by replacing the M-M reaction term with an appropriate expression relating to the kinetics of interest.

In this model, it is assumed that the solute does not interact with the walls of the petri dish, which are further assumed to be impermeable. In reality, the walls of the petri dish may be permeable to gases such as O_2 , and may be fabricated from a material that facilitates absorption or adsorption (surface binding) of the solute. To represent such interactions, additional boundary conditions would need to be implemented at the walls of the petri dish and it would be necessary to solve the model in a higher dimension.

Finally, it is reiterated that the semi-analytical small and large β solutions that are derived in §2.4.2 and §2.5.2 are only applicable under the specific conditions on β , and should not be applied in general.

2.6.2 Utility of the model

Whilst the full solutions for cases A and B may be found by solving the VIEs (2.4.3) and (2.5.3) numerically using the implicit methods outlined in §2.4.3 and §2.5.3, respectively, these solutions alone would not provide a detailed insight into the relationships between key model parameters. The approximate solutions derived in §2.4.2 and §2.5.2 highlight the dependency of the cell surface solute concentration on the non-dimensional parameters α , β and μ , and can be used to provide useful information about the cell culture environment without requiring the implementation of complicated numerical techniques; this would be particularly useful for experimental researchers with a limited understanding of the mathematical methods used in this chapter.

In cases where it is known that β is either small or large, the semi-analytical solutions given by (2.4.10) and (2.4.14) for case A, or (2.5.11) and (2.5.15) for case B, may be used to quickly provide information about the solute concentration at the cell surface. In cases where the solute concentration at early stages of the experiment is of importance, the small t solutions given by (2.4.19) for case A, or (2.5.26) for case B, may be used to infer how changes in key parameters influence the solution at early times. Similarly, in cases where the non-zero steady-state solute concentration is of interest, the solution given by (2.5.27) for case B may be used to easily compute the steady-state solute concentration, given that the values of the non-dimensional parameters α , β and μ are known.

In order to fulfil the aim of aiding in the set-up of experiments, the results presented in this chapter may be used to answer the following key questions:

- How much solute has been metabolised at each stage of the experiment?
- How long does it take for the cell surface solute concentration to reach steady-state?
- How can the experiment be configured to ensure that the solute concentration at the cell surface remains above a desired concentration for a certain amount of time?

In dimensional parameters, the total amount of solute that has been metabolised in a given time may be calculated by integrating the M-M reaction term as follows:

$$M(T) = A \int_0^T \frac{V_{max}c(d, t)}{K_m + c(d, t)} dt, \quad (2.6.1)$$

where $M(T)$ (mol) is the total amount of solute that has been metabolised in the time of interest, T (s), and A (m^2) is the area covered by the cells. In order to make use of the solutions presented in this chapter, it is necessary to non-dimensionalise (2.6.1) using the scalings

$$c = c_0c^*, \quad t = \frac{d^2}{D}t^*,$$

to obtain

$$M^*(T^*) = \int_0^{T^*} \frac{\alpha c^*(1, t^*)}{1 + \beta c^*(1, t^*)} dt^*, \quad (2.6.2)$$

where $M^*(T^*) = M(T)/Adc_0$ is the non-dimensional amount of solute that has been metabolised in the non-dimensional time of interest, $T^* = TD/d^2$. Generally, $M^*(T^*)$ is calculated first by numerically computing $c^*(1, t^*)$ and then performing the integration. However, recall that when β is either small or large, the M-M term can be reduced to linear kinetics, so under these conditions (2.6.2) may be approximated as

$$M^*(T^*) \approx \begin{cases} \int_0^{T^*} \alpha c^*(1, t^*) dt^*, & \beta \ll 1 \\ \int_0^{T^*} \frac{\alpha}{\beta} dt^*, & \beta \gg 1 \end{cases}.$$

When $\beta \ll 1$, $M^*(T^*)$ may be evaluated by replacing $c^*(1, t^*)$ by the small β solutions (2.4.10) and (2.5.11), for cases A and B, respectively, and performing the integration to obtain

$$M^*(T^*) \approx \alpha \left(\sum_{n=1}^{\infty} \frac{2 \sin(\kappa_n) [1 - e^{-\kappa_n^2 T^*}]}{\kappa_n^2 [\kappa_n \cos(\kappa_n) + (\alpha + 1) \sin(\kappa_n)]} + \mathcal{O}(\beta) \right), \quad (2.6.3)$$

for case A, and

$$M^*(T^*) \approx \alpha \left(\frac{\mu T^*}{\alpha \mu + \alpha + \mu} + \sum_{n=1}^{\infty} \frac{2 [\mu \cos(\xi_n) - \xi_n \sin(\xi_n)] [1 - e^{-\xi_n^2 T^*}]}{\xi_n^2 [(\alpha \mu + \alpha + \mu - \xi_n^2) \cos(\xi_n) - \xi_n (2 + \alpha + \mu) \sin(\xi_n)]} + \mathcal{O}(\beta) \right), \quad (2.6.4)$$

for case B. When $\beta \gg 1$, solute metabolism is approximately constant and equal to

$$M^*(T^*) \approx \frac{\alpha}{\beta} T^*, \quad (2.6.5)$$

for both cases A and B. Thus, the non-dimensional amount of solute that has been metabolised may be approximated by (2.6.3), (2.6.4) and (2.6.5), under certain parameter regimes. These expressions can easily be re-dimensionalised to provide an approximation for the number of moles of solute metabolised by simply multiplying by Adc_0 , i.e.

$$M(T) = Adc_0 M^*(T^*),$$

recalling that d (m) is the depth of the fluid and c_0 (mol m^{-3}) is the initial concentration of the solute within the fluid.

In non-dimensional parameters, the time taken for the solute concentration at the cell surface to reach a desired concentration, $c_D(d, t)$ (mol m^{-3}), may be obtained via

$$c^*(1, t^*) = c_D^*(1, t^*), \quad (2.6.6)$$

where $c_D^*(1, t^*) = c_D(d, t)/c_0$ is the non-dimensional desired cell surface solute concentration. Generally, this equation would be solved by first numerically computing $c^*(1, t^*)$, but if it is known that β is either small or large, $c^*(1, t^*)$ may be replaced by the approximate solutions derived in §2.4.2 and §2.5.2, for cases A and B, respectively. Thus, the approximate non-dimensional time taken to reach a desired cell surface solute concentration may be determined by solving (2.6.6) for t^* , with $c^*(1, t^*)$ replaced by (2.4.10), (2.4.14), (2.5.11) or (2.5.15) depending on the parameter regime under consideration. The time in seconds can then be easily obtained by re-dimensionalising t^* by simply multiplying by d^2/D .

Note that to calculate how long it takes for the cell surface solute concentration to reach steady-state, $c_D^*(1, t^*)$ may be replaced by the cell surface solute concentration as $t \rightarrow \infty$. In case B, this may be calculated via (2.5.27), but recall that in case A, where the solute cannot cross the fluid-air interface and is therefore not replenished, the steady-state solute concentration is simply zero. In this special case, the time taken to reach steady-state may be calculated by solving

$$c^*(1, t^*) = 0,$$

or equivalently,

$$M^*(T^*) = 1,$$

since the solute will be fully depleted when the amount of solute metabolised is equal to the initial amount of solute.

Finally, in order to ensure that the cell surface solute concentration remains above a desired amount for a specified duration of time, the model parameters must be chosen such that the following inequality is satisfied:

$$c^*(1, t^*) > c_D^*(1, t^*). \quad (2.6.7)$$

To summarise, the results presented in this chapter may be used to answer commonly asked questions as follows:

- How much solute has been metabolised after a certain amount of time?
 - Use (2.6.3), (2.6.4) or (2.6.5) to approximate $M^*(T^*)$, then multiply by Adc_0 .
- How long does it take for the cell surface solute concentration to reach a desired amount?
 - Use (2.4.10), (2.4.14), (2.5.11) or (2.5.15) to approximate $c^*(1, t^*)$, solve (2.6.6) for t^* , then multiply by d^2/D .
- How can the experiment be configured to ensure that the cell surface solute concentration remains above a desired amount for a certain length of time?
 - Use (2.4.10), (2.4.14), (2.5.11) or (2.5.15) to approximate $c^*(1, t^*)$ and ensure that (2.6.7) is satisfied by adjusting the values of α , β and/or μ accordingly.

The simple relationships derived in this section may readily be used to guide the design of experiments by providing researchers with information on how to tailor experimentally controlled parameters, such as initial solute concentration and fluid depth, in order to achieve a certain cell culture environment. For example, understanding the rate of depletion of the solute could aid in the selection of the initial solute concentration or help to determine the optimal time points at which to replenish the solute, if this were necessary. This information would be invaluable in streamlining the set-up of experiments in terms of both time and use of resources.

Chapter 3

Modelling fluid flow and solute transport in a dynamic *in vitro* cell culture system

Whilst static cell culture methods remain an important tool for *in vitro* experimentation, the inclusion of fluid flow is essential for accurately representing the *in vivo* environment. As described in Chapter 1, a wide variety of bioreactor systems have been developed that incorporate fluid flow with the aim of providing cells with more physiologically relevant culture conditions. However, the addition of fluid flow invites new challenges, particularly in relation to shear stress levels and solute transport limitations. In their native environment, cells that are exposed to fluid flow will be subject to some level of shear stress, i.e. the tangential force imposed on the cells by the flow of the fluid. This is often essential for regulating key cellular functions, but if artificially high levels of shear stress are generated in *in vitro* devices, this can be damaging to the cells. Also vital for maintaining a healthy cell culture is an adequate supply of oxygen (O_2) and nutrients, as well as the presence of realistic concentration gradients. Thus, in order to control the *in vitro* environment such that cells are cultured under the most appropriate conditions, it is imperative to gain an understanding of the fluid dynamics and solute transport within flow-based cell culture systems. Mathematical models can be useful for characterising quantities of interest that are often difficult to obtain experimentally, and can provide insight into how the device should be configured in order to obtain the desired cell culture environment.

This chapter begins with a brief summary of a selection of studies available in the literature that use mathematics to describe the conditions within various *in vitro* cell culture systems. A description of the mathematical equations that are required to characterise the fluid flow and solute transport within a flow-based device is then provided. These equations are used to develop a computational model of the environment within a commercially available bioreactor system, and the results of the model are presented for a range of input parameter values. Finally, simple relationships are derived to predict solute concentrations prior to experimentation, with the aim of allowing researchers with a limited knowledge of mathematics to use the results of the computational model to set up their experiments in an optimal manner.

3.1 Existing models from the literature

There are an increasingly large number of mathematical and computational models available in the literature that describe different cell culture techniques and the environment to which cells are exposed within *in vitro* systems. Many reviews can be found detailing models that have been developed for a wide range of applications, including characterising cell growth in monolayer and 3D formations [54], modelling cell seeded scaffolds under static and dynamic conditions [30], describing the cell culture environment within microfluidic devices [29], and using modelling techniques to aid in toxicity testing [55]. Of particular relevance to the work in the remainder of this thesis are models that characterise the fluid flow and solute transport within perfusion bioreactors; here, a few examples are briefly discussed, although it is acknowledged that this does not represent a comprehensive or extensive selection of models of this type.

One of the greatest advantages of mathematical modelling is that it can aid in the design of experimental set-up. In order to provide a strategy for determining an optimal cell culture environment, Shipley et al. [56] developed a mathematical model of fluid flow and O_2 transport in a hollow fibre bioreactor. Valid for all O_2 concentrations, a numerical model of O_2 uptake by the cells provides graphical results that can be interpreted in order to select the geometrical features and operating conditions of the bioreactor that allow the required O_2 levels to be maintained. In the special case when O_2 concentrations are high, an analytical approach yields equations that offer a greater insight into the relationships between O_2 concentration and bioreactor set-up. The analytical results were validated against the numerical model with strong agreement within the regions of applicability, and case studies were presented to demonstrate how the results of the mathematical model may be utilised to create an optimal culture environment for cell types with a high or low O_2 requirement.

Mathematical modelling is also useful in predicting quantities that are difficult or even impossible to measure experimentally. Allen et al. [57] developed a mathematical model to describe O_2 transport and uptake in a simple parallel-plate perfusion bioreactor system, designed to enable the formation of steady-state O_2 concentration gradients. The mathematical model was used to predict the formation of such gradients for a range of input flow rates and inlet O_2 concentrations, with analytical and numerical techniques being employed to describe O_2 uptake for high and low concentrations, respectively. The model predictions were found to be in good agreement with experimental measurements of outlet O_2 levels.

A further benefit of mathematical models is their ability to provide insight into the transport of multiple solutes over an extended time period, as illustrated by Hsu et al. [58]. Here, a mathematical model was developed to simulate a three day experiment in a cylindrical perfusion-based cell culture chamber that was designed to provide control over shear stress levels and improve solute transfer to the cells. The model was used to investigate the effects of cell surface O_2 concentrations and shear stress levels on the production of albumin and ammonia, and the consumption of glucose and glutamine. Experimental measurements of albumin concentration

were found to be in good agreement with model predictions.

In addition to predicting concentration gradients, mathematical models can be used for the optimisation of bioreactor geometry prior to experimentation. Vozzi et al. [59] designed a gradient-generating microfluidic bioreactor system for the purpose of toxicity testing. The system consists of two inlets followed by a serpentine-shaped circuit of microchannels that facilitate fluid mixing, with the channels converging to connect the flow circuit to the cell culture chamber. Prior to fabrication of the device, a computational model was developed to optimise the geometry of the flow circuit such that smooth concentration gradients would be established in the cell culture chamber. The model was then used to estimate these gradients for various diffusion coefficients and a fixed input flow rate. Using a different coloured dye in each inlet, experiments were performed to visualise the generation of a concentration gradient in the cell culture chamber, the results of which correlated well with model predictions.

Mathematical modelling can also be used to design a novel bioreactor device, as demonstrated by Mazzei et al. [60]. With the aim of producing a generic perfusion system that can be used with existing cell culture protocols, the modular chamber featuring an inlet and an outlet has dimensions based on the size of a standard microwell. Prior to fabrication of the device, a mathematical model was developed to study the fluid dynamics and O_2 transport within the chamber, for various chamber heights. Upon analysing the cell surface O_2 concentrations and shear stress levels, an optimal chamber height was chosen as the best compromise between lowering shear stress-induced damage to the cells and ensuring a sufficient supply of O_2 . A prototype was then manufactured to test the performance of the system, and it was found that a build-up of air bubbles caused turbulent flow within the chamber, leading to unpredictable levels of shear stress. To eliminate these issues, the bioreactor was redesigned with a sloping roof and larger outlet to facilitate the removal of bubbles. The mathematical model was then used to calculate the O_2 concentrations, shear stress levels and flow speeds at the cell surface for various input flow rates. The bioreactor developed here (the MCmB) is an early prototype version of the commercially available Kirkstall cell culture systems.

With the aim of investigating the relationships between bioreactor geometry, O_2 delivery to the cells and flow-induced shear stress, Mattei et al. [61] developed mathematical models of fluid flow and O_2 transport within three devices. As well as the MCmB, two simple parallelepiped channels of different heights were considered, with the height of the channel varied over an order of magnitude to compare the environment within microfluidic and millifluidic cell culture systems. A cell-seeded hydrogel was included at the base of each device, the size of which was based on calculations to determine the minimum volume and density of a physiologically relevant 3D cell structure. The mathematical models were solved computationally to evaluate the flow profiles and O_2 concentrations within each of the bioreactors in order to assess if it is possible to achieve a balance between suitable shear stress and sufficient O_2 supply so that cell viability can be maintained.

Most relevant to this study, Pedersen et al. [62] also developed mathematical models of fluid flow and solute transport within three perfusion bioreactor systems: an internally developed device consisting of a cell culture compartment housed between two fluid channels, and the commercially available RealBio and QV900 devices. Model predictions of O_2 concentrations and shear stress levels at the cells, as well as the time taken for the distribution of a test solute to reach steady-state, were used to determine which bioreactor was most suitable for the culture of cell-seeded alginate beads. After further investigations to test a range of input flow rates and inlet O_2 concentrations, the QV900 was identified as the most successful system.

Even from this small selection of studies from the literature, it is evident that a diverse array of perfusion bioreactors exist for use across a wide range of applications. A common approach is for mathematics to be employed alongside experimentation, where models are often developed under a limited set of input parameters that describe an individual study. Whilst there is no doubt that this can provide invaluable information for optimising or predicting the specific situation at hand, there is typically little scope for generalisation of the model results. An alternative approach, and one that may prove useful to a wider audience, is to develop a mathematical model under a more comprehensive set of conditions; if multiple parameter combinations are tested, patterns and trends should emerge to provide a general overview of the behaviour of the device. This could promote a more widespread utilisation of the mathematical model, since the results could be interpreted and adapted to suit a range of experimental set-ups. It is important to remember that the goal of this type of modelling is ultimately to aid experimental researchers who likely have limited expertise in the field of mathematics. Thus, the accessibility of the models must be considered, and where possible, simple equations should be provided that allow experimentalists to make use of the results without requiring an in-depth understanding of the complicated underlying mathematics.

3.2 Modelling fluid flow and solute transport in an arbitrary bioreactor device

In this chapter, mathematical models are developed to characterise the environment within a specific bioreactor device for a variety of input parameters. However, in theory, the governing equations used to describe the fluid dynamics and solute transport should be applicable in any flow-based cell culture system; these equations are presented here.

3.2.1 Fluid dynamics

In vitro cell culture is typically performed using a culture medium consisting of multiple components, such as nutrients or growth factors, which may vary depending on the desired experimental conditions. In the literature, it is widely assumed that this medium has properties consistent

with water, i.e. it is considered to be an incompressible Newtonian fluid with constant density and viscosity [29]. Under this assumption, the flow velocity and pressure within a bioreactor device can be described via the continuity equation and Navier-Stokes equations, namely

$$\nabla \cdot \mathbf{u} = 0, \quad (3.2.1)$$

$$\rho \frac{\partial \mathbf{u}}{\partial t} + \rho (\mathbf{u} \cdot \nabla) \mathbf{u} = -\nabla p + \mu \nabla^2 \mathbf{u}, \quad (3.2.2)$$

where \mathbf{u} (m s^{-1}) is the velocity field, ρ (kg m^{-3}) is the fluid density, p (Pa) is the pressure and μ (Pa s) is the dynamic viscosity.

3.2.2 Solute transport

As well as the fluid dynamics, it is also of interest to characterise the transport of solutes that are present in the culture medium. Solutes can be naturally occurring within the fluid, or manually added to fulfil the purpose of the experiment; examples of commonly considered solutes include O_2 , vital for maintaining healthy cells, or drugs such as paracetamol (APAP), widely used for *in vitro* toxicity studies. Applicable to solutes present in culture medium, a common approach in the literature is to adopt the dilute assumption, where it is assumed that if a fluid contains multiple solutes, their concentrations are sufficiently low such that the presence of one solute does not affect the transport of another [29]. Under this assumption, solute transport in a flow-based bioreactor system can be described by both convection and diffusion via

$$\frac{\partial c_j}{\partial t} + (\mathbf{u} \cdot \nabla) c_j = D_j \nabla^2 c_j, \quad (3.2.3)$$

where c_j (mol m^{-3}) is the concentration of solute j and D_j ($\text{m}^2 \text{s}^{-1}$) is the isotropic diffusion coefficient associated with solute j . Note that (3.2.3) assumes no interaction between the solute and other components of the culture medium (e.g. proteins), but if necessary, D_j may be adjusted to account for this process [63].

3.2.3 Interaction between the solute and the cells

Depending on the specific bioreactor design, cells may be cultured in various configurations, such as in a monolayer or within 3D cellular structures. In either case, the cells will occupy some volume within the bioreactor device, and where transport through the cell region is important, this volume may be modelled as a separate domain. Fluid flow within the cell region, either in the interstitium between cells in a monolayer, or through the pores of a 3D cellular structure, can be characterised using Darcy's law. This equation states that fluid flow through a porous region is driven by differences in pressure, and is related to the permeability of the region and the viscosity of the fluid. However, since the cell region is typically much wider than it is tall, the pressure gradient in the vertical direction is negligible and so the presence of fluid flow in

this domain is commonly neglected. In this case, transport of the solute and the interaction between the solute and the cells within a 3D cell region may be described via the following reaction-diffusion equation:

$$\frac{\partial c_j}{\partial t} = D_j^{cell} \nabla^2 c_j - R_j^{3D}, \quad (3.2.4)$$

where D_j^{cell} ($\text{m}^2 \text{s}^{-1}$) is the isotropic diffusion coefficient associated with solute j within the cell region, and R_j^{3D} ($\text{mol m}^{-3} \text{s}^{-1}$) describes the bulk reaction between solute j and the cells. Note that (3.2.4) assumes that the diffusion coefficient is constant throughout the cell region, but more generally, D_j^{cell} may be replaced by a diffusivity tensor to account for any heterogeneity.

In certain cases, it is unnecessary to consider the cell region as a separate domain; for example, when transport within the region is not considered important (an appropriate assumption if the height of the cell region is negligible in comparison to its width, as is common in many cell culture applications) or when the reaction of interest occurs only at the surface of the region, the volume of this domain can reasonably be neglected. Instead, the interaction between the solute and the cells may be represented by a flux boundary condition of the following form:

$$\mathbf{n} \cdot (-D_j \nabla c_j + \mathbf{u} c_j) = R_j^{2D}, \quad (3.2.5)$$

where \mathbf{n} is an outward facing normal and R_j^{2D} ($\text{mol m}^{-2} \text{s}^{-1}$), describing the surface reaction between solute j and the cells, can be obtained by adjusting the components of the bulk reaction term, R_j^{3D} , to account for the reduction from a 3D cell region to a boundary. It should be noted that both (3.2.4) and (3.2.5) do not account for cell proliferation, but these equations may be amended to incorporate this process if it is considered to be of importance [30].

3.2.4 Solving the model

The governing equations for fluid flow and solute transport, coupled with appropriate initial and boundary conditions, can be solved using a wide range of mathematical techniques. It may be possible to take an analytical approach in cases where the bioreactor design is relatively simple; however, since many flow-based cell culture systems have complex geometries, it is often necessary to proceed numerically. Whilst programming platforms may be used to implement a variety of numerical methods, there are many commercially available software packages that provide a user-friendly interface for solving systems of differential equations.

The mathematical models developed in this chapter are solved using the finite element method, implemented via COMSOL Multiphysics[®]. This method is a popular choice for solving problems where the computational domain is complicated, and involves discretising the original domain into smaller parts called elements. The original equations, typically partial differential equations, are approximated on each element by either algebraic equations or ordinary differential equations for steady-state or time-dependent problems, respectively. The simple equations

from each element are then assembled into a system of equations that can readily be solved to provide an approximate solution to the original, more complicated, problem. For further details on the mathematics behind this method, the reader is referred to [64].

COMSOL Multiphysics® [65] offers a straightforward workflow for setting up and solving sophisticated models using the finite element method. Once the geometry has been created or imported, the governing equations and initial and boundary conditions can be applied using the built-in physics-based modules or by manually defining mathematical expressions using the equations-based interface. Then, the computational domain is discretised by generating an automated or customised mesh to provide the elements on which the model equations will be solved. Based on the model set-up, the software provides optimised solver settings as a default, but these can be manually adjusted to suit the requirements of the user. The various settings used to set-up and solve the models developed in this chapter will be discussed in a later section.

3.3 Modelling fluid flow and solute transport in the Kirkstall QV900

In this section, the equations detailed in §3.2 are applied to describe the fluid flow and solute transport within the QV900 cell culture system, shown in Fig. 3.3.1. This commercially available device is part of the Quasi Vivo® family of bioreactors developed by Kirkstall Ltd. (York, UK) and is designed to provide cells with a physiologically relevant culture environment. Six self-contained culture chambers reside within each QV900 tray, whose standard footprint allows for easy integration with existing experimental techniques and equipment. Using flexible tubing, the chambers may be connected together in various configurations, offering the option to run experiments in series, enabling co-culture of different cell types, or in parallel, which makes it possible to produce multiple replicates simultaneously within one experiment. At the



Figure 3.3.1: The Kirkstall QV900 cell culture system [1].

base of each chamber, cells can be cultured in a 2D array on a cover slip, or alternatively 3D structures of cells can be incorporated directly within this system. The modular design of the QV900 makes this a versatile device where the user can easily adjust the set-up to generate tailored conditions that satisfy the requirements of a wide range of experiments. Thus, in order to demonstrate the full potential of this system, it is essential to gain an understanding of the cell culture environment under different configurations; here, models are developed to describe the fluid flow and solute transport within both single and connected chambers.

3.3.1 Single chamber models

By consulting the technical drawings of the QV900 system (supplied by Kirkstall Ltd.), a computational representation of a single chamber was created in COMSOL Multiphysics[®] 5.3. For the purpose of solving the models developed in this section, only the areas in which fluid can flow are of interest and so a few simplifications were made in order to avoid generating an unnecessarily complicated geometry. In reality, each chamber is comprised of a well covered by a lid, but rather than including each of these as separate components, the computational geometry simply represents the internal volume enclosed by the well and the lid. Additionally, the chamber is not perfectly cylindrical, with the diameter marginally decreasing with decreasing height, but this was assumed to be negligible and the diameter of the chamber is taken to be constant. Furthermore, the cultured cells are supported by several pillars located at the base of

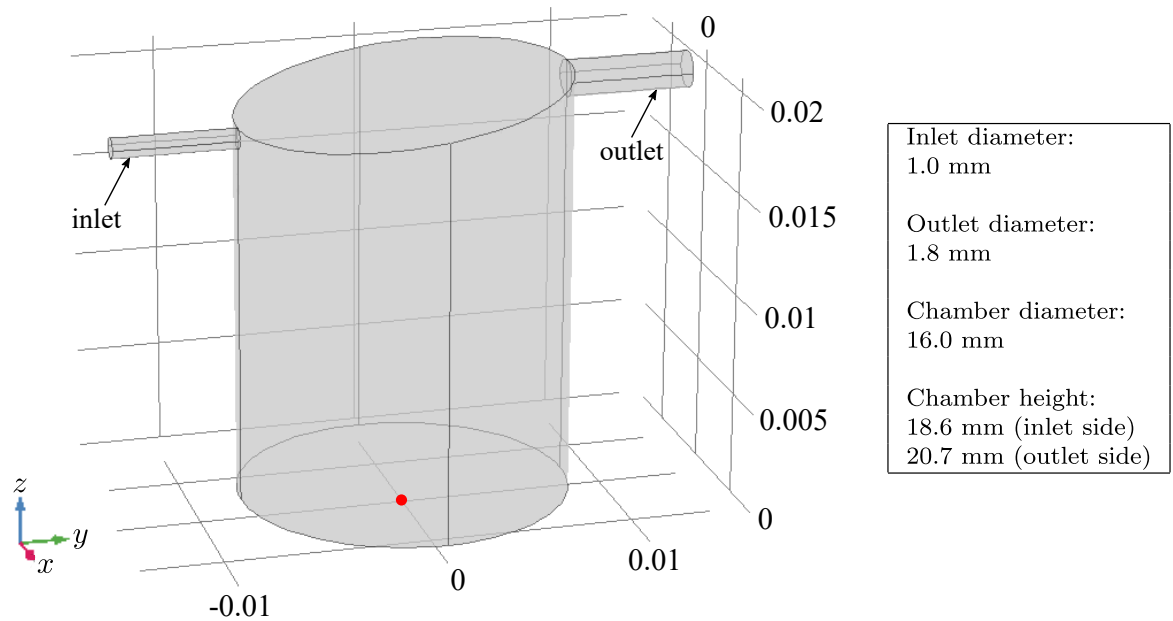


Figure 3.3.2: Idealised 3D representation of a single QV900 chamber generated in COMSOL Multiphysics[®] 5.3, showing the orientation of the x -, y - and z - axes with the origin located at the centre of the base of the chamber (indicated by the red dot). Note that length scales on the axes are in metres.

the chamber which are not included in the computational geometry. Assuming that the diameter of the cell region is equal to that of the chamber, and since fluid flow within the cell region is neglected as described in §3.2.3, it was assumed that no flow can occupy the volume beneath the cell region and therefore the height of the pillars is subtracted from the total height of the chamber. It is noted that, as a result of applying these assumptions and excluding the thickness of the solid outer walls of the chamber, the external measurements of the device differ from those of the geometry illustrated in Fig. 3.3.2, whose dimensions relate to the computational domain only.

Since the QV900 chambers are designed to support cells cultured in both 2D and 3D formations, two models are developed to demonstrate different types of interaction between the solute and the cells; the cell region is first represented by a separate domain (Model 1), and then by a flux boundary condition applied at the base of the chamber (Model 2). For both methods of modelling the cell region, the fluid dynamics and solute transport within the main body of the chamber are described using the governing equations detailed in §3.2.1 and §3.2.2.

The fluid dynamics within the chamber are described using the continuity equation and Navier-Stokes equations given by (3.2.1) and (3.2.2), where initially the fluid velocity is equal to zero ($\mathbf{u} = \mathbf{0}$). A steady parabolic velocity profile of the form $u(r) = C(a^2 - r^2)$ is imposed at the inlet, where a is the radius of the inlet and r is the radial distance. The experimentally prescribed flow rate, Q , is used to derive the magnitude, C , of the inlet velocity profile:

$$Q = 2\pi \int_0^a u(r) r dr \implies C = \frac{2Q}{\pi a^4},$$

by performing the integration and rearranging. Zero normal stress ($-p\mathbf{I} + \mu(\nabla\mathbf{u} + (\nabla\mathbf{u})^T)\mathbf{n} = \mathbf{0}$) is prescribed at the outlet, and no slip and no penetration conditions ($\mathbf{u} = \mathbf{0}$) are applied on the chamber walls, meaning that the flow velocity on the walls of the chamber is equal to zero and the fluid cannot pass through the chamber walls. When the cell region is modelled as a separate domain where fluid flow is neglected, these conditions also apply to the interface between the cell region and the main body of the chamber.

The transport of solute within the chamber is described using the convection-diffusion equation given by (3.2.3), where initially the solute concentration is equal to zero ($c_j = 0$) in the chamber, and where applicable, the cell region. At the inlet, a constant supply of solute ($c_j = c_j^{\text{in}}$) is provided, and a convective flux ($-\mathbf{n} \cdot D_j \nabla c_j = 0$) is applied at the outlet so that the solute is driven out of the chamber via the fluid flow. Finally, a zero flux condition ($\mathbf{n} \cdot (-D_j \nabla c_j + \mathbf{u}c_j) = 0$) is imposed on the walls of the chamber which are assumed to be impermeable.

The interaction between the solute and the cells is described differently depending on whether the cell region is represented by a separate domain or by a flux boundary condition. As well as demonstrating two methods for modelling the cell region, the reaction terms, R_j^{3D} and R_j^{2D} , in the governing equations from §3.2.3, are replaced by two common reaction mechanisms in order

to showcase how the models may be used to characterise different types of interaction between the solute and the cells.

When the cell region is represented by a separate domain within which solute transport is important, continuity of concentration is assumed at the interface between the cell region and the main body of the chamber. The transport of solute within the cell region is described using a reaction-diffusion equation of the form of (3.2.4), where the reaction term is replaced by nonlinear saturable binding kinetics. This reaction mechanism is commonly used to characterise the effect of drugs whose mode of action is governed by ligand-receptor interactions, and the following equations enable tracking of the concentration of free and bound drug within the cell region:

$$\frac{\partial c_j}{\partial t} = D_j^{cell} \nabla^2 c_j - k_j^f c_j (B_j - b_j) + k_j^r b_j, \quad (3.3.1)$$

$$\frac{\partial b_j}{\partial t} = k_j^f c_j (B_j - b_j) - k_j^r b_j, \quad (3.3.2)$$

where c_j and b_j (mol m^{-3}) are the concentrations of free and bound drug, respectively, B_j (mol m^{-3}) is the local density of binding sites, and k_j^f ($\text{mol}^{-1} \text{m}^3 \text{s}^{-1}$) and k_j^r (s^{-1}) are the forward and reverse reaction rates, respectively.

When the cell region is represented by a flux boundary condition applied at the base of the chamber, the interaction between the solute and the cells is described by (3.2.5), where the reaction term is replaced by Michaelis-Menten (M-M) kinetics:

$$\mathbf{n} \cdot (-D_j \nabla c_j + \mathbf{u} c_j) = \sum_{i=1}^m \frac{V_j^i c_j}{K_j^i + c_j}, \quad (3.3.3)$$

where m is the number of metabolic pathways involved in the reaction, K_j^i (mol m^{-3}) is the M-M constant for solute j and pathway i , and V_j^i ($\text{mol m}^{-2} \text{s}^{-1}$) is the maximum reaction rate for solute j and pathway i . Recall from Chapter 2 that M-M kinetics are commonly used to characterise the metabolism of O_2 (via one metabolic pathway) or drugs such as APAP (via three metabolic pathways).

For clarity, the governing equations, boundary conditions and initial conditions are summarised for each single chamber model on pages 71 and 72 alongside a schematic drawing of each computational geometry, where the cell region is represented by a separate domain (Fig. 3.3.4) and by a flux boundary condition (Fig. 3.3.5).

3.3.2 Connected chamber model

As well as characterising the cell culture environment in a single QV900 chamber, it is also important to describe the fluid flow and solute transport in connected chambers (Model 3), and in particular, to investigate the effect of metabolism on the solute concentration profiles observed

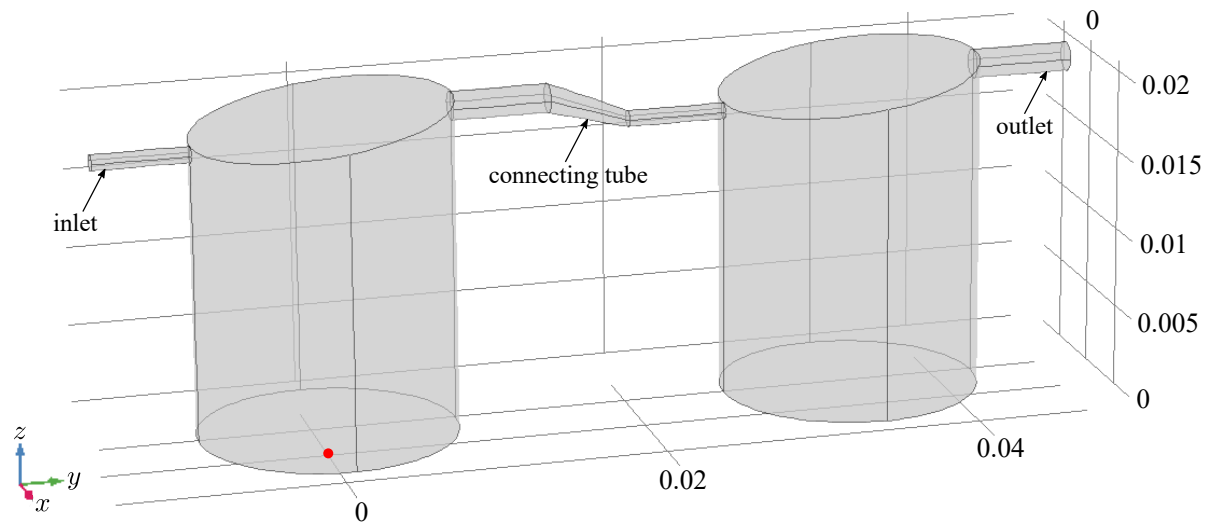


Figure 3.3.3: Idealised 3D representation of two connected QV900 chambers generated in COMSOL Multiphysics[®] 5.3, showing the orientation of the x -, y - and z - axes with the origin located at the centre of the base of the first chamber (indicated by the red dot). Note that length scales on the axes are in metres.

in downstream chambers. To create a computational representation of six chambers connected in series, the existing geometry for a single chamber was duplicated and simple tubes were generated to connect the chambers together; as an example, the computational domain for two connected chambers is provided in Fig. 3.3.3.

As in §3.3.1, the computational domain represents a simplified version of the true QV900 device. In reality, a QV900 tray consists of two rows of three chambers that can be connected together using flexible tubing (see Fig. 3.3.1). The complex arrangement of the connecting tubes is difficult to replicate computationally and may vary from user to user, so for simplicity, the chambers are instead arranged side by side and connected by a short straight tube of decreasing diameter. The length of the connecting tube was chosen to equal the distance between two chambers on the QV900 tray (obtained from the technical drawings) but it is noted that, in practice, the flexible tubing is longer than this and its length may differ between chambers depending on the chosen order of connection. Furthermore, in the computational domain, it is necessary for the connecting tube to vary in diameter since the diameter of the chamber outlet is larger than that of the inlet. In reality, the connecting tube has a constant diameter since, with the inclusion of the solid outer walls of the chamber, the outer diameters of the inlet and the outlet are equal. Due to the various elements of choice regarding the geometry of the connecting tube, a sensitivity study was conducted to ensure that the tube length and diameter would not significantly impact the results; simulations were performed using connecting tubes with constant and varying diameter of length 5 mm and 100 mm, and it was verified that altering these features had a negligible effect on the quantities of interest.

To develop a model of fluid flow and solute transport in six connected chambers, the same governing equations, boundary conditions and initial conditions as described in §3.3.1 are applied to the connected chamber geometry. It is noted that, here, the inlet refers only to the inlet of the first chamber and the outlet to that of the last chamber, and continuity of flux and concentration is assumed at the interfaces between each chamber and the connecting tubes. In connected chambers, it is of interest to monitor the depletion of the solute as the number of chambers in the series increases, so here, the interaction between the solute and the cells is described by M-M kinetics and the cell region in each chamber is represented by a flux boundary condition. Using two chambers as an illustrative example, the governing equations, boundary conditions and initial conditions as applied to chambers connected in series are summarised on page 73, alongside a schematic drawing of the computational geometry for two connected chambers (Fig. 3.3.6).

3.3.3 Numerical implementation

The fluid flow and solute transport parameters used for each model are provided in Table 3.1. Simulations were performed over a range of input flow rates in order to gain an understanding of the cell culture environment under various conditions, and for each model, representative parameter values were chosen for appropriate solutes and cell types to illustrate the effects of the different reaction mechanisms.

Although the fluid density and viscosity may vary depending on the composition of the culture medium, here it is assumed that the fluid is water and the values of ρ and μ have been chosen accordingly. Recall that in Model 1, the diffusion coefficient within the cell region is not necessarily the same as the diffusion coefficient in the main body of the chamber, but here, for simplicity, it is assumed that the rates of diffusion in these domains are equal (i.e. $D_j^{cell} = D_j$). Model 1 was used to describe the action of sirolimus on smooth muscle cells, an immunosuppressant commonly used to coat arterial stents, whilst Model 2 was used to describe the metabolism of both APAP and O_2 . APAP is the most commonly used solute for liver toxicity studies, and the parameter values relating to this solute were acquired from an *in vivo* study carried out in humans. Since an adequate supply of O_2 is vital for the majority of cell cultures, metabolism of this solute was described for four different cell types commonly used in *in vitro* studies: rat cardiomyocytes, human cardiomyocytes, rat hepatocytes and HepG2 cells. Model 3 was used to describe the metabolism of O_2 by rat cardiomyocytes only. Note that to obtain the maximum metabolic rates in appropriate units, it was necessary to adjust the values from the literature by multiplying the O_2 parameters by the cell density, d , and dividing the APAP parameters by the cell area, A .

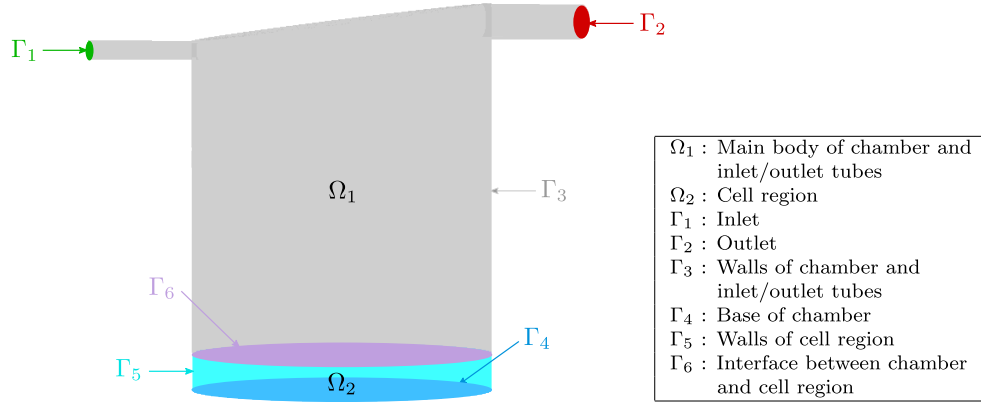
Model 1: Single chamber with cell region represented by a separate domain

Figure 3.3.4: Schematic drawing of the computational geometry for a single QV900 chamber where the cell region is represented by a separate domain (not to scale). Here, Ω and Γ are used to label domains and boundaries, respectively.

$$\nabla \cdot \mathbf{u} = 0 \text{ in } \Omega_1,$$

$$\rho \frac{\partial \mathbf{u}}{\partial t} + \rho (\mathbf{u} \cdot \nabla) \mathbf{u} = -\nabla p + \mu \nabla^2 \mathbf{u} \text{ in } \Omega_1,$$

$$\frac{\partial c_j}{\partial t} + (\mathbf{u} \cdot \nabla) c_j = D_j \nabla^2 c_j \text{ in } \Omega_1,$$

$$\frac{\partial c_j}{\partial t} = D_j^{cell} \nabla^2 c_j - k_j^f c_j (B_j - b_j) + k_j^r b_j \text{ in } \Omega_2,$$

$$\frac{\partial b_j}{\partial t} = k_j^f c_j (B_j - b_j) - k_j^r b_j, \text{ in } \Omega_2,$$

with the following boundary conditions

$$u(r) = \frac{2Q}{\pi a^2} \left(1 - \frac{r^2}{a^2} \right) \text{ on } \Gamma_1,$$

$$-p\mathbf{I} + \mu(\nabla \mathbf{u} + (\nabla \mathbf{u})^T) \mathbf{n} = \mathbf{0} \text{ on } \Gamma_2,$$

$$\mathbf{u} = \mathbf{0} \text{ on } \Gamma_3, \Gamma_6,$$

$$c_j = c_j^{in} \text{ on } \Gamma_1,$$

$$-\mathbf{n} \cdot D_j \nabla c_j = 0 \text{ on } \Gamma_2, \Gamma_4, \Gamma_5,$$

$$\mathbf{n} \cdot (-D_j \nabla c_j + \mathbf{u} c_j) = 0 \text{ on } \Gamma_3,$$

and initial conditions

$$\mathbf{u} = \mathbf{0} \text{ in } \Omega_1 \text{ at } t = 0,$$

$$c_j = 0 \text{ in } \Omega_1, \Omega_2 \text{ at } t = 0.$$

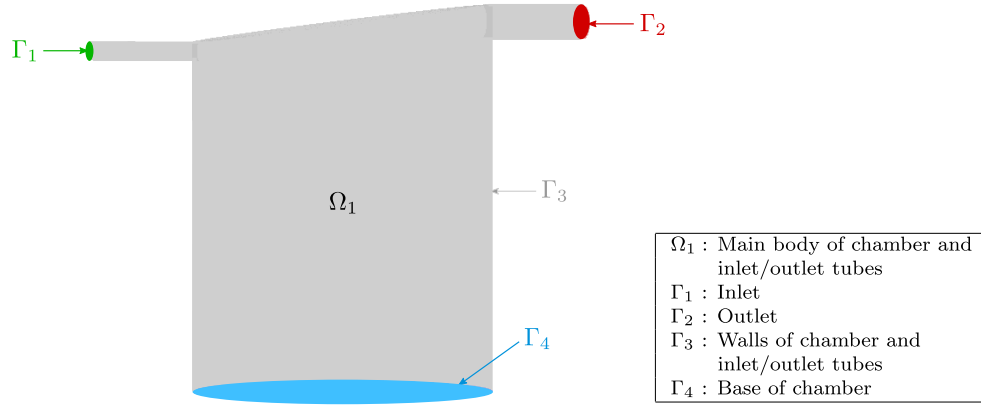
Model 2: Single chamber with cell region represented by a flux boundary condition

Figure 3.3.5: Schematic drawing of the computational geometry for a single QV900 chamber where the cell region is represented by a flux boundary condition. Here, Ω and Γ are used to label domains and boundaries, respectively.

$$\nabla \cdot \mathbf{u} = 0 \text{ in } \Omega_1,$$

$$\rho \frac{\partial \mathbf{u}}{\partial t} + \rho (\mathbf{u} \cdot \nabla) \mathbf{u} = -\nabla p + \mu \nabla^2 \mathbf{u} \text{ in } \Omega_1,$$

$$\frac{\partial c_j}{\partial t} + (\mathbf{u} \cdot \nabla) c_j = D_j \nabla^2 c_j \text{ in } \Omega_1,$$

with the following boundary conditions

$$u(r) = \frac{2Q}{\pi a^2} \left(1 - \frac{r^2}{a^2} \right) \text{ on } \Gamma_1,$$

$$-p\mathbf{I} + \mu(\nabla \mathbf{u} + (\nabla \mathbf{u})^T)\mathbf{n} = \mathbf{0} \text{ on } \Gamma_2,$$

$$\mathbf{u} = \mathbf{0} \text{ on } \Gamma_3, \Gamma_4,$$

$$c_j = c_j^{in} \text{ on } \Gamma_1,$$

$$-\mathbf{n} \cdot D_j \nabla c_j = 0 \text{ on } \Gamma_2,$$

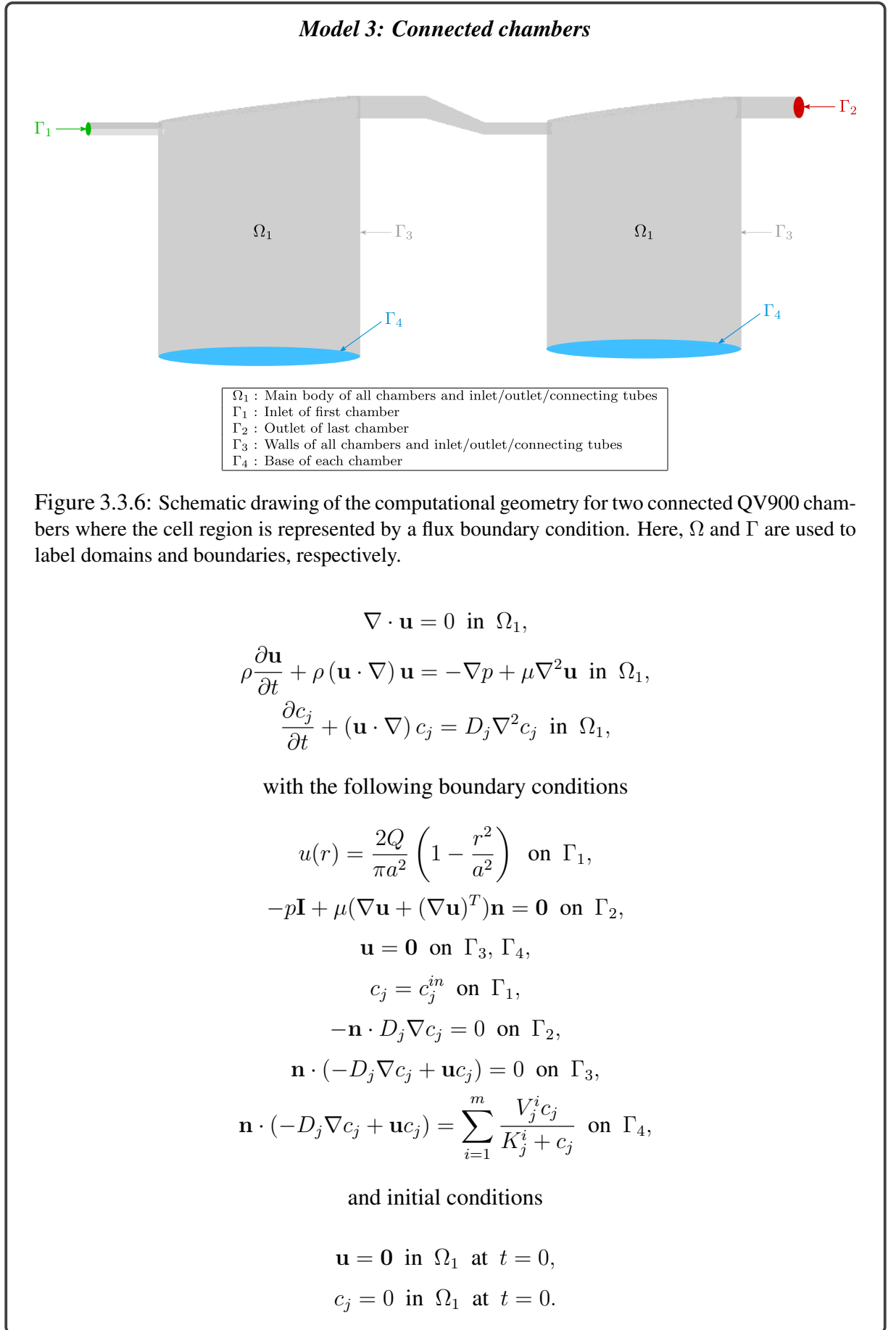
$$\mathbf{n} \cdot (-D_j \nabla c_j + \mathbf{u} c_j) = 0 \text{ on } \Gamma_3,$$

$$\mathbf{n} \cdot (-D_j \nabla c_j + \mathbf{u} c_j) = \sum_{i=1}^m \frac{V_j^i c_j}{K_j^i + c_j} \text{ on } \Gamma_4,$$

and initial conditions

$$\mathbf{u} = \mathbf{0} \text{ in } \Omega_1 \text{ at } t = 0,$$

$$c_j = 0 \text{ in } \Omega_1 \text{ at } t = 0.$$



<i>All models</i>			
<i>Parameter</i>	<i>Description</i>	<i>Value</i>	<i>Ref.</i>
ρ	Density of fluid	$9.94 \times 10^2 \text{ kg m}^{-3}$	[66]
μ	Dynamic viscosity of fluid	$6.89 \times 10^{-4} \text{ Pa s}$	[66]
N	Total number of cells	1.00×10^5	*
A	Area covered by the cells	$2.01 \times 10^{-4} \text{ m}^2$	†

<i>Model 1 (solute = sirolimus, cell type = smooth muscle cells)</i>			
<i>Parameter</i>	<i>Description</i>	<i>Value</i>	<i>Ref.</i>
V_{cell}	Volume of a smooth muscle cell	$1.50 \times 10^{-14} \text{ m}^3$	[67]
h	Height of cell region	$7.46 \times 10^{-6} \text{ m}$	‡
D_S	Diffusion coefficient for sirolimus	$2.50 \times 10^{-10} \text{ m}^2 \text{ s}^{-1}$	[68]
c_S^{in}	Inlet concentration for sirolimus	$5.00 \times 10^{-3} \text{ mol m}^{-3}$	**
k_S^f	Forward reaction rate	$2.00 \text{ mol}^{-1} \text{ m}^3 \text{ s}^{-1}$	[68]
k_S^r	Reverse reaction rate	$5.20 \times 10^{-3} \text{ s}^{-1}$	[68]
B_S	Density of binding sites	$3.63 \times 10^{-1} \text{ mol m}^{-3}$	[68]

<i>Model 2 (solute = paracetamol, cell type = human liver cells)</i>			
<i>Parameter</i>	<i>Description</i>	<i>Value</i>	<i>Ref.</i>
D_{APAP}	Diffusion coefficient for APAP	$6.00 \times 10^{-10} \text{ m}^2 \text{ s}^{-1}$	[69]
c_{APAP}^{in}	Inlet concentration for APAP	0.40 mol m^{-3}	[49]
K_{APAP}^1	Michaelis-Menten constant for pathway 1	6.89 mol m^{-3}	[49]
K_{APAP}^2	Michaelis-Menten constant for pathway 2	$9.70 \times 10^{-2} \text{ mol m}^{-3}$	[49]
K_{APAP}^3	Michaelis-Menten constant for pathway 3	$3.03 \times 10^{-1} \text{ mol m}^{-3}$	[49]
V_{APAP}^1	Maximum metabolic rate for pathway 1	$8.86 \times 10^{-2} \text{ mol m}^{-2} \text{ s}^{-1}$	[49]
V_{APAP}^2	Maximum metabolic rate for pathway 2	$1.02 \times 10^{-3} \text{ mol m}^{-2} \text{ s}^{-1}$	[49]
V_{APAP}^3	Maximum metabolic rate for pathway 3	$3.41 \times 10^{-4} \text{ mol m}^{-2} \text{ s}^{-1}$	[49]

<i>Model 2 and Model 3 (solute = oxygen, cell type = various)</i>			
<i>Parameter</i>	<i>Description</i>	<i>Value</i>	<i>Ref.</i>
d	Cell density	$4.97 \times 10^8 \text{ m}^{-2}$	††
D_{O_2}	Diffusion coefficient for O_2	$3.00 \times 10^{-9} \text{ m}^2 \text{ s}^{-1}$	[60]
$c_{O_2}^{in}$	Inlet concentration for O_2	0.21 mol m^{-3}	[60]
K_{O_2}	Michaelis-Menten constant	$6.60 \times 10^{-4} \text{ mol m}^{-3}$	[60]
V_{O_2}	Maximum metabolic rate for human cardiomyocytes	$9.81 \times 10^{-8} \text{ mol m}^{-2} \text{ s}^{-1}$	[70]
	Maximum metabolic rate for rat cardiomyocytes	$4.01 \times 10^{-8} \text{ mol m}^{-2} \text{ s}^{-1}$	[70]
	Maximum metabolic rate for rat hepatocytes	$2.39 \times 10^{-8} \text{ mol m}^{-2} \text{ s}^{-1}$	[71]
	Maximum metabolic rate for HepG2 cells	$1.17 \times 10^{-8} \text{ mol m}^{-2} \text{ s}^{-1}$	[71]

Table 3.1: Parameter values. *Representative cell number chosen following discussions with experimental researchers. †Area covered by the cells calculated by assuming the cells occupy the entire base of the chamber. ‡Height of cell region calculated by multiplying the total number of cells by the volume of a smooth muscle cell, then dividing by the area covered by the cells ($h = NV_{cell}/A$). **Nominal value chosen for inlet sirolimus concentration. ††Cell density calculated by dividing the total number of cells by the area covered by the cells ($d = N/A$).

After inputting the parameter values, the governing equations, boundary conditions and initial conditions for fluid flow and solute transport were applied using the COMSOL built-in ‘Laminar Flow’ and ‘Transport of Diluted Species’ modules, respectively. To ensure that turbulent effects could be neglected, a range of typical Reynolds numbers were calculated via

$$Re = \frac{\rho UL}{\mu},$$

where U (m s^{-1}) and L (m) represent a typical flow speed and length scale, respectively. Taking U as the maximum inlet velocity across a range of input flow rates, and taking L as a range of values from the inlet diameter to the height of the chamber to account for the various length scales in the system, $Re \approx 3 - 600$. Thus, given that the typical Reynolds numbers are relatively low, the assumption of laminar flow was found to be appropriate. Similarly, to anticipate the dependency of the fluid dynamics on the effects of both convection and diffusion, a range of typical Péclet numbers were obtained via

$$Pe = \frac{UL}{D}.$$

Again, considering a range of input flow rates and length scales, this parameter was found to vary from $\mathcal{O}(10^3)$ to $\mathcal{O}(10^5)$. Therefore, since the typical Péclet numbers are large, the solute transport is expected to be convection-dominated.

Following preliminary simulations that indicated symmetric solutions, each geometry was simplified by implementing a symmetry boundary condition on the y, z plane passing through the origin; this approach significantly reduced computation time since it required solving only half of the original problem to obtain the same results. Each simplified geometry was then discretised using the built-in mesh settings available in COMSOL.

To determine the optimal mesh density in terms of computation time and solution accuracy, a sensitivity study was conducted using the connected chamber geometry from Model 3. Simulations were performed with an input flow rate of $Q = 100 \mu\text{l min}^{-1}$ using each of the nine built-in mesh settings, and the quantities of interest were calculated and compared for consecutive meshes. Here, the quantities of interest were identified as the shear stress and O_2 concentration profiles at the cell surface, as well as mass flux, both overall and within each chamber. The solutions were deemed of sufficient accuracy when the difference between the results for consecutive meshes was less than 1%, and of the nine available settings, three were found to be suitable for producing accurate solutions under this metric: ‘Finer’, ‘Extra fine’ and ‘Extremely fine’ (see Table 3.2). Where cell surface shear stress and O_2 concentration profiles are the quantities of most interest, any of these mesh settings are considered acceptable. However, where flux calculations are of importance (as will be demonstrated later in this chapter), the preferred mesh settings are ‘Extra fine’ or ‘Extremely fine’ since the percentage difference is 3 orders of magnitude lower than the difference between ‘Finer’ and ‘Extra fine’.

<i>Mesh setting</i>	<i>Cell surface shear</i>	<i>Cell surface O₂</i>	<i>Flux at inlet</i>
'Finer' to 'Extra fine'	0.11	0.83	0.82
'Extra fine' to 'Extremely fine'	0.30	0.08	7.43×10^{-4}

Table 3.2: Percentage difference in cell surface shear stress, cell surface O₂ concentration and mass flux at the inlet when comparing results between consecutive mesh settings. These results have been provided for chamber 1 as an example, with similar errors calculated for the remaining chambers.

For each model, 'Extremely fine' was chosen as the final mesh setting for discretising the main body of the chamber(s), inlet and outlet tubes, and where applicable in Model 3, the connecting tubes. Recall that the geometry for Model 1 contains an additional domain to represent the cell region, and due to its aspect ratio, it was appropriate to generate an additional swept mesh to discretise this domain. For each model, the final number of mesh elements and the typical time taken to perform a single simulation are listed in Table 3.3.

Each model was solved using the optimised solver settings provided by COMSOL, since the software is designed to automatically select the most robust and least computationally intensive settings as default. For each model, a segregated approach was used to divide the problem into two steps that were solved sequentially: first, the fluid flow equations were solved using the iterative generalised minimal residual method (GMRES) in combination with the algebraic multigrid preconditioner, then the solute transport equations were solved using the iterative GMRES solver.

Whilst each model can be used to produce time-dependent solutions, the results presented in this chapter relate only to steady-state, since many experiments span over the course of several days to allow for the establishment of equilibrium. To obtain an indicative timescale for this, time-dependent simulations were performed using the single chamber geometry from Model 2 with rat cardiomyocytes as an example cell type, for input flow rates of $Q = 100$ and $1000 \mu\text{l min}^{-1}$. Patterns of fluid flow and O₂ distribution as well as the cell surface shear stress and O₂ concentration profiles were compared at different time points, and it was found that for the fluid flow, steady-state was achieved within one minute for both input flow rates, whereas the time taken for the O₂ transport to reach steady-state was more variable, ranging from 5 to 20 hours for the highest and lowest input flow rates. It is stressed that the timescales mentioned here are specific to the input parameters under which these simulations were performed, and that the time taken to achieve equilibrium will vary from model to model.

<i>Model</i>	<i>Number of mesh elements</i>	<i>Typical simulation time</i>
1	2,155,540	21 mins
2	2,152,947	23 mins
3	11,861,343	2 hrs 24 mins

Table 3.3: Number of mesh elements and typical simulation time for each model using a quad core Intel® Core™ i7-6700 CPU @ 3.40GHz.

3.4 Results

In this section, results are shown for various input flow rates from $Q = 100 - 1000 \mu\text{l min}^{-1}$ to represent a range of typical operating speeds offered by commonly used pumps. The fluid flow and solute transport results are discussed in turn, and are displayed on pages 82 to 88, and 89 to 94, respectively. First, the fluid dynamics are characterised by describing the streamlines, flow speeds and cell surface shear stresses in single and connected chambers, and the relationships between input flow rate and cell surface flow speed and shear stress are investigated. Then, the distributions and concentrations of the solutes of interest are described both throughout the chamber and at the cell surface in single and connected chambers, and the relationship between input flow rate and cell surface solute concentration is investigated. To be clear, ‘cell surface’ does not refer to the surface of a single cell; when the cell region is represented by a separate domain, this refers to the surface of the cell region, i.e. Γ_6 in Fig. 3.3.4, and when the cell region is represented by a flux boundary condition, ‘cell surface’ refers to the surface on which this condition is imposed, i.e. the base of the chamber, Γ_4 in Fig. 3.3.5.

3.4.1 Fluid dynamics

Figs. 3.4.1 - 3.4.5 illustrate the flow environment within a single chamber, showing the streamlines, flow speed and cell surface shear stress for each input flow rate. Each streamline represents a typical path that a particle may follow as it travels through the chamber (upper plots). These are coloured by the magnitude of the flow velocity, but since the flow speeds at the inlet and outlet are considerably higher than those observed elsewhere in the chamber, the scale of these plots proves unhelpful for determining how the flow speed varies with chamber depth. To demonstrate this more clearly, the flow speed is also shown on a logarithmic scale (middle plots). The lower plots show the flow-induced shear stress on the cell surface, calculated by multiplying the shear rate by the dynamic viscosity of the fluid, i.e.

$$\tau = \mu \left(\frac{\partial u}{\partial z} + \frac{\partial v}{\partial z} \right).$$

Streamlines

For the lowest input flow rate of $Q = 100 \mu\text{l min}^{-1}$, small recirculation zones can be observed at the periphery of the base of the chamber. Similar streamlines are generated for $Q = 200 \mu\text{l min}^{-1}$, with an additional small recirculation zone appearing just beneath the inlet; referred to as lip vorticity, this flow separation is analogous to solutions of the classical problem of flow over a backward-facing step [72]. This is more prominent for larger input flow rates of $Q = 300 - 500 \mu\text{l min}^{-1}$, where the flow patterns begin to change dramatically. For

$Q = 300 \mu\text{l min}^{-1}$, the streamlines are similar to those for the lowest flow rates, but for $Q = 400 \mu\text{l min}^{-1}$, the recirculation zone below the inlet is larger and another large zone of recirculation zone can be observed near the base of the chamber. Upon increasing to $Q = 500 \mu\text{l min}^{-1}$, it appears that all recirculation zones have merged together to form one large zone of recirculation. For the highest input flow rates of $Q = 600 - 1000 \mu\text{l min}^{-1}$, the flow patterns are more predictable, with one large recirculation zone taking up the majority of the chamber; in particular, the streamlines do not appear to change substantially from $Q = 700 \mu\text{l min}^{-1}$ onwards. For these input flow rates, the emergence of a dividing streamline seems to drive the recirculation of fluid in the main body of the chamber, and the flow patterns are comparable to those generated in the classical lid-driven cavity problem [73].

Flow speed

The pattern of the recirculation zones influences the ‘distribution’ of the flow speed, as illustrated in the logarithmic scale plots. For each input flow rate, the maximum flow speed is located at the inlet, and the flow speeds throughout the remainder of the chamber decrease with increasing chamber depth. Due to the no slip and no penetration conditions imposed on the chamber walls and base, the flow speeds are equal to zero around the periphery of the chamber. As expected, the maximum flow speed increases as input flow rate is increased.

Cell surface shear stress

For each input flow rate, the cell surface shear stress profile is governed by the flow patterns. For the lowest input flow rates of $Q = 100 - 200 \mu\text{l min}^{-1}$, the magnitude of the shear stress across the cell surface increases from all sides of the chamber towards the maximum value located at the centre. For $Q = 300 \mu\text{l min}^{-1}$, where the flow patterns begin to differ considerably, the distribution of shear stress across the cell surface is more complex with the maximum value located near the centre, surrounded by an area of low shear stress, further surrounded by an area of high shear stress. For $Q = 400 \mu\text{l min}^{-1}$, the cell surface shear stress profile resembles those observed for the lowest input flow rates, with the magnitude reaching a maximum value near the centre of the cell surface and decreasing towards the chamber walls. Further increasing the input flow rate does not appear to substantially alter the distribution of shear stress across the cell surface, but the magnitude tends to increase as input flow rate is increased.

Relationship between input flow rate and cell surface flow speed and shear stress

Fig. 3.4.6 shows the nonlinear relationships between input flow rate and the maximum flow speed (upper plot) and shear stress (lower plot) observed at the cell surface. As previously described, due to the application of the no slip and no penetration conditions, the flow speed on the cell surface is necessarily zero. Therefore, the ‘cell surface’ flow speed was calculated just

above the cell surface at a height of $z = h$, the parameter used for the height of the cell region in Model 1. It is clear that, in general, as input flow rate is increased, the maximum flow speed and shear stress at the cell surface also increase, where the rate of increase is higher for higher input flow rates. The exception to this trend is a dip observed at $Q = 300 \mu\text{l min}^{-1}$, the input flow rate where the flow patterns begin to change dramatically. These relationships could prove useful for determining the required input flow rate for experiments in which the desired cell surface flow speed or shear stress is known.

Connected chambers

Finally, Fig. 3.4.7 illustrates the streamlines (upper plots), flow speed (middle plots) and cell surface shear stress (lower plots) in six connected chambers; as an example, these results are shown for $Q = 100 \mu\text{l min}^{-1}$, but similar trends can be observed for the remaining input flow rates. The flow environment does not appear to change substantially from one chamber to the next, so the results from the first chamber are applicable in all downstream chambers. Thus, if the fluid dynamics are the quantity of most interest, it is only necessary to simulate the fluid flow in a single chamber which is less computationally intensive.

3.4.2 Solute transport

First, results are discussed for the case where the interaction between the solute and the cells is described by nonlinear saturable binding kinetics. It is noted that the graphical data obtained from these simulations is omitted as it does not provide additional insight due to the triviality of the results. For each input flow rate between $Q = 100 - 1000 \mu\text{l min}^{-1}$, the distribution of sirolimus is uniform; throughout the chamber, the concentration of free drug is equal to the inlet concentration, i.e. $c_S = 5.00 \times 10^{-3} \text{ mol m}^{-3}$, and the concentration of bound drug takes the value $b_S = 0.24 \text{ mol m}^{-3}$ throughout the cell region. This highlights that, for this type of reaction kinetics, the steady-state solute concentration profile is not dependent on the choice of input flow rate, and therefore this parameter will influence only the fluid dynamics and the time taken for the system to reach equilibrium.

Results corresponding to the cases where the interaction between the solute and the cells is described by M-M kinetics are displayed on pages 89 to 94. It is noted here that the scale on each legend is not consistent across all figures: different scales were used for the purpose of highlighting variations between each set of results that may not be discernable if the plots were displayed on the same scale.

Effect of input flow rate on solute distribution

Figs. 3.4.8 to 3.4.10 show the distribution of APAP throughout a single chamber (left plots) and the cell surface APAP concentration profiles (right plots) for each input flow rate. Note that although these results are specific to APAP, the trends are also applicable to other solutes; since solute transport is dominated by convection, the distribution of solute is largely governed by the fluid dynamics and so similar patterns can be observed for O_2 . For each input flow rate, as the depth of the chamber increases, the solute concentration decreases from the maximum value (equal to the inlet concentration) located at the top of the chamber. For the highest input flow rates of $Q = 700 - 1000 \mu\text{l min}^{-1}$, the distribution of solute throughout the majority of the chamber is practically uniform, with the majority of the chamber exposed to high solute concentrations.

It is perhaps surprising that the solute concentrations are so high for input flow rates of $Q = 700 - 1000 \mu\text{l min}^{-1}$, given the flow patterns illustrated in Figs. 3.4.4 and 3.4.5. It seems that a dividing streamline emerges, separating the fluid travelling from the inlet to the outlet and the fluid recirculating in the main body of the chamber, and no streamlines appear to carry fluid (containing solute) from the inlet into the recirculation zone. However, since the concentrations in the majority of the chamber are high for these input flow rates, solute must cross the dividing streamline. One explanation for this is that there may in fact exist streamlines that transport solute directly from the inlet to the main body of the chamber, but the resolution used to display the flow profiles is not sufficient to capture this. It is further noted that the streamlines are illustrated on only the y, z plane through the centre of the chamber, and there could be 3D effects that allow solute to enter the recirculation zone. Finally, although the system is strongly convective, there will exist some level of diffusion, however small, that could account for some solute crossing the dividing streamline.

The flow patterns also influence the distribution of solute across the cell surface. For low input flow rates of $Q = 100 - 300 \mu\text{l min}^{-1}$, the maximum cell surface solute concentration is located close to the inlet side of the chamber. Upon increasing to $Q = 400 \mu\text{l min}^{-1}$, approximately half of the cell surface is exposed to the maximum cell surface solute concentration. For $Q = 500 \mu\text{l min}^{-1}$, the maximum cell surface solute concentration is located close to the outlet side of the chamber, and further increasing the input flow rate does not appear to substantially alter the distribution of solute across the cell surface. Whilst the distribution of solute is similar for many of the input flow rates, the magnitude of the concentration profiles tends to increase as input flow rate is increased. Clearly, for different solutes, the magnitude will also vary due to differences in metabolism. Here, specific to APAP, the cell surface concentration is very low for all input flow rates due to the high metabolic rates associated with this solute.

Effect of metabolic rate on solute concentration

Fig. 3.4.11 shows the O_2 concentration profiles throughout a single chamber (left plots) and at the cell surface (right plots) for four different cell types. These results are shown for an input flow rate of $Q = 100 \mu\text{l min}^{-1}$ only, since the purpose here is to demonstrate the effect of different rates of metabolism on the magnitude of the solute concentration. The distribution of solute throughout the chamber and at the cell surface does not vary significantly between cell type, since as previously discussed, this is largely governed by the fluid dynamics. However, the magnitude of the concentration profiles does vary due to differences in the metabolic rates exhibited by the various cell types. As expected, the solute concentration increases as the rate of metabolism decreases, from human cardiomyocytes with the highest metabolic rate, to HepG2 cells with the lowest metabolic rate.

Relationship between input flow rate and cell surface solute concentration

Fig. 3.4.12 shows the relationships between input flow rate and the mean APAP concentration (upper plot) and O_2 concentration (lower plot) observed at the cell surface. For both solutes and all cell types, it is clear that as input flow rate increases, the mean cell surface solute concentration tends to increase. Corresponding to the input flow rates where the flow patterns change considerably, an exception to this trend is observed for $Q = 300 - 400 \mu\text{l min}^{-1}$ where the mean cell surface solute concentration declines. These relationships could be utilised when configuring the input flow rate for experiments in which the desired cell surface solute concentration is known.

Connected chambers

Finally, Fig. 3.4.13 illustrates the distribution of O_2 (upper plots) and the cell surface O_2 concentration profiles (lower plots) in six connected chambers, for $Q = 100 \mu\text{l min}^{-1}$. As shown in §3.4.1, the fluid dynamics do not vary significantly between chambers, so as expected, the distribution of solute throughout the chamber and at the cell surface is not substantially different from one chamber to the next. However, the magnitude of the concentration in downstream chambers decreases as chamber number increases due to metabolism of the solute by the cells.

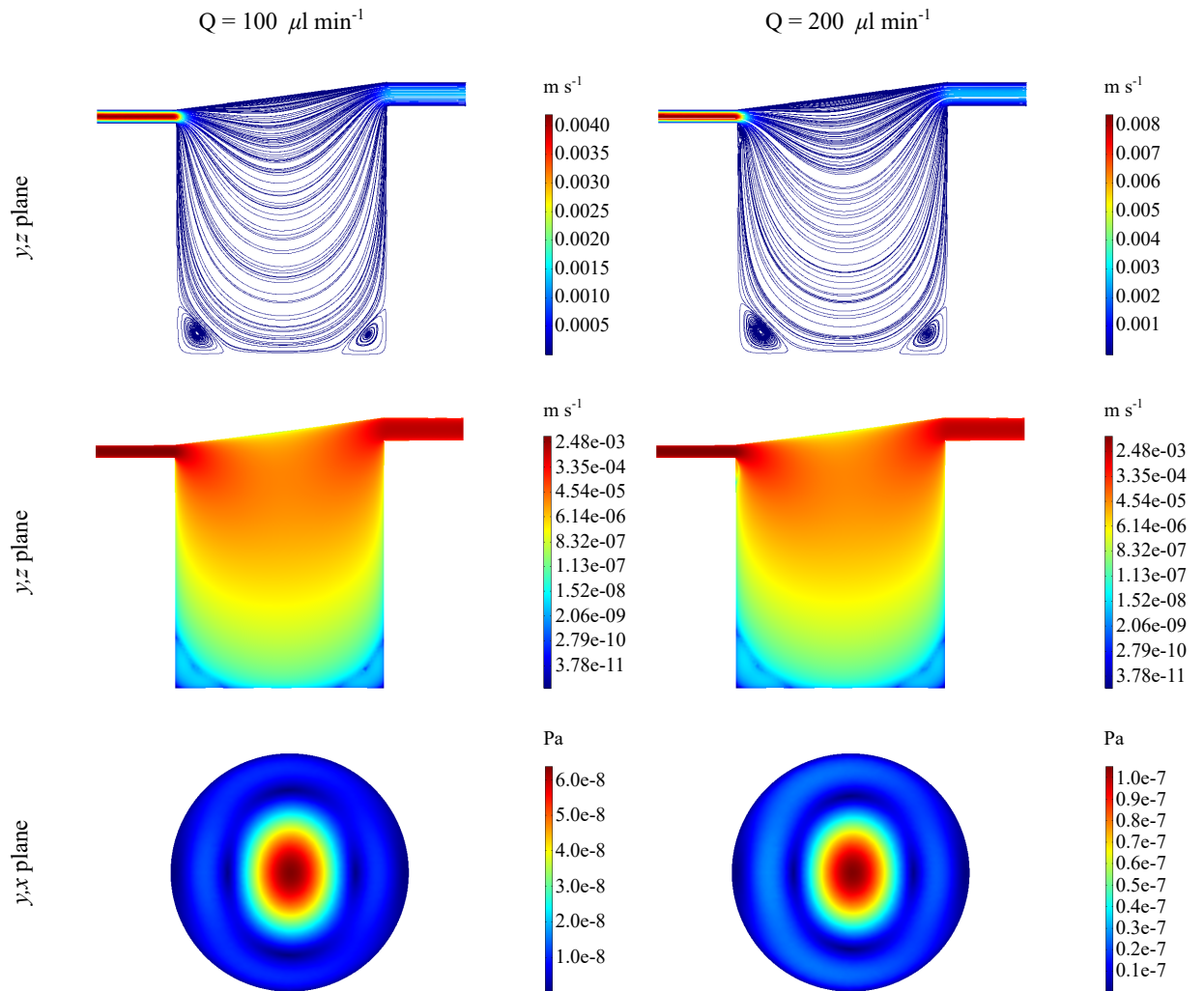


Figure 3.4.1: Streamlines and magnitude of velocity through the centre of the chamber (y, z plane, upper plots), magnitude of velocity through the centre of the chamber in a log scale (y, z plane, middle plots) and magnitude of shear stress at the cell surface (y, x plane), for $Q = 100 - 200 \mu\text{l min}^{-1}$.

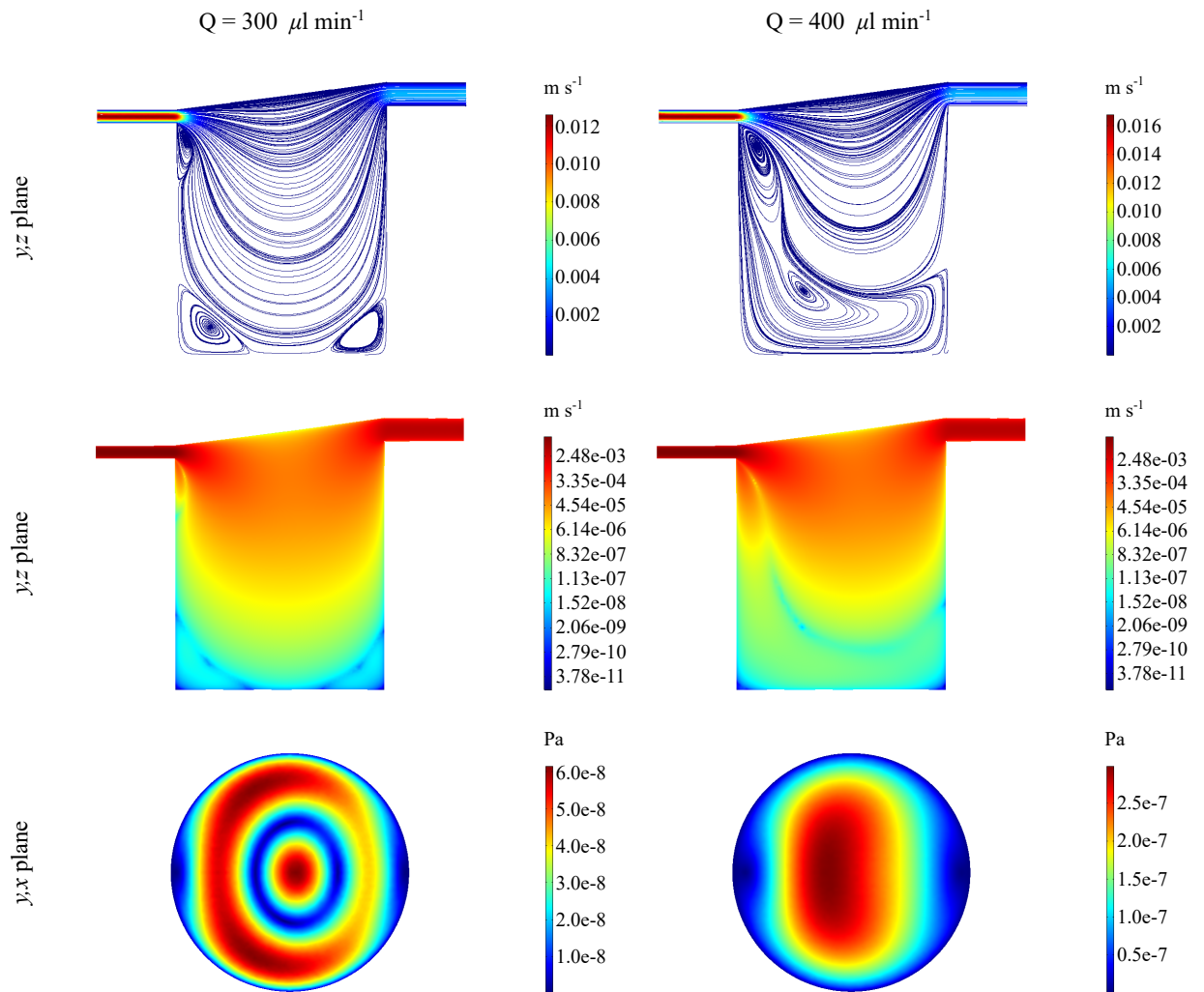


Figure 3.4.2: Streamlines and magnitude of velocity through the centre of the chamber (y, z plane, upper plots), magnitude of velocity through the centre of the chamber in a log scale (y, z plane, middle plots) and magnitude of shear stress at the cell surface (y, x plane), for $Q = 300 - 400 \mu\text{l min}^{-1}$.

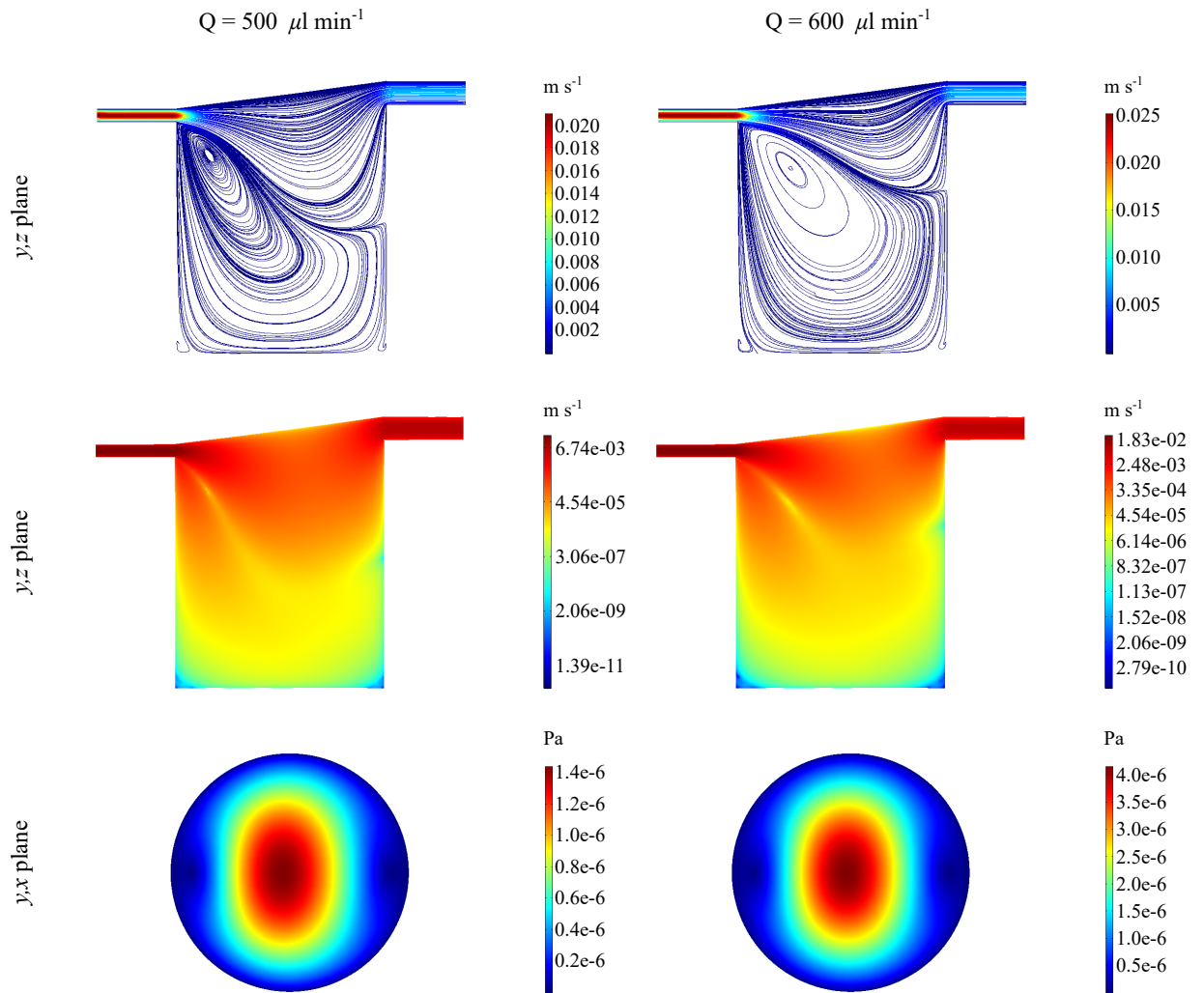


Figure 3.4.3: Streamlines and magnitude of velocity through the centre of the chamber (y, z plane, upper plots), magnitude of velocity through the centre of the chamber in a log scale (y, z plane, middle plots) and magnitude of shear stress at the cell surface (y, x plane), for $Q = 500 - 600 \mu\text{l min}^{-1}$.

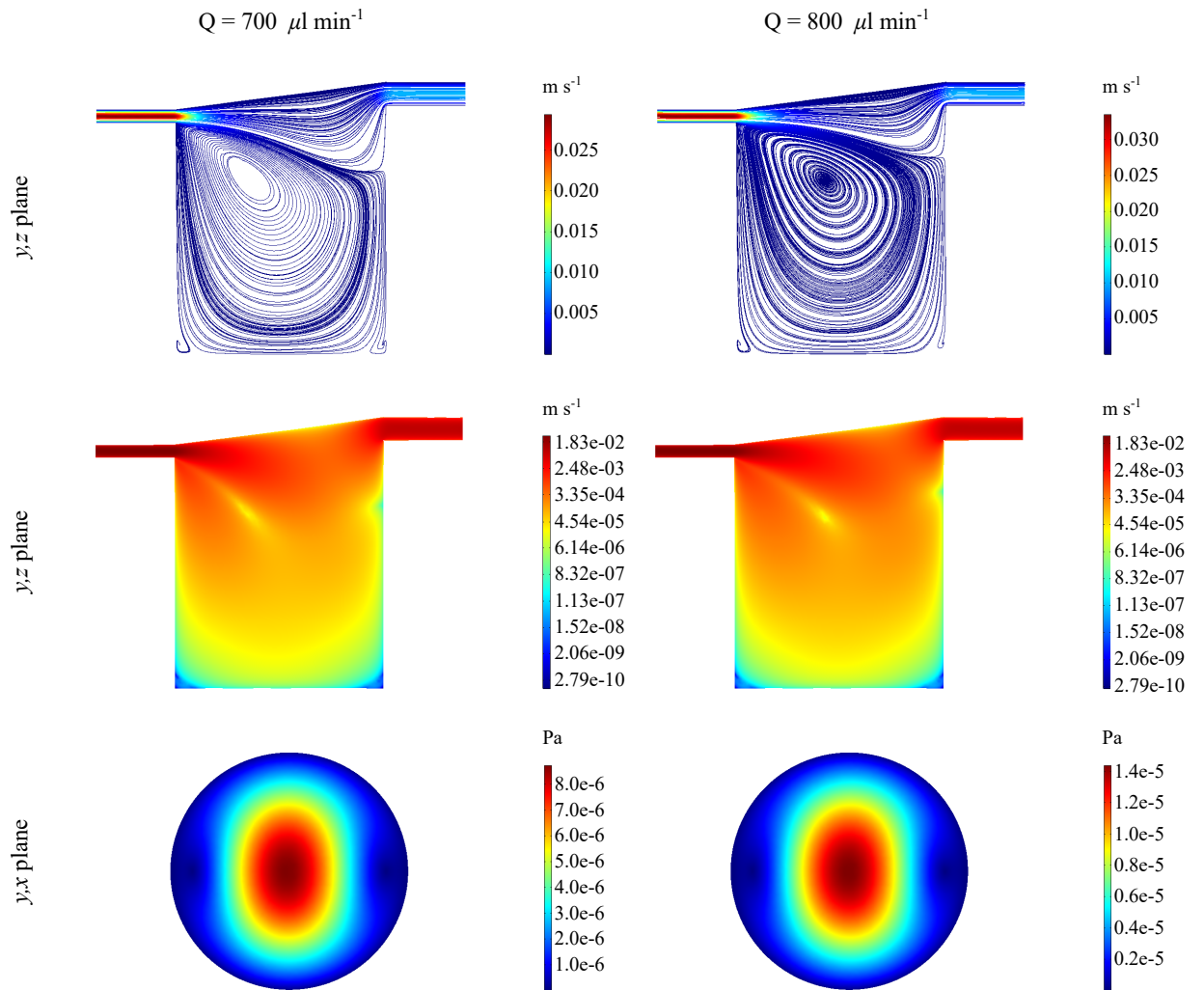


Figure 3.4.4: Streamlines and magnitude of velocity through the centre of the chamber (y, z plane, upper plots), magnitude of velocity through the centre of the chamber in a log scale (y, z plane, middle plots) and magnitude of shear stress at the cell surface (y, x plane), for $Q = 700 - 800 \mu\text{l min}^{-1}$.

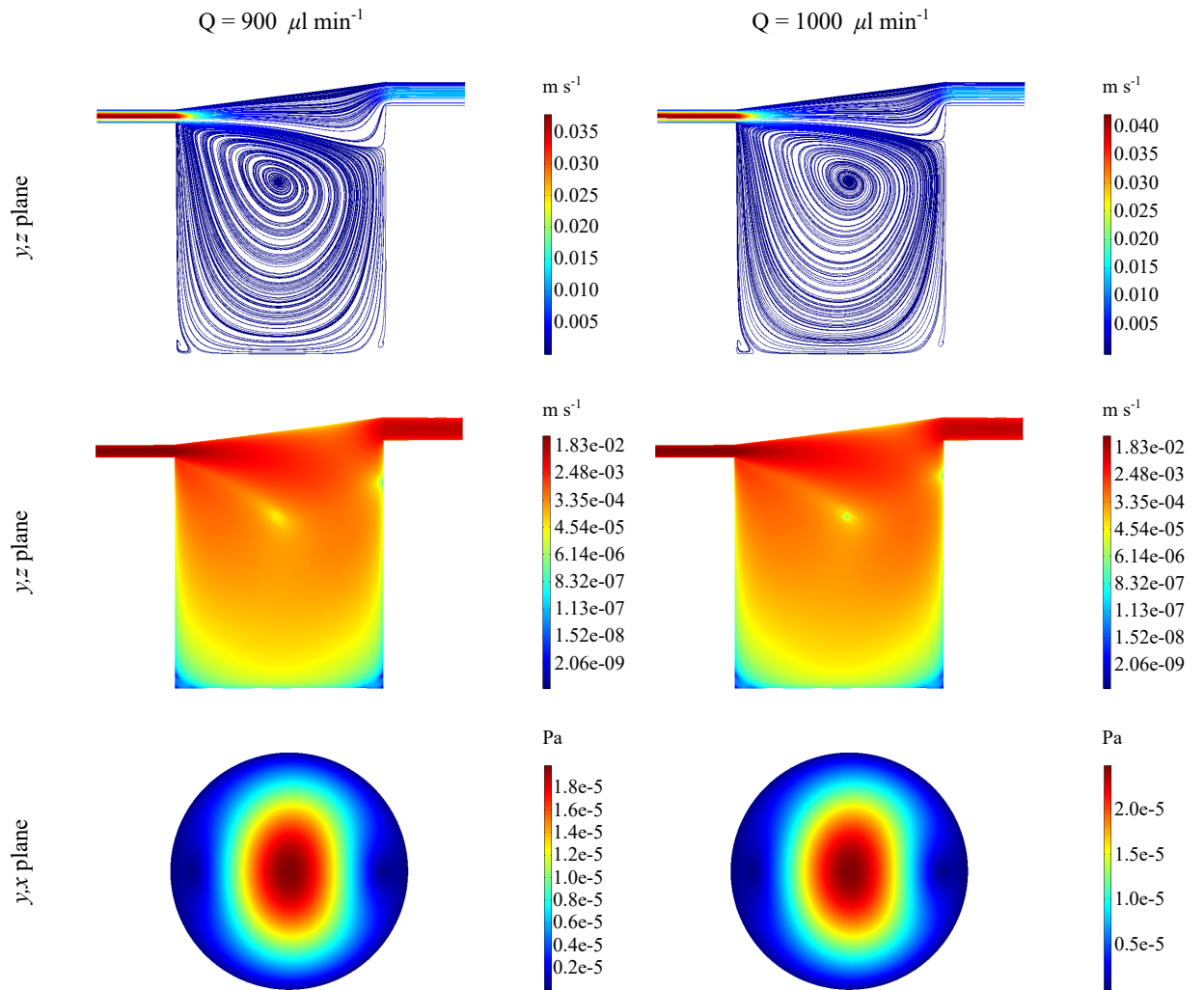


Figure 3.4.5: Streamlines and magnitude of velocity through the centre of the chamber (y, z plane, upper plots), magnitude of velocity through the centre of the chamber in a log scale (y, z plane, middle plots) and magnitude of shear stress at the cell surface (y, x plane), for $Q = 900 - 1000 \mu\text{l min}^{-1}$.

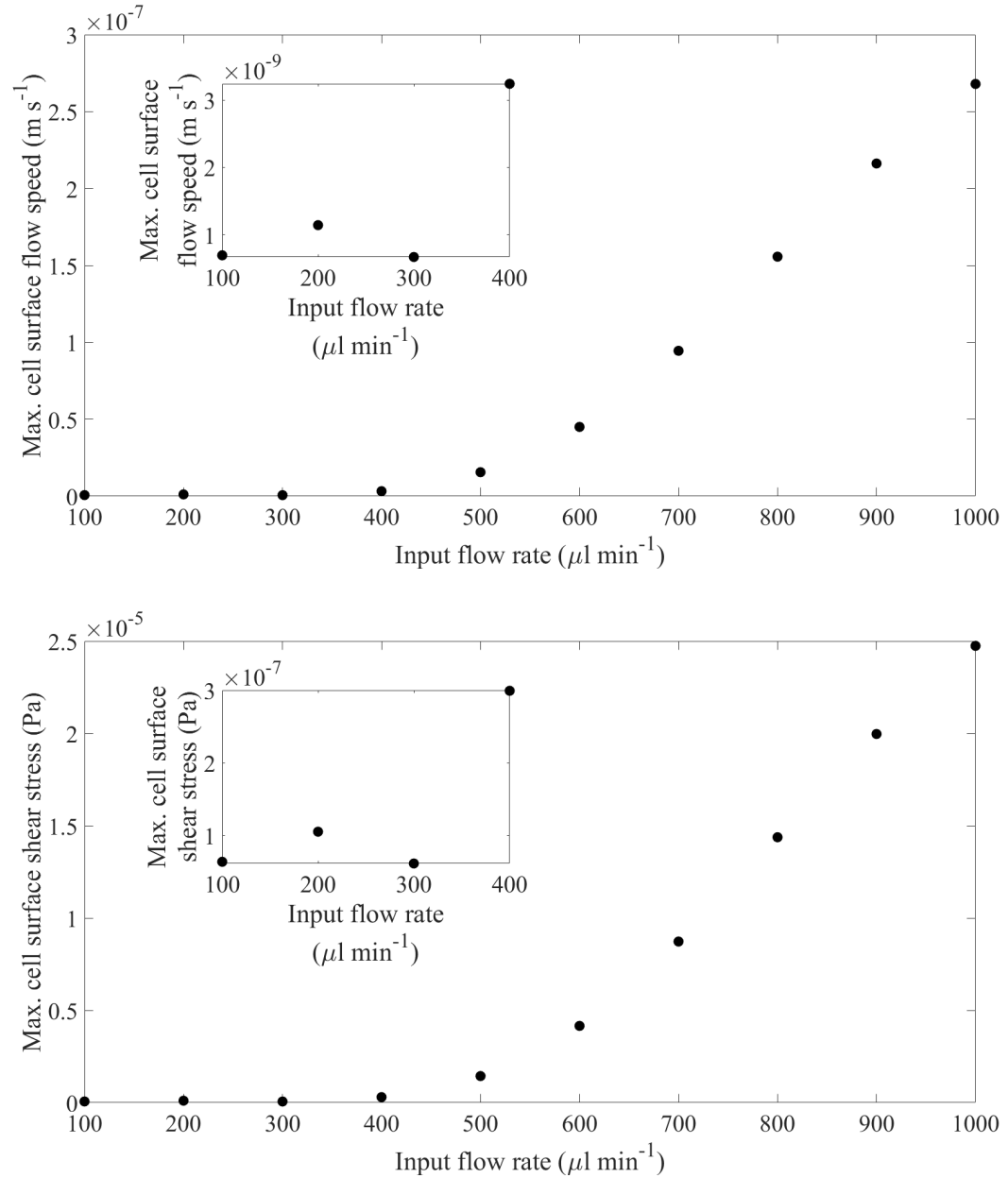


Figure 3.4.6: Relationships between input flow rate and maximum flow speed at the cell surface (upper plot) and maximum shear stress magnitude at the cell surface (lower plot), with the inset plots highlighting each relationship for $Q = 100 - 400 \mu\text{l min}^{-1}$. Note that since the velocity is equal to zero on the cell surface, the flow speed is evaluated just above the cell surface at a height of $z = h$.

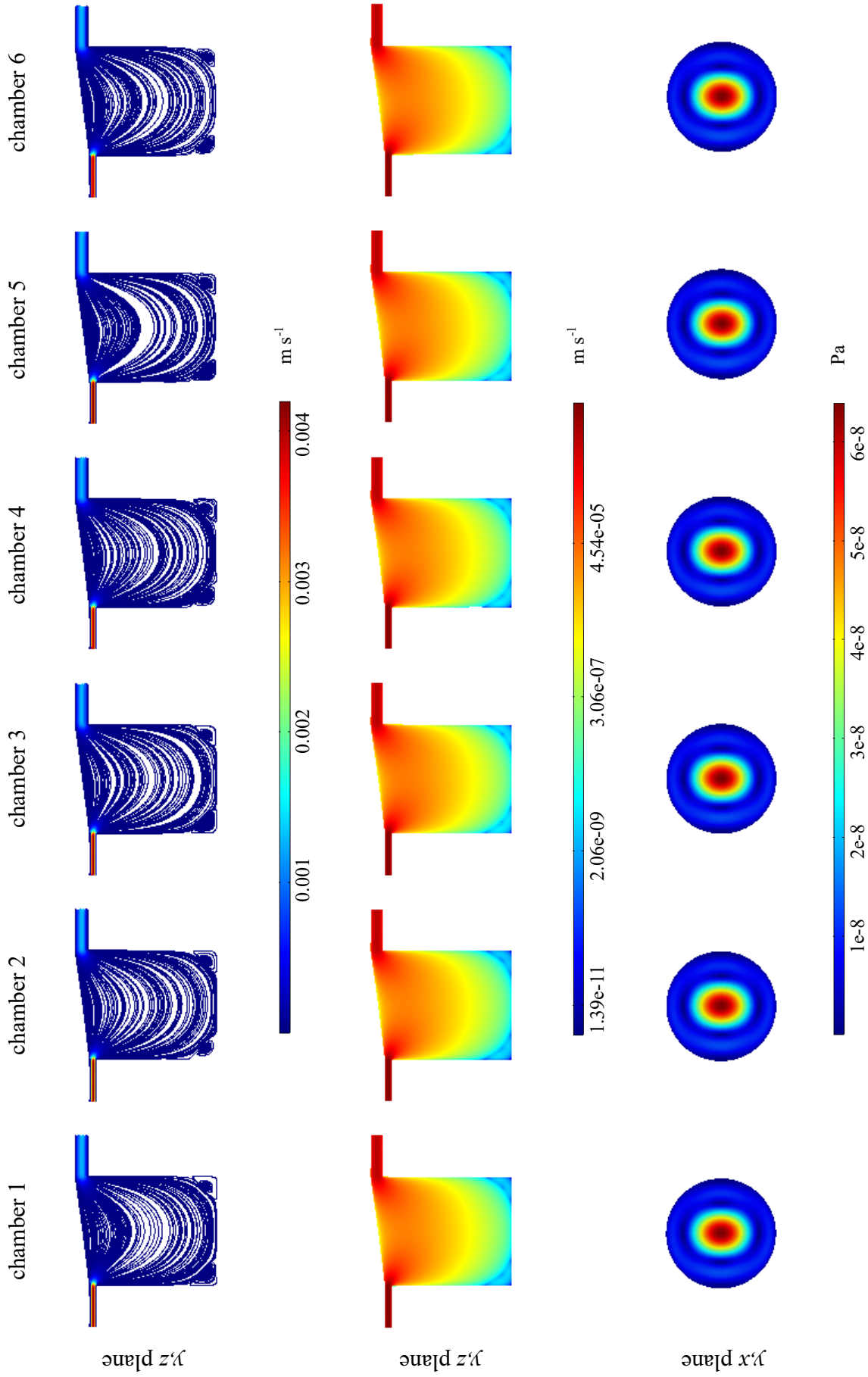


Figure 3.4.7: Streamlines and magnitude of velocity through the centre of each connected chamber (y, z plane, upper plots), magnitude of velocity through the centre of each connected chamber in a log scale (y, z plane, middle plots) and magnitude of shear stress at the cell surface of each connected chamber (y, x plane), for $Q = 100 \mu\text{l min}^{-1}$.

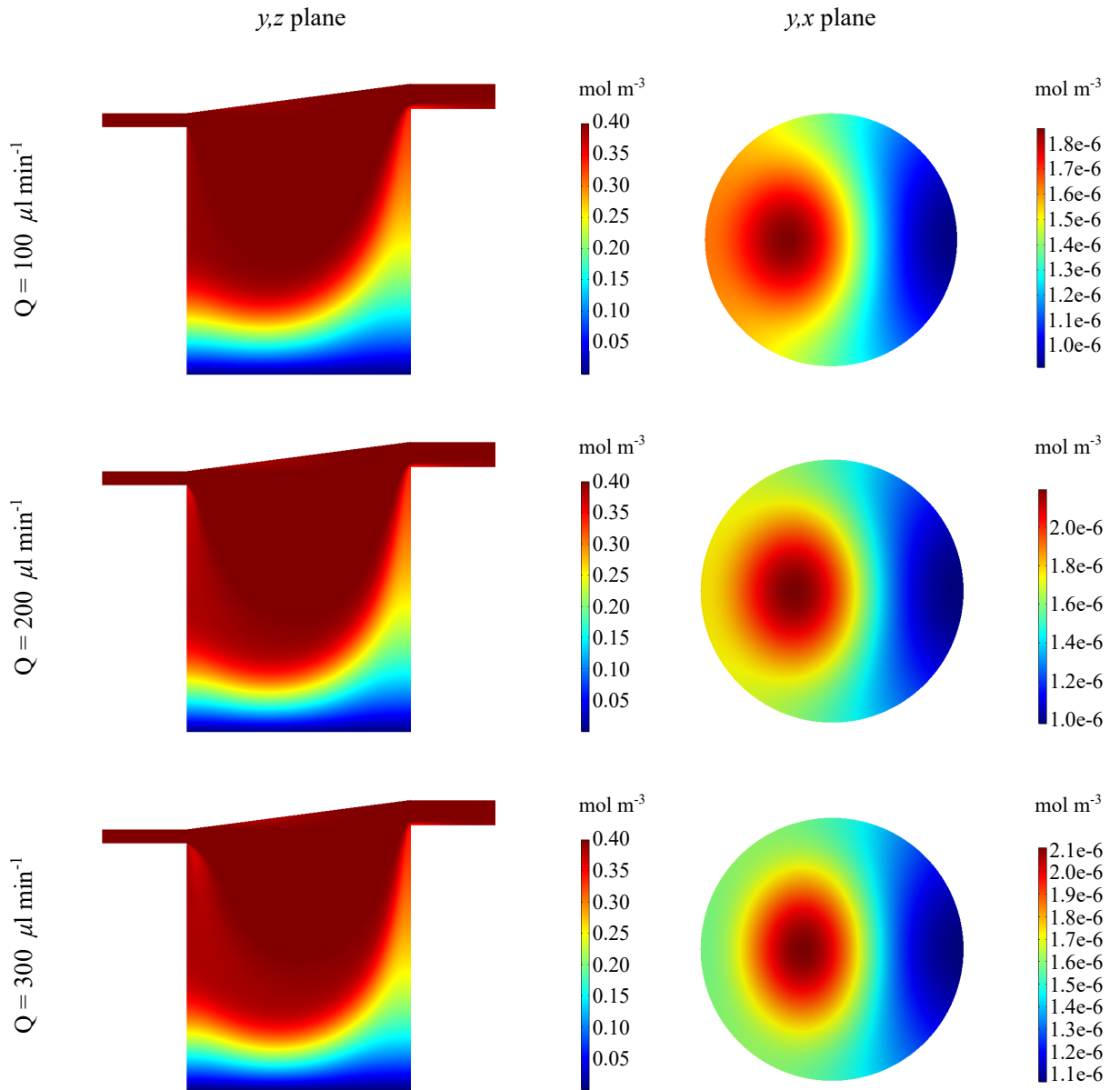


Figure 3.4.8: APAP concentration profiles through the centre of the chamber (y, z plane) and at the cell surface (y, x plane), for $Q = 100 - 300 \mu\text{l min}^{-1}$ and $c_{APAP}^{in} = 0.4 \text{ mol m}^{-3}$.

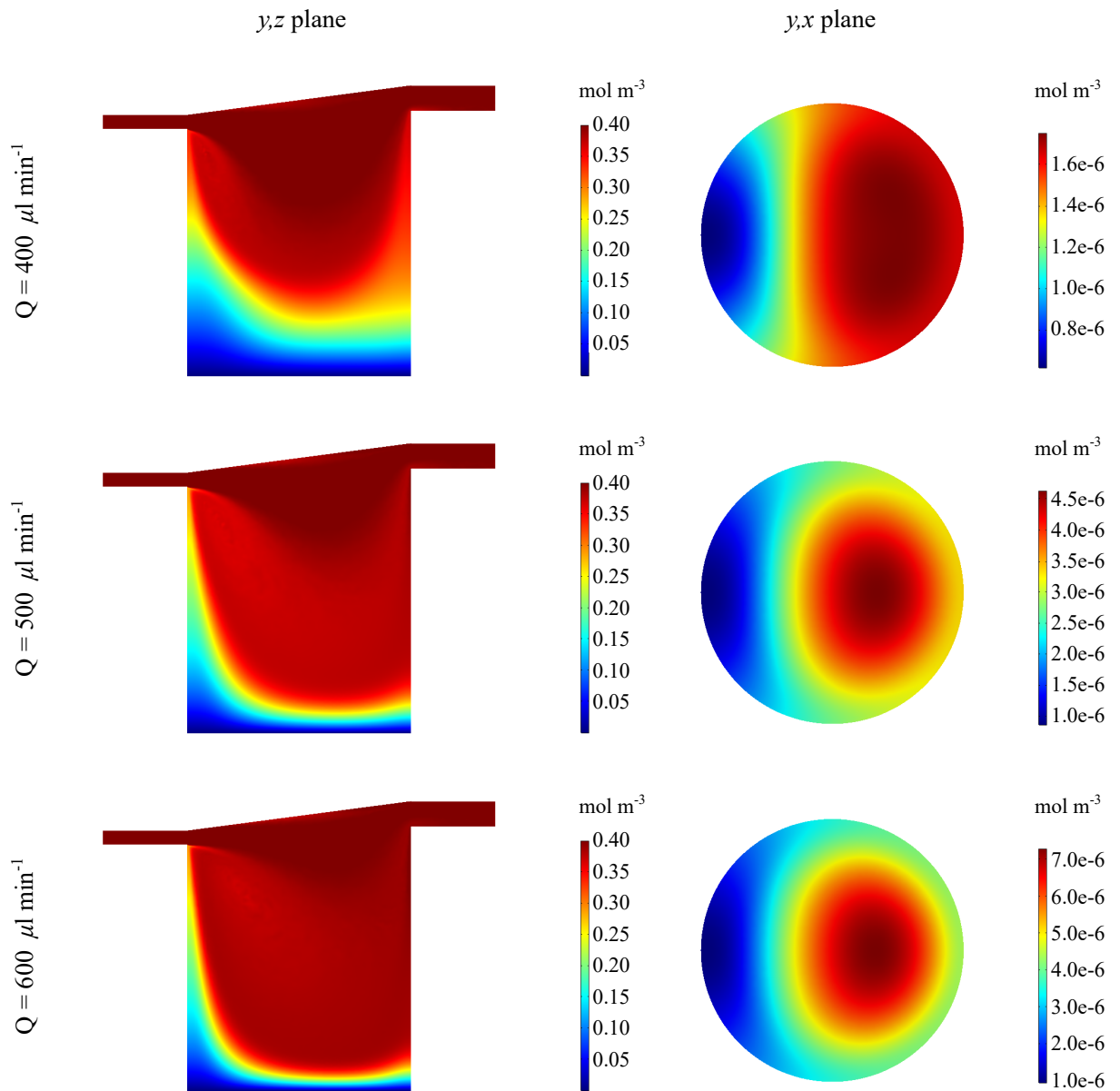


Figure 3.4.9: APAP concentration profiles through the centre of the chamber (y, z plane) and at the cell surface (y, x plane), for $Q = 400 - 600 \mu\text{l min}^{-1}$ and $c_{APAP}^{in} = 0.4 \text{ mol m}^{-3}$.

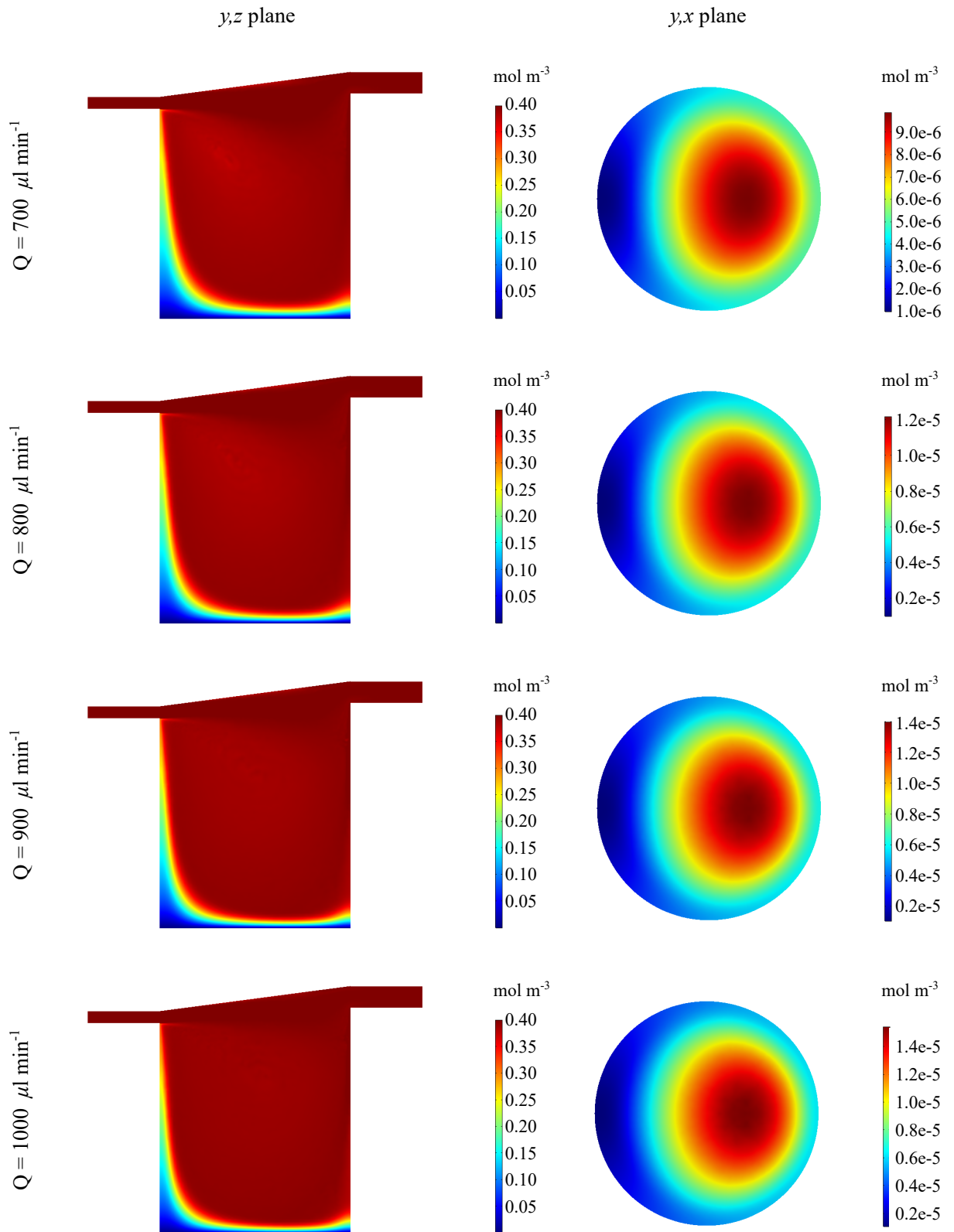


Figure 3.4.10: APAP concentration profiles through the centre of the chamber (y, z plane) and at the cell surface (y, x plane), for $Q = 700 - 1000 \mu\text{l min}^{-1}$ and $c_{APAP}^{in} = 0.4 \text{ mol m}^{-3}$.

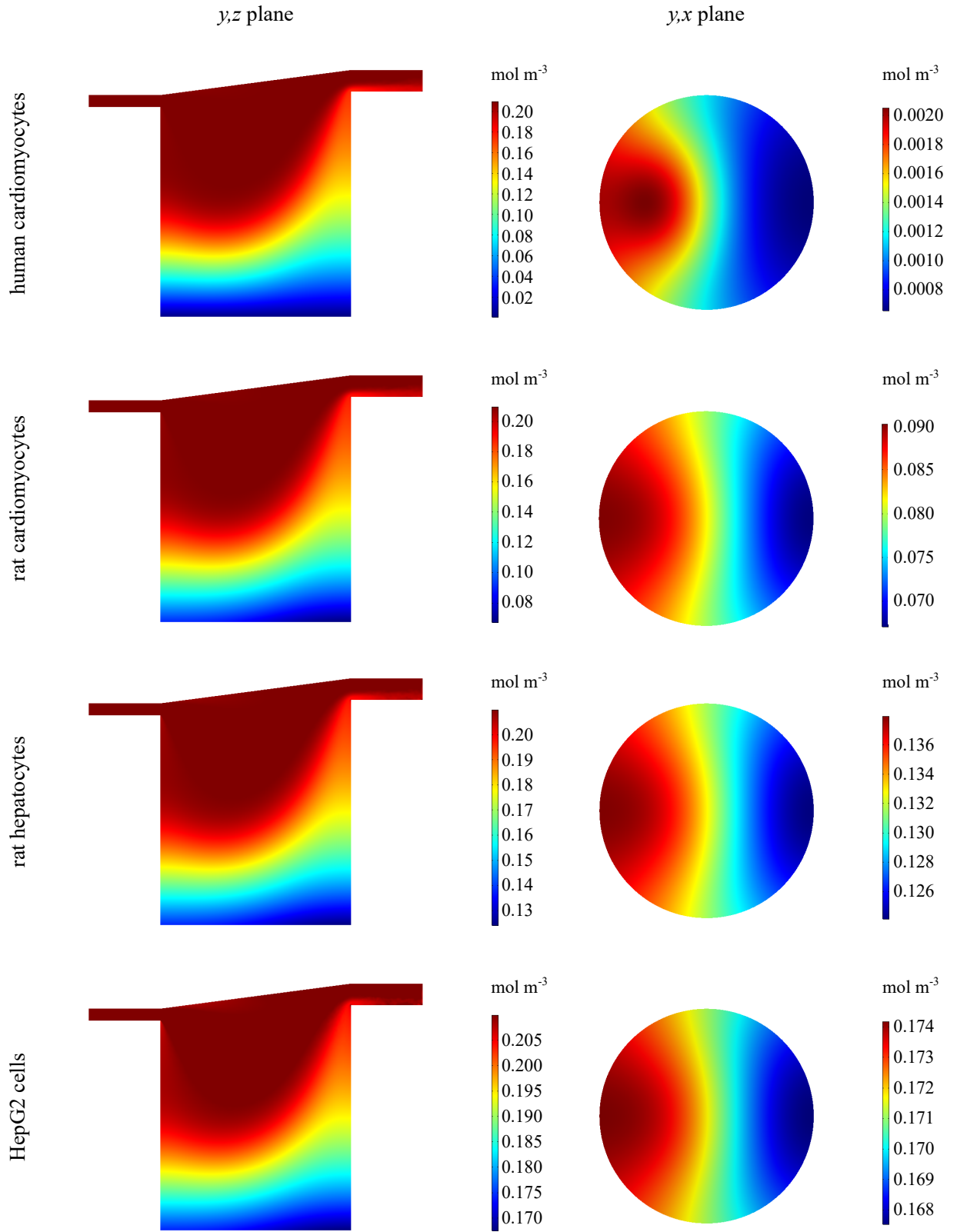


Figure 3.4.11: O_2 concentration profiles through the centre of the chamber (y, z plane) and at the cell surface (y, x plane) for different cell types, for $Q = 100 \mu\text{l min}^{-1}$ and $c_{O_2}^{in} = 0.21 \text{ mol m}^{-3}$.

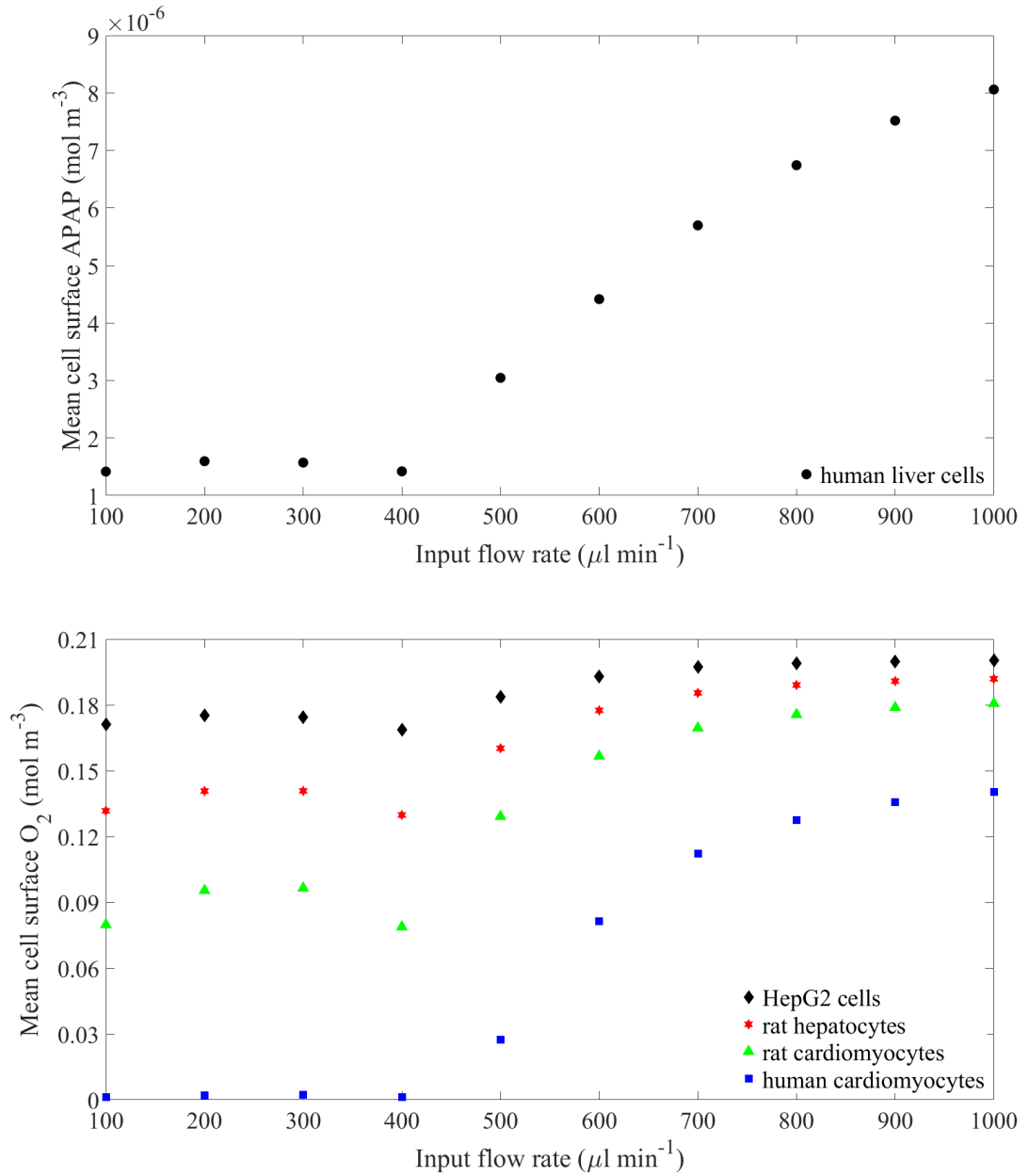


Figure 3.4.12: Relationships between input flow rate and mean APAP concentration at the cell surface (upper plot) and mean O_2 concentration at the cell surface (lower plot), for $c_{APAP}^{in} = 0.4 \text{ mol m}^{-3}$ and $c_{\text{O}_2}^{in} = 0.21 \text{ mol m}^{-3}$, respectively.

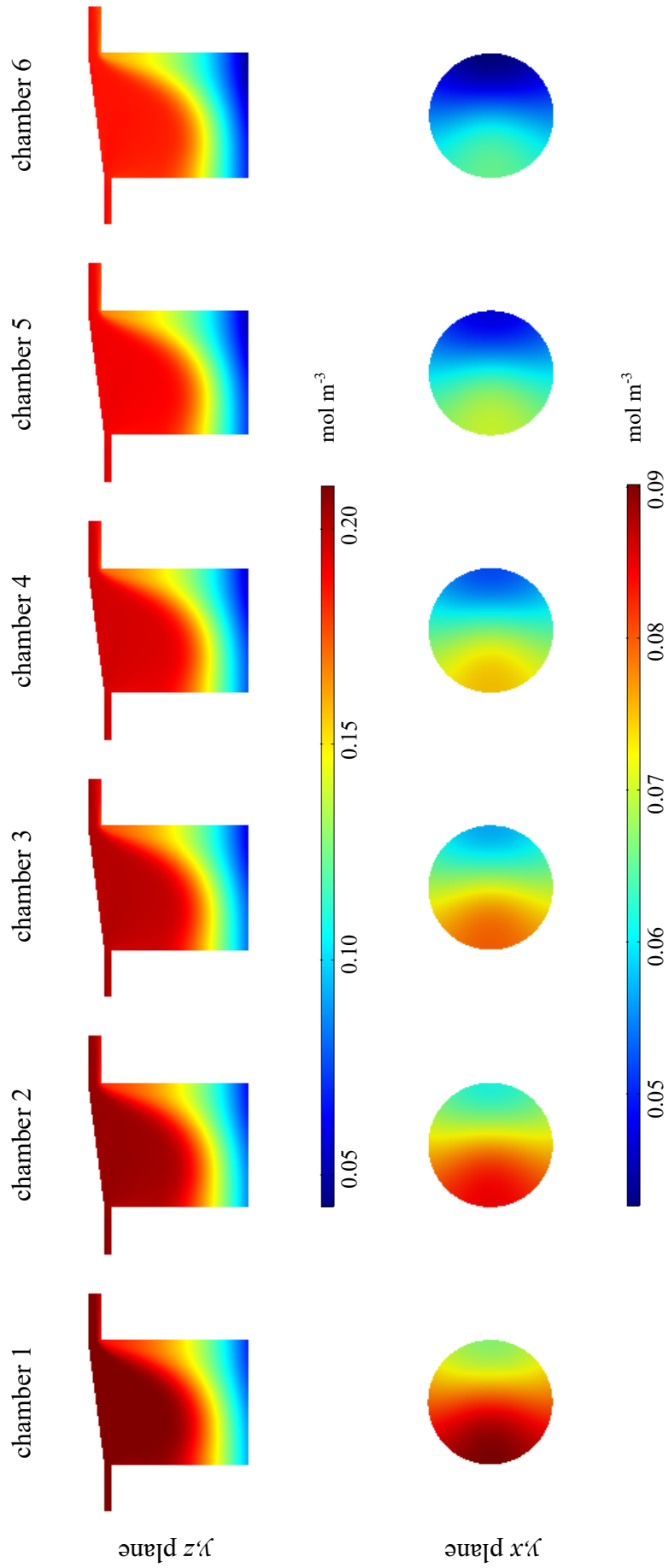


Figure 3.4.13: O₂ concentration profiles through the centre of each connected chamber (y, z plane) and at the cell surface of each connected chamber (y, x plane), for $Q = 100 \mu\text{l min}^{-1}$ and $c_{O_2}^{in} = 0.21 \text{ mol m}^{-3}$.

3.5 Discussion

In this section, both the advantages and challenges associated with mathematical modelling are discussed. In particular, the utility of the results presented in this chapter is highlighted, with simple but useful relationships being derived to predict solute concentrations with the aim of guiding experimental set-up.

3.5.1 Utility of the models

One of the main advantages of mathematical modelling is that it can provide a prediction of the outcomes of different experimental configurations so that devices may be set up efficiently, reducing the need for a trial and error approach and thus saving time and resources. By providing an understanding of how the input parameters impact the fluid dynamics and solute concentration profiles throughout the chambers, the mathematical models developed here offer insight that would not be uncovered by experimentation alone. Analysis of the results shown in §3.4 highlights key observations that could prove useful when choosing the operating parameters for the device. For example, it is clear that the choice of input flow rate is critical for controlling the fluid environment within the chambers, since this parameter significantly influences the flow patterns and speeds, as well as the cell surface shear stress profiles. The non-uniform distribution of these quantities throughout the chambers suggests that the spatial location of the cells within the chamber could also be an important factor in designing experimental set-up. The relationships between input flow rate and the quantities of interest observed at the cell surface, including flow speed, shear stress and solute concentration, give an indication of the effect of the choice of input flow rate on the conditions to which the cells are exposed. In particular, the nonlinear behaviour displayed in Figs. 3.4.6 and 3.4.12 is not intuitive and is unlikely to have emerged without the use of mathematical modelling. Furthermore, the results of the model highlight that the rate of metabolism of the solute by the cells plays a vital role in determining the solute concentration observed within the chamber, and it is apparent from Fig. 3.4.13 that in connected chambers, the solute depletes as chamber number increases. This has important implications for experimental configuration, suggesting that the metabolic capacity of the cells, as well as the number of chambers, must be considered carefully if, for example, a minimum solute concentration is to be maintained throughout the experiment.

Whilst there is no doubt that mathematics can help to provide invaluable information regarding the environment within cell culture systems, the majority of researchers carrying out the experiments, and who would therefore most benefit from this information, likely do not possess the level of expertise required to develop and interpret a mathematical model. With this in mind, it is helpful to highlight simple relationships that can be derived from the complicated mathematics, that can be used independently of understanding how the model was developed. This would allow experimentalists to gain some of the insight that mathematical modelling provides

without requiring an in-depth knowledge of the mathematics itself. One of the major challenges associated with maintaining a healthy cell culture is the adequate supply of nutrients, such as O_2 . Therefore, the ability to quickly and easily predict cell surface solute concentrations would be instrumental in effectively tailoring the inlet solute concentration in order to achieve the desired experimental conditions. For each of the models considered in this chapter, simple mathematical relationships that are applicable under certain conditions have been derived from the governing equations for this purpose.

Predicting concentrations of free and bound drug in a single chamber

Here, equations are presented to provide information on how the drug partitions between the free and bound states. This could prove useful in situations where it is important to find out how much of the drug has bound to the cells; in an experimental setting, limitations of measurement devices and techniques often dictate that only the total concentration of drug present within the sample is acquired, rather than assessing the free and bound drug concentrations separately. Therefore, expressions that account for the partitioning of the drug could provide additional insight into quantities that may be impossible to obtain experimentally.

As discussed in §3.4.2, the steady-state concentrations of free and bound drug are constant, with the free drug concentration equal to the inlet concentration, i.e.

$$c_j = c_j^{in}. \quad (3.5.1)$$

To derive an expression for predicting the steady-state bound drug concentration prior to experimentation or simulation, recall from (3.3.2) that the concentration of bound drug is tracked via

$$\frac{\partial b_j}{\partial t} = k_j^f c_j (B_j - b_j) - k_j^r b_j.$$

At steady-state, the time derivative is equal to zero and rearranging this equation gives

$$b_j = \frac{B_j c_j}{k_j^d + c_j}, \quad (3.5.2)$$

where $k_j^d = k_j^r/k_j^f$ is the equilibrium dissociation constant. Thus, provided that the density of binding sites and the rates of binding and unbinding are known, (3.5.1) and (3.5.2) may be used to quickly calculate the concentrations of free and bound drug, respectively, at steady-state. Clearly, the total concentration of drug, T_j , can be obtained by simply summing up the free and bound drug concentrations, i.e.

$$T_j = c_j + b_j. \quad (3.5.3)$$

If it is of interest to determine drug concentrations outwith steady-state, (3.5.3) can be used

to derive expressions for predicting how the drug partitions between the free and bound states prior to the establishment of equilibrium. First, it is assumed that binding occurs rapidly; this is appropriate in cases where the rate of the reaction is significantly faster than the rate of diffusion [74]. In this limit of rapid binding, a quasi-equilibrium is achieved between the free and bound drug concentrations, where the concentration of bound drug can be approximated by

$$b_j \approx \frac{B_j c_j}{k_j^d + c_j}. \quad (3.5.4)$$

Substituting this expression into (3.5.3) and rearranging yields a quadratic equation in c_j that can be solved to obtain

$$c_j \approx -\frac{1}{2}(k_j^d + B_j - T_j) + \frac{1}{2}\sqrt{(k_j^d + B_j - T_j)^2 + 4k_j^d T_j}. \quad (3.5.5)$$

Thus, given that the density of binding sites and the rates of binding and unbinding are known, (3.5.5) and (3.5.4) may be used to estimate how the drug partitions between the free and bound states prior to equilibrium, provided that the total drug concentration has been either predicted via simulation or experimentally measured. To predict the total drug concentration, the governing equations from §3.3.1 can be adapted to derive a reduced model in T_j . Recall that the coupled partial differential equations for tracking the concentrations of free and bound drug are given by

$$\begin{aligned} \frac{\partial c_j}{\partial t} &= D_j^{cell} \nabla^2 c_j - k_j^f c_j (B_j - b_j) + k_j^r b_j, \\ \frac{\partial b_j}{\partial t} &= k_j^f c_j (B_j - b_j) - k_j^r b_j. \end{aligned}$$

Then, since $T_j = c_j + b_j$, combining these equations gives

$$\begin{aligned} \frac{\partial T_j}{\partial t} &= D_j^{cell} \nabla^2 c_j \\ &= D_j^{cell} \left(\frac{\partial^2 c_j}{\partial x^2} + \frac{\partial^2 c_j}{\partial y^2} + \frac{\partial^2 c_j}{\partial z^2} \right) \\ &= D_j^{cell} \left[\frac{\partial}{\partial x} \left(\frac{\partial c_j}{\partial x} \right) + \frac{\partial}{\partial y} \left(\frac{\partial c_j}{\partial y} \right) + \frac{\partial}{\partial z} \left(\frac{\partial c_j}{\partial z} \right) \right] \\ &= D_j^{cell} \left[\frac{\partial}{\partial x} \left(\frac{dc_j}{dT_j} \frac{\partial T_j}{\partial x} \right) + \frac{\partial}{\partial y} \left(\frac{dc_j}{dT_j} \frac{\partial T_j}{\partial y} \right) + \frac{\partial}{\partial z} \left(\frac{dc_j}{dT_j} \frac{\partial T_j}{\partial z} \right) \right] \\ &= D_j^{cell} \nabla \cdot \left(\frac{dc_j}{dT_j} \nabla T_j \right) \\ &= \nabla \cdot (D_j^* \nabla T_j), \end{aligned}$$

where

$$D_j^* = D_j^{cell} \frac{dc_j}{dT_j}$$

is an effective concentration-dependent diffusion coefficient. Substituting (3.5.4) into (3.5.3) and differentiating with respect to c_j yields

$$\frac{dT_j}{dc_j} \approx 1 + \frac{B_j k_j^d}{(k_j^d + c_j)^2},$$

and so the coupled equations for c_j and b_j may be replaced by the following single partial differential equation in T_j :

$$\frac{\partial T_j}{\partial t} = \nabla \cdot (D_j^* \nabla T_j), \quad D_j^* \approx \frac{D_j^{cell}}{1 + \frac{B_j k_j^d}{(k_j^d + c_j)^2}}, \quad (3.5.6)$$

where c_j is given by (3.5.5). Here, the role of binding is accounted for through a reduced diffusion coefficient, and it is noted that (3.5.6) simplifies to a simple diffusion equation for tracking the concentration of free drug in the case of no binding. The solution to this reduced model provides the total drug concentration which can then be used to predict the concentrations of free and bound drug via (3.5.5) and (3.5.4), respectively.

Predicting steady-state cell surface solute concentrations in a single chamber

Here, an equation is presented to provide information on how varying the inlet concentration will impact the solute concentration at the cell surface. Based on knowledge of the cell surface solute concentration for a given inlet concentration, the cell surface solute concentration may be predicted for a new inlet concentration, without the need for further simulations or experimentation. This could be useful in situations where a researcher from an experimental background wishes to use the results of a mathematical model to predict the outcome of an experiment, but the results are presented using a different inlet concentration. Rather than having to adapt the model, the proposed equation could be used to indicate how the results may have varied if a different inlet concentration was used. Furthermore, such an equation could also prove useful in situations where an experiment has been performed, but the solute concentrations observed at the cell surface were not found to be appropriate. Then, rather than starting the experiment again with different operating parameters, the proposed equation could be used to indicate how the available experimental results may differ if the inlet concentration is changed.

The two main features of the cell surface solute concentration profile are the distribution of solute, and the magnitude of the concentration. Clearly, the magnitude is governed by both metabolism of the solute by the cells and the inlet concentration. As previously established, the distribution of solute is largely influenced by the choice of input flow rate, but solute metabolism also plays a role here. The cell surface solute concentration profile is only predictable when the distribution of solute does not change, i.e. when both input flow rate and metabolic rate are fixed. Recall from (3.3.3) that M-M reaction kinetics are described by the following nonlinear

term:

$$R_j = \sum_{i=1}^m \frac{V_j^i c_j}{K_j^i + c_j}.$$

Clearly, the rate of metabolism is dependent on the concentration of solute available at the cell surface. As shown in §3.4.2, the distribution of solute across the cell surface is not uniform and so metabolism is variable, with cells at different locations metabolising the solute at different rates. This means that the metabolic rate is not fixed, and the distribution of solute across the cell surface will vary as inlet concentration is varied. However, if the same amount of solute is metabolised across the entire cell surface, the distribution of solute will not vary as inlet concentration is varied, as long as the input flow rate is fixed. It is noted that, if the cell surface solute concentration is above a certain threshold ($c_j \gg K_j^i$), it may be shown that the rate of metabolism is approximately constant and equal to the maximum metabolic rate, i.e.

$$R_j \approx \sum_{i=1}^m V_j^i \quad \text{when} \quad c_j \gg K_j^i.$$

If this condition is satisfied, then varying the inlet concentration results in a variation of only the magnitude of the concentration, with the distribution of the solute remaining unchanged. Since the only variable is the inlet concentration, the change in magnitude must correspond to the change in this parameter. Therefore, under the criteria that both input flow rate and metabolic rate are fixed, if the cell surface solute concentration profile is known for a given c_j^{in} , the cell surface solute concentration profile for any c_j^{in*} may be predicted via the following equation:

$$c_j^*(y) \approx c_j(y) + \Delta c_j^{in}, \quad \Delta c_j^{in} = c_j^{in*} - c_j^{in}, \quad (3.5.7)$$

where y is the axis through the centre of the cell surface from the inlet side to the outlet side of the chamber. Here, $c_j^*(y)$ and $c_j(y)$ are the solute concentration profiles across the centre of the cell surface corresponding to inlet concentrations of c_j^{in*} and c_j^{in} , respectively. Note that this equation may be generalised to predict the solute concentration profile across the entire cell surface, but for simplicity, only the profile across the centre of the cell surface is considered.

In theory, (3.5.7) could be used to predict the cell surface concentration profile of any solute whose metabolism is approximately constant. For the parameters presented in Table 3.1, $c_j \gg K_j^i$ is not satisfied for APAP, so in order to demonstrate the utility of (3.5.7), results are illustrated for O_2 only, using rat cardiomyocytes as an example cell type. When the solute is O_2 , the use of (3.5.7) remains valid given that $c_{O_2} \gg K_{O_2}$, i.e. $K_{O_2}/c_{O_2} \ll 1$. Fig. 3.5.1 shows the values of K_{O_2}/c_{O_2} calculated over a range of inlet concentrations for the lowest and highest input flow rates of $Q = 100$ and $1000 \mu\text{l min}^{-1}$, where c_{O_2} is taken to be the mean O_2 concentration across the cell surface. Here, it is noted that although $K_{O_2}/c_{O_2} \ll 1$ is not satisfied for the lowest inlet concentrations, especially for the lowest input flow rate, this condition is met for the

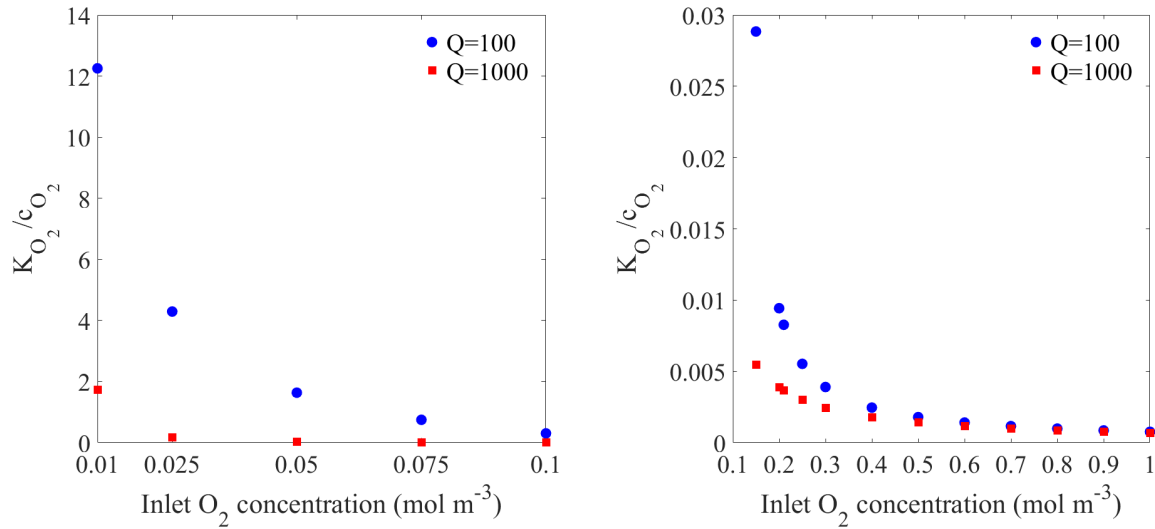


Figure 3.5.1: Values of K_{O_2}/c_{O_2} calculated over a range of inlet concentrations from $c_{O_2}^{in} = 0.01 - 0.10 \text{ mol m}^{-3}$ (left) and from $c_{O_2}^{in} = 0.15 - 1.00 \text{ mol m}^{-3}$ (right), for the lowest and highest input flow rates of $Q = 100$ and $1000 \mu\text{l min}^{-1}$.

majority of the parameter combinations. In particular, as previously discussed, the cell surface O_2 concentration increases with increasing input flow rate, so it follows that the assumption of $K_{O_2}/c_{O_2} \ll 1$ is more accurate as input flow rate increases. Therefore, based on these calculations, it is expected that (3.5.7) will provide good predictions of the cell surface O_2 concentration profile for most of the parameter values under consideration.

For an input flow rate of $Q = 100 \mu\text{l min}^{-1}$, Fig. 3.5.2 compares the original simulated cell surface O_2 concentration profile for $c_{O_2}^{in} = 0.21 \text{ mol m}^{-3}$, and a new simulated cell surface O_2 concentration profile when the inlet concentration is increased to $c_{O_2}^{in*} = 0.30 \text{ mol m}^{-3}$. Here, it is clear that the distribution of O_2 across the cell surface is indeed unchanged as inlet concentration is increased, but the magnitude of the cell surface O_2 concentration varies by approximately the change in inlet concentration. A prediction of the new cell surface O_2 concentration profile was made using (3.5.7) and displays excellent agreement with the simulated result, as shown by the dashed line.

A metric by which to define the strength of the predictions can be obtained by integrating (3.5.7) with respect to y over the diameter of the cell surface ($-r < y < r$). Performing the integration and rearranging gives $\gamma \approx 1$, where

$$\gamma = \frac{\int_{-r}^r c_j^*(y) dy - \int_{-r}^r c_j(y) dy}{2r \Delta c_j^{in}}, \quad (3.5.8)$$

and the proximity of γ to one indicates how accurate the prediction is. Fig. 3.5.3 shows the values of γ calculated over a range of new inlet concentrations from $c_{O_2}^{in*} = 0.01 - 1.00 \text{ mol m}^{-3}$ for the lowest and highest input flow rates of $Q = 100$ and $1000 \mu\text{l min}^{-1}$, using $c_{O_2}^{in} = 0.21 \text{ mol m}^{-3}$ as the original inlet concentration. For the majority of these cases, $\gamma \approx 1$, demon-

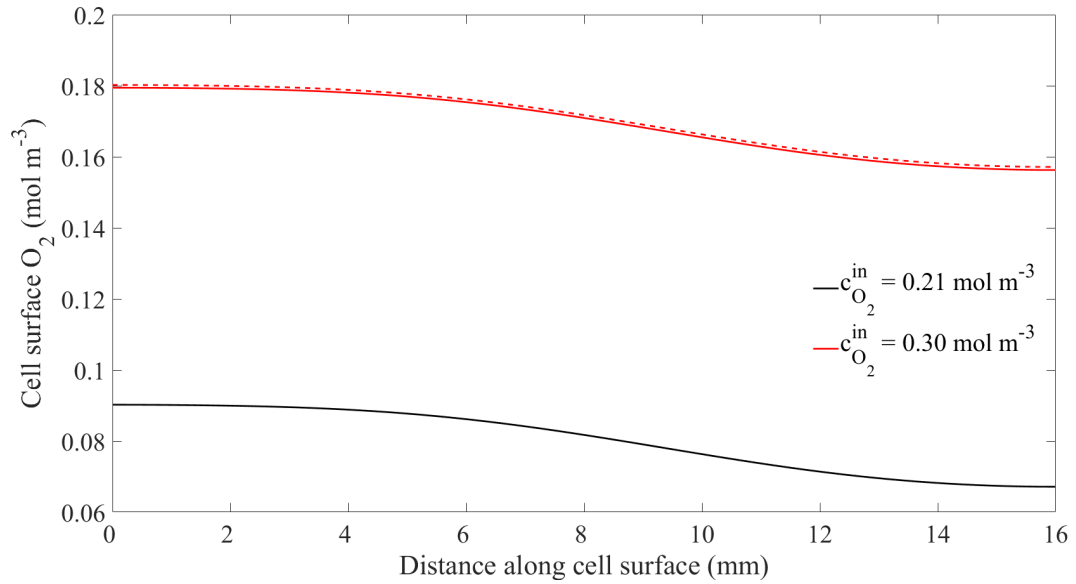


Figure 3.5.2: Comparison between simulated cell surface O₂ concentration profiles for the original inlet concentration ($c_{O_2}^{in} = 0.21 \text{ mol m}^{-3}$) and a new inlet concentration ($c_{O_2}^{in*} = 0.30 \text{ mol m}^{-3}$), for $Q = 100 \mu\text{l min}^{-1}$. The prediction obtained from (3.5.7) is illustrated by the dashed line.

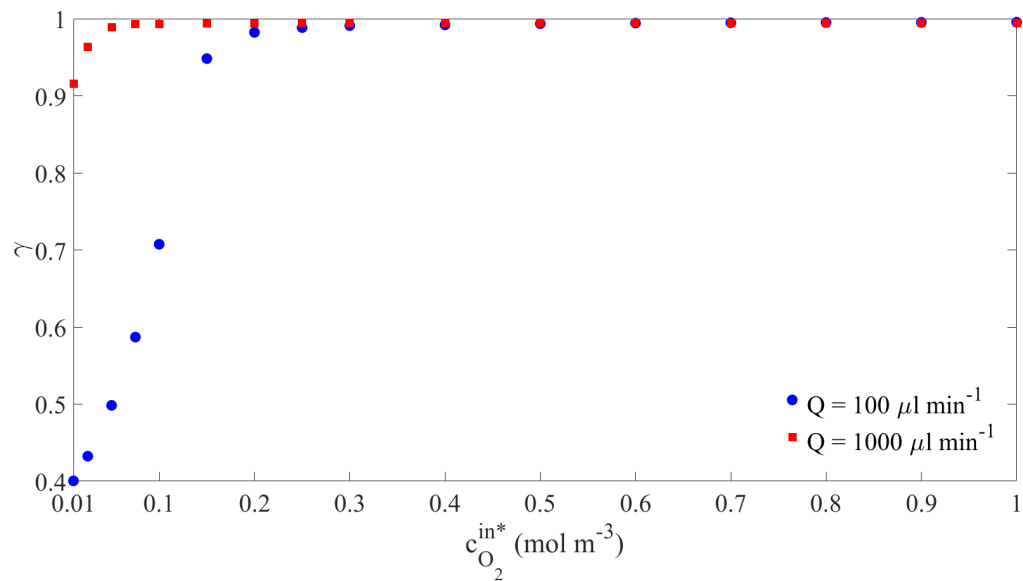


Figure 3.5.3: Values of γ calculated over a range of new inlet concentrations from $c_{O_2}^{in*} = 0.01 - 1.00 \text{ mol m}^{-3}$ for the lowest and highest input flow rates of $Q = 100$ and $1000 \mu\text{l min}^{-1}$, using $c_{O_2}^{in} = 0.21 \text{ mol m}^{-3}$ as the original inlet concentration.

strating that (3.5.7) is valid for predicting the cell surface O_2 concentration profile for various combinations of input parameters. As expected, the strength of the predictions is weakest for the lowest inlet concentrations where $c_{O_2} \gg K_{O_2}$ is less likely to be satisfied, and is strongest for the higher input flow rate where the assumption of $c_{O_2} \gg K_{O_2}$ is more accurate.

As well as predicting the solute concentration profile across the cell surface, (3.5.7) can also be used to predict the mean cell surface solute concentration by replacing $c_j(y)$ by \bar{c}_j , i.e.

$$\bar{c}_j^* \approx \bar{c}_j + \Delta c_j^{in}, \quad \Delta c_j^{in} = c_j^{in*} - c_j^{in}, \quad (3.5.9)$$

where \bar{c}_j^* and \bar{c}_j are the mean solute concentrations at the cell surface corresponding to inlet concentrations of c_j^{in*} and c_j^{in} , respectively. Fig. 3.5.4 compares the simulated and predicted mean cell surface O_2 concentrations for $c_{O_2}^{in*} = 0.01 - 1.00 \text{ mol m}^{-3}$, $c_{O_2}^{in} = 0.21 \text{ mol m}^{-3}$ and $Q = 100$ and $1000 \text{ } \mu\text{l min}^{-1}$. It is clear that (3.5.9) can be used to make accurate predictions of the mean O_2 concentration at the cell surface for parameters that satisfy $c_{O_2} \gg K_{O_2}$, and the linear relationship between inlet concentration and mean cell surface O_2 concentration within the region of validity is highlighted.

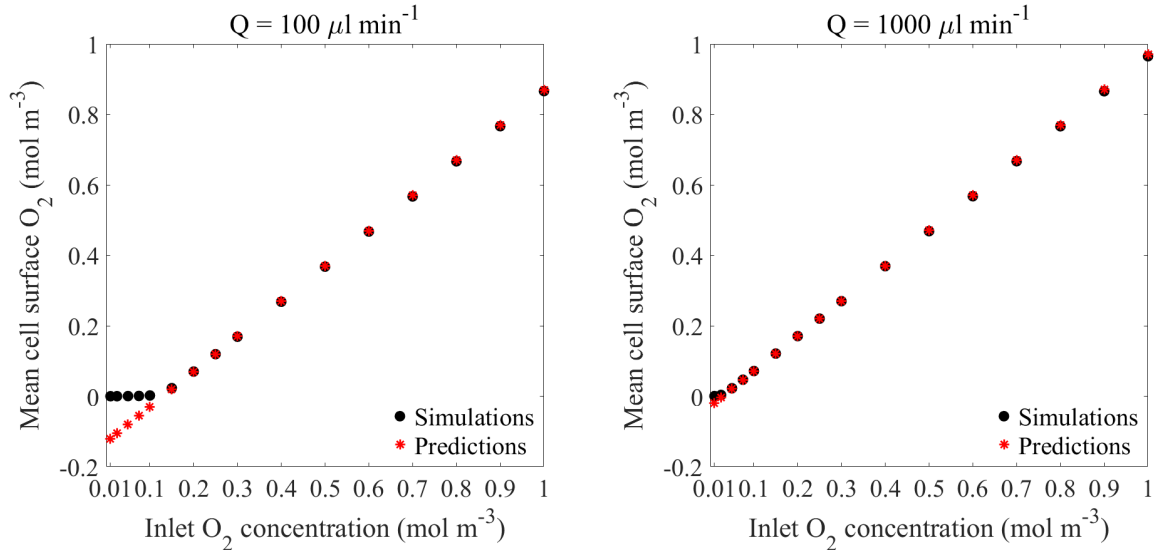


Figure 3.5.4: Comparison between simulated and predicted mean cell surface O_2 concentrations for $Q = 100 \text{ } \mu\text{l min}^{-1}$ (left) and $Q = 1000 \text{ } \mu\text{l min}^{-1}$ (right).

Predicting steady-state cell surface solute concentrations in connected chambers

Here, an equation is presented to provide information on how the solute concentration varies at the cell surface in connected chambers. As shown in §3.4.2, the solute concentration depletes as chamber number increases as a consequence of metabolism of the solute by the cells. Since an adequate supply of solute is often a limiting factor in the success of experiments, it would be beneficial to obtain a relationship between the cell surface solute concentration profiles across connected chambers. For this purpose, (3.5.7) is adapted to enable the prediction of the cell

surface solute concentration in chamber n , based on knowledge of the cell surface solute concentration in chamber 1. This could be useful in situations where the solute concentration at the cell surface has already been simulated or experimentally measured in a single chamber. Then, rather than having to repeat perhaps difficult measurements in multiple chambers, or having to perform further simulations using a more computationally intensive connected chamber geometry, the proposed equation could be used to easily predict the cell surface solute concentration in downstream chambers.

As demonstrated by (3.5.7), a known cell surface solute concentration profile can be used to predict a new cell surface solute concentration profile when the inlet concentration is varied. This concept can also be applied to chambers connected in series; assuming that metabolism is approximately constant, the cell surface solute concentration profile in chamber n may be predicted via the following equation:

$$c_j^n(y) \approx c_j^1(y) + \Delta c_j^{in}, \quad \Delta c_j^{in} = c_j^{in^n} - c_j^{in^1}, \quad (3.5.10)$$

where $c_j^n(y)$ and $c_j^1(y)$ are the solute concentration profiles across the centre of the cell surface in chamber n and chamber 1, respectively, and $c_j^{in^n}$ and $c_j^{in^1}$ are the inlet concentrations in chamber n and chamber 1, respectively. The key difference between (3.5.7) and (3.5.10) is that, here, the ‘new’ inlet concentration, i.e. the concentration at the inlet to a downstream chamber, is not manually adjusted and is instead determined by the rate of metabolism. Therefore, in order to make use of (3.5.10), a method for estimating $c_j^{in^n}$ must first be derived.

At steady-state, as a consequence of mass conservation, the amount of solute leaving a chamber must be equal to the difference between the amount of solute that entered the chamber and the amount of solute that was metabolised by the cells. Considering the mass fluxes (mol s^{-1}) in chamber 1, the mass flux at the outlet must be equal to the mass flux at the inlet minus the mass flux at the cell surface, i.e.

$$\begin{aligned} & \int_{A_{out}} \mathbf{n} \cdot \left(-D_j \nabla c_j^{out^1} + \mathbf{u}^{out^1} c_j^{out^1} \right) dA_{out} \\ &= \int_{A_{in}} \mathbf{n} \cdot \left(-D_j \nabla c_j^{in^1} + \mathbf{u}^{in^1} c_j^{in^1} \right) dA_{in} - \alpha, \end{aligned} \quad (3.5.11)$$

where $c_j^{out^1}$ and $c_j^{in^1}$ (mol m^{-3}) are the solute concentrations at the outlet and inlet faces of chamber 1, respectively, A_{out} and A_{in} (m^2) are the areas of the outlet and inlet faces, respectively, and α represents the mass flux at the cell surface, i.e. the moles of solute that are metabolised per second. Here, since metabolism is assumed constant,

$$\alpha \approx \int_{A_{cells}} \sum_{i=1}^m V_j^i dA_{cells} = A_{cells} \sum_{i=1}^m V_j^i, \quad (3.5.12)$$

where A_{cells} (m^2) is the area of the cell surface. Also at steady-state and due to conservation of

mass, the amount of solute leaving one chamber must be equal to the amount of solute entering the next chamber. Thus, the mass flux leaving chamber 1 must be equal to the mass flux entering chamber 2, i.e.

$$\begin{aligned} & \int_{A_{out}} \mathbf{n} \cdot \left(-D_j \nabla c_j^{out^1} + \mathbf{u}^{out^1} c_j^{out^1} \right) dA_{out} \\ &= \int_{A_{in}} \mathbf{n} \cdot \left(-D_j \nabla c_j^{in^2} + \mathbf{u}^{in^2} c_j^{in^2} \right) dA_{in}, \end{aligned} \quad (3.5.13)$$

where $c_j^{in^2}$ (mol m⁻³) is the solute concentration at the inlet face of chamber 2. Now, with α given by (3.5.12), combining (3.5.11) and (3.5.13) gives

$$\begin{aligned} & \int_{A_{in}} \mathbf{n} \cdot \left(-D_j \nabla c_j^{in^2} + \mathbf{u}^{in^2} c_j^{in^2} \right) dA_{in} \\ & \approx \int_{A_{in}} \mathbf{n} \cdot \left(-D_j \nabla c_j^{in^1} + \mathbf{u}^{in^1} c_j^{in^1} \right) dA_{in} - \alpha. \end{aligned} \quad (3.5.14)$$

A few simplifications can be made to (3.5.14) so that $c_j^{in^2}$ may be quickly estimated. Firstly, assuming the inlet concentrations are constant, the gradient of the solute concentration across the face of each chamber inlet is equal to zero, i.e.

$$\nabla c_j^{in^1} = \nabla c_j^{in^2} = 0.$$

This suggests that the diffusive components of the fluxes may be neglected, an appropriate assumption in a convection-dominated system. Thus, (3.5.14) simplifies to

$$c_j^{in^2} \int_{A_{in}} \mathbf{u}^{in^2} \cdot \mathbf{n} dA_{in} \approx c_j^{in^1} \int_{A_{in}} \mathbf{u}^{in^1} \cdot \mathbf{n} dA_{in} - \alpha. \quad (3.5.15)$$

Now, since the fluid dynamics do not vary substantially between connected chambers (as established in §3.4.1), it is reasonable to assume that the velocity profiles at the inlet to each chamber are the same, i.e. $\mathbf{u}^{in^1} = \mathbf{u}^{in^2}$, and hence

$$\int_{A_{in}} \mathbf{u}^{in^1} \cdot \mathbf{n} dA_{in} = \int_{A_{in}} \mathbf{u}^{in^2} \cdot \mathbf{n} dA_{in}.$$

Then, (3.5.15) becomes

$$c_j^{in^2} \approx c_j^{in^1} - \frac{\alpha}{\int_{A_{in}} \mathbf{u}^{in^1} \cdot \mathbf{n} dA_{in}} = c_j^{in^1} - \frac{\alpha}{Q},$$

where Q is the input flow rate in m³ s⁻¹. By repeating this process, it may readily be shown that for n chambers,

$$c_j^{in^n} \approx c_j^{in^1} - \frac{(n-1)\alpha}{Q}. \quad (3.5.16)$$

Therefore, the inlet concentration in chamber n may be estimated using (3.5.16), and substituting this expression into (3.5.10) gives

$$c_j^n(y) \approx c_j^1(y) - \frac{(n-1)\alpha}{Q}. \quad (3.5.17)$$

Thus, given that the cell surface solute concentration profile in chamber 1 is known, metabolism is approximately constant, the diffusive fluxes at the inlet to each chamber are negligible and the velocity profiles at the inlet to each chamber are the same, (3.5.17) may be used to predict the cell surface solute concentration profile in chamber n . It is noted that this equation may be generalised to provide a prediction of the solute concentration profile across the entire cell surface, but for simplicity, only the profile across the centre of the cell surface is considered here.

To demonstrate the utility of (3.5.17), results are presented for O_2 using rat cardiomyocytes as an example cell type, since it has already been established that the assumption of constant metabolism is valid for a wide range of parameter values for this solute and cell type. Fig. 3.5.5 illustrates that the remaining assumptions are valid for an example input flow rate of $Q = 100 \mu\text{l min}^{-1}$, and it has been verified that similar trends may be observed for other input flow rates. First, the values for the total flux and the convective flux at the inlet to each chamber are compared (Fig. 3.5.5, left). Since these values are not significantly different, it is reasonable to assume that the diffusive component of the flux provides a minimal contribution to the total flux and can therefore be neglected. Next, the velocity profiles at the inlet to each chamber are compared (Fig. 3.5.5, right), and as expected, the fluid dynamics do not differ dramatically between chambers.

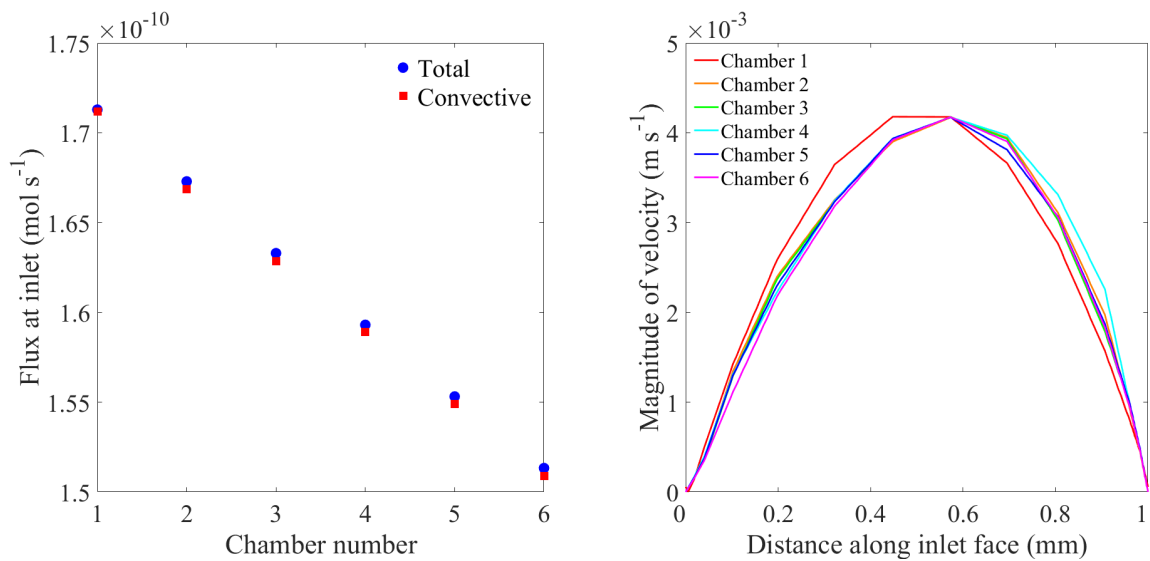


Figure 3.5.5: Comparison of the total and convective fluxes at the inlet to each chamber (left) and the velocity profiles along the diameter (from bottom to top) of each chamber inlet (right), for $Q = 100 \mu\text{l min}^{-1}$.

With all assumptions satisfied, (3.5.17) may now be used to provide predictions of the O_2 concentration profiles at the cell surface in downstream chambers. For an inlet concentration of $c_{O_2}^{in} = 0.21 \text{ mol m}^{-3}$, Fig. 3.5.6 displays the simulated cell surface O_2 concentration profiles in each chamber for a selection of input flow rates. Results beyond $Q = 700 \mu\text{l min}^{-1}$ are omitted since, as previously shown, increasing the input flow rate beyond this value does not substantially alter the distribution of the solute. It is further noted that, although the amount of solute metabolised in each chamber is the same across all input flow rates, the depletion of O_2 reduces as input flow rate increases as a consequence of more O_2 being delivered to downstream chambers. Thus, since the cell surface O_2 concentration profiles do not vary considerably between connected chambers for the higher input flow rates, the use of (3.5.17) may be more valuable in cases where the depletion of solute is more apparent, such as for the lower input flow rates. Predictions of the cell surface O_2 concentration profiles in chambers 2 to 6 were made using (3.5.17), as illustrated by the dashed lines in Fig. 3.5.6. For all input flow rates, agreement with the simulated results is excellent, with the strongest predictions observed for the higher input

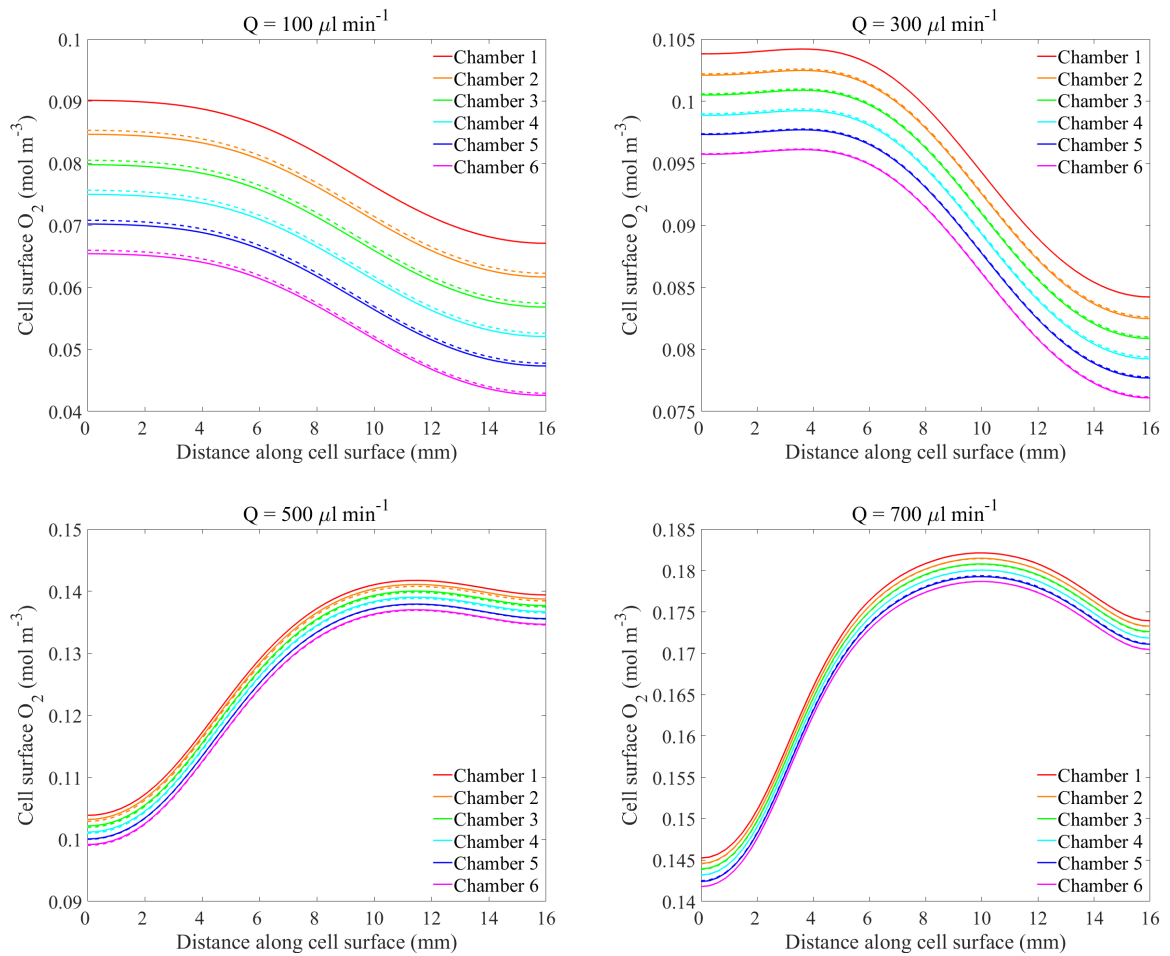


Figure 3.5.6: Comparison between simulated (solid lines) and predicted (dashed lines) cell surface O_2 concentration profiles for $c_{O_2}^{in} = 0.21 \text{ mol m}^{-3}$ and $Q = 100 \mu\text{l min}^{-1}$ (upper left), $Q = 300 \mu\text{l min}^{-1}$ (upper right), $Q = 500 \mu\text{l min}^{-1}$ (lower left) and $Q = 700 \mu\text{l min}^{-1}$ (lower right).

flow rates where the assumption of constant metabolism is more accurate. It has also been verified that, in a similar way to (3.5.9) for a single chamber, (3.5.17) allows for the prediction of the mean cell surface O_2 concentration in downstream chambers (data not shown).

Equations (3.5.7) and (3.5.17) may potentially be used in conjunction with one another, thus increasing their usefulness. For example, a situation could arise where the cell surface solute concentration in chamber 1, $c_j^1(y)$, has been simulated or experimentally measured for a given inlet concentration. As demonstrated above, (3.5.17) can be used to obtain predictions of the cell surface solute concentration in the remainder of the connected chambers. If the predicted concentrations are found to be inappropriate for the purposes of the given experiment, it may be necessary to alter the inlet concentration in the first chamber. In this scenario, (3.5.7) can be used to predict how the cell surface solute concentration will vary in chamber 1 if the inlet concentration is adjusted. This will provide a new $c_j^1(y)$ that can be used in (3.5.17) to obtain estimates of the cell surface solute concentration in downstream chambers for the new inlet concentration, without requiring any extra simulations or experimentation. Using this approach could greatly reduce the amount of trial and error that is required to optimally configure experiments for which the desired cell surface solute concentration is known.

3.5.2 Challenges associated with mathematical modelling

Although mathematics is clearly a valuable asset for aiding in the set-up of experiments, there are also a number of challenges associated with modelling, namely in relation to parameter values and model validation. The models presented in this chapter, as well as the simple relationships derived in §3.5.1, depend on the knowledge of reliable parameter values that relate to physical processes such as diffusion, binding and metabolism. Whilst such parameters are of key interest from a mathematical perspective, they are rarely the main focus of experiments, so processes such as diffusion are not often routinely measured. This means that limited data exists for use in mathematical models, and it is common to find discrepancies in parameter values since these are typically obtained from a variety of data sets where different measurement techniques have been used under different experimental conditions. It is important to have confidence in the accuracy of the input parameters, particularly if the model is to be used in a predictive sense, since quantitative results will be affected by the values of parameters such as diffusion coefficients and metabolic rates.

Intrinsically linked to the challenge of obtaining accurate parameter values is the problem of model validation. In order to confidently use the mathematical model in a predictive capacity, the results must be validated by comparison with experimental data, but as alluded to above, it is common that the quantities predicted by the mathematical model are not typically measured in an experimental setting. This means there is a lack of data with which to make a like-for-like comparison between simulation and experimentation, which is essential for verifying that the model accurately captures the cell culture environment. Therefore, interdisciplinary

communication is vital for ensuring that, not only are models developed with the needs of the experimental researcher in mind, but also that relevant quantities are experimentally measured so that model validation can be completed.

Whilst inconsistencies in model parameters can present an obstacle, this does not negate the usefulness of mathematical models. In particular, the results discussed in this chapter show that the same general trends can be observed even if key parameter values vary; for example, there is a similar relationship between input flow rate and cell surface solute concentration, regardless of cell type. Furthermore, although the limited availability of experimental data somewhat hinders the model validation process, it also highlights one of the main advantages of mathematical modelling, in that insight can be provided into quantities that are either difficult or impossible to obtain experimentally, such as flow patterns or concentration gradients.

Chapter 4

Informing experimental set-up in the Kirkstall QV900 for two different applications

Arguably one of the greatest advantages of mathematical modelling is that it can be used as part of a multidisciplinary approach to drive scientific advances across a broad range of applications. Here, the research area of interest is cell culture, where mathematics can be used to predict the outcome of experiments *a priori* and provide insight into key parameters that are challenging to obtain empirically. In cases where the desired cell culture conditions are known, this allows for the more efficient tailoring of experimental set-up since multiple combinations of input parameters can be trialled computationally before the final configuration is chosen. Furthermore, the information provided by mathematical modelling is often supplementary to the results of experimental assays which are typically performed to assess cellular behaviour and function, with little attention paid to the environment to which those cells are exposed. This is an area that mathematics excels in, offering insight into features such as flow patterns and shear stress levels that can be used to interpret and gain a deeper understanding of the experimental results.

The work presented in this chapter makes use of the mathematical models developed in Chapter 3 to guide the experimental configuration of the Kirkstall QV900 bioreactor system. The first section reminds the reader of the model equations described in detail in Chapter 3, and outlines how the model may be adapted to match the experimental conditions proposed by two groups of collaborators, who each used the device for different applications. In their respective sections (§4.2 and §4.3), a short introduction to each research area of interest is provided, followed by a description of the mathematical modelling and experimentation undertaken for each project. Briefly, the first group, led by Parveen Sharma of the University of Liverpool, sought to replicate the phenomenon known as liver zonation in an *in vitro* environment, whereas the second group, headed by Simon Croft of the London School of Hygiene and Tropical Medicine, aimed to study the effect of fluid flow on the process of parasite infection.

4.1 Overview of the mathematical modelling

In this chapter, the aim of the mathematical modelling is to determine how the Kirkstall QV900 system should be configured so that the desired cell culture conditions can be achieved for each set of experiments. The most intuitive way of controlling the environment within the chambers is to adjust the input flow rate and/or the inlet concentration; however, for the applications mentioned in this chapter, the choice of input flow rate was somewhat limited by the settings available on the equipment, and the inlet O_2 concentration was restricted to being fixed at atmospheric levels, as is common in many *in vitro* experiments. Since the results from Chapter 3 indicate that the flow patterns and speeds vary with chamber depth, and the solute concentrations observed throughout the chamber are not uniformly distributed, in this chapter the spatial placement of the cells within the chamber is explored as an additional means of controlling the environment to which the cells are exposed. Specifically, the depth at which the cells reside is investigated as an option for tailoring the cell culture conditions to meet the requirements of the experiment at hand. Practically, this can be achieved by placing custom-built inserts (fabricated via 3D printing) at the base of the chamber, effectively reducing the chamber depth and thus raising the position of the cells.

For each application, the computational geometry described in Chapter 3 was adapted to match the experimental conditions. Briefly, in both cases, the base of the chamber was altered to account for the cells being cultured on a cover slip. To incorporate the presence of a depth-reducing insert within the chamber, the geometry was adjusted by simply decreasing the overall height of the chamber by h , the height of the insert, assuming that no fluid can occupy the volume beneath the insert. A detailed illustration of the computational geometry used for each application will be shown in subsequent sections.

Simulations were performed in COMSOL Multiphysics® to characterise the fluid flow and solute transport over a range of h values. For a full description of the governing equations, initial conditions and boundary conditions, the reader is referred back to Chapter 3. To recap, the fluid dynamics are described via the continuity equation and steady Navier-Stokes equations. Initially, the fluid velocity is equal to zero. A parabolic velocity profile is applied at the inlet, zero pressure is prescribed at the outlet, and no slip and no penetration conditions are imposed on the walls of the chamber. In this chapter, the solute of most interest is O_2 , and its transport is described via steady convection and diffusion. Initially, the O_2 concentration is equal to zero within the chamber. A constant supply of O_2 is provided at the inlet, a convective flux is imposed at the outlet, and a zero flux condition is applied on the chamber walls. Here, the interaction between the O_2 and the cells is represented by a flux boundary condition imposed on the area covered by the cells, with the metabolism of O_2 described via one Michaelis-Menten (M-M) reaction term. For clarity, the governing equations, boundary conditions and initial conditions are summarised on page 111, alongside a schematic drawing of the computational geometry.

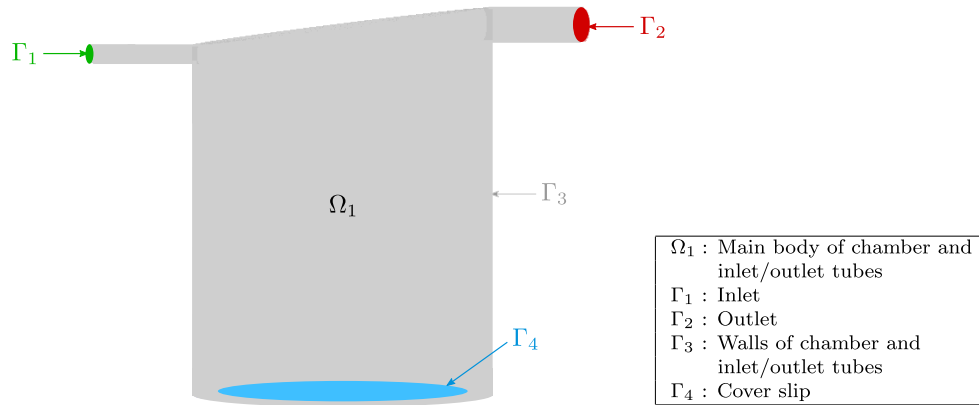


Figure 4.1.1: Schematic drawing of the computational geometry for a single QV900 chamber where the cells reside on a cover slip at the base of the chamber. Here, Ω and Γ are used to label domains and boundaries, respectively.

$$\begin{aligned}\nabla \cdot \mathbf{u} &= 0 \text{ in } \Omega_1, \\ \rho(\mathbf{u} \cdot \nabla) \mathbf{u} &= -\nabla p + \mu \nabla^2 \mathbf{u} \text{ in } \Omega_1, \\ (\mathbf{u} \cdot \nabla) c_{O_2} &= D_{O_2} \nabla^2 c_{O_2} \text{ in } \Omega_1,\end{aligned}$$

with the following boundary conditions

$$\begin{aligned}u(r) &= \frac{2Q}{\pi a^2} \left(1 - \frac{r^2}{a^2}\right) \text{ on } \Gamma_1, \\ p &= 0 \text{ on } \Gamma_2, \\ \mathbf{u} &= \mathbf{0} \text{ on } \Gamma_3, \Gamma_4, \\ c_{O_2} &= c_{O_2}^{in} \text{ on } \Gamma_1, \\ -\mathbf{n} \cdot D_{O_2} \nabla c_{O_2} &= 0 \text{ on } \Gamma_2, \\ \mathbf{n} \cdot (-D_{O_2} \nabla c_{O_2} + \mathbf{u} c_{O_2}) &= 0 \text{ on } \Gamma_3, \\ \mathbf{n} \cdot (-D_{O_2} \nabla c_{O_2} + \mathbf{u} c_{O_2}) &= \frac{V_{O_2} c_{O_2}}{K_{O_2} + c_{O_2}} \text{ on } \Gamma_4,\end{aligned}$$

and initial conditions

$$\begin{aligned}\mathbf{u} &= \mathbf{0} \text{ in } \Omega_1 \text{ at } t = 0, \\ c_{O_2} &= 0 \text{ in } \Omega_1 \text{ at } t = 0.\end{aligned}$$

4.2 Application to liver zonation

As discussed in Chapter 1, the development of a new drug involves several stages, and all compounds must undergo a series of tests designed to prove efficacy and safety prior to approval for use in humans. The traditional approach was to perform animal testing as a precursor to clinical trials, but it is now widely accepted that animal studies are poorly predictive of the human response due to species differences in vital processes such as absorption, distribution, metabolism and elimination [18, 75]. Thus, modern research in the pharmaceutical industry has been directed towards improving the preclinical stage of drug development, with particular focus on producing more physiologically relevant results through the use of *in vitro* studies.

Despite recent advances in this area, only a small proportion of potential drugs are granted approval, and it is not uncommon for ‘safe’ drugs to be subsequently withdrawn from the market due to the presence of previously unknown adverse effects [18, 75]. This can be attributed to the fact that many standard *in vitro* methods fail to adequately emulate the native *in vivo* environment, providing a misleading understanding of long-term drug safety and toxicity. Drug-induced liver injury is responsible for the majority of drug recalls [75] and poses a major human health concern, with an associated mortality rate of around 10% [76]. As the primary organ for the metabolism of foreign substances, it is essential that the role of the liver is accurately represented *in vitro*.

The liver has a highly complex architecture: repeating units of cells, or lobules, surround a central vein that is supplied with blood from the hepatic artery and portal vein by vessels called sinusoids [18, 77]. As illustrated in Fig. 4.2.1, the sinusoid can be split into three main zones: periportal, central and perivenous. Hepatocytes located along the length of the liver sinusoid are exposed to varying concentrations of O_2 , nutrients, hormones and metabolites, contributing to a phenomenon known as liver zonation [18, 77, 78]. In particular, it is believed that the O_2 gradients generated as a result of the dynamic environment within the liver give rise to variations in the metabolic functionality of hepatocytes located in different zones of the sinusoid [57, 78].

Existing studies in the literature have modelled liver zonation within hollow fibre bioreactors [79] and spheroids [80, 81], aiming to improve upon standard cell culture methods where hepatocytes are often considered as a homogeneous cell population, with traditional static conditions and a lack of concentration gradients resulting in a loss of zone-specific functionality [33, 75]. Here, the aim of this study was to generate a more physiologically relevant cell culture environment by introducing fluid flow via the QV900 bioreactor system. Cells were cultured in three separate chambers and exposed to varying concentrations of O_2 in order to represent the three main zones of the liver sinusoid, and several tests were performed to confirm the existence of zonation. Prior to experimentation, the mathematical model was used to predict the O_2 concentrations at the cell surface within chambers containing inserts of various heights, and a recommendation for the insert heights that should be used to generate a realistic O_2 gradient across the three chambers was provided to the experimental team.

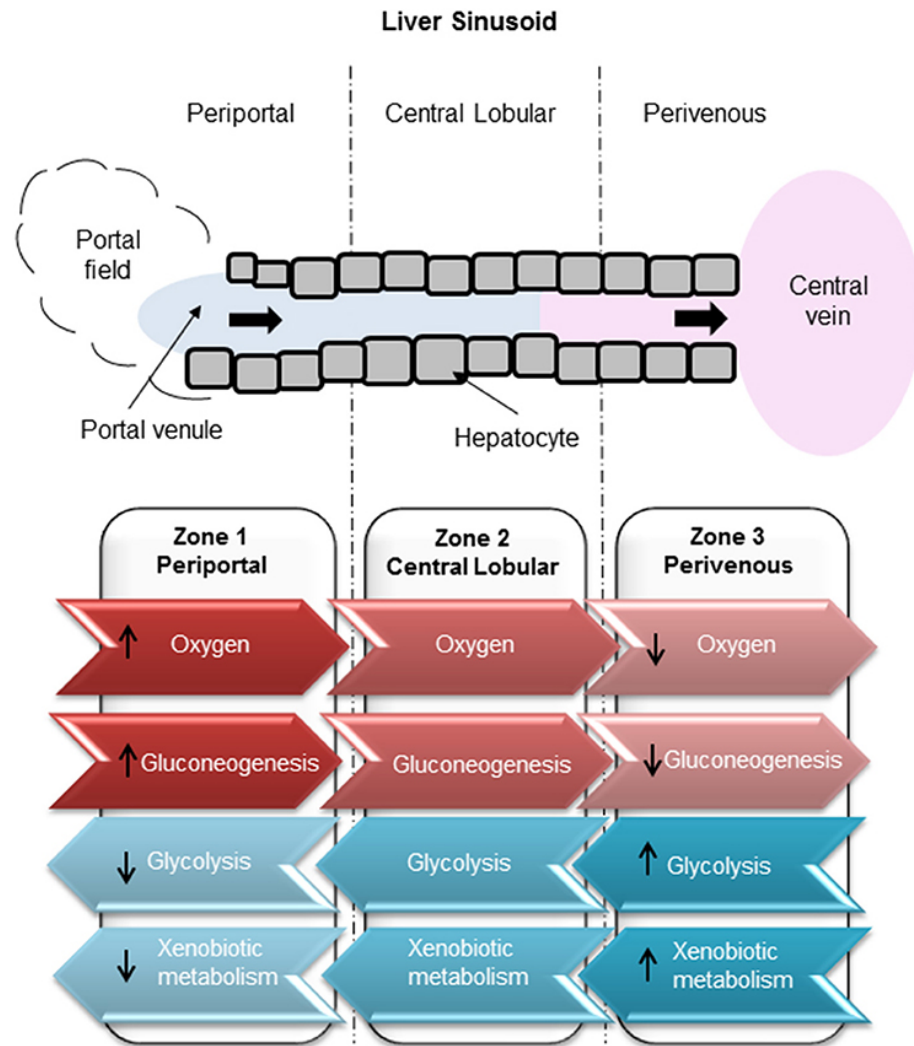


Figure 4.2.1: Zonation of liver metabolism. High oxygen exposure of hepatocytes in the periportal region compared to low exposure in the perivenous zone. Glucose production carried out through gluconeogenesis in the periportal zone. Glucose utilisation carried out by glycolysis in the perivenous zone. [2]

4.2.1 The mathematical model

For this work, the mathematical model was employed to simulate the O_2 transport within QV900 chambers that had their depth modified by the addition of an insert. An estimation of the cell surface O_2 concentration was provided for each chamber depth and compared with the O_2 gradient expected to arise in the human liver. Whilst there are some minor discrepancies in the values reported in the literature (e.g. [61, 78, 82, 83]), it is generally accepted that the O_2 concentration varies from approximately $0.04 - 0.15 \text{ mol m}^{-3}$ [60]. Based on these values, the final insert heights were chosen such that a physiologically relevant gradient of O_2 was created from the first chamber, designed to represent the periportal zone where the O_2 concentration is highest, to the third chamber, designed to represent the perivenous zone where the O_2 concentration is lowest.

Computational geometry

The computational geometry was created by modifying the existing single chamber geometry (shown in Fig. 3.3.2) to align with the proposed experimental conditions. Here, the cells were to be cultured on a cover slip of diameter 13 mm, so an additional circular area was added to the base of the chamber to account for this, as illustrated in Fig. 4.2.2. The first simulations were performed assuming that no insert was present, thus using the original chamber height. For subsequent simulations, the computational geometry was altered by decreasing the overall height of the chamber in 1 mm increments to represent the reduction in chamber depth due to the addition of an insert of height h .

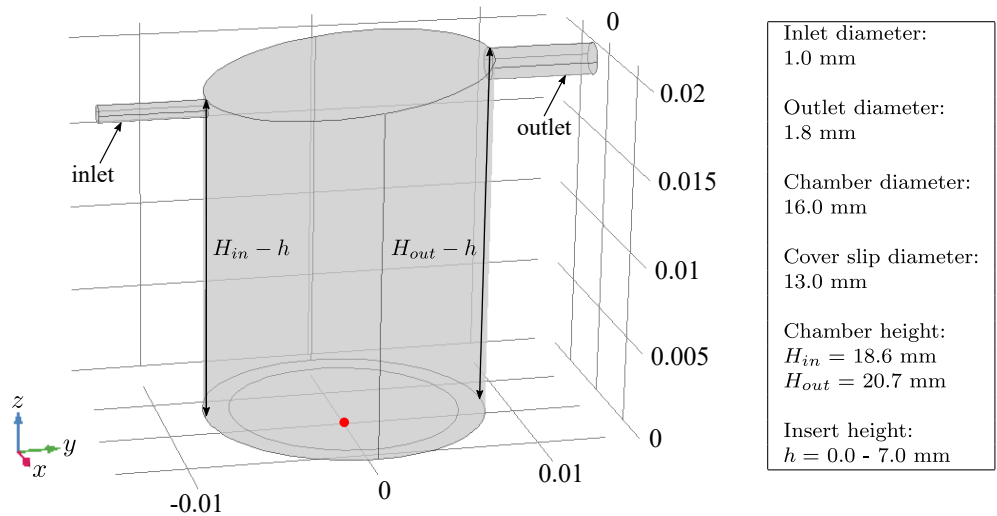


Figure 4.2.2: Idealised 3D representation of a single QV900 chamber generated in COMSOL Multiphysics[®] 5.3, showing the orientation of the x -, y - and z - axes with the origin located at the centre of the base of the chamber (indicated by the red dot). Here, H_{in} and H_{out} denote the height of the chamber at the inlet side and the outlet side, respectively, and h is the height of the insert. Note that length scales on the axes are in metres.

Numerical implementation

The governing equations, boundary conditions and initial conditions shown on page 111 were implemented in COMSOL Multiphysics[®] using the built-in ‘Laminar Flow’ and ‘Transport of Diluted Species’ modules to characterise the fluid flow and O_2 transport, respectively. As in Chapter 3, the computational geometry was simplified by imposing a symmetry boundary condition on the y, z plane passing through the origin in order to reduce computation time. For each insert height, the geometry was then discretised using the built-in ‘Finer’ mesh setting, in line with the results of the mesh sensitivity study described in §3.3.3. A stationary solver was employed to provide the steady-state solution to the model equations, with the solver settings automatically optimised by COMSOL (refer to §3.3.3 for details). Table 4.1 lists the number of mesh elements and the typical simulation time for each value of h .

<i>Insert height (mm)</i>	<i>Number of mesh elements</i>	<i>Typical simulation time</i>
0	314,827	3 mins 21 secs
1	355,072	4 mins 38 secs
2	337,419	4 mins 23 secs
3	363,633	4 mins 43 secs
4	333,817	3 mins 44 secs
5	277,906	3 mins 54 secs
6	299,429	3 mins 54 secs
7	303,725	3 mins 14 secs

Table 4.1: Number of mesh elements and typical simulation time for each insert height using a quad core Intel® Core™ i7-6700 CPU @ 3.40GHz.

The parameter values used in the simulations are listed in Table 4.2. The properties of the culture medium are assumed to be consistent with those of water, so the values of the fluid density, ρ , and dynamic viscosity, μ , were chosen to reflect this, using a temperature of 37°C to match the experimental conditions. The values of Q and $c_{O_2}^{in}$ were fixed to represent the input flow rate and inlet O₂ concentration used in the experiments. The maximum rate of O₂ metabolism, V_{O_2} , relates to the chosen cell type, primary rat hepatocytes, and it is noted that for this parameter, it was necessary to adjust the value reported in the literature by multiplying the metabolic rate by the cell density, d . The cell density refers to the ratio of the total cell number to the area covered by the cells: it was advised by the experimental team that the cell number, N , should be equal to 20% of the total number of cells seeded during the initial cell culture, and the area covered by the cells, A , was calculated by assuming that the cells occupy the entire circular cover slip of diameter 13 mm.

<i>Parameter</i>	<i>Description</i>	<i>Value</i>	<i>Ref.</i>
ρ	Density of fluid	$9.94 \times 10^2 \text{ kg m}^{-3}$	[66]
μ	Dynamic viscosity of fluid	$6.89 \times 10^{-4} \text{ Pa s}$	[66]
D_{O_2}	Diffusion coefficient for O ₂	$3.00 \times 10^{-9} \text{ m}^2 \text{ s}^{-1}$	[60]
Q	Input flow rate	$150 \text{ } \mu\text{L min}^{-1}$	*
$c_{O_2}^{in}$	Inlet concentration for O ₂	0.21 mol m^{-3}	[60]
V_{O_2}	Maximum metabolic rate for rat hepatocytes	$7.20 \times 10^{-8} \text{ mol m}^{-2} \text{ s}^{-1}$	[71]
K_{O_2}	Michaelis-Menten constant	$6.60 \times 10^{-4} \text{ mol m}^{-3}$	[60]
N	Total number of cells	2.00×10^5	†
A	Area covered by the cells	$1.33 \times 10^{-4} \text{ m}^2$	‡
d	Cell density	$1.50 \times 10^9 \text{ m}^{-2}$	**

Table 4.2: Parameter values. *Input flow rate used in experiments. †Cell number chosen assuming 20% of 1 million hepatocytes attach to the cover slip during cell culture. ‡Area covered by the cells on a 13 mm diameter cover slip. **Cell density calculated by dividing the total number of cells by the area covered by the cells ($d = N/A$).

Results

Based on the observations made in Chapter 3, where the results for solute distribution indicate that concentration decreases as chamber depth increases, it is expected that a shallower chamber should give rise to higher cell surface concentrations. From Fig. 4.2.3, it is clear that the O_2 concentration to which the cells are exposed does indeed increase as chamber depth decreases, or equivalently, as insert height increases. The simulations performed with no insert, i.e. $h = 0$ mm, provide a baseline from which the cell surface concentration can only increase. With a minimum O_2 concentration of approximately 0.04 mol m^{-3} , this configuration was selected to represent the perivenous zone in correspondence with the lower limit of the desired O_2 range.

Evident from the profiles displayed in Fig. 4.2.3, the O_2 concentration at the cell surface is not uniform: a gradient of O_2 is generated within the chamber for each insert height, with a variation of approximately 0.06 mol m^{-3} observed across the cell surface for all values of h . In order to estimate the average availability of O_2 to the cells, the mean cell surface concentration was calculated for each insert height (see Table 4.3) and these values were then used to determine the configuration for the remaining chambers. Providing a mean cell surface O_2 concentration of 0.15 mol m^{-3} , an insert height of $h = 7$ mm was selected as the best option for representing the periportal zone, whilst an intermediary insert height of $h = 4$ mm was deemed appropriate for representing the central zone.

It is important to acknowledge that using an insert to amend the depth of the chamber has a significant impact on not only the O_2 concentrations, but also the fluid dynamics observed within the chamber. As shown in Table 4.3, the shear stress to which the cells are exposed

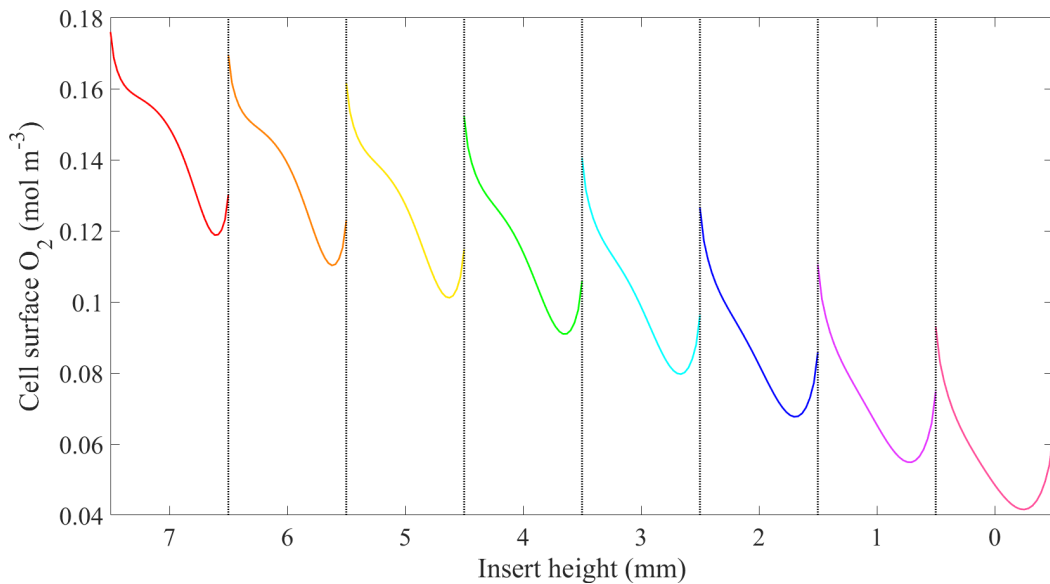


Figure 4.2.3: Simulated cell surface O_2 concentration profiles for each value of h . For each insert height, the concentration profiles are plotted across the diameter of the cover slip from the inlet to the outlet side of the chamber (left to right).

<i>Insert height (mm)</i>	<i>Mean cell surface O_2 (mol m^{-3})</i>	<i>Max. cell surface shear stress (Pa)</i>
0	0.06	9.02×10^{-8}
1	0.07	1.96×10^{-7}
2	0.09	3.63×10^{-7}
3	0.10	6.23×10^{-7}
4	0.12	1.01×10^{-6}
5	0.13	1.57×10^{-6}
6	0.14	2.38×10^{-6}
7	0.15	3.50×10^{-6}

Table 4.3: Mean O_2 concentration and maximum shear stress observed at the cell surface for each insert height.

increases with increasing insert height. Like most cell types, hepatocytes are highly sensitive to mechanical stimuli in their environment, and retention of optimal cell health and function depends on appropriate levels of shear stress. It has been reported that hepatocytes can continue to function under shear stress levels of the order of 10^{-5} Pa, whilst cells overlaid with collagen can tolerate much higher shear stress levels of the order of 10^{-2} Pa [33]. Here, for each insert height, the cell surface shear stress values are estimated to be of the order of 10^{-6} Pa or lower, so it is not expected that the flow environment will damage the cells.

An illustration of the predicted O_2 concentration gradient that could be achieved across three chambers under the recommended configuration is shown in Fig. 4.2.4, using insert heights of $h = 7, 4$ and 0 mm to represent the periportal, central and perivenous zones, respectively. It is

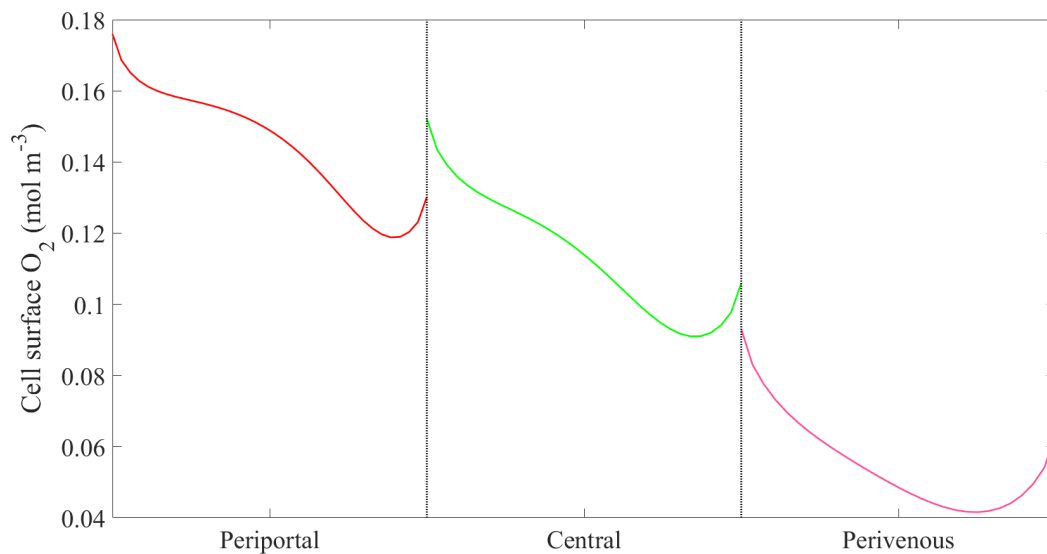


Figure 4.2.4: Simulated O_2 concentration profiles across the centre of the cell surface for $h = 7$ mm (periportal), $h = 4$ mm (central) and $h = 0$ mm (perivenous), illustrating the estimated O_2 gradient that could be achieved across three QV900 chambers.

noted that due to the complex fluid environment within each chamber, it is impossible to generate a perfectly linear concentration gradient from exactly $0.04 - 0.15 \text{ mol m}^{-3}$, a range of values whose true magnitude is somewhat uncertain in the literature. Thus, the aim here was not to accurately predict the specific quantity of O_2 at the cell surface, but rather, the true purpose of the mathematical model was to demonstrate that it is possible to manipulate the experimental set-up such that different cell culture conditions can be created within each chamber. The final recommendation for the height of the inserts was made with the anticipation that this configuration would elicit a more physiologically relevant response from the cells than that observed in a standard static environment; this was tested by the experimental team.

4.2.2 The experiments

Primary rat hepatocytes were cultured in a sandwich formation on 13 mm cover slips at a density of 1 million cells per well in a standard 24-well plate. The cover slips were then transferred to three separate QV900 chambers configured to represent the periportal, central and perivenous zones (illustrated in Fig. 4.2.5), as recommended by the mathematical model. After running the flow system for 72 hours, a series of assays were conducted to determine the health and metabolic function of the cells in each chamber, and to ascertain whether any zone-specific behaviour was achieved. Here, the results of each assay are discussed, with the reader directed to [2] for a comprehensive overview of the methods used to carry out each procedure.

Adenosine triphosphate (ATP), a source of energy found in all living cells, is an established biomarker of cell viability, where ATP concentration positively correlates with the number of healthy cells. Therefore, ATP levels were measured to determine the viability of the cell culture in each chamber, with a higher expression of ATP being observed in the periportal chamber when compared to the perivenous chamber (see Fig. 4.2.6A). It is noted that the estimated shear stress levels provided by the mathematical model suggest that the fluid environment should

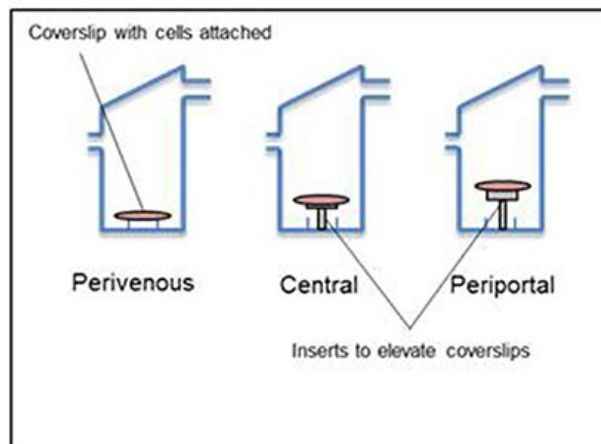


Figure 4.2.5: Schematic setup on the inside of the QV900 wells. [2]

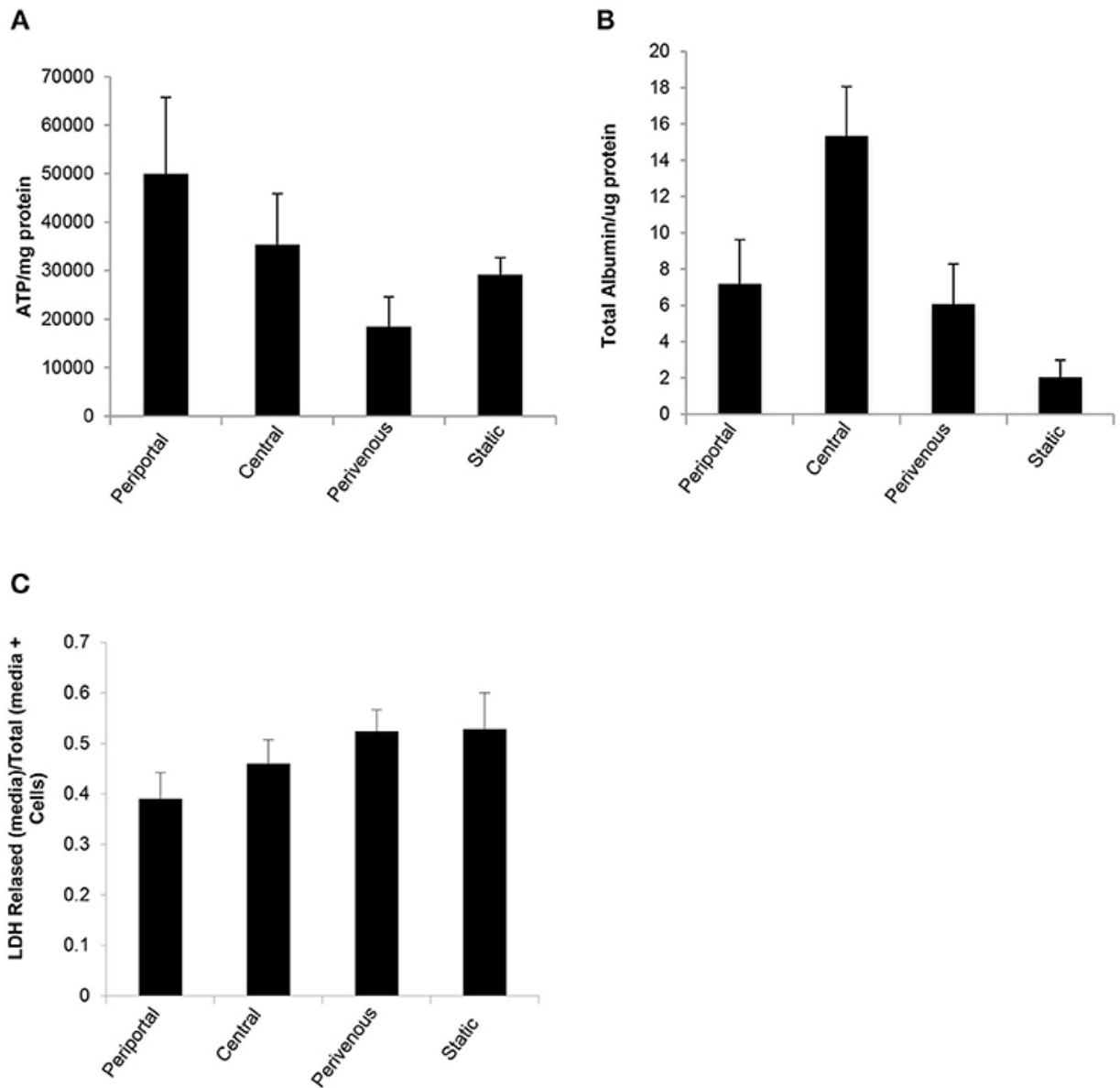


Figure 4.2.6: Functional analysis of primary rat hepatocytes in each zone compared to standard 2D static conditions. After 48 h under flow conditions or static conditions functional parameters were assessed (**A**) ATP ($n = 4$), (**B**) Albumin secretion ($n = 4$). Both were normalised to protein concentration calculated using a Bradford assay, and (**C**) Cytotoxicity of shear stress analysed by LDH assay. Data shown as LDH released (in media)/Total LDH (present in cells + media). [2]

be suitable for maintaining a healthy cell population, but to account for the possibility of cell loss, either from apoptosis or due to cells being swept away by the flow, ATP concentrations were normalised with respect to protein count. This means that the variation in ATP levels observed between the chambers must be due to differences in the metabolic functionality of the cells, rather than cell loss, pointing to the achievement of zone-specific behaviour.

To further assess the health of the cells, albumin production was evaluated in each chamber (see Fig. 4.2.6B). Synthesised by healthy liver cells, low levels of this protein serve as an indicator of potential cell damage. A marked increase in albumin production was observed in each of the flow chambers when compared to the static culture, verifying that the cells remained healthy and functional when subjected to fluid flow.

To confirm that the flow-induced shear stress did not harm the cell population, lactate dehydrogenase (LDH) levels were measured in each chamber (see Fig. 4.2.6C). Analysis of this biomarker of liver damage is a standard method for evaluating cell death, and it was found that no additional LDH was released by the cells in each of the flow chambers when compared to the static culture. This indirectly validates the shear stress predictions provided by the mathematical model: although specific shear stress values were not quantified experimentally, the lack of an increase in LDH release suggests the cells remained stable, implying that the shear stress to which the cells were exposed was of an acceptable level, in agreement with the conclusions drawn from the mathematical model.

A Western blot analysis was carried out to measure the expression of various markers of zone-specific functionality and metabolism, where the visibility of each band reflects the detected levels of the protein of interest (see Fig. 4.2.7, left). It is clear that glutamine synthetase and CYP3A4 were more highly expressed in the perivenous chamber, whereas carbamoyl phosphate synthetase 1 and arginase 1 were more highly expressed in the periportal chamber. Measured as a control, β -actin was present in consistent levels across all three chambers as expected. The results of this assay demonstrate differential metabolic function across the three chambers that is representative of the *in vivo* environment.

Finally, paracetamol (APAP) was introduced to the flow system in order to monitor the effects of this known zone-specific toxin on the cells in each chamber (see Fig. 4.2.7, right). As expected, APAP elicited a toxic response from cells in both the perivenous and the periportal chambers, with normalised ATP levels decreasing after cells were exposed to the drug. The difference in ATP production between undosed and dosed cells was most significant in the perivenous chamber; this is in line with evidence that, *in vivo*, cells in the perivenous zone of the liver sinusoid are known to generate high levels of the enzyme that produces the toxic metabolite associated with the breakdown of APAP, leading to greater cell death. The considerable difference in the effect of APAP on the cells in each chamber verifies that a zone-specific drug response has been achieved in this flow system.

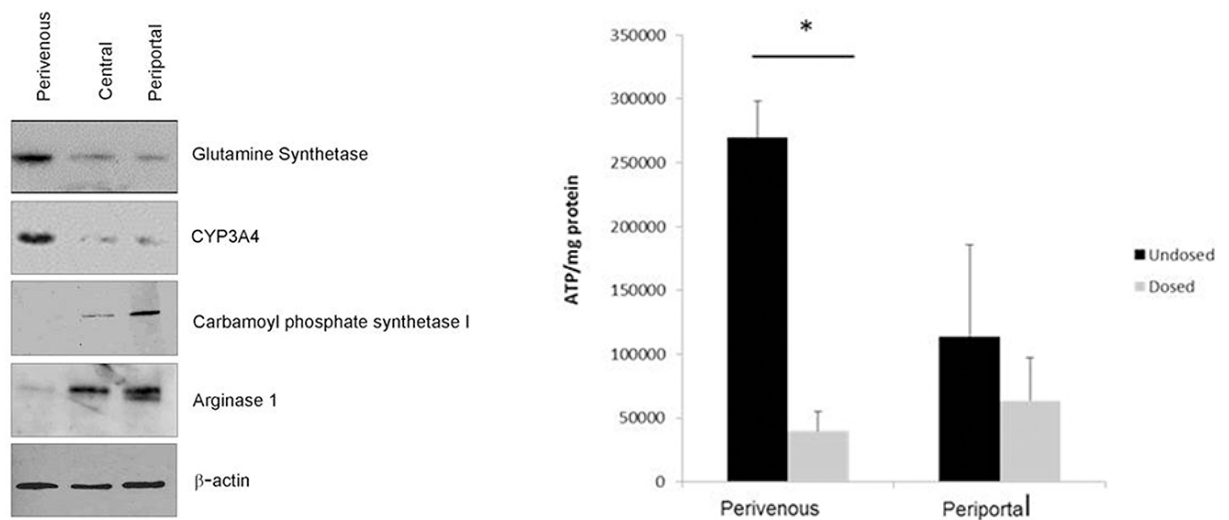


Figure 4.2.7: **Left:** Verification of zonation. Western blot analysis of zone specific protein markers. **Right:** Confirmation of zone specific metabolism. Cells were dosed with 50 mM paracetamol for 48 h. Viability (calculated using ATP assay) was normalised to protein concentration calculated using a Bradford assay. $n = 3$, student's test used for statistical analysis. $*p < 0.05$. [2]

4.2.3 Summary

In this study, it has been demonstrated that the mathematical model can be used to help configure the QV900 chambers such that hepatocytes remain viable under flow and retain zone-specific functionality. Here, the goal was to generate a physiologically relevant O_2 concentration gradient that would give rise to zonation, so it was essential to gain an understanding of the O_2 concentrations to which the cells would be exposed. Measurement of this key parameter is challenging, so in order to avoid a lengthy trial-and-error approach to optimise experimental design, the mathematical model was employed to estimate the cell surface O_2 concentrations. Experiments were performed using the recommended configuration provided by the mathematical model, and a series of assays evaluating cell health and metabolic function were used to confirm that a zone-specific cell response was achieved in the QV900 chambers.

4.3 Application to parasite infection

Transmitted to humans via the bite of sandflies, leishmaniasis is the name given to a group of infectious diseases caused by the parasite *Leishmania*. Parasites are transferred from the sandfly to the human host as extracellular promastigotes which become internalised by host macrophages. Within the host cell, the promastigotes transform into intracellular amastigotes which can multiply and subsequently infect additional host cells. There are two main types of leishmaniasis: the potentially fatal visceral form, and the more common cutaneous form. Endemic in over 70 countries, hundreds of millions of people worldwide are at risk from infection of cutaneous leishmaniasis; this form of the disease causes painful skin lesions that can persist for many

months, usually resulting in permanent disfiguration or even disability. The standard treatment for cutaneous leishmaniasis involves an invasive course of injections, and the recommended drugs are associated with serious side effects including renal failure and hepatotoxicity, which, if present, necessitate further medical attention. The cost of the initial drugs coupled with the expense of any additional healthcare means that few patients successfully complete their course of treatment. Therefore, it is vital that research is undertaken to improve the affordability and accessibility of treatment options, with a focus on developing new drugs that do not induce harmful side effects [84].

The majority of existing *in vitro* studies within the *Leishmania* field of research are performed using traditional static cell culture methods [85–87] which do not realistically represent the environment within the human body. Even within the skin, cells are exposed to slow-moving interstitial flow that occurs due to plasma leaking from blood vessels into the extracellular matrix [14]. These dynamic conditions promote the transfer of O_2 and nutrients, as well as facilitating interactions between the parasite and the host cell. Thus, the presence of fluid flow could ultimately have an impact on the infection process, so its inclusion is essential for increasing the relevance of results obtained from cell-based assays carried out during the preclinical stage of drug development.

The aim of this study was to assess the effect of fluid flow on the infection of macrophages by *Leishmania* parasites. In order to subject the cells to a physiologically relevant flow rate, the mathematical model was first used to estimate the flow speeds within QV900 chambers containing inserts of various heights. Based on these results, experiments were performed in six connected chambers under varying flow conditions, and tests were carried out to evaluate infection levels and monitor cell function. Using a computational representation of the final experimental set-up, a second set of simulations were performed to characterise the environment generated within the chambers, providing additional insight and possible explanations for the outcomes of the experiments.

4.3.1 The mathematical model

For this study, the first role of the mathematical model was to determine the insert height that would give rise to cell surface flow speeds corresponding to that of interstitial flow. The fluid dynamics within a single chamber were simulated for various h values, and the insert height was deemed suitable when flow speeds fell within the range of interstitial flow speeds reported in the literature; whilst the flow speeds to which infected cells are exposed remains unknown, it is widely accepted that $0.1 - 2 \mu\text{m s}^{-1}$ is representative of the flow speeds experienced within healthy skin [14]. The secondary purpose of the mathematical model was to predict the flow patterns, shear stress levels and O_2 concentrations within a computational geometry matching the chamber configuration used in the experiments.

Computational geometry

For the initial simulations performed in a single chamber, the computational geometry (see Fig. 4.3.1) is almost identical to that used in §4.2.1, except in this case, the cover slip has a diameter of 12 mm. To obtain a baseline for the cell surface flow speeds, the first simulations were performed using the original chamber height (i.e. assuming that no insert was present). The results of these simulations indicated that, under this configuration, the flow speeds to which the cells were exposed are much too low to be representative of interstitial flow. Therefore, rather than increasing the height of the insert incrementally from a starting point of $h = 0$ mm (as in §4.2.1), here an initial insert height of 5 mm was chosen, with the value of h then increasing in 1 mm increments for the remainder of the simulations.

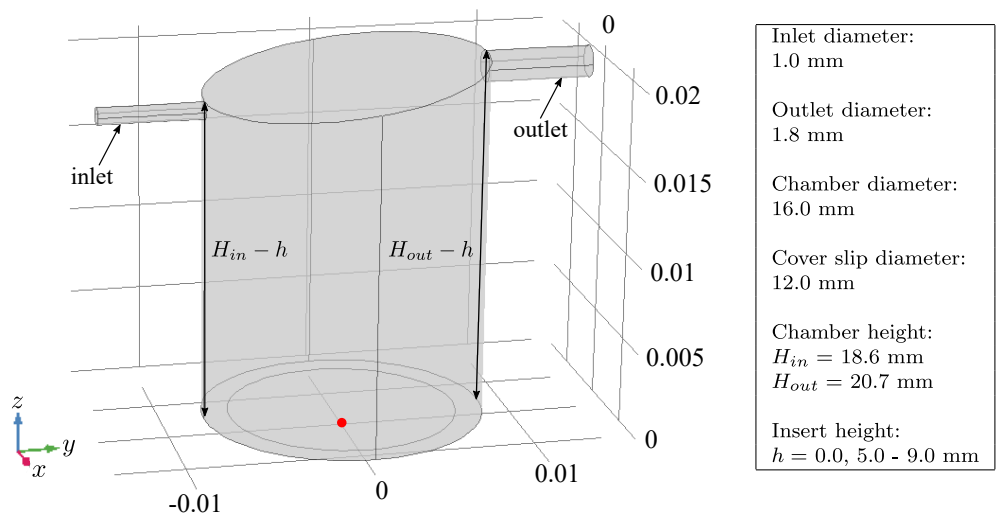


Figure 4.3.1: Idealised 3D representation of a single QV900 chamber generated in COMSOL Multiphysics[®] 5.3, showing the orientation of the x -, y - and z - axes with the origin located at the centre of the base of the chamber (indicated by the red dot). Here, H_{in} and H_{out} denote the height of the chamber at the inlet side and the outlet side, respectively, and h is the height of the insert. Note that length scales on the axes are in metres.

In the experiments, the QV900 system was to be configured such that all six chambers were connected in series, with the first three chambers remaining unmodified and the final three chambers containing an insert, the height of which was to be recommended by the results of the initial mathematical modelling. After an appropriate insert height was determined, an additional computational geometry was created to represent the final experimental set-up in order to provide a visualisation of the flow environment and concentration profiles within the final configuration. The connected chamber geometry (see Fig. 4.3.2) was generated by duplicating the single chamber geometry shown in Fig 4.3.1 using the method described in §3.3.2, and then adjusting the depth of the final three chambers to account for the presence of the inserts.

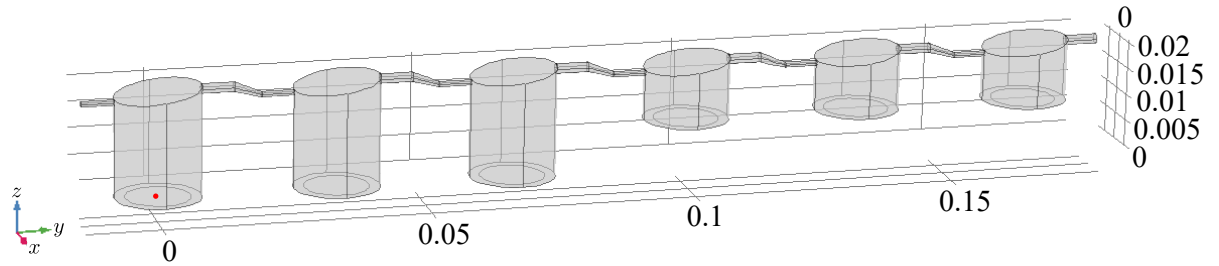


Figure 4.3.2: Idealised 3D representation of the final experimental configuration of six connected QV900 chambers generated in COMSOL Multiphysics[®] 5.3, showing the orientation of the x -, y - and z -axes with the origin located at the centre of the base of the first chamber (indicated by the red dot). Note that length scales on the axes are in metres.

Numerical implementation

The fluid flow in a single chamber, and the fluid flow and O_2 transport in connected chambers, are described by the governing equations, boundary conditions and initial conditions shown on page 111. As described in Chapter 3, when these equations are applied to the connected chamber geometry, the inlet and the outlet refer only to the inlet of the first chamber and the outlet of the last chamber, and it is assumed that flux and concentration are continuous across the interfaces between each chamber and connecting tube. As in §4.2.1, the ‘Laminar Flow’ and ‘Transport of Diluted Species’ modules were used to implement the fluid flow and O_2 transport equations in COMSOL, respectively. Again, each computational geometry was simplified by applying a symmetry boundary condition on the y, z plane, and the built-in ‘Finer’ mesh setting was then used to discretise both the single and connected chamber domains. In each case, the steady-state solution was obtained by solving the system using a stationary solver, the settings of which were automatically optimised by COMSOL. For a single chamber, the number of mesh elements and typical simulation time is listed in Table 4.4 for each insert height. The final number of mesh elements in the connected chamber geometry was 2,018,537 with a typical simulation time of 19 mins 25 secs.

<i>Insert height (mm)</i>	<i>Number of mesh elements</i>	<i>Typical simulation time</i>
0	263,139	2 mins 37 secs
5	277,334	2 mins 39 secs
6	299,072	2 mins 39 secs
7	303,648	2 mins 41 secs
8	308,106	2 mins 49 secs
9	297,381	2 mins 47 secs

Table 4.4: The number of mesh elements in a single chamber and the typical simulation time for each insert height using a quad core Intel[®] Core[™] i7-6700 CPU @ 3.40GHz.

Table 4.5 provides the parameter values used in the simulations. The values of ρ and μ refer to the density and dynamic viscosity, respectively, of water at 34°C, matching the temperature used in the experiments. The input flow rate and inlet O₂ concentration were also chosen to reflect the experimental conditions, and the maximum metabolic rate for the chosen cell type, macrophages, is given by V_{O_2} . In order to obtain this parameter in appropriate units, the value reported in the literature was multiplied by the cell density, d , which was calculated by dividing the total cell number, provided by the experimental team, by the area covered by the cells, computed by assuming the cells occupy the entire 12 mm diameter cover slip.

<i>Parameter</i>	<i>Description</i>	<i>Value</i>	<i>Ref.</i>
ρ	Density of fluid	$9.95 \times 10^2 \text{ kg m}^{-3}$	[66]
μ	Dynamic viscosity of fluid	$7.32 \times 10^{-4} \text{ Pa s}$	[66]
D_{O_2}	Diffusion coefficient for O ₂	$3.00 \times 10^{-9} \text{ m}^2 \text{ s}^{-1}$	[60]
Q	Input flow rate	$360 \text{ } \mu\text{L min}^{-1}$	*
$c_{O_2}^{in}$	Inlet concentration for O ₂	0.21 mol m^{-3}	[60]
V_{O_2}	Maximum metabolic rate for macrophages	$3.54 \times 10^{-9} \text{ mol m}^{-2} \text{ s}^{-1}$	[88]
K_{O_2}	Michaelis-Menten constant	$6.30 \times 10^{-3} \text{ mol m}^{-3}$	[89]
N	Total number of cells	4.00×10^5	†
A	Area covered by the cells	$1.13 \times 10^{-4} \text{ m}^2$	‡
d	Cell density	$3.54 \times 10^9 \text{ m}^{-2}$	**

Table 4.5: Parameter values. *Input flow rate used in experiments. †Number of cells used in experiments. ‡Area covered by the cells on a 12 mm diameter cover slip. **Cell density calculated by dividing the total number of cells by the area covered by the cells ($d = N/A$).

Results

The initial simulations in a single chamber were used to estimate the mean cell surface flow speeds for each insert height. As described in Chapter 3, the flow speed *on* the cell surface is equal to zero due to the application of the no slip and no penetration conditions on this boundary. Therefore, it is noted that the ‘cell surface’ flow speed was calculated just above the cell surface at a height of $1.77 \times 10^{-5} \text{ m}$, corresponding to the height of a single layer of cells where the volume of a macrophage is given by $5 \times 10^{-15} \text{ m}^3$ [67]. From Table 4.6, it is clear that cell surface flow speed increases as insert height increases; this was expected based on the observations made in Chapter 3, where it was shown that flow speeds within the chamber decrease with increasing chamber depth. Here, it was found that an insert of height $h = 9 \text{ mm}$ provides a flow speed within the desired range of $0.1 - 2 \text{ } \mu\text{m s}^{-1}$. Corresponding to an increase in flow speed, the shear stress observed at the cell surface also increases as insert height increases. For this study, a range of acceptable shear stress levels for macrophages could not be sourced in the literature, so whilst the recommended insert height provides the desired cell surface flow speed, it cannot be guaranteed that the levels of shear stress to which the cells are exposed under this

<i>Insert height (mm)</i>	<i>Mean 'cell surface' flow speed ($m s^{-1}$)</i>	<i>Max. cell surface shear stress (Pa)</i>
0	1.33×10^{-9}	1.04×10^{-7}
5	1.80×10^{-8}	2.82×10^{-6}
6	3.05×10^{-8}	4.54×10^{-6}
7	5.01×10^{-8}	7.06×10^{-6}
8	7.77×10^{-8}	1.08×10^{-5}
9	1.17×10^{-7}	1.60×10^{-5}

Table 4.6: Mean flow speed just above the cell surface and maximum shear stress at the cell surface in a single chamber for each insert height.

configuration will not affect the functionality of the cells.

With an insert height of $h = 9$ mm, additional simulations were performed using the connected chamber geometry shown in Fig. 4.3.2, matching the proposed experimental configuration. Fig. 4.3.3 illustrates the flow environment in the first chamber (left) and the fourth chamber, i.e. the first modified chamber (right). Recall from Chapter 3 that the fluid dynamics do not change substantially between identical connected chambers; therefore, the results shown for chamber 1 are representative of the environment within the first three chambers in the series, whilst the results shown for chamber 4 are representative of the environment within the final three chambers in the series.

The upper plots in Fig. 4.3.3 show the streamlines, colour coded by the magnitude of the fluid velocity, through the centre of each chamber. For chambers containing no inserts (left), recirculation zones are observed at the base of the chamber as well as beneath the inlet, with a mean cell surface flow speed of approximately $1.45 \times 10^{-9} m s^{-1}$. In contrast, for chambers containing inserts (right), the only zone of recirculation appears below the inlet, and the mean cell surface flow speed is two orders of magnitude higher at approximately $1.23 \times 10^{-7} m s^{-1}$.

Due to the dramatic variation in the flow profiles, the shear stress patterns observed at the base of chambers with and without inserts are considerably different, as shown by the lower plots in Fig. 4.3.3. For chambers containing no insert (left), shear stress levels rise from the periphery of the chamber to a region of high shear stress, with a maximum value of the order of 10^{-7} Pa, that surrounds an area of low shear stress near the centre of the base of the chamber. The shear stress profiles in chambers containing inserts (right) are less complex, with the magnitude of the shear stress increasing from the periphery of the chamber to a maximum value of the order of 10^{-5} Pa at the centre of the base of the chamber.

Fig. 4.3.4 displays the O_2 concentration profiles across the base of each chamber. It should be stressed that O_2 metabolism occurs only where the cells reside on the cover slip, namely from a distance of 2 – 14 mm, giving rise to higher O_2 concentrations at the edges of the base of each chamber. As expected, the concentration of O_2 decreases between consecutive identical chambers due to metabolism, but since the metabolic rate for this cell type is low, the concentration of O_2 remains high in all chambers. Within chambers containing an insert, cells

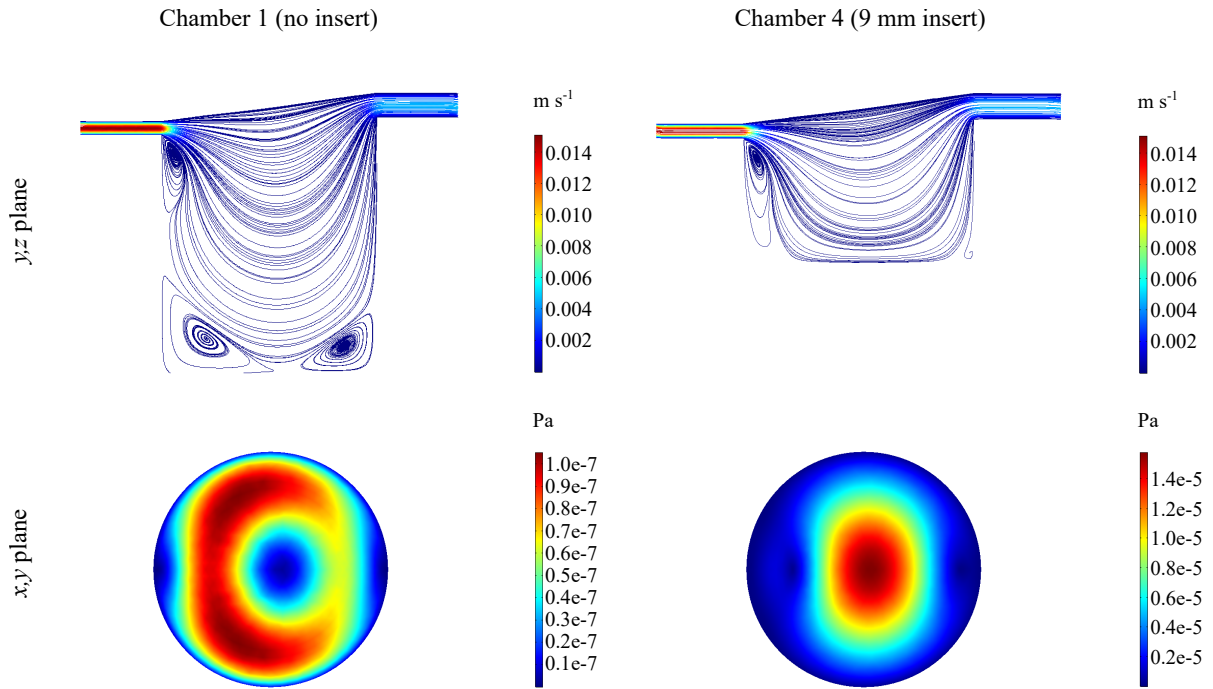


Figure 4.3.3: Streamlines and magnitude of velocity through the centre of the chamber (y, z plane, upper plots) and magnitude of shear stress at the base of the chamber (x, y plane, lower plots), for chamber 1 containing no insert (left) and chamber 4 containing a 9 mm insert (right).

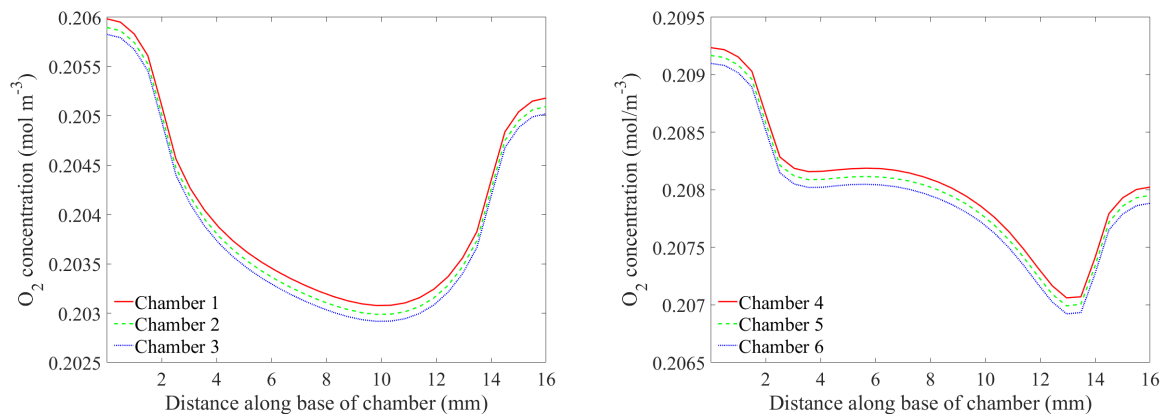


Figure 4.3.4: Simulated O_2 concentration profiles at the base of chambers 1, 2 and 3 containing no inserts (left) and chambers 4, 5 and 6 containing 9 mm inserts (right). Note that the concentration profiles are plotted across the diameter of the base of each chamber from the inlet to the outlet side of the chamber (left to right).

are exposed to elevated concentrations of O_2 due to their increased proximity to the chamber inlet, with a mean cell surface O_2 concentration of approximately 0.208 mol m^{-3} observed in the final three chambers, compared with 0.204 mol m^{-3} in the first three chambers.

4.3.2 The experiments

Mouse peritoneal macrophages (PEMs) were cultured on 12 mm cover slips at a density of 4×10^5 cells per well in a standard 24-well plate. Cells were infected with different concentrations of *L. major* parasites prior to being transferred to six connected QV900 chambers. The first three chambers contained no inserts to represent so-called ‘low flow’ conditions, with the mathematical model predicting cell surface flow speeds of the order of 10^{-9} m s^{-1} . With the aim of generating physiologically relevant cell surface flow speeds of the order of 10^{-7} m s^{-1} , so-called ‘high flow’ conditions, the final three chambers contained inserts of height 9 mm as recommended by the initial mathematical modelling. After running the flow system for 72 hours, levels of parasite infection and proliferation were evaluated and compared to the static control, and two key cellular functions were assessed. A brief description of the results of each assay is provided here, with the reader referred to [3] for a detailed account of the methods used to carry out each set of experiments.

Parasite infection levels were assessed by using microscopic techniques to count the number of infected cells for the three flow conditions (static, ‘low’, and ‘high’ flow) over a range of parasite to macrophage infection ratios. Whilst it was to be expected that higher infection ratios led to higher levels of infection, the results shown in Fig. 4.3.5 highlight that the presence of flow plays an important role in the infection process: with the exception of the highest infection ratio, the percentage of infection significantly decreased with increasing flow speed.

The visualisations of the flow patterns within the QV900 chambers provided by the mathematical model could help to explain why the infection levels are reduced under ‘low’ flow conditions, and further reduced under ‘high’ flow conditions. After the infected macrophages were transferred to the flow system, it is likely that some extracellular parasites remained on the cover slips. The addition of fluid flow would have carried the parasites away from the cells, leading to a lower rate of infection than that observed in the static case. The streamlines shown in Fig. 4.3.3 suggest that in chambers containing an insert, the parasites would be swept directly out of the chamber at an increased flow speed when compared to chambers containing no inserts, where the flow speed is slower and the zones of recirculation at the base of the chamber could encourage entrapment of the parasites, promoting increased contact with the cells and thus increasing infection levels.

To determine the rate of parasite proliferation within the host cells, a fluorescently labelled DNA base (EdU) was added to the culture medium. This base can be used by dividing parasites to create the DNA required for cell multiplication, and so the fluorescent label provides a means of tracking the generation of new parasites. An imaging kit was used to measure the incor-

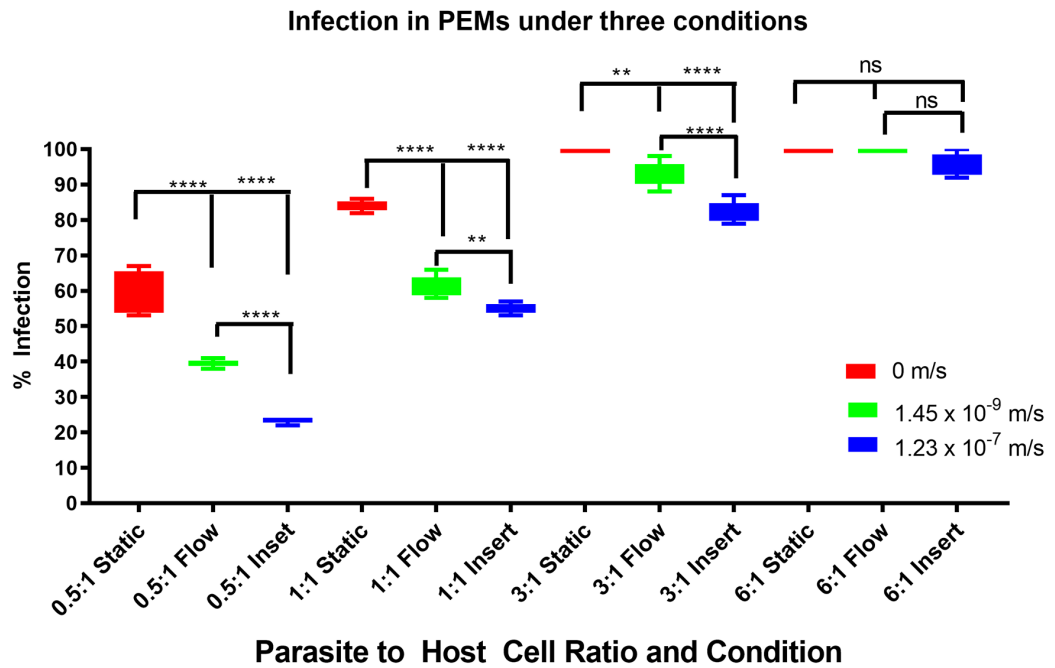


Figure 4.3.5: Box and whisker diagram showing the percentage of infected cells over a range of different infection ratios, of parasite:macrophage number, and different flow conditions. Significance tested using a two tailed t-test $p < 0.01 = **$ $p < 0.0001 = ****$ ns = not significant $N = 6$. [3]

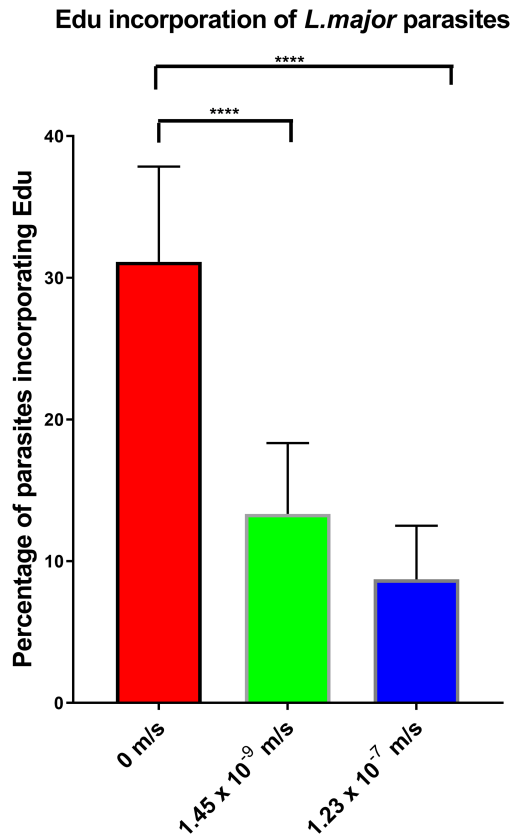


Figure 4.3.6: Bar graph showing percentage of *L. major* amastigotes that incorporated the EdU marker into DNA at the three different conditions, static (0 m/s), low flow (1.45×10^{-9} m/s) and high flow (1.23×10^{-7} m/s). * = $p < 0.05$ $N = 3$. [3]

poration of EdU (indicating that parasite replication has occurred) by counting the number of fluorescent parasites inside each macrophage. Fig. 4.3.6 shows that the percentage of parasites that incorporated EdU significantly reduced as cell surface flow speed increased, i.e. increasing flow speed leads to a reduction in parasite proliferation within the host cell. This provides another possible explanation for the lower infection levels observed as flow speed increases: since a successful infection process requires both parasite internalisation and multiplication, if the rate of proliferation is decreased within host cells maintained under flow conditions, then it follows that the level of infection will also decrease.

The metabolic function of the macrophages was assessed by evaluating phagocytosis and macropinocytosis. Respectively, these internalisation processes, initiated by ligand-receptor interactions, essentially describe the ‘eating’ and ‘drinking’ of extracellular particles and fluids by the host cell. Phagocytosis was quantified by the internalisation of fluorescent latex beads by infected macrophages, and similarly, macropinocytosis was evaluated by measuring the concentration of dextran (a fluorescent dye) within the host cells. From Fig. 4.3.7 and Fig. 4.3.8, it is clear that both internalisation processes decreased as cell surface flow speed increased. The significantly higher rate of phagocytosis observed in cells cultured without flow could be explained by the static environment allowing for sedimentation of the latex beads, and similarly, cells cultured under static conditions will be exposed to uniform concentrations of dextran; in both cases, this could promote an increased rate of internalisation. Furthermore, it is well established that cells are highly sensitive to changes in their microenvironment, so the reduction in phagocytosis and macropinocytosis in the flow system could be due to changes in cellular behaviour in response to increased levels of shear stress, which could influence the strength of ligand-receptor binding. Since parasite internalisation plays an essential role in the infection process, these results complement the decreased levels of infection observed under flow conditions.

4.3.3 Summary

In this study, the mathematical model was used to determine an appropriate configuration for the QV900 chambers such that the parasite infection process could be monitored under physiologically relevant flow speeds. Accurate calculations of cell surface flow speeds are difficult, or even impossible, to obtain experimentally, so here, the mathematical model was employed to provide estimations of this. Based on these predictions, experiments were performed using an insert of height 9 mm with the aim of generating flow speeds consistent with that of interstitial flow. Assays evaluating parasite infection and proliferation within the host cells confirmed that fluid flow plays an important role in the infection process, with percentage infection levels decreasing for increasing flow speeds. Additional results provided by simulating the final QV900 configuration provided insight into features of the flow system that could not be quantified experimentally, such as flow patterns and shear stress levels, allowing for a more in depth interpretation of the experimental results.

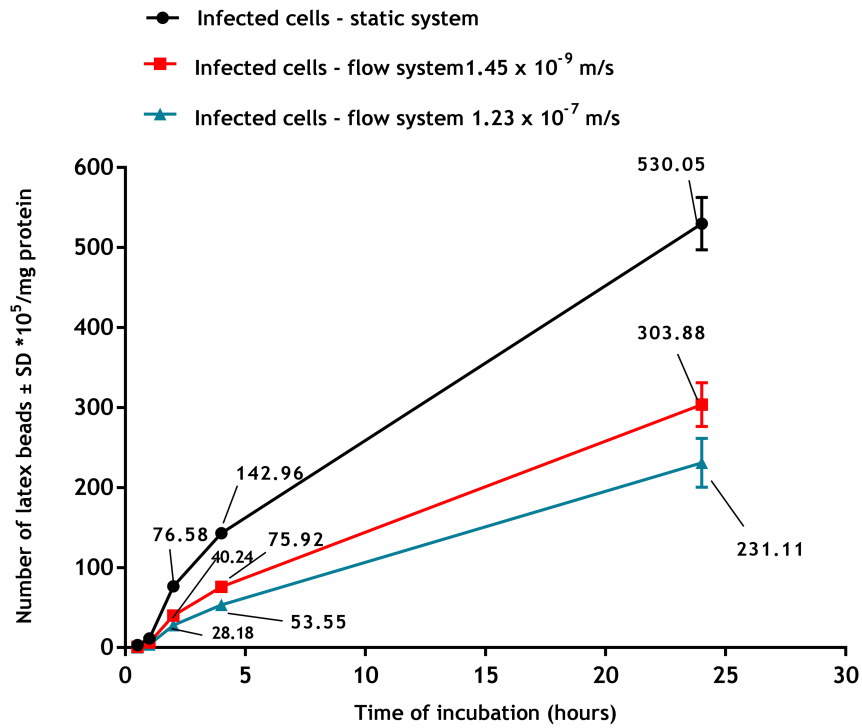


Figure 4.3.7: Phagocytosis of fluorescent latex beads ($2\mu\text{m}$) by infected PEMs in the three culture systems (static, slow flow rate 1.45×10^{-9} m/s and fast flow rate 1.23×10^{-7} m/s). Phagocytosis is significantly higher in static that in flow system ($p < 0.05$ by one-way ANOVA). The data are means \pm standard deviations (SD), $N = 3$. Infection rate $> 80\%$. [3]

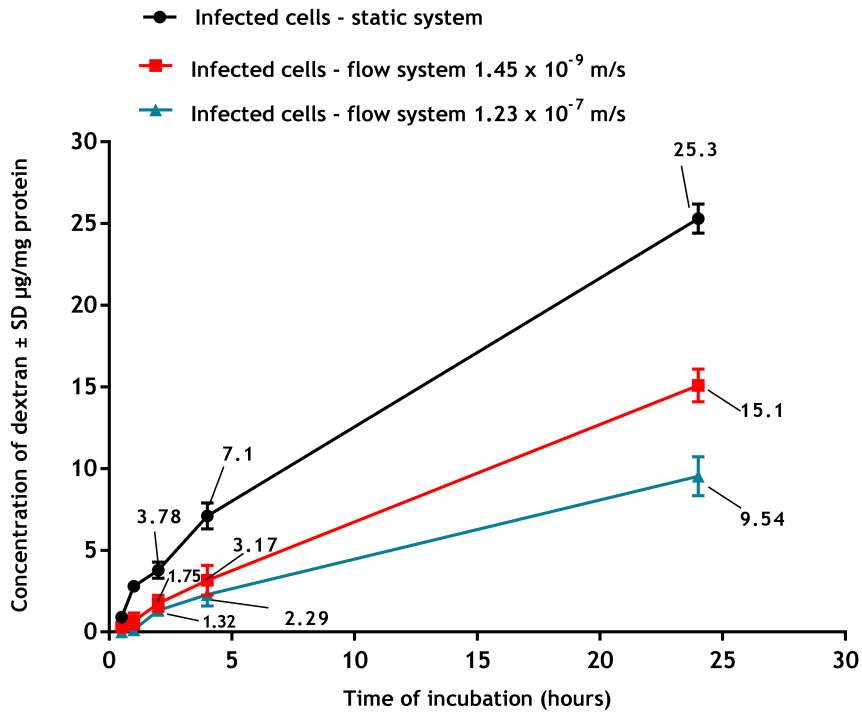


Figure 4.3.8: Macropinocytosis of pHrodo Red dextran by infected PEMs in the three culture systems (static, slow flow rate 1.45×10^{-9} m/s and fast flow rate 1.23×10^{-7} m/s). Macropinocytosis is significantly higher in static that in flow system ($p < 0.05$ by one-way ANOVA). The data are means \pm standard deviations (SD), $N = 3$. Infection rate $> 80\%$. [3]

4.3.4 Conclusions

As evidenced by the work presented in this chapter, mathematical modelling is an invaluable tool for not only guiding experimental set-up, but also for gaining a deeper understanding of experimental results. Here, it was shown that, in the case of liver zonation, the cell culture conditions generated by the recommended chamber configuration led to a physiologically relevant cellular response, whereby zone-specific functionality of hepatocytes was retained in the *in vitro* system. In the case of parasite infection, it was shown that the flow environment induced by the recommended experimental set-up led to a significant reduction in the infection of macrophages by *Leishmania* parasites. Moreover, the mathematical model was used to offer information about features of the flow environment that would have otherwise remained unknown, such as streamlines and shear stress profiles, providing additional insight that aided in the interpretation of the experimental results.

It is becoming increasingly evident that there is a growing need for mathematical and experimental teams of researchers to work in collaboration with one another. As *in vitro* cell culture techniques continue to advance in pursuit of more physiologically relevant results, the utility of mathematical modelling will continue to be made apparent as cell culture devices grow in complexity. Novel *in vitro* systems tend to be more expensive to source and maintain compared to their traditional static counterparts, so a lengthy trial-and-error approach for choosing the optimal experimental configuration should be avoided. Furthermore, the generation of more sophisticated cell culture conditions, such as concentration gradients and flow patterns, can be difficult to investigate without the help of mathematics due to challenges associated with device geometry and integration with standard measurement equipment. By estimating quantities that cannot be obtained experimentally, mathematical models greatly benefit experimental researchers by providing them with information that they would otherwise be unable to obtain. However, whilst this is an advantage of mathematical modelling, it is directly linked to its greatest challenge: validation. In order to prove accuracy, and to confidently use the mathematical model in a truly predictive sense, it is essential that model results are compared like-for-like with experimental measurements. The obtainment of experimental data with which to validate models must be pursued in order to increase the relevance of predictions made by mathematical modelling.

Although a lack of validation could be considered a major drawback, it should be noted that the qualitative results of unvalidated mathematical models, such as general trends, are still relevant. For example, in the case of liver zonation, the final experimental configuration was chosen with the aim of generating an O_2 concentration gradient from approximately $0.04 - 0.15 \text{ mol m}^{-3}$ across three QV900 chambers. The concentration of O_2 was never explicitly measured by the experimental team, so there is no guarantee that the mathematical model accurately predicted these quantities. However, the results of the experimental assays did confirm that the cells exhibited a response in line with that expected of cells in the native liver, i.e.

cells that are believed to be exposed to an O₂ gradient of approximately 0.04 – 0.15 mol m⁻³. This indicates that the cell culture conditions must have been appropriate for representing the *in vivo* environment, and therefore indirectly provides a degree of confidence in the mathematical predictions.

Chapter 5

Conclusions and future work

The drug development process consists of four key stages: discovery, where potential drugs are identified; preclinical, where the safety and efficacy of potential drugs are tested using *in vitro* and animal-based methods; clinical, where potential drugs are tested on humans; and finally, marketing and approval. Due to a poor correlation between the human response and the results of simplistic *in vitro* assays and non-representative animal studies, the majority of potential drugs that reach the clinical stage of development are eliminated. In order to increase efficiency, and therefore to reduce the expense of drug development, it is vital that the techniques employed during the preclinical stage are improved upon so that seemingly promising potential drugs are not carried through to the final stages of development, only to fail at the final hurdle. In addition to ethical concerns, it is also now well understood that animal-based studies do not provide a reliable prediction of the human response; in recent years, the reduction and even the replacement of animal testing has been made possible due to the advancement of *in vitro* cell culture methods.

Conventional *in vitro* cell culture techniques typically involve culturing cells in a petri dish containing culture medium. Whilst there are disadvantages associated with static conditions that do not fully capture the complexity of the *in vivo* environment, these traditional methods remain a popular choice and are still considered to be the ‘gold standard’ in many areas of research. A good understanding of the key features of the *in vitro* environment allows for the effective customisation of cell culture conditions, reducing the time and cost associated with obtaining the desired outcome via a trial-and-error approach.

In Chapter 2, mathematical models were developed to describe the transport and metabolism of two different types of solute within a traditional static *in vitro* cell culture system. The method of Laplace transforms was used to derive a Volterra integral equation (VIE) for each model, and under certain parameter regimes, approximations to the full solution were obtained using further analytical techniques. For each type of solute, the approximate solutions were found to be in good agreement with the numerical solution of the VIE. Thus, within each parameter regime, the approximations to the full solution may be employed to quickly estimate the solute

concentration to which the cells are exposed. Although a purely numerical approach could have been used to solve each model directly, the use of analytical methods allowed for additional insight into the dependencies of the solution on key model parameters. It was found that the cell surface solute concentration depends on the rate of diffusion of the solute through the culture medium, the rate of solute metabolism by the cells, the initial solute concentration and, where applicable, the rate of solute transfer across the fluid-air interface. Furthermore, the approximate analytical solutions derived for each model were used to obtain simple mathematical relationships that, when satisfied, provide information on how to adjust controllable parameters (e.g. the depth of the fluid or the initial solute concentration) such that a desired set of cell culture conditions can be achieved; this information could prove useful for determining optimal experimental configuration.

Whilst traditional static cell culture methods remain an important tool in *in vitro* experimentation, it is widely acknowledged that they do not provide an accurate representation of the *in vivo* environment. Rather than using these techniques in isolation, a common approach is to employ standard cell culture methods in conjunction with more advanced systems; for example, the initial cell culture is often carried out in petri dishes prior to transferring the established cells to more sophisticated devices that incorporate fluid flow, such as perfusion bioreactors. In order to bridge the gap between simplistic static cell culture and the true *in vivo* environment, flow-based devices have been designed with the aim of providing cells with more physiologically relevant culture conditions, thus improving the relevance of the results of *in vitro* studies. As cell culture systems continue to increase in complexity, it is important to gain a good understanding of the conditions to which cells are exposed so that *in vitro* devices may be configured efficiently, and so that experimental results may be interpreted in relation to the features of the cell culture environment.

In Chapter 3, the governing equations for describing fluid flow and solute transport in a dynamic cell culture system were provided, and subsequently applied to the commercially-available Kirkstall QV900 bioreactor device [90]. Mathematical models were developed to characterise the environment within single and connected cell culture chambers, where the interaction between the solute and the cells was described by two common reaction mechanisms. COMSOL Multiphysics was used to implement the finite element method to solve each model, and results were presented for a variety of input parameters. Analysis of the mathematical results provided valuable insight into the influence of the experimental configuration on the environment generated within the chambers. It was found that the fluid dynamics and solute distribution within the chamber change dramatically depending on the choice of input flow rate, and in particular, this parameter influences the cell surface flow speed, shear stress and solute concentration. The non-uniformity of the flow patterns and solute distributions throughout the chamber implies that the environment to which the cells are exposed could be modified by adjusting their spatial location. Intuitively, it was also found that the metabolic capacity of the

cells plays a role in dictating the cell surface solute concentration, and in downstream connected chambers, the solute concentration depletes due to metabolism by the cells. Finally, for each reaction mechanism, simple relationships were derived from the governing equations to further aid in the configuration of the system.

- When the interaction between the solute and the cells was described by nonlinear saturable binding, equations were provided for predicting the concentration of free and bound drug, both at steady-state and prior to the establishment of equilibrium.
- When the interaction between the solute and the cells was described by Michaelis-Menten kinetics, an equation was provided for estimating the cell surface solute concentration profile in a single chamber when the inlet concentration was varied, subject to certain conditions. Similarly, for chambers connected in series, an equation was provided for predicting the cell surface solute concentration profile in downstream chambers.

The main purpose of deriving these equations was to provide a method for obtaining useful information without requiring an in-depth knowledge of the underlying mathematical model, and to reduce the number of simulations and/or experiments needed to gather this information. It is important that mathematical models are developed with experimental researchers in mind; in order to maximise the utility of the model, it is essential to highlight simple relationships between key parameters so that researchers from different areas of expertise are empowered to make use of the mathematical results. In this way, mathematical modelling can be an effective tool in *in vitro* cell culture, for configuring equipment, providing valuable information that may be impossible to obtain experimentally, and interpreting results.

One of the primary goals of this thesis was to develop mathematical models of the environment within *in vitro* cell culture systems with the aim of guiding experimental set-up, and this was achieved by working in collaboration with two different groups of researchers [2, 3]. In Chapter 4, the mathematical models developed in Chapter 3 were employed to aid in the configuration of the Kirkstall QV900 chambers. By providing estimations of the cell surface oxygen (O_2) concentrations and flow speeds, a recommendation was provided to each experimental team regarding the insert height that should be used to modify the depth of the QV900 chambers such that the desired cell culture conditions could be generated. For the application to liver zonation, experiments confirmed the achievement of a zone-specific cell response, suggesting that physiologically relevant O_2 levels were generated within the chambers. For the application to parasite infection, fluid flow was found to have a significant effect on the parasite infection process, and the mathematical model was used to aid in the interpretation of the experimental results.

There is much scope for the work presented in this thesis to be extended, and a brief discussion of some ideas for future research is provided here. A number of assumptions were made during the development of each mathematical model, one of which was that the cells do not proliferate; this decision was made based on information provided by experimental collaborators

who advised that the cell types under consideration do not tend to reproduce in standard culture medium. However, there will undoubtedly be applications where cell proliferation does occur and is an important feature of the experiment, and in such cases, the mathematical models could be adapted to incorporate this process.

For each model, it was also assumed that the initial solute concentration and the supply of solute was constant, and furthermore, only one solute was considered at any one time. Discussions with a group of experimental researchers from the University of Dundee (who are working to develop new drug treatments for tropical diseases) highlighted that as animal testing continues to be replaced by cell-based studies, it is necessary to develop *in vitro* methods for determining optimal dosage and for studying the effect of different drug combinations. In such experiments, the cells could be exposed to multiple solutes simultaneously, and the supply of solute may have a time-dependency; for example, drug could be added to the cell culture periodically, or could be diluted over time. In order to widen the applicability and utility of the models developed in this thesis, a possible next step could be to explore various combinations of solutes and their method of supply.

Another way to expand upon the work carried out this thesis could be to combine the mathematical models presented here with models that describe the fluid flow and solute transport within 3D cell structures, such as spheroids and scaffolds. Since the relevance of *in vitro* studies improves as the level of complexity grows, it will become increasingly common to combine fluid flow with more sophisticated cellular arrangements. Within such cell structures, it is important to have a good understanding of the local fluid dynamics and solute concentration profiles, particularly since one of the main drawbacks associated with 3D cell culture (most notably, in spheroids) is the development of a necrotic core due to solute transport limitations. Therefore, it could be useful to develop a mathematical model that characterises not only the global cell culture conditions, but also the local environment generated within 3D cell structures.

There is also potential for the projects undertaken in Chapter 4 to be extended to various application areas and cell types. One example that could be explored is nanokicking, where the differentiation of stem cells can be manipulated by applying mechanical stress. Recall that in Chapter 4, the elevation of the cover slip was investigated as a means of controlling the conditions to which the cells were exposed, namely the O_2 concentrations and flow speeds. In a similar way, the shear stress induced on cells cultured at various heights within the chambers could be examined as a means of guiding the evolution of a population of stem cells that respond to different levels of stress. The ability to control the generation of specialised cells could one day revolutionise organ transplantation as well as the treatment of many diseases.

Finally, it is noted that the work carried out in Chapter 4 has led to the creation of a new PhD project, in relation to the effect of fluid flow on parasite infection levels. Although analysis of the flow patterns provided by the mathematical model helped to offer explanations for the behaviour observed in the experiments, it was decided that further investigation is required in

order to fully understand the process of parasite internalisation under flow. Thus, at present, mathematical models are being developed to characterise the process of phagocytosis, with the ultimate goal of combining this with the models presented here.

Appendix A

Solutions of the multiple pathway models from Chapter 2

In this appendix, the VIE and approximate solutions to the governing equations from §2.2 are derived where solute metabolism is described by multiple M-M pathways, i.e. where (2.2.4) is replaced by

$$\frac{\partial c}{\partial x}(1, t) = - \sum_{i=1}^m \frac{\alpha_i c}{\beta_i + c}, \quad (\text{A.1})$$

and the non-dimensional parameters α_i and β_i are defined as

$$\alpha_i = \frac{V_{max,i}d}{DK_{m,i}}, \quad \beta_i = \frac{c_0}{K_{m,i}}.$$

A.1 Solutions for case A

Recall that from §2.4.1, (2.2.1) is solved subject to (2.2.2) and (2.2.3A) to obtain

$$\bar{c}(x, s) = a(s) \cosh(\sqrt{s}x) + \frac{1}{s},$$

and taking the inverse Laplace transform gives

$$c(x, t) = 1 + \mathcal{L}^{-1} \{ a(s) \cosh(\sqrt{s}x) \}.$$

Now, applying (A.1) gives rise to the following VIE:

$$c(1, t) = 1 - \int_0^t k_A(t - \tau) \sum_{i=1}^m \frac{\alpha_i c(1, \tau)}{1 + \beta_i c(1, \tau)} d\tau, \quad (\text{A.1.1})$$

where $k_A(t)$ is defined as before. Note that this equation takes the same form as the VIE derived when $m = 1$, with α and β replaced by α_i and β_i , respectively.

Small β solution for case A

Assuming $\beta_i \ll 1$ for $i = 1, 2, \dots, m$, consider the following perturbation expansion about the small parameter β_j where $j \in [1, 2, \dots, m]$:

$$c(1, t) = c_0(1, t) + \beta_j c_1(1, t) + \mathcal{O}(\beta_j^2).$$

Substituting this expression into (A.1.1) gives

$$\begin{aligned} & c_0(1, t) + \beta_j c_1(1, t) + \mathcal{O}(\beta_j^2) \\ &= 1 - \int_0^t k_A(t - \tau) \sum_{i=1}^m \frac{\alpha_i [c_0(1, \tau) + \beta_j c_1(1, \tau) + \mathcal{O}(\beta_j^2)]}{1 + \beta_i [c_0(1, \tau) + \beta_j c_1(1, \tau) + \mathcal{O}(\beta_j^2)]} d\tau. \end{aligned}$$

Now, assuming that β_i is of the same order as β_j , this becomes

$$\begin{aligned} & c_0(1, t) + \beta_j c_1(1, t) + \mathcal{O}(\beta_j^2) \\ &= 1 - \bar{\alpha} \int_0^t k_A(t - \tau) \frac{[c_0(1, \tau) + \beta_j c_1(1, \tau) + \mathcal{O}(\beta_j^2)]}{1 + \beta_j [c_0(1, \tau) + \beta_j c_1(1, \tau) + \mathcal{O}(\beta_j^2)]} d\tau, \end{aligned}$$

where

$$\bar{\alpha} = \sum_{i=1}^m \alpha_i.$$

Note that this expression is equivalent to the expression derived when $m = 1$, with α replaced by $\bar{\alpha}$. Thus, when $\beta_j \sim \mathcal{O}(\beta_i)$, and $\beta_i \ll 1$ for $i = 1, 2, \dots, m$, the solution is given by

$$c(1, t) = \sum_{n=1}^{\infty} \frac{2 \sin(\gamma_n) e^{-\gamma_n^2 t}}{\gamma_n \cos(\gamma_n) + (\bar{\alpha} + 1) \sin(\gamma_n)} + \beta_j c_1(1, t) + \mathcal{O}(\beta_j^2),$$

where γ_n are the roots of $\gamma \sin(\gamma) - \bar{\alpha} \cos(\gamma) = 0$.

Large β solution for case A

Assuming $\beta_i \gg 1$ for $i = 1, 2, \dots, m$ and defining $\varepsilon_i = 1/\beta_i$, consider the following perturbation expansion about the small parameter ε_j where $j \in [1, 2, \dots, m]$:

$$c(1, t) = c_0(1, t) + \varepsilon_j c_1(1, t) + \mathcal{O}(\varepsilon_j^2).$$

Substituting this expression into (A.1.1) gives

$$\begin{aligned} & c_0(1, t) + \varepsilon_j c_1(1, t) + \mathcal{O}(\varepsilon_j^2) \\ &= 1 - \int_0^t k_A(t - \tau) \sum_{i=1}^m \frac{\alpha_i [c_0(1, \tau) + \varepsilon_j c_1(1, \tau) + \mathcal{O}(\varepsilon_j^2)]}{1 + \varepsilon_i^{-1} [c_0(1, \tau) + \varepsilon_j c_1(1, \tau) + \mathcal{O}(\varepsilon_j^2)]} d\tau. \end{aligned}$$

Similarly to the case when $\beta_i \ll 1$, assuming that ε_i is of the same order as ε_j , this becomes

$$\begin{aligned} & c_0(1, t) + \varepsilon_j c_1(1, t) + \mathcal{O}(\varepsilon_j^2) \\ &= 1 - \bar{\alpha} \int_0^t k_A(t - \tau) \frac{[c_0(1, \tau) + \varepsilon_j c_1(1, \tau) + \mathcal{O}(\varepsilon_j^2)]}{1 + \varepsilon_j^{-1} [c_0(1, \tau) + \varepsilon_j c_1(1, \tau) + \mathcal{O}(\varepsilon_j^2)]} d\tau. \end{aligned}$$

Note that this expression is equivalent to the expression derived when $m = 1$, with α replaced by $\bar{\alpha}$. Thus, when $\beta_j \sim \mathcal{O}(\beta_i)$, and $\beta_i \gg 1$ for $i = 1, 2, \dots, m$, the solution is given by

$$c(1, t) = 1 - \frac{\bar{\alpha}}{\beta_j} \left(t + \frac{1}{3} - \sum_{n=1}^{\infty} \frac{2e^{-n^2\pi^2 t}}{n^2\pi^2} \right) + \sum_{n=2}^{\infty} \frac{(-1)^n \bar{\alpha}}{\beta_j^n} \int_0^t k_A(t - \tau) [c_1(1, \tau) + 1]^{n-2} d\tau.$$

Small t solution for case A

Recall that $k_A(t) \sim 1/\sqrt{\pi t}$ for $t \ll 1$ and consider the following expansion in t :

$$c(1, t) = a_1 + a_2 t^{1/2} + a_3 t + a_4 t^{3/2} + \mathcal{O}(t^2).$$

Substituting this expression into (A.1.1) and taking a series expansion of

$$\left(1 + \beta_i [a_1 + a_2 \tau^{1/2} + a_3 \tau + a_4 \tau^{3/2} + \mathcal{O}(\tau^2)] \right)^{-1}$$

about $\tau = 0$ gives

$$\begin{aligned} & a_1 + a_2 t^{1/2} + a_3 t + a_4 t^{3/2} + \mathcal{O}(t^2) \\ &= 1 - \frac{1}{\sqrt{\pi}} \int_0^t (t - \tau)^{-1/2} \sum_{i=1}^m \alpha_i [a_1 + a_2 \tau^{1/2} + a_3 \tau + a_4 \tau^{3/2} + \mathcal{O}(\tau^2)] \\ & \quad \times \left[\frac{1}{a_1 \beta_i + 1} - \frac{a_2 \beta_i}{(a_1 \beta_i + 1)^2} \tau^{1/2} + \frac{(a_2^2 - a_1 a_3) \beta_i^2 - a_3 \beta_i}{(a_1 \beta_i + 1)^3} \tau + \mathcal{O}(\tau^{3/2}) \right] d\tau. \\ &= 1 - \frac{1}{\sqrt{\pi}} \sum_{i=1}^m \alpha_i \left[\frac{a_1}{a_1 \beta_i + 1} \int_0^t (t - \tau)^{-1/2} d\tau + \frac{a_2}{(a_1 \beta_i + 1)^2} \int_0^t (t - \tau)^{-1/2} \tau^{1/2} d\tau \right. \\ & \quad \left. + \frac{a_3 + \beta_i (a_1 a_3 - a_2^2)}{(a_1 \beta_i + 1)^3} \int_0^t (t - \tau)^{-1/2} \tau d\tau + \dots \right] \\ &= 1 - \frac{1}{\sqrt{\pi}} \sum_{i=1}^m \alpha_i \left[\frac{2a_1}{a_1 \beta_i + 1} t^{1/2} + \frac{a_2 \pi}{2(a_1 \beta_i + 1)^2} t + \frac{4(a_3 + \beta_i (a_1 a_3 - a_2^2))}{3(a_1 \beta_i + 1)^3} t^{3/2} + \mathcal{O}(t^2) \right]. \end{aligned}$$

Equating powers of t gives

$$\begin{aligned} a_1 &= 1, \\ a_2 &= - \sum_{i=1}^m \frac{2\alpha_i}{\sqrt{\pi}(\beta_i + 1)}, \end{aligned}$$

$$a_3 = \sum_{i=1}^m \sum_{j=1}^m \frac{\alpha_i \alpha_j}{(\beta_i + 1)^2 (\beta_j + 1)},$$

$$a_4 = -\frac{4}{3\sqrt{\pi}} \left(\sum_{i=1}^m \sum_{j=1}^m \sum_{k=1}^m \frac{\alpha_i \alpha_j \alpha_k}{(\beta_i + 1)^2 (\beta_j + 1)^2 (\beta_k + 1)} - \sum_{i=1}^m \sum_{j=1}^m \frac{4\alpha_i \beta_i \alpha_j^2}{\pi (\beta_i + 1)^3 (\beta_j + 1)^2} \right).$$

Note that these expressions are equivalent to those derived when $m = 1$. Thus, the solution when $t \ll 1$ is given by

$$c(1, t) = 1 - \sum_{i=1}^m \frac{2\alpha_i}{\sqrt{\pi}(\beta_i + 1)} t^{1/2} + \sum_{i=1}^m \sum_{j=1}^m \frac{\alpha_i \alpha_j}{(\beta_i + 1)^2 (\beta_j + 1)} t$$

$$- \frac{4}{3\sqrt{\pi}} \left(\sum_{i=1}^m \sum_{j=1}^m \sum_{k=1}^m \frac{\alpha_i \alpha_j \alpha_k}{(\beta_i + 1)^2 (\beta_j + 1)^2 (\beta_k + 1)} - \sum_{i=1}^m \sum_{j=1}^m \frac{4\alpha_i \beta_i \alpha_j^2}{\pi (\beta_i + 1)^3 (\beta_j + 1)^2} \right) t^{3/2} + \mathcal{O}(t^2).$$

Steady-state solution for case A

As in the case when $m = 1$, it is clear that $c(x, t) \rightarrow 0$ as $t \rightarrow \infty$ when solute metabolism is described by multiple M-M pathways. To derive this trivial solution, the steady version of the governing equations from §2.2 are solved with (2.2.4) replaced by (A.1).

A.2 Solutions for case B

Recall that from §2.5.1, (2.2.1) is solved subject to (2.2.2) and (2.2.3B) to obtain

$$\bar{c}(x, s) = a(s) \cosh(\sqrt{s}x) + \frac{\mu a(s)}{\sqrt{s}} \sinh(\sqrt{s}x) + \frac{1}{s}.$$

and taking the inverse Laplace transform gives

$$c(x, t) = 1 + \mathcal{L}^{-1} \left\{ a(s) \left[\cosh(\sqrt{s}x) + \frac{\mu}{\sqrt{s}} \sinh(\sqrt{s}x) \right] \right\}.$$

Now, applying (A.1) gives rise to the following VIE:

$$c(1, t) = 1 - \int_0^t k_B(t - \tau) \sum_{i=1}^m \frac{\alpha_i c(1, \tau)}{1 + \beta_i c(1, \tau)} d\tau, \quad (\text{A.2.1})$$

where $k_B(t)$ is defined as before. Note that, as in case A, this equation takes the same form as the VIE derived when $m = 1$, with α and β replaced by α_i and β_i , respectively.

Small β solution for case B

Assuming $\beta_i \ll 1$ for $i = 1, 2, \dots, m$, consider the following perturbation expansion about the small parameter β_j where $j \in [1, 2, \dots, m]$:

$$c(1, t) = c_0(1, t) + \beta_j c_1(1, t) + \mathcal{O}(\beta_j^2).$$

Similarly to case A, substituting this expression into (A.2.1) and assuming that β_i is of the same order as β_j gives

$$\begin{aligned} & c_0(1, t) + \beta_j c_1(1, t) + \mathcal{O}(\beta_j^2) \\ &= 1 - \bar{\alpha} \int_0^t k_B(t - \tau) \frac{[c_0(1, \tau) + \beta_j c_1(1, \tau) + \mathcal{O}(\beta_j^2)]}{1 + \beta_j [c_0(1, \tau) + \beta_j c_1(1, \tau) + \mathcal{O}(\beta_j^2)]} d\tau. \end{aligned}$$

Note that this expression is equivalent to the expression derived when $m = 1$, with α replaced by $\bar{\alpha}$. Thus, when $\beta_j \sim \mathcal{O}(\beta_i)$, and $\beta_i \ll 1$ for $i = 1, 2, \dots, m$, the solution is given by

$$\begin{aligned} c(1, t) &= \frac{\mu}{\bar{\alpha}\mu + \bar{\alpha} + \mu} + \sum_{n=1}^{\infty} \frac{2[\mu \cos(\xi_n) - \xi_n \sin(\xi_n)] e^{-\xi_n^2 t}}{(\bar{\alpha}\mu + \bar{\alpha} + \mu - \xi_n^2) \cos(\xi_n) - \xi_n(2 + \bar{\alpha} + \mu) \sin(\xi_n)} \\ &+ \beta_j c_1(1, t) + \mathcal{O}(\beta_j^2). \end{aligned}$$

where ξ_n are the roots of $(\bar{\alpha}\mu - \xi^2) \sin(\xi) + \xi(\bar{\alpha} + \mu) \cos(\xi) = 0$.

Large β solution for case B

Assuming $\beta_i \gg 1$ for $i = 1, 2, \dots, m$ and defining $\varepsilon_i = 1/\beta_i$, consider the following perturbation expansion about the small parameter ε_j where $j \in [1, 2, \dots, m]$:

$$c(1, t) = c_0(1, t) + \varepsilon_j c_1(1, t) + \mathcal{O}(\varepsilon_j^2).$$

As in case A, substituting this expression into (A.2.1) and assuming that ε_i is of the same order as ε_j gives

$$\begin{aligned} & c_0(1, t) + \varepsilon_j c_1(1, t) + \mathcal{O}(\varepsilon_j^2) \\ &= 1 - \bar{\alpha} \int_0^t k_B(t - \tau) \frac{[c_0(1, \tau) + \varepsilon_j c_1(1, \tau) + \mathcal{O}(\varepsilon_j^2)]}{1 + \varepsilon_j^{-1} [c_0(1, \tau) + \varepsilon_j c_1(1, \tau) + \mathcal{O}(\varepsilon_j^2)]} d\tau. \end{aligned}$$

Note that this expression is equivalent to the expression derived when $m = 1$, with α replaced by $\bar{\alpha}$. Thus, when $\beta_j \sim \mathcal{O}(\beta_i)$, and $\beta_i \gg 1$ for $i = 1, 2, \dots, m$, the solution is given by

$$c(1, t) = 1 - \frac{\bar{\alpha}}{\beta_j} \left(1 + \frac{1}{\mu} - \sum_{n=1}^{\infty} \frac{2[\lambda_n \cos(\lambda_n) + \mu \sin(\lambda_n)] e^{-\lambda_n^2 t}}{\lambda_n^2 [\lambda_n \cos(\lambda_n) + (\mu + 1) \sin(\lambda_n)]} \right) \\ + \sum_{n=2}^{\infty} \frac{(-1)^n \bar{\alpha}}{\beta_j^n} \int_0^t k_B(t - \tau) [c_1(1, \tau) + 1]^{n-2} d\tau,$$

where λ_n are the roots of $\mu \cos(\lambda) - \lambda \sin(\lambda) = 0$.

Small t solution for case B

As in the case when $m = 1$, the governing equations may be re-characterised using Corollary 2.1 and Lemma 2.2 to obtain the following coupled VIEs:

$$c(0, t) = 1 + \int_0^t \mu k_A(t - \tau) [1 - c(0, \tau)] - 2g(t - \tau) \sum_{i=1}^m \frac{\alpha_i c(1, \tau)}{1 + \beta_i c(1, \tau)} d\tau, \quad (\text{A.2.2})$$

$$c(1, t) = 1 + \int_0^t 2\mu g(t - \tau) [1 - c(0, \tau)] - k_A(t - \tau) \sum_{i=1}^m \frac{\alpha_i c(1, \tau)}{1 + \beta_i c(1, \tau)} d\tau. \quad (\text{A.2.3})$$

Now consider the following expansions in t :

$$c(0, t) = a_1 + a_2 t^{1/2} + a_3 t + a_4 t^{3/2} + a_5 t^2 + \mathcal{O}(t^{5/2}), \quad (\text{A.2.4})$$

$$c(1, t) = b_1 + b_2 t^{1/2} + b_3 t + b_4 t^{3/2} + b_5 t^2 + \mathcal{O}(t^{5/2}). \quad (\text{A.2.5})$$

Recalling that $k_A(t) \sim 1/\sqrt{\pi t}$ and $g(t) \sim 1/2$ for $t \ll 1$, substituting (A.2.4) and (A.2.5) into (A.2.2) and taking a series expansion of

$$\left(1 + \beta_i [b_1 + b_2 \tau^{1/2} + b_3 \tau + b_4 \tau^{3/2} + b_5 \tau^2 + \mathcal{O}(\tau^{5/2})] \right)^{-1}$$

about $\tau = 0$ gives

$$a_1 + a_2 t^{1/2} + a_3 t + a_4 t^{3/2} + a_5 t^2 + \mathcal{O}(t^{5/2}) \\ = 1 + \int_0^t \frac{\mu}{\sqrt{\pi}} (t - \tau)^{-1/2} [1 - a_1 - a_2 \tau^{1/2} - a_3 \tau - a_4 \tau^{3/2} - a_5 \tau^2 - \mathcal{O}(\tau^{5/2})] \\ - \sum_{i=1}^m \alpha_i [b_1 + b_2 \tau^{1/2} + b_3 \tau + b_4 \tau^{3/2} + b_5 \tau^2 + \mathcal{O}(\tau^{5/2})] \\ \times \left[\frac{1}{b_1 \beta_i + 1} - \frac{b_2 \beta_i}{(b_1 \beta_i + 1)^2} \tau^{1/2} + \frac{(b_2^2 - b_1 b_3) \beta_i^2 - b_3 \beta_i}{(b_1 \beta_i + 1)^3} \tau + \mathcal{O}(\tau^{3/2}) \right] d\tau \\ = 1 + \frac{\mu}{\sqrt{\pi}} \left[(1 - a_1) \int_0^t (t - \tau)^{-1/2} d\tau - a_2 \int_0^t (t - \tau)^{-1/2} \tau^{1/2} d\tau - a_3 \int_0^t (t - \tau)^{-1/2} \tau d\tau \right. \\ \left. - a_4 \int_0^t (t - \tau)^{-1/2} \tau^{3/2} d\tau - \dots \right] - \sum_{i=1}^m \alpha_i \left[\frac{b_1}{b_1 \beta_i + 1} \int_0^t 1 d\tau + \frac{b_2}{(b_1 \beta_i + 1)^2} \int_0^t \tau^{1/2} d\tau \right. \\ \left. + \frac{(b_1 b_3 - b_2^2) \beta_i + b_3}{(b_1 \beta_i + 1)^3} \int_0^t \tau d\tau + \dots \right]$$

$$\begin{aligned}
&= 1 + \frac{2\mu(1-a_1)}{\sqrt{\pi}}t^{1/2} - \left(\sum_{i=1}^m \frac{\alpha_i b_1}{b_1 \beta_i + 1} + \frac{\mu\sqrt{\pi}a_2}{2} \right) t - \left(\sum_{i=1}^m \frac{2\alpha_i b_2}{3(b_1 \beta_i + 1)^2} + \frac{4\mu a_3}{3\sqrt{\pi}} \right) t^{3/2} \\
&\quad + \mathcal{O}(t^2).
\end{aligned}$$

Equating powers of t gives

$$\begin{aligned}
a_1 &= 1, \\
a_2 &= 0, \\
a_3 &= - \sum_{i=1}^m \frac{\alpha_i b_1}{b_1 \beta_i + 1}, \\
a_4 &= \sum_{i=1}^m \frac{2\alpha_i(2\mu b_1^2 \beta_i + 2\mu b_1 - \sqrt{\pi} b_2)}{3\sqrt{\pi}(b_1 \beta_i + 1)^2}.
\end{aligned} \tag{A.2.6}$$

Now, similarly, (A.2.4) and (A.2.5) are substituted into (A.2.3) to give

$$\begin{aligned}
&b_1 + b_2 t^{1/2} + b_3 t + b_4 t^{3/2} + b_5 t^2 + \mathcal{O}(t^{5/2}) \\
&= 1 + \int_0^t \mu \left[1 - a_1 - a_2 \tau^{1/2} - a_3 \tau - a_4 \tau^{3/2} - a_5 \tau^2 - \mathcal{O}(\tau^{5/2}) \right] - \frac{1}{\sqrt{\pi}} (t - \tau)^{-1/2} \\
&\quad \times \sum_{i=1}^m \alpha_i \left[b_1 + b_2 \tau^{1/2} + b_3 \tau + b_4 \tau^{3/2} + b_5 \tau^2 + \mathcal{O}(\tau^{5/2}) \right] \left[\frac{1}{b_1 \beta_i + 1} - \frac{b_2 \beta_i}{(b_1 \beta_i + 1)^2} \tau^{1/2} \right. \\
&\quad \left. + \frac{(b_2^2 - b_1 b_3) \beta_i^2 - b_3 \beta_i}{(b_1 \beta_i + 1)^3} \tau - \frac{(b_1^2 b_4 - 2b_1 b_2 b_3 + b_2^3) \beta_i^3 + 2(b_1 b_4 - b_2 b_3) \beta_i^2 + b_4 \beta_i}{(b_1 \beta_i + 1)^4} \tau^{3/2} \right. \\
&\quad \left. + \mathcal{O}(\tau^2) \right] d\tau \\
&= 1 + \mu \left[(1 - a_1) \int_0^t 1 d\tau - a_2 \int_0^t \tau^{1/2} d\tau - a_3 \int_0^t \tau d\tau - \dots \right] - \frac{1}{\sqrt{\pi}} \sum_{i=1}^m \alpha_i \\
&\quad \times \left[\frac{b_1}{b_1 \beta_i + 1} \int_0^t (t - \tau)^{-1/2} d\tau + \frac{b_2}{(b_1 \beta_i + 1)^2} \int_0^t (t - \tau)^{-1/2} \tau^{1/2} d\tau \right. \\
&\quad \left. + \frac{(b_1 b_3 - b_2^2) \beta_i + b_3}{(b_1 \beta_i + 1)^3} \int_0^t (t - \tau)^{-1/2} \tau d\tau + \frac{(b_1^2 b_4 - 2b_1 b_2 b_3 + b_2^3) \beta_i^2 + 2(b_1 b_4 - b_2 b_3) \beta_i + b_4}{(b_1 \beta_i + 1)^4} \right. \\
&\quad \left. \times \int_0^t (t - \tau)^{-1/2} \tau^{3/2} d\tau + \dots \right] \\
&= 1 - \sum_{i=1}^m \frac{2\alpha_i b_1}{\sqrt{\pi}(b_1 \beta_i + 1)} t^{1/2} + \left(\mu(1 - a_1) - \sum_{i=1}^m \frac{\alpha_i \sqrt{\pi} b_2}{2(b_1 \beta_i + 1)^2} \right) t \\
&\quad - \left(\frac{2\mu a_2}{3} + \sum_{i=1}^m \frac{4\alpha_i [(b_1 b_3 - b_2^2) \beta_i + b_3]}{3\sqrt{\pi}(b_1 \beta_i + 1)^3} \right) t^{3/2} \\
&\quad - \left(\frac{\mu a_3}{2} + \sum_{i=1}^m \frac{3\alpha_i \sqrt{\pi} [(b_1^2 b_4 - 2b_1 b_2 b_3 + b_2^3) \beta_i^2 + 2(b_1 b_4 - b_2 b_3) \beta_i + b_4]}{8(b_1 \beta_i + 1)^4} \right) t^2 + \mathcal{O}(t^{5/2}).
\end{aligned}$$

Equating powers of t gives

$$\begin{aligned} b_1 &= 1, \\ b_2 &= -\sum_{i=1}^m \frac{2\alpha_i}{\sqrt{\pi}(\beta_i + 1)}, \\ b_3 &= \sum_{i=1}^m \sum_{j=1}^m \frac{\alpha_i \alpha_j}{(\beta_i + 1)^2 (\beta_j + 1)}, \\ b_4 &= -\frac{4}{3\sqrt{\pi}} \left(\sum_{i=1}^m \sum_{j=1}^m \sum_{k=1}^m \frac{\alpha_i \alpha_j \alpha_k}{(\beta_i + 1)^2 (\beta_j + 1)^2 (\beta_k + 1)} - \sum_{i=1}^m \sum_{j=1}^m \frac{4\alpha_i \beta_i \alpha_j^2}{\pi(\beta_i + 1)^3 (\beta_j + 1)^2} \right). \end{aligned}$$

Then, from (A.2.6), it follows that

$$\begin{aligned} a_1 &= 1, \\ a_2 &= 0, \\ a_3 &= -\sum_{i=1}^m \frac{\alpha_i}{\beta_i + 1}, \\ a_4 &= \frac{4}{3\sqrt{\pi}} \left(\sum_{i=1}^m \frac{\alpha_i \mu}{\beta_i + 1} + \sum_{i=1}^m \sum_{j=1}^m \frac{\alpha_i \alpha_j}{(\beta_i + 1)^2 (\beta_j + 1)} \right). \end{aligned}$$

Note that these expressions are equivalent to those derived when $m = 1$. Thus, from (A.2.4) and (A.2.5), the solutions when $t \ll 1$ are given by

$$\begin{aligned} c(0, t) &= 1 - \sum_{i=1}^m \frac{\alpha_i}{\beta_i + 1} t + \frac{4}{3\sqrt{\pi}} \left(\sum_{i=1}^m \frac{\alpha_i \mu}{\beta_i + 1} + \sum_{i=1}^m \sum_{j=1}^m \frac{\alpha_i \alpha_j}{(\beta_i + 1)^2 (\beta_j + 1)} \right) t^{3/2} - \mathcal{O}(t^2), \\ c(1, t) &= 1 - \sum_{i=1}^m \frac{2\alpha_i}{\sqrt{\pi}(\beta_i + 1)} t^{1/2} + \sum_{i=1}^m \sum_{j=1}^m \frac{\alpha_i \alpha_j}{(\beta_i + 1)^2 (\beta_j + 1)} t \\ &\quad - \frac{4}{3\sqrt{\pi}} \left(\sum_{i=1}^m \sum_{j=1}^m \sum_{k=1}^m \frac{\alpha_i \alpha_j \alpha_k}{(\beta_i + 1)^2 (\beta_j + 1)^2 (\beta_k + 1)} \right. \\ &\quad \left. - \sum_{i=1}^m \sum_{j=1}^m \frac{4\alpha_i \beta_i \alpha_j^2}{\pi(\beta_i + 1)^3 (\beta_j + 1)^2} \right) t^{3/2} + \mathcal{O}(t^2). \end{aligned}$$

Steady-state solution for case B

As in the case when $m = 1$, the solution as $t \rightarrow \infty$ is derived by solving the steady version of the governing equations from §2.2 with (2.2.4) replaced by (A.1). Integrating the steady diffusion equation twice with respect to x and applying (2.2.3B) results in

$$c(x, \infty) = Ax + \frac{A}{\mu} + 1,$$

where A is a constant of integration. Then, applying (A.1) gives the following expression for A which may be solved numerically:

$$A = - \sum_{i=1}^m \frac{\alpha_i \left(A + \frac{A}{\mu} + 1 \right)}{1 + \beta_i \left(A + \frac{A}{\mu} + 1 \right)}.$$

Appendix B

Solutions of the linear models from Chapter 2

In this appendix, solutions to the governing equations from §2.2 are derived where (2.2.4) is replaced by

$$\frac{\partial c}{\partial x}(1, t) = \begin{cases} -\alpha c(1, t), & \beta \ll 1, \\ -\frac{\alpha}{\beta}, & \beta \gg 1. \end{cases} \quad \begin{array}{l} \text{(B.1)} \\ \text{(B.2)} \end{array}$$

For cases A and B, each linear boundary condition is applied in turn and the resulting solutions are shown to be equivalent to the small and large β solutions derived in §2.4.2 and §2.5.2.

B.1 Solutions for case A

Recall that from §2.4.1, (2.2.1) is solved subject to (2.2.2) and (2.2.3A) to obtain

$$\bar{c}(x, s) = a(s) \cosh(\sqrt{s}x) + \frac{1}{s}, \quad \text{(B.1.1)}$$

and taking the inverse Laplace transform gives

$$c(x, t) = 1 + \mathcal{L}^{-1} \{a(s) \cosh(\sqrt{s}x)\}. \quad \text{(B.1.2)}$$

Now, (B.1) and (B.2) are applied in turn.

Small β solution for case A

Differentiating (B.1.1) and applying (B.1) gives

$$a(s) = -\frac{\alpha}{s[\sqrt{s} \sinh(\sqrt{s}) + \alpha \cos(\sqrt{s})]},$$

so it follows from (B.1.2) that

$$c(x, t) = 1 - \alpha \mathcal{L}^{-1} \left\{ \frac{\cosh(\sqrt{s}x)}{s[\sqrt{s} \sinh(\sqrt{s}) + \alpha \cosh(\sqrt{s})]} \right\}. \quad (\text{B.1.3})$$

After verifying that no branch points exist, the residue theorem is used to evaluate this inverse Laplace transform. The poles are given by

$$s = 0 \quad \text{and} \quad \sqrt{s} \sinh(\sqrt{s}) + \alpha \cosh(\sqrt{s}) = 0,$$

and, for convenience, setting $\sqrt{s} = i\gamma$ in the transcendental equation gives

$$\gamma \sin(\gamma) - \alpha \cos(\gamma) = 0. \quad (\text{B.1.4})$$

Hence there is a simple pole at $s = 0$ and infinitely many simple poles at $s_n = -\gamma_n^2$ for $n \in \mathbb{N}$, where γ_n are the roots of (B.1.4). After a trivial calculation, it is clear that

$$\text{Res}_{s=0} = \frac{1}{\alpha},$$

and, using L'Hôpital's rule, the residue at $s = s_n$ is given by

$$\text{Res}_{s=s_n} = -\frac{2 \cos(\gamma_n x) e^{-\gamma_n^2 t}}{\gamma_n [\gamma_n \cos(\gamma_n) + (\alpha + 1) \sin(\gamma_n)]}.$$

Then, applying the residue theorem, it follows from (B.1.3) that

$$c(x, t) = \sum_{n=1}^{\infty} \frac{2\alpha \cos(\gamma_n x) e^{-\gamma_n^2 t}}{\gamma_n [\gamma_n \cos(\gamma_n) + (\alpha + 1) \sin(\gamma_n)]}.$$

Re-arranging (B.1.4) to obtain $\alpha \cos(\gamma_n) = \gamma_n \sin(\gamma_n)$ and choosing $x = 1$ results in

$$c(1, t) = \sum_{n=1}^{\infty} \frac{2 \sin(\gamma_n) e^{-\gamma_n^2 t}}{\gamma_n \cos(\gamma_n) + (\alpha + 1) \sin(\gamma_n)},$$

the small β solution from case A, given by (2.4.10), to leading-order.

Large β solution for case A

Differentiating (B.1.1) and applying (B.2) gives

$$a(s) = -\frac{\alpha}{\beta [s^{3/2} \sinh(\sqrt{s})]},$$

so it follows from (B.1.2) that

$$c(x, t) = 1 - \frac{\alpha}{\beta} \mathcal{L}^{-1} \left\{ \frac{\cosh(\sqrt{s}x)}{s^{3/2} \sinh(\sqrt{s})} \right\}. \quad (\text{B.1.5})$$

After verifying that no branch points exist, this inverse Laplace transform is evaluated using the residue theorem. The poles are given by

$$s^{3/2} = 0 \quad \text{and} \quad \sinh(\sqrt{s}) = 0,$$

i.e. there is a pole of order 2 at $s = 0$ and infinitely many simple poles at $s_n = -n^2\pi^2$ for $n \in \mathbb{N}$. The residues are calculated by using L'Hôpital's rule to obtain

$$\begin{aligned} \text{Res}_{s=0} &= \frac{x^2}{2} + t - \frac{1}{6}, \\ \text{Res}_{s=s_n} &= \frac{2 \cos(n\pi x) e^{-n^2\pi^2 t}}{(-1)^{n+1} n^2 \pi^2}. \end{aligned}$$

Then, applying the residue theorem, it follows from (B.1.5) that

$$c(x, t) = 1 - \frac{\alpha}{\beta} \left(\frac{x^2}{2} + t - \frac{1}{6} + 2 \sum_{n=1}^{\infty} \frac{\cos(n\pi x) e^{-n^2\pi^2 t}}{(-1)^{n+1} n^2 \pi^2} \right).$$

Noting that $\cos(n\pi) = (-1)^n$ and choosing $x = 1$ results in

$$c(1, t) = 1 - \frac{\alpha}{\beta} \left(t + \frac{1}{3} - 2 \sum_{n=1}^{\infty} \frac{e^{-n^2\pi^2 t}}{n^2 \pi^2} \right),$$

the large β solution from case A, given by (2.4.14), to first-order.

B.2 Solutions for case B

Recall that from §2.5.1, (2.2.1) is solved subject to (2.2.2) and (2.2.3B) to obtain

$$\bar{c}(x, s) = a(s) \cosh(\sqrt{s}x) + \frac{\mu a(s)}{\sqrt{s}} \sinh(\sqrt{s}x) + \frac{1}{s}. \quad (\text{B.2.1})$$

and taking the inverse Laplace transform gives

$$c(x, t) = 1 + \mathcal{L}^{-1} \left\{ a(s) \left[\cosh(\sqrt{s}x) + \frac{\mu}{\sqrt{s}} \sinh(\sqrt{s}x) \right] \right\}. \quad (\text{B.2.2})$$

Now, (B.1) and (B.2) are applied in turn.

Small β solution for case B

Differentiating (B.2.1) and applying (B.1) gives

$$a(s) = -\frac{\alpha}{\sqrt{s}[(s + \alpha\mu) \sinh(\sqrt{s}) + \sqrt{s}(\alpha + \mu) \cosh(\sqrt{s})]},$$

so it follows from (B.2.2) that

$$c(x, t) = 1 - \alpha \mathcal{L}^{-1} \left\{ \frac{\sqrt{s} \cosh(\sqrt{s}x) + \mu \sinh(\sqrt{s}x)}{s[(s + \alpha\mu) \sinh(\sqrt{s}) + \sqrt{s}(\alpha + \mu) \cosh(\sqrt{s})]} \right\}. \quad (\text{B.2.3})$$

After verifying that no branch points exist, the residue theorem is used to evaluate this inverse Laplace transform. The poles are given by

$$s = 0 \quad \text{and} \quad (s + \alpha\mu) \sinh(\sqrt{s}) + \sqrt{s}(\alpha + \mu) \cosh(\sqrt{s}) = 0,$$

and, for convenience, setting $\sqrt{s} = i\xi$ in the transcendental equation gives

$$(\alpha\mu - \xi^2) \sin(\xi) + \xi(\alpha + \mu) \cos(\xi) = 0. \quad (\text{B.2.4})$$

Hence there is a simple pole at $s = 0$ and infinitely many simple poles at $s_n = -\xi_n^2$ for $n \in \mathbb{N}$, where ξ_n are the roots of (B.2.4). Using L'Hôpital's rule to calculate the residues gives

$$\begin{aligned} \text{Res}_{s=0} &= \frac{\mu x + 1}{\alpha\mu + \alpha + \mu}, \\ \text{Res}_{s=s_n} &= \frac{2[\xi_n \cos(\xi_n x) + \mu \sin(\xi_n x)] e^{-\xi_n^2 t}}{\xi_n [(\alpha\mu + \alpha + \mu - \xi_n^2) \cos(\xi_n) - \xi_n(2 + \alpha + \mu) \sin(\xi_n)]}. \end{aligned}$$

Then, applying the residue theorem, it follows from (B.2.3) that

$$c(x, t) = 1 - \alpha \left(\frac{\mu x + 1}{\alpha\mu + \alpha + \mu} + \sum_{n=1}^{\infty} \frac{2[\xi_n \cos(\xi_n x) + \mu \sin(\xi_n x)] e^{-\xi_n^2 t}}{\xi_n [(\alpha\mu + \alpha + \mu - \xi_n^2) \cos(\xi_n) - \xi_n(2 + \alpha + \mu) \sin(\xi_n)]} \right).$$

Re-arranging (B.2.4) to obtain $-\alpha[\xi_n \cos(\xi_n) + \mu \sin(\xi_n)] = \xi_n[\mu \cos(\xi_n) - \xi_n \sin(\xi_n)]$ and choosing $x = 1$ results in

$$c(1, t) = \frac{\mu}{\alpha\mu + \alpha + \mu} + \sum_{n=1}^{\infty} \frac{2[\mu \cos(\xi_n) - \xi_n \sin(\xi_n)] e^{-\xi_n^2 t}}{(\alpha\mu + \alpha + \mu - \xi_n^2) \cos(\xi_n) - \xi_n(2 + \alpha + \mu) \sin(\xi_n)},$$

the small β solution from case B, given by (2.5.11), to leading-order.

Large β solution for case B

Differentiating (B.2.1) and applying (B.2) gives

$$a(s) = -\frac{\alpha}{\beta s [\sqrt{s} \sinh(\sqrt{s}) + \mu \cosh(\sqrt{s})]},$$

so it follows from (B.2.2) that

$$c(x, t) = 1 - \frac{\alpha}{\beta} \mathcal{L}^{-1} \left\{ \frac{\sqrt{s} \cosh(\sqrt{s}x) + \mu \sinh(\sqrt{s}x)}{s^{3/2} [\sqrt{s} \sinh(\sqrt{s}) + \mu \cosh(\sqrt{s})]} \right\}. \quad (\text{B.2.5})$$

After verifying that no branch points exist, this inverse Laplace transform is evaluated using the residue theorem. The poles are given by

$$s^{3/2} = 0 \quad \text{and} \quad \sqrt{s} \sinh(\sqrt{s}) + \mu \cosh(\sqrt{s}) = 0,$$

and, for convenience, setting $\sqrt{s} = i\lambda$ in the transcendental equation gives

$$\mu \cos(\lambda) - \lambda \sin(\lambda) = 0. \quad (\text{B.2.6})$$

Hence there is a pole of order 2 at $s = 0$ and infinitely many simple poles at $s_n = -\lambda_n^2$ for $n \in \mathbb{N}$, where λ_n are the roots of (B.2.6). The residues are calculated by using L'Hôpital's rule to obtain

$$\begin{aligned} \text{Res}_{s=0} &= x + \frac{1}{\mu}, \\ \text{Res}_{s=s_n} &= -\frac{2[\lambda_n \cos(\lambda_n x) + \mu \sin(\lambda_n x)] e^{-\lambda_n^2 t}}{\lambda_n^2 [\lambda_n \cos(\lambda_n) + (\mu + 1) \sin(\lambda_n)]}. \end{aligned}$$

Then, applying the residue theorem, it follows from (B.2.5) that

$$c(x, t) = 1 - \frac{\alpha}{\beta} \left(x + \frac{1}{\mu} - \sum_{n=1}^{\infty} \frac{2[\lambda_n \cos(\lambda_n x) + \mu \sin(\lambda_n x)] e^{-\lambda_n^2 t}}{\lambda_n^2 [\lambda_n \cos(\lambda_n) + (\mu + 1) \sin(\lambda_n)]} \right).$$

Choosing $x = 1$ results in

$$c(1, t) = 1 - \frac{\alpha}{\beta} \left(1 + \frac{1}{\mu} - \sum_{n=1}^{\infty} \frac{2[\lambda_n \cos(\lambda_n) + \mu \sin(\lambda_n)] e^{-\lambda_n^2 t}}{\lambda_n^2 [\lambda_n \cos(\lambda_n) + (\mu + 1) \sin(\lambda_n)]} \right),$$

the large β solution from case B, given by (2.5.15), to first-order.

Bibliography

- [1] <https://www.kirkstall.com>. Accessed: Jan-2021.
- [2] L. Tomlinson, L. Hyndman, J. W. Firman, R. Bentley, J. A. Kyffin, S. D. Webb, S. McGinty, and P. Sharma. *In vitro* Liver Zonation of Primary Rat Hepatocytes. *Front Bioeng Biotechnol*, 7:17, 2019. doi: 10.3389/fbioe.2019.00017.
- [3] A. O’Keeffe, L. Hyndman, S. McGinty, A. Riezk, S. Murdan, and S. L. Croft. Development of an *in vitro* media perfusion model of *Leishmania major* macrophage infection. *PLoS One*, 14(7):e0219985, 2019. doi: 10.1371/journal.pone.0219985.
- [4] R. Ng. *Drugs: From Discovery to Approval*. John Wiley & Sons, Hoboken, NJ, 3rd edition, 2015. ISBN 978-1-118-90727-6.
- [5] R. Greek and L. A. Kramer. The Scientific Problems with Using Non-Human Animals to Predict Human Response to Drugs and Disease. In *Animal Experimentation: Working Towards a Paradigm Change*. Brill, 2019. ISBN 978-90-04-39119-2.
- [6] K. Archibald, R. Coleman, and T. Drake. Replacing Animal Tests to Improve Safety for Humans. In *Animal Experimentation: Working Towards a Paradigm Change*. Brill, 2019. ISBN 978-90-04-39119-2.
- [7] M. Wilkinson. The Potential of Organ on Chip Technology for Replacing Animal Testing. In *Animal Experimentation: Working Towards a Paradigm Change*. Brill, 2019. ISBN 978-90-04-39119-2.
- [8] K. Duval, H. Grover, L.-H. Han, Y. Mou, A. F. Pegoraro, J. Fredberg, and Z. Chen. Modeling Physiological Events in 2D vs. 3D Cell Culture. *Physiology*, 32:266–277, 2017. doi: 10.1152/physiol.00036.2016.
- [9] R. Edmondson, J. J. Broglie, A. F. Adcock, and L. Yang. Three-Dimensional Cell Culture Systems and Their Applications in Drug Discovery and Cell-Based Biosensors. *ASSAY Drug Dev Technol*, 12(4):207–218, 2014. doi: 10.1089/adt.2014.573.

- [10] S. Silvani, M. Figliuzzi, and A. Remuzzi. Toxicological evaluation of airborne particulate matter. Are cell culture technologies ready to replace animal testing? *J Appl Toxicol*, 39: 1484–1491, 2019. doi: 10.1002/jat.3804.
- [11] A. G. Souza, I. C. C. Ferreira, K. Marangoni, V. A. F. Bastos, and V. A. Goulart. Advances in Cell Culture: More than a Century after Cultivating Cells. *J Biotechnol Biomater*, 6(2): 1–4, 2016. doi: 10.4172/2155-952X.1000221.
- [12] C. Jensen and Y. Teng. Is It Time to Start Transitioning From 2D to 3D Cell Culture? *Front Mol Biosci*, 7:33, 2020. doi: 10.3389/fmolb.2020.00033.
- [13] M. Thiriet and K. H. Parker. Physiology and pathology of the cardiovascular system: A physical perspective. In *Cardiovascular Mathematics: Modeling and simulation of the circulatory system*. Springer Milan, Milano, 2009. ISBN 978-88-470-1152-6.
- [14] M. A. Swartz and M. E. Fleury. Interstitial Flow and Its Effects in Soft Tissues. *Annu Rev Biomed Eng*, 9:229–256, 2007. doi: 10.1146/annurev.bioeng.9.060906.151850.
- [15] J. Shemesh, I. Jalilian, A. Shi, G. H. Yeoh, M. L. K. Tate, and M. E. Warkiani. Flow-induced stress on adherent cells in microfluidic devices. *Lab Chip*, 15:4114–4127, 2015. doi: 10.1039/C5LC00633C.
- [16] A. Ravichandran, Y. Liu, and S.-H. Teoh. Review: bioreactor design towards generation of relevant engineered tissues: focus on clinical translation. *J Tissue Eng Regen Med*, 12: e7–e22, 2018. doi: 10.1002/term.2270.
- [17] G. Mestres, R. A. Perez, N. L. D’Elía, and L. Barbe. Advantages of microfluidic systems for studying cell-biomaterial interactions-focus on bone regeneration applications. *Biomed Phys Eng Express*, 5:032001, 2019. doi: 10.1088/2057-1976/ab1033.
- [18] U. Marx. Trends in cell culture technology. In *New Technologies for Toxicity Testing*. Springer, New York, NY, 2012. ISBN 978-1-4614-3054-4.
- [19] Y. Wen, X. Zhang, and S.-T. Yang. Medium to high throughput screening: microfabrication and chip-based technology. In *New Technologies for Toxicity Testing*. Springer, New York, NY, 2012. ISBN 978-1-4614-3054-4.
- [20] N. Salehi-Nik, G. Amoabediny, B. Pouran, H. Tabesh, M. A. Shokrgozar, N. Haghhighipour, N. Khatibi, F. Anisi, K. Mottaghy, and B. Zandieh-Doulabi. Engineering parameters in bioreactor’s design: a critical aspect in tissue engineering. *Biomed Res Int*, 2013:762132, 2013. doi: 10.1155/2013/762132.

- [21] P. Godara, C. D. McFarland, and R. E. Nordon. Design of bioreactors for mesenchymal stem cell tissue engineering. *J Chem Technol Biotechnol*, 83:408–420, 2008. doi: 10.1002/jctb.1918.
- [22] S. Damiati, U. B. Kompella, S. A. Damiati, and R. Kodzius. Microfluidic Devices for Drug Delivery Systems and Drug Screening. *Genes*, 9:103, 2018. doi: 10.3390/genes9020103.
- [23] J. Sun, A. R. Warden, and X. Ding. Recent advances in microfluidics for drug screening. *Biomicrofluidics*, 13:061503, 2019. doi: 10.1063/1.5121200.
- [24] P. Cui and S. Wang. Application of microfluidic chip technology in pharmaceutical analysis: A review. *J Pharm Anal*, 9:238–247, 2019. doi: 10.1016/j.jpha.2018.12.001.
- [25] Q. Wu, J. Liu, X. Wang, L. Feng, J. Wu, X. Zhu, W. Wen, and X. Gong. Organ-on-a-chip: recent breakthroughs and future prospects. *BioMed Eng OnLine*, 19:9, 2020. doi: 10.1186/s12938-020-0752-0.
- [26] M. D. Atkins. Velocity Field Measurement Using Particle Image Velocimetry (PIV). In *Application of Thermo-Fluidic Measurement Techniques*. Butterworth-Heinemann, 2016. ISBN 978-0-12-809731-1.
- [27] P. K. Panigrahi. Shear Stress Sensors. In *Encyclopedia of Microfluidics and Nanofluidics*. Springer, New York, NY, 2015. ISBN 978-1-4614-5491-5.
- [28] C. B. Allen, B. K. Schneider, and C. W. White. Limitations to oxygen diffusion and equilibration in in vitro cell exposure systems in hyperoxia and hypoxia. *Am J Physiol Lung Cell Mol Physiol*, 281:L1021–L1027, 2001. doi: 10.1152/ajplung.2001.281.4.L1021.
- [29] J. F. Wong, C. A. Simmons, and E. W. K. Young. Modeling and Measurement of Biomolecular Transport and Sensing in Microfluidic Cell Culture and Analysis Systems. In *Modeling of Microscale Transport in Biological Processes*. Academic Press, 2017. ISBN 978-0-12-804595-4.
- [30] R. D. O’Dea, H. M. Byrne, and S. L. Waters. Continuum Modelling of In Vitro Tissue Engineering: A Review. In *Computational Modeling in Tissue Engineering*. Springer, Berlin, Heidelberg, 2013. ISBN 978-3-642-32563-2.
- [31] S. L. Waters, L. J. Schumacher, and A. J. El Haj. Regenerative medicine meets mathematical modelling: developing symbiotic relationships. *npj Regen Med*, 6(24):1–8, 2021. doi: 10.1038/s41536-021-00134-2.
- [32] R. J. Shipley, A. F. Smith, P. W. Sweeney, A. R. Pries, and T. W. Secomb. A hybrid discrete–continuum approach for modelling microcirculatory blood flow. *Math Med Biol*, 37:40–57, 2019. doi: 10.1093/imammb/dqz006.

- [33] T. Sbrana and A. Ahluwalia. Engineering Quasi-Vivo[®] in Vitro Organ Models. In *New Technologies for Toxicity Testing*. Springer, New York, NY, 2012. ISBN 978-1-4614-3054-4.
- [34] W. Zhao, Y. Cheng, Z. Pan, K. Wang, and S. Liu. Gas diffusion in coal particles: A review of mathematical models and their applications. *Fuel*, 252:77–100, 2019. doi: 10.1016/j.fuel.2019.04.065.
- [35] R. Dohmen and R. Milke. Diffusion in Polycrystalline Materials: Grain Boundaries, Mathematical Models, and Experimental Data. *Rev Mineral Geochem*, 72:921–970, 2010. doi: 10.2138/rmg.2010.72.21.
- [36] P. Baveye and A. Valocchi. An evaluation of mathematical models of the transport of biologically reacting solutes in saturated soils and aquifers. *Water Resour Res*, 25(6): 1413–1421, 1989. doi: 10.1029/WR025i006p01413.
- [37] P. Tracqui. From passive diffusion to active cellular migration in mathematical models of tumour invasion. *Acta Biotheor*, 43:443–464, 1995. doi: 10.1007/BF00713564.
- [38] S. Wang, S. Mahali, A. McGuinness, and X. Lou. Mathematical models for estimating effective diffusion parameters of spherical drug delivery devices. *Theor Chem Acc*, 125: 659–669, 2010. doi: 10.1007/s00214-009-0649-2.
- [39] J. Demol, D. Lambrechts, L. Geris, J. Schrooten, and H. Van Oosterwyck. Towards a quantitative understanding of oxygen tension and cell density evolution in fibrin hydrogels. *Biomaterials*, 32:107–118, 2011. doi: 10.1016/j.biomaterials.2010.08.093.
- [40] F. Zhao, P. Pathi, W. Grayson, Q. Xing, B. R. Locke, and T. Ma. Effects of Oxygen Transport on 3-D Human Mesenchymal Stem Cell Metabolic Activity in Perfusion and Static Cultures: Experiments and Mathematical Model. *Biotechnol Prog*, 21:1269–1280, 2005. doi: 10.1021/bp0500664.
- [41] A. Przekwas and M. R. Somayaji. Computational pharmacokinetic modeling of organ-on-chip devices and microphysiological systems. In *Organ-on-a-chip*. Academic Press, 2020. ISBN 978-0-12-817202-5.
- [42] I. Burova, C. Peticone, D. De Silva Thompson, J. C. Knowles, I. Wall, and R. J. Shipley. A parameterised mathematical model to elucidate osteoblast cell growth in a phosphate-glass microcarrier culture. *J Tissue Eng*, 10:2041731419830264, 2019. doi: 10.1177/2041731419830264.
- [43] M. L. Yarmush, M. Toner, J. C. Y. Dunn, A. Rotem, A. Hubel, and R. G. Tompkins. Hepatic Tissue Engineering: Development of Critical Technologies. *Ann N Y Acad Sci*, 665:238–252, 1992. doi: 10.1111/j.1749-6632.1992.tb42588.x.

- [44] R. Chang and J. Overby. *Chemistry*. McGraw-Hill Higher Education, New York, NY, 13th edition, 2019. ISBN 978-1-259-91115-6.
- [45] P. Atkins, J. de Paula, and J. Keeler. *Atkins' Physical Chemistry*. Oxford University Press, Oxford, UK, 11th edition, 2018. ISBN 978-0-19-876986-6.
- [46] K. A. Johnson and R. S. Goody. The Original Michaelis Constant: Translation of the 1913 Michaelis-Menten Paper. *Biochemistry*, 50(39):8264–8269, 2011. doi: 10.1021/bi201284u.
- [47] D. B. Northrop. On the Meaning of K_m and V/K in Enzyme Kinetics. *J Chem Ed*, 75(9): 1153–1157, 1998. doi: 10.1021/ed075p1153.
- [48] L. L. Mazaleuskaya, K. Sangkuhl, C. F. Thorn, G. A. FitzGerald, R. B. Altman, and T. E. Klein. PharmGKB summary: Pathways of acetaminophen metabolism at the therapeutic versus toxic doses. *Pharmacogenet Genomics*, 25(8):416–426, 2015. doi: 10.1097/FPC.0000000000000150.
- [49] D. Reith, N. J. Medlicott, R. K. De Silva, L. Yang, J. Hickling, and M. Zacharias. Simultaneous Modelling of the Michaelis-Menten Kinetics of Paracetamol Sulphation and Glucuronidation. *Clin Exp Pharmacol Physiol*, 36:35–42, 2009. doi: 10.1111/j.1440-1681.2008.05029.x.
- [50] M. R. Spiegel. *Schaum's outline of theory and problems of Laplace transforms*. McGraw-Hill Book Co., New York, NY, 1965. ISBN 978-0-07-060231-1.
- [51] B. Jumarhon, S. McKee, and T. Tang. The proof of an inequality arising in a reaction-diffusion study in a small cell. *J Comp App Math*, 51:99–101, 1994. doi: 10.1016/0377-0427(94)90092-2.
- [52] J. R. Cannon. *The One-Dimensional Heat Equation*. Cambridge University Press, Cambridge, UK, 1984. ISBN 978-0-521-30243-2.
- [53] B. Jumarhon and S. Mckee. On the Heat Equation with Nonlinear and Nonlocal Boundary Conditions. *J Math Anal App*, 190:806–820, 1995. doi: 10.1006/jmaa.1995.1113.
- [54] B. D. MacArthur and R. O. C. Oreffo. From Mathematical Models to Clinical Reality. In *Principles of Tissue Engineering (Fourth Edition)*. Academic Press, Boston, MA, 2014. ISBN 978-0-12-398358-9.
- [55] J. C. Lipscomb, S. Haddad, T. Poet, and K. Krishnan. Physiologically-Based Pharmacokinetic (PBPK) Models in Toxicity Testing and Risk Assessment. In *New Technologies for Toxicity Testing*. Springer, New York, NY, 2012. ISBN 978-1-4614-3054-4.

- [56] R. J. Shipley, A. J. Davidson, K. Chan, J. B. Chaudhuri, S. L. Waters, and M. J. Ellis. A strategy to determine operating parameters in tissue engineering hollow fiber bioreactors. *Biotechnol Bioeng*, 108(6):1450–1461, 2011. doi: 10.1002/bit.23062.
- [57] J. W. Allen and S. N. Bhatia. Formation of steady-state oxygen gradients in vitro: application to liver zonation. *Biotechnol Bioeng*, 82(3):253–262, 2003. doi: 10.1002/bit.10569.
- [58] M. N. Hsu, G.-D. S. Tan, M. Tania, E. Birgersson, and H. L. Leo. Computational fluid model incorporating liver metabolic activities in perfusion bioreactor. *Biotechnol Bioeng*, 111(5):885–895, 2014. doi: 10.1002/bit.25157.
- [59] G. Vozzi, D. Mazzei, A. Tirella, F. Vozzi, and A. Ahluwalia. Finite element modelling and design of a concentration gradient generating bioreactor: application to biological pattern formation and toxicology. *Toxicol In Vitro*, 24:1828–1837, 2010. doi: 10.1016/j.tiv.2010.05.010.
- [60] D. Mazzei, M. A. Guzzardi, S. Giusti, and A. Ahluwalia. A low shear stress modular bioreactor for connected cell culture under high flow rates. *Biotechnol Bioeng*, 106(1): 127–137, 2010. doi: 10.1002/bit.22671.
- [61] G. Mattei, S. Giusti, and A. Ahluwalia. Design Criteria for Generating Physiologically Relevant In Vitro Models in Bioreactors. *Processes*, 2:548–569, 2014. doi: 10.3390/pr2030548.
- [62] J. M. Pedersen, Y.-S. Shim, V. Hans, M. B. Phillips, J. M. Macdonald, G. Walker, M. E. Andersen, H. J. Clewell, and M. Yoon. Fluid Dynamic Modeling to Support the Development of Flow-Based Hepatocyte Culture Systems for Metabolism Studies. *Front Bioeng Biotechnol*, 4:72, 2016. doi: 10.3389/fbioe.2016.00072.
- [63] P. Pearce, P. Brownbill, M. Janáček, J. and Jirkovská, L. Kubínová, I. L. Chernyavsky, and O. E. Jensen. Image-Based Modeling of Blood Flow and Oxygen Transfer in Feto-Placental Capillaries. *PLoS ONE*, 11(10):e0165369, 2016. doi: 10.1371/journal.pone.0165369.
- [64] S. C. Brenner and L. Ridgway Scott. *The Mathematical Theory of Finite Element Methods*. Springer Science & Business Media, New York, NY, 3rd edition, 2007. ISBN 978-0-387-75933-3.
- [65] <https://uk.comsol.com>. Accessed: Jan-2021.
- [66] J. C. Crittenden, R. R. Trussell, D. W. Hand, K. J. Howe, and G. Tchobanoglous. *MWH's Water Treatment: Principles and Design*. John Wiley & Sons, Hoboken, NJ, 3rd edition, 2012. ISBN 978-0-470-40539-0.

- [67] R. Milo and R. Phillips. *Cell Biology by the Numbers*. Garland Science, New York, NY, 2015. ISBN 978-0-8153-4537-4.
- [68] S. Mcginty and G. Pontrelli. On the role of specific drug binding in modelling arterial eluting stents. *J Math Chem*, 54:967–976, 2016. doi: 10.1007/s10910-016-0618-7.
- [69] A. C. F. Ribeiro, M. C. F. Barros, L. M. P. Veríssimo, C. I. A. V. Santos, A. M. T. D. P. V. Cabral, G. D. Gaspar, and M. A. Estesó. Diffusion coefficients of paracetamol in aqueous solutions. *J Chem Thermodyn*, 54:97–99, 2012. doi: 10.1016/j.jct.2012.03.014.
- [70] K. Sekine, Y. Kagawa, E. Maeyama, H. Ota, Y. Haraguchi, K. Matsuura, and T. Shimizu. Oxygen consumption of human heart cells in monolayer culture. *Biochem Biophys Res Commun*, 452:834–839, 2014. doi: 10.1016/j.bbrc.2014.09.018.
- [71] S. L. Nyberg, R. P. Remmel, H. J. Mann, M. V. Peshwa, W. S. Hu, and F. B. Cerra. Primary hepatocytes outperform Hep G2 cells as the source of biotransformation functions in a bioartificial liver. *Ann Surg*, 220(1):59–67, 1994.
- [72] L. Chen, K. Asai, T. Nonomura, G. Xi, and T. Liu. A review of Backward-Facing Step (BFS) flow mechanisms, heat transfer and control. *Therm Sci Eng Prog*, 6:194–216, 2018. doi: 10.1016/j.tsep.2018.04.004.
- [73] H. Kuhlmann and F. Romanò. The Lid-Driven Cavity. In *Computational Methods in Applied Sciences*. 2018. ISBN 978-3-319-91493-0.
- [74] A. R. Tzafriri, A. D. Levin, and E. R. Edelman. Diffusion-limited binding explains binary dose response for local arterial and tumour drug delivery. *Cell Prolif*, 42:348–363, 2009. doi: 10.1111/j.1365-2184.2009.00602.x.
- [75] F. Noor. The Changing Paradigm in Preclinical Toxicology: in vitro and in silico Methods in Liver Toxicity Evaluations. In *Animal Experimentation: Working Towards a Paradigm Change*. Brill, 2019. ISBN 978-90-04-39119-2.
- [76] D. Singh, W. C. Cho, and G. Upadhyay. Drug-Induced Liver Toxicity and Prevention by Herbal Antioxidants: An Overview. *Front Physiol*, 6:363, 2016. doi: 10.3389/f-phys.2015.00363.
- [77] E. L. LeCluyse, R. P. Witek, M. E. Andersen, and M. J. Powers. Organotypic liver culture models: meeting current challenges in toxicity testing. *Crit Rev Toxicol*, 42(6):501–548, 2012. doi: 10.3109/10408444.2012.682115.
- [78] T. Kietzmann. Metabolic zonation of the liver: The oxygen gradient revisited. *Redox Biol*, 11:622–630, 2017. doi: 10.1016/j.redox.2017.01.012.

- [79] I. Sorrell, R. J. Shipley, S. Regan, I. Gardner, M. P. Storm, M. Ellis, J. Ward, D. Williams, P. Mistry, J. D. Salazar, A. Scott, and S. Webb. Mathematical modelling of a liver hollow fibre bioreactor. *J Theor Biol*, 475:25–33, 2019. doi: 10.1016/j.jtbi.2019.05.008.
- [80] J. Leedale, H. E. Colley, H. Gaskell, D. P. Williams, R. N. Bearon, A. E. Chadwick, C. Murdoch, and S. D. Webb. In silico-guided optimisation of oxygen gradients in hepatic spheroids. *Comput Toxicol*, 12:100093, 2019. doi: 10.1016/j.comtox.2019.100093.
- [81] J. A. Leedale, B. Lucendo-Villarin, J. Meseguer-Ripolles, A. Kasarinaite, S. D. Webb, and D. C. Hay. Mathematical modelling of oxygen gradients in stem cell-derived liver tissue. *PLoS ONE*, 16(2):e0244070, 2021. doi: 10.1371/journal.pone.0244070.
- [82] R. E. Jeffries, M. P. Gamcsik, K. R. Keshari, P. Padiaditakis, A. P. Tikunov, G. B. Young, H. Lee, P. B. Watkins, and J. M. Macdonald. Effect of Oxygen Concentration on Viability and Metabolism in a Fluidized-Bed Bioartificial Liver Using ^{31}P and ^{13}C NMR Spectroscopy. *Tissue Eng Part C*, 19(2):93–100, 2013. doi: 10.1089/ten.tec.2011.0629.
- [83] F. T. Lee-Montiel, S. M. George, A. H. Gough, A. D. Sharma, J. Wu, R. DeBiasio, L. A. Verneti, and D. L. Taylor. Control of oxygen tension recapitulates zone-specific functions in human liver microphysiology systems. *Exp Biol Med*, 242:1617–1632, 2017. doi: 10.1177/1535370217703978.
- [84] R. Reithinger, J.-C. Dujardin, H. Louzir, C. Pirmez, B. Alexander, and S. Brooker. Cutaneous leishmaniasis. *Lancet Infect Dis*, 7:581–596, 2007. doi: 10.1016/S1473-3099(07)70209-8.
- [85] P. Kaye and P. Scott. Leishmaniasis: complexity at the host–pathogen interface. *Nat Rev Microbiol*, 9:604–615, 2011. doi: 10.1038/nrmicro2608.
- [86] D. Tegazzini, R. Díaz, F. Aguilar, I. Peña, J. L. Presa, V. Yardley, J. J. Martin, J. M. Coteron, S. L. Croft, and J. Cantizani. A Replicative In Vitro Assay for Drug Discovery against *Leishmania donovani*. *Antimicrob Agents Chemother*, 60(6):3524–3532. doi: 10.1128/AAC.01781-15.
- [87] E. Calvo-Álvarez, K. Stamatakis, C. Punzón, R. Álvarez Velilla, A. Tejería, J. Escudero-Martínez, Y. Pérez-Pertejo, M. Fresno, R. Balaña Fouce, and R. M. Reguera. Infrared Fluorescent Imaging as a Potent Tool for In Vitro, Ex Vivo and In Vivo Models of Visceral Leishmaniasis. *PLoS Neg Trop Dis*, 9(3):e0003666, 2015. doi: 10.1371/journal.pntd.0003666.
- [88] A. V. Yakh'ev, A. N. Osipov, O. A. Azizova, L. G. Korkina, B. T. Velichkovskii, and Y. A. Vladimirov. Oxygen consumption by peritoneal macrophages measured using electron paramagnetic resonance. *Biull Eksp Biol Med*, 99(4):443–445, 1985.

- [89] F. Weise, U. Fernekorn, J. Hampl, M. Klett, and A. Schober. Analysis and comparison of oxygen consumption of HepG2 cells in a monolayer and three-dimensional high density cell culture by use of a MatriGrid. *Biotechnol Bioeng*, 110(9):2504–2512, 2013. doi: 10.1002/bit.24912.
- [90] L. Hyndman, S. McKee, N. J. Mottram, B. Singh, S. D. Webb, and S. McGinty. Mathematical modelling of fluid flow and solute transport to define operating parameters for in vitro perfusion cell culture systems. *Interface Focus*, 10:20190045, 2020. doi: 10.1098/rsfs.2019.0045.